Modelling Dravet syndrome with human iPSC-derived neural circuits

Riccio, Federica

Awarding institution:
King's College London

Modelling Dravet syndrome with human iPSC-derived neural circuits

Federica Riccio

Primary supervisor: Dr Ivo Lieberam[1,2]

Secondary supervisor: Prof Juan Burrone[2]

1. Centre for Gene Therapy and Regenerative Medicine, King's College London

2. Centre for Developmental Neurobiology, King's College London

This thesis is submitted for the degree of

Doctor of Philosophy

February 2023

Acknowledgement

First and foremost, a huge thanks to Dr Ivo Lieberam and Prof Juan Burrone, who have both offered their unrelenting support and guidance throughout my PhD. The freedom you have given me over the past four years to develop my project and explore new ideas has provided the perfect backdrop for a PhD. Ivo, alongside your fun and inspiring supervision, I'll never forget your encyclopedic knowledge of spiders and taste for cosmopolitans! Juan, thanks for introducing me into the crazy and cool world of electrophysiology, and for giving me the opportunity to perform my first choreographed lab dance routine! I'd also like to offer special thanks to my 'third supervisor' Guilherme, who has been so incredibly generous with his time and support, spending hours teaching me patch clamping, assisting in experiments and offering invaluable advice – a massive thank you!

I would also like to thank my lab mates over the past few years from the Lieberam lab – Aimee, Caoimhe G, Sofia, Ieva, Lea, Steph, Vic and Gaby. A particularly big thank you to Pete, for making lab life so fun, for the great chats and cheeky pints, and to Caoimhe K for the friendship and enormous help taking care of the cell babies while I was writing up – I owe you more than one pint! Also, a huge thanks to the rest of the Burrone lab – Rachel, Winnie, Marcio, Vincenzo, Sally, Ben and Lily. You guys have been so welcoming and kind. A big thanks too to my PhD cohort who I'm sure are all going to go on to have amazing careers – you are all brilliant. To my other friends that I made along the way, Chris, Ella, Cristina and the entire 28th floor for creating such a fun working environment over the last few years. Thank you also to my family, friends and boyfriend, who have tolerated me at my craziest during this PhD journey – you're the best.

Finally, an enormous thanks to Francesca and Fiona for giving me the opportunity to carry out my PhD in such an incredible place, surrounded by such brilliant people. Also, to Fay, your support for me and all the other students in the department has been nothing short of heroic. You're always the go to person when there's a problem or issue and I've never known you not to be able to find a solution – thank you! It's been a fun and exciting journey and the Stem Cell Centre will always hold a special place in my heart.

Abstract

Dravet syndrome is a rare form of severe epilepsy primarily caused by loss-of-function mutations of the *SCN1A* gene. This gene encodes for the α1-subunit of the voltage-gated sodium channel NaV1.1, which is predominantly found in GABAergic inhibitory interneurons. Unlike most epilepsy conditions, that are characterised by increased activity of excitatory neurons, in Dravet syndrome the disease mechanism is thought to be associated with reduced activity of inhibitory interneurons. The leading hypothesis in the field is that expression of NaV1.1 mutant channels impairs the ability of interneurons to regulate network activity, therefore leading to generalised hyperexcitation and seizure events. This has been termed the 'interneuron hypothesis'. Current treatment options for Dravet syndrome are very limited, with many GABA agonists having surprisingly little effect.

Human induced Pluripotent Stem Cell (hiPSC) technology has permitted initial studies on neuronal cells derived from patients with Dravet syndrome. However, an *in vitro* disease model that accounts for the interaction between excitatory and inhibitory components of cortical circuits has yet to be established. Such a model could provide important insights into disease and drug mechanisms, as well as facilitating the discovery of novel treatments. For this study, we used a Dravet patient-derived hiPSC line (DS1) harbouring the $SCN1A^{IVS14+3A>T}$ loss-of-function mutation to generate a novel and comprehensive *in vitro* model of Dravet syndrome. Specifically, we have generated wildtype, DS1 and CRISPR-corrected isogenic control hiPSC lines suitable for differentiation into excitatory cortical neurons and inhibitory interneurons. We then combined inhibitory and excitatory neurons, together with mouse astrocytes, into a co-culture at physiological cell-type ratios to generate an *in vitro* model of cortical circuits.

Interestingly, single-neuron and network analysis show opposing phenotypes when comparing excitatory and inhibitory neurons over time. DS1 inhibitory interneurons undergo an initial phase of hyperactivity followed by a general reduction in firing properties in mature cultures, in line with previously reported GABAergic phenotypes. In contrast, in mature cultures, analysis of excitatory neurons shows a phenotype characterised by hyperexcitability and network hyperactivity in the DS1 model compared to controls. These findings are consistent in excitatory mono-cultures as well as in co-cultures, suggesting this is an innate phenotype of DS1 excitatory neurons that is independent from the compromised function of interneurons. Furthermore, using mixed genotype co-culture models we demonstrated that the presence of

the *SCN1A*$^{IVS14+3A>T}$ mutation in either the excitatory *or* the inhibitory component of the network is sufficient to cause a disease phenotype characterised by increased network activity.

With this work we present evidence of a previously uncharacterised contribution of excitatory neurons in Dravet syndrome pathogenesis. This previously overlooked excitatory contribution could explain the poor efficacy of current treatments mainly aimed at restoring basal levels of inhibition. Although these observations were made specifically in the context of the *SCN1A*$^{IVS14+3A>T}$ mutation, there have been a number of studies on other DS-related mutations that also demonstrate hyperexcitability of excitatory neurons, suggesting that our findings have potentially wider reaching implications, beyond the *SCN1A*$^{IVS14+3A>T}$ mutation.

Table of Contents

List of Figures

List of Tables

Nomenclature

Acronyms	Abbreviations
AAVS1	adeno-associated virus integration site 1
AED	Anti Epileptic Drugs
AIS	Axon Initial Segment
Ank-G	Ankyrin-G
AP	Action potential
Ara-C	cytosine arabinoside, cytarabine
Ca^{2+}	Calcium ions
CaV	Voltage-gated calcium channels
CBD	Cannabidiol
cDNA	complementary DNA
CNS	Central Nervous System
CRISPR	clustered regularly interspaced short palindromic repeats
D-V1	Directed dorsal differentiation version 1
D-V2	Directed dorsal differentiation version 2
D(number)	Day in vitro (number)
DEE	Developmental and Epileptic Encephalopathy
dNIM-1	Dorsal Neuronal Induction Medium-1
dNIM-2	Dorsal Neuronal Induction Medium-2
Dox	Doxycyclin
DS	Dravet syndrome
dsOligo	double strand oligonucleotide
FACS	Fluorescence-activated cell sorting
gDNA	genomic DNA
GECIs	Genetically Encoded Calcium Indicators
GOF	Gain-of-function
HDR	Homology-Directed Repair
hESCs	human Embrionic Stem Cells
hiPSCs	human induced Pluripotent Stem Cells
iAstro	inducible astrocytes

ICC	immunocytochemistry
iGABA	inducible GABAergic inhibitory interneruons
iGlut	inducible glutamatergic excitatory neruons
K^+	Potassium ions
Kv	Voltage-gated potassium channels
LOF	Loss-of-function
MACS	Magnetic-activated cell sorting
mAstro	mouse-derived astrocytes
MEAs	Multi-electrode arrays
mESCs	mouse Embrionic Stem Cells
MG	Matrigel
Na^+	Sodium ions
NaV	Voltage-gated sodium channels
NMM-1	Neuronal Maintenance Medium-1
NMM-2	Neuronal Maintenance Medium-2
P(number)	Post-natal day (number)
PB	PiggyBAC
PCR	**polymerase chain reaction**
PLO	Poly-L-Ornithine
PV	Parvalbumin
rtTA	reverse tetracycline transactivator
sEPSCs	spontaneous excitatory post-synaptic currents
sgRNA	Single guide RNA
sIPSCs	spontaneous inhibitory post-synaptic currents
SMEI	Severe Myoclonic Epilepsy of Infancy
SST	Somatostatin
SUDEP	Sudden Unexpected Death in Epilepsy
TC	Tissue culture
TRE	tetracycline response element
VIP	Vasoactive intestinal peptide
vNIM-1	Ventral Neuronal Induction Medium-1
vNIM-2	Ventral Neuronal Induction Medium-2

Chapter 1

Introduction

1.1 Human iPSC-derived cortical neural circuits

Historically, strategies to generate differentiated cell types from hiPSCs have focused on faithfully reproducing, in a dish using extrinsic factors, the molecular processes taking place during *in vivo* development. This approach, called directed differentiation, consists of the temporally controlled application of numerous small molecules and recombinant signalling proteins in order to differentiate hiPSCs into specific cell types. Directed differentiation has been successfully adopted to derive multiple cell lineages *in vitro*, however, a new approach is now emerging as a promising alternative for stem cell differentiation. Similar to direct reprogramming of somatic cells, this strategy, termed forward programming (Moreau et al., 2016), relies on the induced expression of lineage-specific transcription factors to directly convert hiPSCs into the desired cell types. This approach initially requires extensive screening to identify master transcription factors capable of controlling entire regulatory gene networks that determine cellular identity. However, once established, forward programming enables the rapid and homogenous generation of specific cell lineages at relatively low cost. In recent years, both directed differentiation and forward programming have been crucial in supporting the study of human neural circuits, with each approach providing useful platforms to model disease phenotypes *in vitro*.

1.1.1 Directed differentiation of hiPSCs to cortical networks

During *in vivo* development, neural induction is promoted through the inhibition of the bone morphogenetic protein (BMP) signalling pathway (Purves et al., 2001). BMP canonical signalling pathway is mediated by SMAD proteins, which, after being phosphorylated, translocate to the nucleus to regulate the transcription of target genes (R. N. Wang et al., 2014). During neural induction, inhibition of BMP signalling is mediated by BMP inhibitors such as noggin and chordin, which prevent SMAD phosphorylation and transduction (Purves et al., 2001). Following neural induction, ventral versus dorsal forebrain specification is determined by opposite gradients of Wnt and Sonic hedgehog (SHH). High concentrations of Wnt and low

concentrations of SHH promote dorsal forebrain specification by activating the expression of *PAX6*, the transcription factor necessary to generate excitatory neuron progenitors (Urbach & Technau, 2013). Conversely, low concentrations of Wnt and high concentrations of SHH promote ventral forebrain specification by activating the expression of *NKX2.1*, the transcription factor required for the development of GABAergic interneuron progenitors (Fuccillo et al., 2004).

hiPSC directed differentiation approaches have exploited our knowledge of *in vivo* brain development to recapitulate developmental processes *in vitro* and direct the differentiation of hiPSCs towards specific cellular fates. In the past fifteen years significant efforts have been made to develop directed differentiation protocols for the generation of several neuronal lineages (Kawasaki et al., 2000; H. Lee et al., 2007; K. S. Lee et al., 2012; Pang et al., 2011; Tornero et al., 2013; Watanabe et al., 2005). *In vitro*, neural induction is obtained through dual inhibition of SMAD signalling. This blockade, alone, results by default into a dorsal-type differentiation, inducing rapid and complete neural conversion to a predominantly excitatory dorsal forebrain fate (Fig. 1.1-A) (Chambers et al., 2009; Y. Shi et al., 2012). Soon after, this approach was modified to achieve ventral forebrain specification into GABAergic inhibitory interneurons (ventral-type differentiation) via inhibition of Wnt canonical pathways and subsequent activation of SHH signalling (Fig. 1.1-A) (Y. Liu, Liu, et al., 2013; Maroof et al., 2013). With all differentiation protocols, the efficiency in generating the desired cell type is far below 100%. Both ventral- and dorsal-type differentiations produce heterogenous populations of cells, only some of which form mature neurons (Y. Sun et al., 2016). A different approach consists in the differentiation of cortical progenitors capable of generating both excitatory and inhibitory neurons. These cultures are able to form synaptic networks *in vitro*, providing a system for the study of the development and function of cortical circuits in humans (Iida et al., 2018; J.-E. Kim et al., 2011; Kirwan et al., 2015; Mariani et al., 2012; Y. Shi, Kirwan, & Livesey, 2012; J. C. Xu et al., 2016).The approach used in these studies, however, does not permit for tuning of the relative ratios of inhibitory and excitatory neuronal populations, and thus these derived neuronal networks lack a physiological E/I balance (Nadadhur et al., 2017).

Over the last decade, 3-dimensional (3D) directed differentiation methods have been established, taking advantage of cell-intrinsic developmental programs to generate more complex neural tissue (Velasco et al., 2020). Early work from the Sasai and Knoblich groups showed that, when grown in 3D, even in the presence of minimal extrinsic signals, hiPSCs are

able to self-organise and spontaneously give rise to complex 3D structures resembling the developing human brain. These structures, termed whole-brain organoids, are characterised by the presence of broad regional identities, including the cerebral cortex, choroid plexus, and retina (Lancaster et al., 2013; Quadrato et al., 2017). If specific signalling molecules are introduced, the differentiation process can be directed to form specific brain regions, such as the cortex or basal ganglia, to generate so-called patterned brain organoids (Kadoshima et al., 2013; Mariani et al., 2012; Pasca et al., 2015; Qian et al., 2016; Sloan et al., 2017a; Velasco et al., 2019). Both these organoid models can generate many of the major cell types of a complex brain region, and their transcriptional identity correlates to that of the corresponding cell types in the endogenous brain (Camp et al., 2015; Quadrato et al., 2017; Velasco et al., 2019). Furthermore, within the organoid, different cell types are generated in the same temporal sequence observed in the developing human brain (Camp et al., 2015; Velasco et al., 2019). Together, these properties make brain organoids an incredibly valuable model for the study of human brain development and disease, however, some of the limitations associated with this technology must be considered. Most noticeably, organoids can have substantial batch-to-batch and organoid-to-organoid variability, with specific cell types being produced only by a subset of organoids and at variable ratios (Quadrato et al., 2017). Furthermore, organoids lack regional patterning and anatomical structural organisation (Velasco et al., 2020). To improve cellular diversity and make up for the lack of regional patterning, patterned brain organoids of different identity (e.g. dorsal and ventral forebrain identity) can be fused together to form assembloids (Vogt, 2021). For instance, dorsal and ventral forebrain organoids have been fused to study interneurons migration in the context of development and disease (Bagley et al., 2017; Birey et al., 2017; Sloan et al., 2018; Xiang et al., 2017). More recently, cortical, spinal and muscular organoids have been fused to form cortico-motor assembloids, offering a new exciting platform for the study of damage or degeneration of the cortico-motor circuits (Andersen et al., 2020).

Directed differentiation of hiPSCs has pioneered the field of *in vitro* developmental studies and disease modelling of human diseases. However, the high complexity and low reproducibility of these protocols has limited their use. While optimised and more specialised differentiation protocols continue to emerge, other differentiation strategies, such as forward programming, are gaining ground.

1.1.2 Forward programming of hiPSCs to neurons and glia

In recent years, forward programming of hiPSCs for neuronal derivation has become an appealing alternative to directed differentiation. Neural directed differentiation protocols are typically very time-consuming, requiring 4-6 weeks to generate neuronal progenitors and up to 7 additional weeks to achieve functional maturation (Tao & Zhang, 2016). Additionally, directed differentiation is characterised by high variability and low reproducibility. This is mainly caused by variability in the hiPSC response to signalling molecules, which results in intrinsic differences in differentiation potential across cell lines (B. Y. Hu et al., 2010; K. Kim et al., 2011; Koyanagi-Aoi et al., 2013; Osafune et al., 2008). Forward programming overcomes these limitations by rapidly inducing a neuronal fate through the forced expression of lineage-defining transcription factors that supersede the effects of intrinsic heterogeneity between hiPSC lines (Y. Zhang et al., 2013). In forward programming, transgene expression is typically regulated via Tetracycline-Controlled Transcriptional Activation (Gossen et al., 1995) with a Tet-ON system. This system is based on the mechanism of action of reverse tetracycline transactivator (rtTA) protein in response to tetracycline or its derivate, doxycycline. When bound to doxycycline, rtTA interacts with the TetO operator sequences of the tetracycline response element (TRE) present in the transgene promoter region causing initiation of transcription, thus allowing for doxycycline inducible gene expression (Fig. 1.1-B) (Das et al., 2016).

Using this method, hiPSCs can be rapidly converted to functional glutamatergic cortical neurons with high efficiency and purity by inducing the expression of a single gene, Neurogenin-2 (*NGN2*) (Fig. 1.1-C) (Frega et al., 2017; Nehme et al., 2018; Y. Zhang et al., 2013). *NGN2* is a proneural transcription factor expressed throughout the developing nervous system. It was shown to promote the commitment of neuronal progenitors towards dorsal fate (glutamatergic neurons) by inhibiting glial and GABAergic fate, inducing a cascade of pan-neuronal genes, promoting neuronal migration and cell cycle exit (Hulme et al., 2022). Similarly, the combined expression of *ASCL1* and *DLX2* was shown to induce highly efficient differentiation of hiPSCs to exclusively GABAergic interneurons (Fig. 1.1-C) (Barretto et al., 2020; Yang et al., 2017). The transcription factor *ASCL1* plays a role analogous to, but functionally divergent from *NGN2*. Indeed, opposite to *NGN2*, *ASCL1* promotes the specification of a ventral fate (GABAergic neurons) during the initial steps of neurogenesis (Aydin et al., 2019). On the other hand, *DLX2* determines neuronal versus oligodendroglial fate

acquisition by repressing the formation of oligodendrocyte precursor cells and promoting GABAergic interneuron specification (Petryniak et al., 2007). Finally, a culture of pure astrocytes can be obtained through forward programming of hiPSCs, by co-expressing *NF1B* and *SOX9* (Fig. 1.1-C) (Canals et al., 2018; X. Li et al., 2018a). *NF1* genes, including *NF1B*, are transcription factors responsible for the gliogenic switch and act by initiating glial-fate specification in neural progenitors (Rowitch & Kriegstein, 2010). Contrarily, *SOX9* is not required for the initiation of gliogenesis but instead it is necessary to maintain it by suppressing neurogenesis (Vong et al., 2015).

Integration of the rtTA and TRE-regulated transgenes into hiPSC lines is commonly achieved by lentiviral transduction, however, this strategy can result in variability of expression levels, random genomic insertion, transgene silencing and often requires additional purification steps to enrich for the desired cell population (Darabi et al., 2012; J. R. Smith et al., 2008a). An alternative and perhaps more refined approach consists of targeting genomic safe harbour sites (Sadelain et al., 2012) to achieve stable and reproducible transgene integration. Specifically, the AAVS1 (Oceguera-Yanez et al., 2016; J. R. Smith et al., 2008a), CLYBL (Cerbini et al., 2015; Fernandopulle et al., 2018) and Rosa26 loci (Bertero et al., 2016) are commonly targeted for safe integration in hESC/hiPSCs using CRISPS/Cas9 or TALE nuclease (TALEN) technology. This approach has been successfully used to produce engineered hiPSC lines for the generation of glutamatergic neurons (Fernandopulle et al., 2018; C. Wang et al., 2017) and GABAergic interneurons (Rhee et al., 2019).

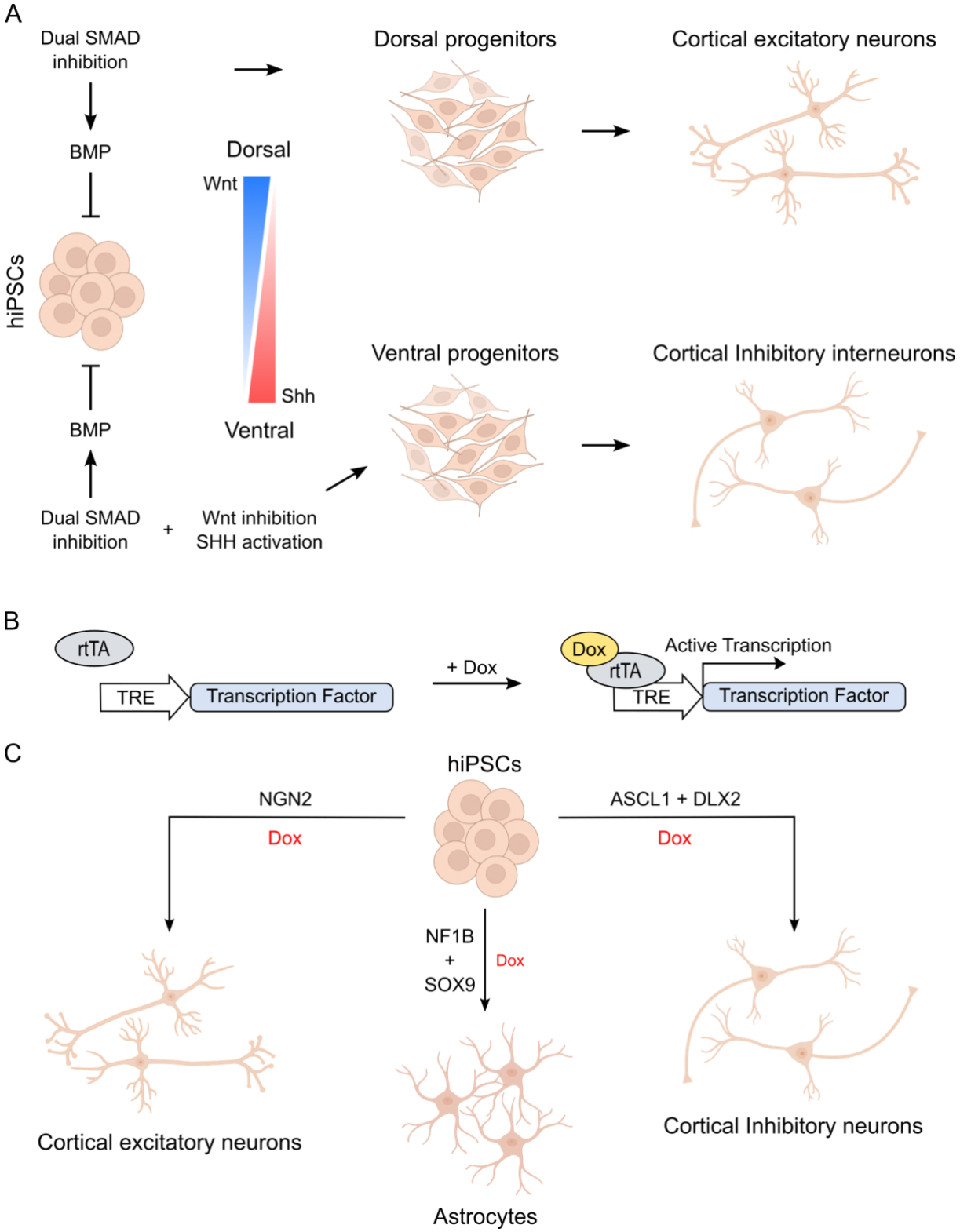
A
Dual SMAD inhibition
BMP
hiPSCs
BMP
Dual SMAD inhibition
+
Wnt inhibition SHH activation
Dorsal
Wnt
Shh
Ventral
Dorsal progenitors
Cortical excitatory neurons
Ventral progenitors
Cortical Inhibitory interneurons
B
rtTA
TRE
Transcription Factor
+ Dox
Dox
rtTA
TRE
Active Transcription
Transcription Factor
C
hiPSCs
NGN2
Dox
ASCL1 + DLX2
Dox
NF1B
+
SOX9
Dox
Cortical excitatory neurons
Astrocytes
Cortical Inhibitory neurons

Figure 1.1. *hiPSC cortical differentiation strategies.* **A –** Schematic representation of dorsal and ventral directed differentiation of hiPSCs. Initially, dual SMAD inhibition prevents BMP-mediated signalling and promotes neural induction. This inhibition is sufficient to direct the differentiation of hiPSCs towards neuronal progenitors of dorsal identity, which will generate cortical excitatory neurons. Instead, dual SMAD inhibition is followed by inhibition of the Wnt canonical pathway and activation of SHH signalling to direct the differentiation of hiPSCs towards neuronal progenitors of ventral identity, which will generate cortical inhibitory neurons. **B –** Tet-ON illustrative scheme. In the absence of doxycycline (Dox), the reverse tetracycline trans-activator (rtTA) is unable to bind to the tetracycline response element (TRE) in the transgene promoter region. When Dox is added, the newly formed Dox-rtTA complex can bind the TRE promoter and initiate transcription. **C –** Schematic representation of forward programming strategies to derive cortical neurons and astrocytes from iPSCs. Excitatory cortical neurons are obtained through the doxycycline-induced expression of NGN2 (left) while cortical inhibitory interneurons are produced by inducing the expression of ASCL1 and DLX2 (right). Similarly, the doxycycline-induced expression of NF1B and SOX9 causes differentiation of hiPSCs into astrocytes (centre).

1.2 Dravet Syndrome

Epilepsy is a disorder of the central nervous system (CNS) characterised by spontaneous, recurrent seizures (R. S. Fisher et al., 2005) that are defined as temporary manifestations of symptoms caused by an abnormal excessive excitation or synchronous neuronal activity in the brain (R. S. Fisher et al., 2014). Dravet syndrome (DS), is a rare form of epilepsy affecting 1 in every 20,000-40,000 births (Hurst, 1990). It was first described by Charlotte Dravet in 1978 as a new epilepsy syndrome characterised by typical myoclonic seizures (brief muscle spasms) and called "Severe Myoclonic Epilepsy of Infancy" (SMEI) (Dravet, 2011). Since many patients diagnosed with SMEI did not experience myoclonic seizures, the syndrome was later renamed Dravet syndrome (Dravet, 2011).

DS is considered an early-onset epilepsy syndrome characterised by three distinguishable stages (Dravet, 2011). The "pre-epileptic/onset" stage comprises the time preceding and including the onset of the disease. DS typically presents between 5 and 8 moths of age with an initial seizure that is usually prolonged and induced by hyperthermia (Verbeek et al., 2015). Indeed, first seizure manifestation triggered by fever is considered typical of DS and observed in up to 55% of subjects (W. Li et al., 2021). Following onset, prolonged and frequent seizures continue during the "severe" stage. This stage, comprising infancy and early childhood, is characterised by severe epileptic symptoms and onset of comorbidities including neurological deterioration and behavioural problems (Dravet, 2011). Tonic-clonic and hemiclonic seizures are the most common types of seizure in DS (W. Li et al., 2021). Tonic-clonic seizures are characterised by generalised, sustained (tonic) and then short and repetitive (clonic) muscle contractions, while hemi-clonic seizures consist of short and repetitive muscle contractions in only one side of the body (hemi). Episodes of status epilepticus are also frequent in DS, occurring with a lifetime prevalence of 75% (Strzelczyk et al., 2019). Status epilepticus is defined as a seizure lasting longer than 5 minutes or consecutive seizures without full recovery of consciousness in between them (D. M. Smith et al., 2016). The final stage of disease progression, termed "stabilisation", typically occurs after the age of 5 and involves convulsive seizures that persist throughout life but become shorter and less severe (Lagae et al., 2018).

In DS, the epileptic symptoms are accompanied by a series of common comorbidities. Developmental delays, associated with cognitive and speech impairment, usually manifest after the second year of life and are observed in 80% of subjects (Lagae et al., 2018). Motor deficits including slower motor development, hypotonia (low muscle tone), ataxia (poor muscle

control) and gait disturbances are described in 74% of patients with DS (Lagae et al., 2018). Furthermore, behavioural disorders are progressively observed with age in nearly 70% of cases, with attention deficit hyperactivity disorder (ADHD) and autism (or autistic-like behaviour) being the most prevalent (Brunklaus et al., 2012).

Patients with DS experience poor quality of life, and the long-term outcome is characterised by high epilepsy-related premature mortality, affecting up to 21% of DS cases (Dravet, 2011; Genton et al., 2011). Sudden Unexpected Death in Epilepsy (SUDEP) and status epilepticus account for up to 81% of fatalities, with 73% of deaths occurring before the age of 10 and 93% before the age of 20 (Shmuely et al., 2016).

1.2.1 Genetics of Dravet syndrome

Dravet syndrome is predominantly associated with mutations in genes encoding for neuronal voltage-gated sodium channels (NaV). These channels comprise of an α-subunit containing four homologous domains forming the channel pore and the inactivation gate (Fig. 1.2) (Catterall, 2000), and two accessory β-subunits that modulate voltage dependence, kinetics and localisation of the α-subunit (Messner & Catterall, 1985). Approximately 70-80% of DS cases are caused by mutations of the gene *SCN1A* encoding for the α1-subunit of the channel NaV1.1 (Marini et al., 2011). More than 500 different DS-associated mutations have been identified distributed throughout the entire *SCN1A* gene, including truncations, nonsense and missense mutations as well as splice-site changes (Marini et al., 2011). Several selected mutations taken from the H. Sun et al. (H. Sun et al., 2010) patient cohort are represented throughout the SCN1A protein in Fig.1.2. Genotype-phenotype association studies suggest that the severity of clinical symptoms may be related to the type or location of the *SCN1A* mutation. For example, nonsense or frameshift mutations and mutations in the pore region of the NaV1.1 channel are typically associated with a more severe phenotype (Meng et al., 2015). Roughly 90% of all *SCN1A* mutations are *de novo*, with familial mutations occurring only in 5-10% of cases (Claes et al., 2002; Harkin et al., 2007). Furthermore, almost all pathogenic *SCN1A* mutations are heterozygous, with their predominant effect considered to be loss-of-function (LOF), demonstrating haploinsufficiency of the *SCN1A* gene (Mantegazza, 2011; Meisler & Kearney, 2005). Considering the fundamental role of NaV channels in generating the rising phase of action potentials (Xu et al., 2019), LOF of the NaV1.1 channel should be consistent with decreased neuronal excitability and reduced network excitation. However, the pathophysiological mechanism of DS is thought to be dictated by the specialised expression of

NaV1.1 channels in inhibitory interneurons, where their LOF causes a lack of network inhibition which indirectly results in an increase in network excitation (Mantegazza, 2011; Ogiwara et al., 2007a) (pathophysiology of DS further discussed in section *1.1.2)*. Based on this mechanism, gain-of-function (GOF) mutations should have the opposite effect, that is to increase the activity of inhibitory interneurons and therefore result in an indirect decrease in network excitation. While *SCN1A* GOF mutations are primarily associated with familial hemiplegic migraine type 3 (FHM3) (Dichgans et al., 2005; Mantegazza & Cestèle, 2018; Vahedi et al., 2009), they have also been reported in several patients with atypical epilepsy phenotypes (Berecki et al., 2019; Clatot et al., 2022; Jaber et al., 2021; Sadleir et al., 2017; Spagnoli et al., 2019; Trump et al., 2016). Recently, a comprehensive study of *SCN1A* GOF mutations revealed an association between pathological presentation and the extent of GOF, with milder GOF causing early infantile epileptic encephalopathy and stronger GOF leading to FHM3 (Brunklaus et al., 2022). FHM3 variants cause hyperexcitability of inhibitory interneurons and the subsequent generation of spreading depolarisation (Chever et al., 2021), a pathological mechanism of migraine and a recognised anti-seizure mechanism (Tamim et al., 2021). Contrarily, epilepsy variants would cause a milder interneuron hyperexcitability, not sufficient to induce spreading depolarisation (Brunklaus et al., 2022). Interestingly, *SCN1A* GOF-associated epilepsies present an equally severe although very different phenotype compared to DS, characterised by a very early onset of non-febrile seizures and profound intellectual disability (Brunklaus et al., 2022). However, how a relatively moderate *SCN1A* GOF can cause such a severe epileptic phenotype is not yet understood.

This supposed indirect effect of *SCN1A* loss-of-function mutations distinguishes DS from most other forms of idiopathic epilepsy, where the effect of the mutation is directly linked to an increase in network excitation. For example, GOF mutations in the α2-subunit (*SCN2A*) of NaV1.2 channels, typical of benign familial neonatal-infantile seizures, exert a direct pro-excitatory effect by inducing hyperexcitability of excitatory neurons (Liao et al., 2010; Scalmani et al., 2006). Similarly, LOF mutations in different subunits of GABA-A receptors (*GABRA1, GABRB2, GABRB3* and *GABRG2*), found in many types of idiopathic epilepsies, exert a direct pro-excitatory effect by causing disinhibition of excitatory neurons (Johannesen et al., 2016; Kang & MacDonald, 2016; Maillard et al., 2022).

While *SCN1A* mutations account for the majority of DS cases, mutations in other genes have also been identified in patients with phenotypes compatible to DS. Specifically, other NaV

mutations affect the α2-subunit (*SCN2A*) of NaV1.2 channels (Ogiwara et al., 2009; X. Shi et al., 2009), the α9-subunit (*SCN9A*) of NaV1.7 channels (N. A. Singh et al., 2009) and the β1-subunit (*SCN1B*) (Patino et al., 2009). Rare mutations in non-NaV genes have also been linked with DS, including *KCNA2* (voltage-gated potassium channel Kv1.2) (Steel et al., 2017), *GABRA1* (GABA-A receptor α1-subunit), *GABRB3* (GABA-A receptor β3-subunit) and *GABRG2* (GABA-A receptor γ2-subunit) (Hernandez et al., 2021). Finally, mutations in non-channel genes, including *PCDH19* (protocadherin 19), *STXBP1* (syntaxin-binding protein 1) and *CHD2* (chromodomain helicase DNA-binding protein 2), have been in some cases associated with a Dravet-like phenotype (Steel et al., 2017). Approximately 15-20% of DS cases are of unknown aetiology, potentially suggesting the involvement of additional, currently unidentified genes (Marini et al., 2009).

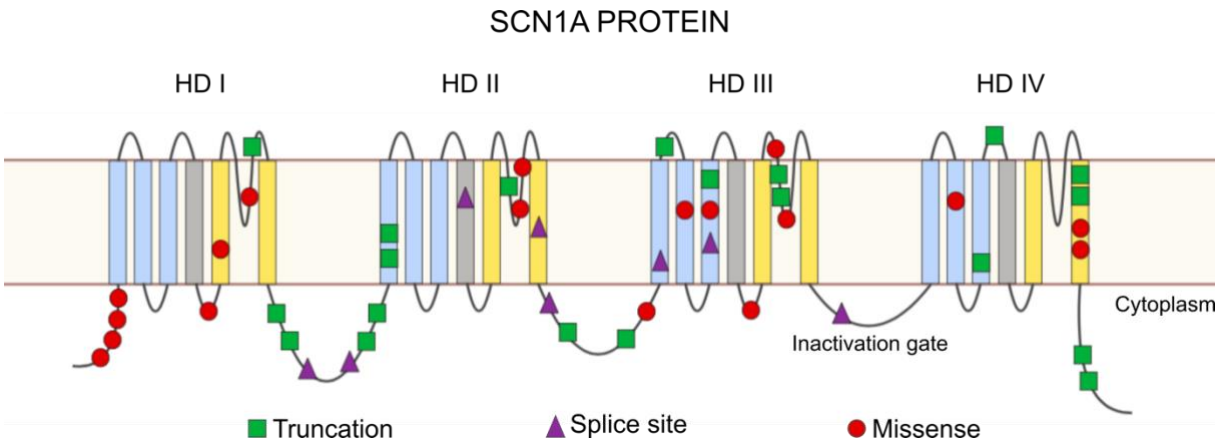

Figure 1.2 *SCN1A-associated mutations.* Schematic representation of the SCN1A protein, comprising of four homologous domains (HD I-IV) each of which containing 6 transmembrane segments: S1-S3 (blue), S4 voltage sensor (grey), S5-S6 pore region (yellow). Several mutations observed in the H. Sun, Y Zhang, X. Liu, et al. (H. Sun et al., 2010) patient cohort are represented throughout the protein.

1.2.2 Pathophysiology of Dravet syndrome

Voltage-gated sodium channels (NaV) contribute to neuronal electrical excitability. These channels are activated by membrane depolarisation which causes a voltage-dependent conformational change that increases the channel permeability to sodium ions (Na^+) (Xu et al., 2019). The influx of Na^+ in the cell causes further depolarisation of the membrane potential which is responsible for the rising phase of an action potential (Xu et al., 2019). The channels are then rapidly inactivated as part of the falling phase of the action potential resulting in its termination (Xu et al., 2019). Different NaV have distinct cellular and subcellular distribution as well as functional properties, and therefore play unique roles in the initiation and propagation of action potentials in distinct neuronal subsets and CNS regions (Escayg & Goldin, 2010). As previously mentioned, considering the important role of NaV in mediating neuronal firing, it is surprising that the reduced function of NaV1.1, one of the main sodium channels in the brain, leads to network hyperactivity.

The expression of *SCN1A,* the gene encoding for the α1-subunit of the channel NaV1.1, begins in infancy and early childhood and continues throughout life (Heighway et al., 2022). Studies in rodents and human brain tissue have demonstrated that NaV1.1 channels are primarily localised at the axon initial segment (AIS) of inhibitory interneurons, particularly somatostatin (SST) and parvalbumin (PV)-positive interneurons (T. Li et al., 2014; Lorincz & Nusser, 2008; Ogiwara et al., 2007a; Tian et al., 2014). Furthermore, the first mouse model of DS revealed that heterozygous *Scn1a* deletion resulted in reduced Na^+ current densities and reduced firing frequency in GABAergic inhibitory interneurons (particularly PV-positive interneurons) but not pyramidal excitatory neurons (F. H. Yu et al., 2006a). In healthy neuronal networks, GABAergic inhibitory interneurons regulate the activity of nearby excitatory neurons in response to feed-forward and feed-back inhibition mechanisms (Somogyi et al., 1998) (Fig. 1.3). Therefore, a reduction/loss of functional NaV1.1 in these neurons is thought to compromise the network balance between excitation and inhibition. Together, these observations gave rise to the so called “interneuron hypothesis”, whereby the impaired function of GABAergic inhibitory local circuits and networks subsequently results in the abnormal hyperexcitation and hypersynchrony responsible for epileptic seizures in DS (Fig. 1.3) (Mantegazza, 2011; Ogiwara et al., 2007a).

More than a decade of research on DS mouse models has supported this hypothesis (discussed in section *1.2.1*). Particularly, studies conducted in interneuron-specific *SCN1A* knock-out mouse models have really consolidated a major role for inhibitory interneurons in driving DS

disease phenotypes. While *SCN1A* deletion in GABAergic interneurons only is sufficient to recapitulate a DS phenotype (Cheah et al., 2012), conditional knock-out in specific interneurons subtypes has provided key insights into the pathophysiology of DS comorbidities. Specifically, deletion of *SCN1A* in PV interneurons resulted in an epileptic phenotype accompanied by ataxia (Ogiwara et al., 2013), hyperactivity and altered spatial memory (Tatsukawa et al., 2018) and social-deficits and autistic-like behaviour (Rubinstein, Han, et al., 2015). Contrarily, SST interneuron-specific *SCN1A* deletion caused epilepsy and hyperactivity but no autistic behaviour (Rubinstein, Han, et al., 2015). This type of studies really highlights the contribution of different interneuron subtypes to the behavioural and epileptic phenotype typical of DS.

However, more recently, studies in global *SCN1A* knock-out mice showed that reduced interneuron activity was only transient and limited to the severe stage of the disease (Favero et al., 2018; Tran et al., 2020a), suggesting that the pathological mechanism of chronic epilepsy in DS may be more complex. While NaV1.1 was reported to be located primarily at the AIS of inhibitory interneurons, in both mouse and human brain tissue this channel was also found to be expressed on the soma of pyramidal excitatory neurons (Ogiwara et al., 2013; Tian et al., 2014; W. Wang et al., 2011). In some mouse models, alongside reduced excitability of inhibitory interneurons, pyramidal neurons displayed increased Na^+ currents and hyperexcitability (Almog et al., 2021; Mistry et al., 2014). These studies would suggest a potential role for excitatory neurons in the pathophysiology of DS, so far however, experimental results across studies have proven to be inconsistent. Indeed, the interneuron-specific deletion of *Scn1a* was found to produce a more severe epileptic phenotype compared to deletion in both excitatory and inhibitory neurons, suggesting that loss of NaV1.1 in pyramidal cells might be partially protective (Ogiwara et al., 2013). A recent study investigated changes in the intrinsic, synaptic and network properties of hippocampal pyramidal neurons in a DS mouse model prior to disease onset, revealing important developmental changes to the intrinsic properties of these neurons. Notably, they reported an early phase of hypoexcitability (P10-12) and disrupted homeostatic plasticity in response to increased network activity (P10-12 and P14-16). Interestingly, these phenotypes were re-normalised by the age of seizure onset (P18-20), suggesting a role for excitatory neurons dysfunction in the early stages of networks development (S. P. Jones et al., 2022). The majority of evidence supporting a functional role for excitatory neurons in DS pathology has come from *in vitro* human models, generated using induced pluripotent stem cells (hiPSCs) derived from DS patients. These studies have reported increased Na^+ current densities and generalised hyperexcitability in hiPSC-derived pyramidal neurons (Jiao et al., 2013; Y. Liu,

Lopez-Santiago, et al., 2013). One recent study in particular, has shown that cultures of *SCN1A*-deficient excitatory neurons are sufficient to recapitulate mutation-specific phenotypes in networks where inhibitory interneurons are not present (van Hugte et al., 2023).

Overall, both mouse and human models provide important insights into the pathophysiology of DS, however, discordant results within and across models suggest that the exact disease mechanisms exerted by *SCN1A* mutations are not yet fully understood. For now, the interneuron hypothesis remains the most accepted disease mechanism. Nevertheless, continuous research and development of more refined disease models would provide further insights into the pathological mechanisms of DS.

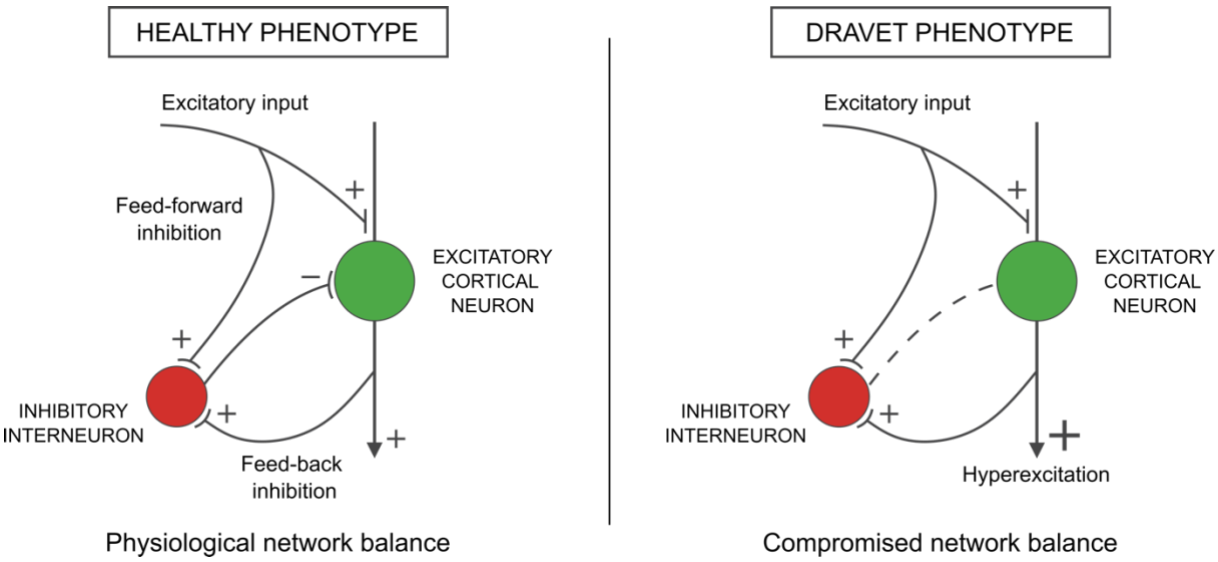

Figure 1.3. *Pathophysiological mechanism of Dravet syndrome, the "interneuron hypothesis".* Schematic representation of physiological and Dravet neuronal circuits. In healthy circuits (left), inhibitory interneurons regulate the activity of nearby excitatory neurons through direct inhibitory synapses activated in response to feed-forward and feedback inhibition mechanisms. When the activity of inhibitory interneurons is compromised, such as in Dravet syndrome (right), the network balance is severely altered, resulting in hyperexcitation.

1.2.3 Treatment strategies for Dravet syndrome

To date there is no effective treatment for Dravet syndrome, with no therapy able to achieve seizure freedom and normal cognitive/behavioural development. The main goal of current treatments is to reduce seizure frequency and improve cognitive and motor symptoms, however, drug resistance is often observed in patients with DS (Gataullina & Dulac, 2017). Until the early 2000s there were no medications specifically approved for DS, and common treatment regimens included combinations of generic Anti-Epileptic Drugs (AEDs) such as valproate, clobazam and topiramate. While the mechanism of action of AEDs is not always fully understood, all three of these compounds have been proposed to elicit a positive GABAergic effect by either increasing the total levels of GABA (valproate) or by acting as GABA receptor agonists (clobazam and topiramate) (Schubert-Bast et al., 2019). Stiripentol was the first drug specifically approved for the treatment of DS after being demonstrated to have antiepileptic efficacy in DS when prescribed in association with clobazam and valproate (Aras et al., 2015; Chiron et al., 2000). Stiripentol is an inhibitor of cytochrome P450 and was initially thought to act by an indirect mechanism, increasing the plasma concentration of concomitant AEDs (Perez et al., 1999). However, recent studies have suggested that stiripentol also possesses a direct anticonvulsant activity through positive allosteric modulation of GABA-A receptors (J. L. Fisher, 2009, 2011; Quilichini et al., 2006). More recently, two new drugs have been approved for use in DS. Cannabidiol (CBD), a phytocannabinoid contained in the cannabis plant, was approved as an additive agent while fenfluramine, an amphetamine derivative, was approved as an "add-on" or stand-alone treatment (He et al., 2022). Both treatments are showing remarkable results in reducing seizure frequency in patients with DS. Emerging surveillance studies revealed that up to 51% of patients treated with fenfluramine have stopped the concomitant dosage of other anti-seizure medications (Guerrini et al., 2022), suggesting that in many cases, the effect mediated by this drug, alone, is sufficient to achieve a satisfactory reduction of seizure frequency. While the exact mechanism of their anticonvulsant activity is not fully understood yet, both CBD and fenfluramine are thought to act through combined effects of increasing GABAergic inhibition as well as decreasing glutamatergic activity (P. Martin et al., 2021; Rosenberg et al., 2017; Y. Sun & Dolmetsch, 2018).

Collectively, observations on the efficacy of treatments in DS provide interesting insights into the mechanisms of DS pathophysiology. Traditional DS treatments involving the use of GABA-agonists aimed at restoring physiological levels of inhibition have demonstrated limited

efficacy in reducing seizure frequency. Instead, successful seizure control seems to be promoted through the synergistic action of enhancing inhibition while simultaneously reducing excitation. This could suggest that both a decrease in inhibition as well as an increase in excitation might play an active role in mediating the epileptic phenotype observed in DS.

Current pharmacological treatments focus on reducing seizure frequency and managing cognitive and behavioural symptoms, but they are often ineffective, rarely provide a long-term solution, and can be associated with significant side effects (Gataullina & Dulac, 2017). In recent years, gene therapy approaches are being investigated as viable alternatives for the treatment of DS (Chilcott et al., 2022; Higurashi et al., 2022). Rather than treating the symptoms, gene therapy aims to address the underlying genetic cause of the disorder. By delivering the corrected gene or modulating its expression, gene therapy seeks to restore normal neuronal function and reduce seizure activity more effectively than pharmacological approaches. In the case of *SCN1A*, gene *replacement* therapy is not the preferred option, due to the cDNA length (~6 kb) exceeding the packaging capacity of adeno-associated virus (AAV) (Chamberlain et al., 2016). However, several gene *regulation* therapies are currently being investigated in clinical trial or pre-clinical models (Chilcott et al., 2022). At the moment, the only therapeutic undergoing clinical trial is STK-001, an antisense oligonucleotide (ASO) developed by Stoke Therapeutics. STK-001 utilises a novel technology called Targeted Augmentation of Nuclear Gene Output (TANGO) (Lim et al., 2020).Specifically, STK-001 targets alternative *SCN1A* splice-sites, reducing the production of non-functional SCN1A mRNA and instead promoting the generation of functional full-length isoforms, thus increasing the production of Nav1.1 protein. This approach has been shown to rescue the excitability of PV interneurons, reduce seizures and improve survival in mouse models of DS (Z. Han et al., 2020; Wengert et al., 2022). Another gene regulation therapy called ETX101 (AAV9-RE^{GABA}-eTF^{SCN1A}) developed by Encoded Therapeutics, will soon undergo clinical trial. ETX101 uses AAV9 to deliver an engineered transcription factor (eTF^{SCN1A}) designed to upregulate the expression of endogenous *SCN1A.* Furthermore, the expression of eTF^{SCN1A} is targeted specifically to GABAergic inhibitory interneurons by a cell type-specific regulatory element (RE^{GABA}) incorporated into the AAV9 vector (Tanenhaus et al., 2022). ETX101 was able to increase *Scn1a* transcripts specifically within GABAergic inhibitory interneurons and resulted in prolonged survival and reduced spontaneous seizures in two DS mouse models (Tanenhaus et al., 2022) . Further gene regulation therapies are currently being developed and tested in animal models. Particularly, a recent CRISPR activation (CRISPRa) strategy has been shown to increase the expression of

endogenous *Scn1a* and restore $Na_V1.1$ protein levels in both cellular and animal models of DS, resulting in significant phenotypic improvements. In this strategy, a catalytically dead Cas9 (dCas9) fused to the transcriptional activator VP64 was packaged into AAV9 and co-delivered with a single gRNA targeting the *Scn1a* proximal promoter (AAV9-*Scn1a*-dCas9A - (Colasante et al., 2020)). In this instance, *Scn1a* activation is targeted to forebrain inhibitory interneurons using the interneuron-specific *Dlx5/6* promoter to control the expression of the regulatory CRISPRa elements. Following delivery of AAV9-*Scn1a*-dCas9A in a DS mouse model, the compromised electrophysiological properties of PV interneurons were rescued and the animals displayed increased threshold to hyperthermia-induced seizures (Colasante et al., 2020). Another ASO-based strategy was designed to target a novel SCN1A natural antisense transcript (SCN1ANAT). SCN1ANAT is a long non-coding RNA transcribed from the opposite strand of *SCN1A* that acts to reduce gene expression (Hsiao et al., 2016). Blocking SCN1ANAT with an ASO (termed AntagoNAT), resulted in upregulation of *SCN1A* in different DS cell models. In a mouse model of DS, AntagoNAT treatment restored the excitability of PV interneurons, reduced the number and duration of spontaneous seizures and increased the threshold to hyperthermia-induced seizures (Hsiao et al., 2016). Finally, a gene *replacement* therapy has been developed, using a high-capacity adenoviral vector (HC-AdV) to deliver a codon optimised version of the *SCN1A* gene (HCA-CAG-*SCN1A* – (Mora-Jimenez et al., 2021). These vectors are barren of all viral genes, allowing a cloning capacity of up to 37 kb and avoiding residual expression of viral genes in transduced cells (Ricobaraza et al., 2020). DS mice treated with HCA-CAG-*SCN1A* showed reduced epileptiform activity and sensitivity to hyperthermia-induced seizures, increased survival as well as improved motor functions and behavioural manifestations (Mora-Jimenez et al., 2021).

Collectively, gene therapy approaches offer a promising new avenue for the treatment of Dravet syndrome. However, the translation of pre-clinical data into trials is still lacking and further efforts will be required to determine the validity of these approaches in patients.

1.2.4 Neuronal excitability in Dravet syndrome

Neuronal excitability is an intrinsic neuronal property describing the propensity of a neuron to generate an action potential (AP) in response to an input stimulus. Intrinsic neuronal excitability can be modulated by various factors, including the neuron's biophysical properties and the profile, quantity and distribution of ion channels and neurotransmitter receptors (Brodal, 2016). Neuronal activity, instead, is an emerging property of neuronal networks and is the result of

numerous factors including the quality and quantity of external input signals, the intrinsic excitability of individual neurons and the excitation/inhibition (E/I) balance of the network, determined by the type, number and strength of synapses and the relative number of excitatory and inhibitory neurons within it (Brodal, 2016).

As previously discussed, reduced intrinsic excitability of GABAergic inhibitory interneurons is considered the predominant phenotype in DS. The first mouse model of DS showed that heterozygous *Scn1a* deletion resulted in reduced Na^+ current densities in inhibitory interneurons but not excitatory neurons. This reduction did not alter the threshold for the generation of single APs but compromised the ability of inhibitory interneurons to fire sustained trains of APs. The reduction in number, frequency and amplitude of action potentials fired by GABAergic interneurons resulted in a generalised decrease in their excitability (Yu et al., 2006). Using different mouse and human *in vitro* models, a similar phenotype has been observed in different interneuron subtypes, including PV, SST and VIP interneurons both in the hippocampus as well as in the cortex (Almog et al., 2021; Favero et al., 2018; Goff & Goldberg, 2019; Higurashi et al., 2013a; H. W. Kim et al., 2018; J. Liu et al., 2016a; Martín-Suárez et al., 2020; Mistry et al., 2014; Ogiwara et al., 2007a; Tai et al., 2014; Tsai et al., 2015). Decreased interneuron excitability, and therefore activity, is thought to compromise the network balance between excitation and inhibition and result in network hyperactivity. While reduced intrinsic excitability of inhibitory interneurons in DS is well documented, analysis of their activity in *in vivo* cortical networks showed no evidence of reduced activity during spontaneous cortical dynamics (De Stasi et al., 2016). However, during the stabilisation phase of DS, the activity of PV interneurons exhibited decreased synchronisation immediately before seizure onset (Tran et al., 2020a).

Alongside well characterised excitability/activity properties of inhibitory interneurons, a few studies reported altered excitability of pyramidal neurons. Indeed, increased Na^+ current densities in pyramidal excitatory neurons were observed in two mouse model studies. This increase was associated with a higher AP firing frequency, indicating an increase in neuronal excitability (Almog et al., 2021; Mistry et al., 2014). Similarly, several iPSC-based human models of DS have shown hyperexcitability of excitatory neurons characterised by increased Na^+ current density, higher AP amplitude and firing frequency as well as increased spontaneous bursting (Jiao et al., 2013; Y. Liu, Lopez-Santiago, et al., 2013; van Hugte et al., 2023).

Intrinsic excitability and neuronal activity are intimately linked and changes to one or the other can trigger the potentiation of homeostatic plasticity mechanisms to restore physiological balance. Synaptic and AIS plasticity are two well-established homeostatic mechanisms. For the purpose of this thesis, AIS-mediated plasticity will be discussed in more detail.

Axon initial segment (AIS) plasticity

The AIS is a specialised domain of the proximal axon molecularly defined by a unique cytoskeletal arrangement of scaffolding proteins and ion channels. The principal scaffolding protein found at the AIS is ankyrin G (Ank-G). This protein is found periodically spaced between actin rings and anchors NaV and Kv channels to the axonal membrane in a periodic manner (Huang & Rasband, 2018). Different types of NaV and Kv channels can be found at the AIS, including NaV1.1, NaV1.2 and NaV1.6 and Kv1.1, Kv1.2, Kv7.2 and Kv7.3. The specific channel composition and distribution along the AIS varies across neuron types and developmental stages (Huang & Rasband, 2018). In particular, while the AIS of GABAergic inhibitory interneurons mainly comprises NaV1.1 channels, in excitatory pyramidal neurons the AIS is populated proximally by NaV1.2 and distally by NaV1.6 channels (Duflocq et al., 2008; W. Hu et al., 2009). The high density of NaV channels found at the AIS was shown to be crucial for the generation and shaping of AP. As such, the AIS was demonstrated to be the primary site of AP initiation (Kole et al., 2008).

The length of the AIS (20-60 μm) and its distance from the soma have been shown to affect neuronal intrinsic excitability and AP properties. Theoretical studies have demonstrated that increasing AIS length is predicted to increase neuronal excitability via increasing sodium conductance density (Gulledge & Bravo, 2016). This directly proportional correlation between AIS length and excitability has also been extensively confirmed in different experimental settings (Chand et al., 2015; Evans et al., 2015; Jamann et al., 2021a; Telenczuk et al., 2017). On the other hand, assessing the correlation between AIS position and neuronal excitability has proven more complicated. Some theoretical models predict that, due to the resistive coupling between the soma and the AIS, a shorter distance between them reduces the axial resistance, which is inversely proportional to the amount of current necessary for axonal depolarisation. Thus, according to these models, a more proximal AIS should be associated with reduced neuronal excitability (Brette, 2013; Telenczuk et al., 2017). In contrast, other theoretical studies have reported that a shorter distance between the soma and the start of the AIS should reduce the dissipation of charges during propagation from the soma, thus, a more proximal AIS should

increase neuronal excitability (Gulledge & Bravo, 2016). Several experimental studies have shown results in line with these latter models, whereby a proximal shift of the AIS is accompanied by increased neuronal excitability characterised by lower current threshold and higher AP firing frequencies (Grubb & Burrone, 2010; Hatch et al., 2017; Lezmy et al., 2017; Wefelmeyer et al., 2015).

Remarkably, the structure of the AIS can undergo different forms of homeostatic plasticity in response to neuronal activity. Studies have shown that, in response to low neuronal activity (achieved through deprivation of input stimuli) the AIS extended in length, causing a homeostatic increase in neuronal excitability characterised by reduced current and voltage thresholds and increased spontaneous AP firing (Fig. 1.4) (Jamann et al., 2021a; Kuba et al., 2010). In contrast, in response to high neuronal activity (achieved through both acute and chronic depolarisation) shortening of the AIS resulted in a decrease in neuronal excitability, associated with higher current threshold and lower AP firing frequencies (Fig. 1.4) (Chand et al., 2015; Evans et al., 2015; Sohn et al., 2019). Furthermore, distal/proximal relocation of the AIS has also been observed in response to neuronal activity. High neuronal activity induced by chronic depolarisation treatments cause a distal relocation of the AIS, which resulted in a homeostatic reduction in excitability characterised by increased current threshold and lower AP firing frequencies. Additionally, this relocation was shown to reverse when neurons were returned to basal levels of activity (Fig. 1.4) (Grubb & Burrone, 2010; Hatch et al., 2017; Lezmy et al., 2017; Wefelmeyer et al., 2015).

Considering the important role of the AIS in mediating neuronal function and regulating neuronal excitability, and given that epilepsy-related mutations are often found in AIS resident proteins (including NaV and Kv), it is unsurprising that AIS dysfunction has been proposed as a possible mechanism in epileptogenesis (Wimmer et al., 2010). Despite this, AIS research in the context of genetic epilepsy is surprisingly limited, with only one study showing AIS dysfunction in a mouse model of DS. This study was limited to cortical PV interneurons, which showed AIS elongation during the severe and stabilisation stages. Lengthening of the AIS, initially, did not result in an increase in neuronal excitability (severe stage) however, neuronal excitability was restored during the stabilisation stage (Favero et al., 2018).

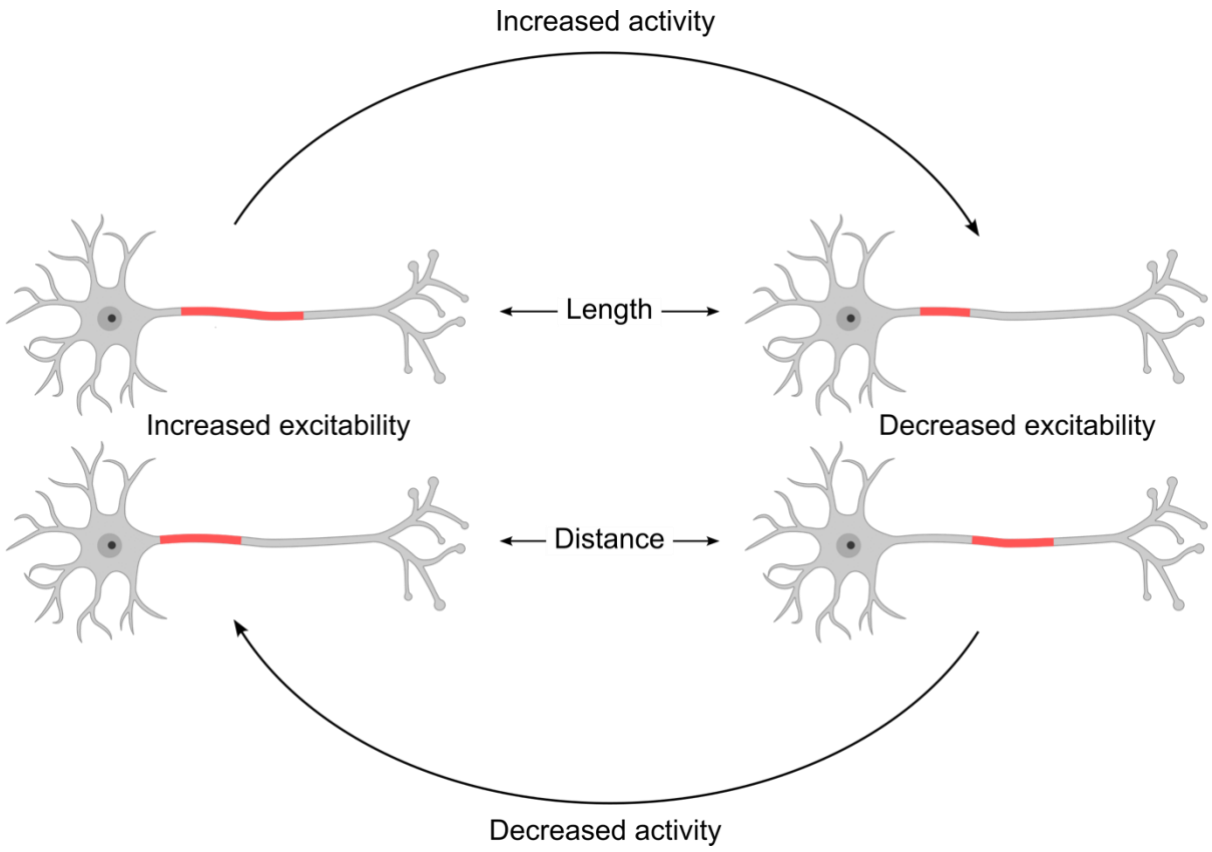

Figure 1.4. *AIS activity-dependent homeostatic plasticity.* Increased levels of neuronal activity can lead to shortening or distal relocation of the AIS (highlighted in red). Both these changes are associated with a decrease in intrinsic neuronal excitability. In contrast, decreased levels of neuronal activity can cause lengthening or proximal relocation of the AIS. These changes are associated with an increase in intrinsic neuronal excitability.

1.3 Current experimental models of Dravet syndrome

Dravet syndrome phenotypes and pathological mechanisms have been investigated with a variety of *in vivo* and *in vitro* experimental models. The first studies to assess the functional effects of *SCN1A* mutations were initially performed *in vitro* using immortalised human cancer cell lines. These studies revealed that most of the tested mutations resulted in complete loss-of-function (Mantegazza, 2011). Instead, the first pathophysiological studies were made possible by the generation of DS model organisms. A number of different model organisms have been adopted to study DS, including zebrafish and flies. However, the vast majority of DS research is typically conducted in mouse models (Griffin et al., 2018). More recently, with the advent of hiPSCs, *in vitro* human models have been established using neurons directly generated from hiPSCs derived from patients with DS (Isom, 2017). For the purpose of this thesis, only mouse

and human models will be discussed, as they represent the two most commonly adopted model systems.

1.3.1 In vivo/ex vivo mouse models of Dravet syndrome

Historically, Dravet syndrome phenotypes and pathological mechanisms have been investigated using mouse models. The first DS model was generated through heterozygous deletion of *Scn1a* exon 26. This loss-of-function deletion resulted in a severe epileptic phenotype and provided the first *in vivo* confirmation that *Scn1a* haploinsufficiency leads to seizures. As previously discussed, this study also demonstrated for the first time that *Scn1a* loss-of-function caused reduced intrinsic excitability of inhibitory interneurons – but not pyramidal neurons – isolated from the hippocampus at post-natal day (P) 14-16 (F. H. Yu et al., 2006a). Subsequent studies using the same loss-of-function mouse models showed reduced intrinsic excitability of putative PV and SST interneurons – but not pyramidal neurons – in cortical layer V at P21 (Tai et al., 2014). However, while these observations were made in dissociated neurons or brain slices, additional *in vivo* studies found no evidence of interneuron hypoexcitability and showed that the firing of PV and SST interneurons is unaltered during spontaneous cortical dynamics at P15-18 (De Stasi et al., 2016).

Another commonly used loss-of-function mouse model has been generated by heterozygous deletion of *Scn1a* exon 1. Similarly to the model previously described, these mice also showed decreased excitability of cortical PV interneurons. Interestingly, decreased PV interneuron excitability was observed at P18-21 but it was found to normalised by P35, while the excitability of pyramidal neurons appeared unaffected across developmental stages (Favero et al., 2018). The same mouse model was found to exhibit reduced Na^+ current densities in hippocampal GABAergic interneurons at P21, but only in a mouse strain associated with more severe epileptic phenotype. In contrast, increased Na^+ current densities and higher spontaneous firing frequency in hippocampal pyramidal neurons were observed independently of the mouse background strain, but only after P21 (Mistry et al., 2014). Additional studies on this mouse model showed that a subset of cortical vasoactive-intestinal peptide (VIP)-expressing interneurons also displayed reduced excitability and reduced repetitive firing in brain slices between P18 and P55 (Goff & Goldberg, 2019). Furthermore, an *in vivo* study showed that, while PV-interneuron firing was unaltered during spontaneous cortical dynamics, they exhibited decreased synchronisation immediately before seizure onset at later disease stages (P90) (Tran et al., 2020a).

Mouse models carrying specific *Scn1a* point mutations found in DS patients were also generated. Heterozygous knock-in of the R1407X truncation mutation resulted in recurrent epileptic seizures and sudden death after P18. Additionally, this study showed impaired fast spiking of putative cortical PV interneurons, while no differences were observed in pyramidal neurons (Ogiwara et al., 2007a). Another study showed that mice carrying the heterozygous R1848H missense mutations exhibited low levels of spontaneous generalised seizures but a higher susceptibility to drug- and hyperthermia-induced seizures. Bipolar inhibitory interneurons isolated from cortical tissue at P13-15 showed reduced Na^+ current densities but no signs of reduced intrinsic excitability. On the other hand, pyramidal neurons showed a tendency towards increased Na^+ current densities (M. S. Martin et al., 2010). Heterozygous knock-in of the E1099X truncation mutation resulted in early-onset spontaneous seizures and higher susceptibility to hyperthermia-induced seizures. PV-positive interneurons of the hippocampal dentate gyrus at P21-28 showed reduced intrinsic excitability and lower action potential amplitudes, while pyramidal neurons were not characterised. Furthermore, the number of NaV1.1 expressing interneurons was found to be reduced and the characterisation of spontaneous inhibitory/excitatory post-synaptic currents (sIPSCs/sEPSCs) showed decreased frequency of sIPSCs and increased frequency of sEPSCs (Tsai et al., 2015). Finally, mice carrying the heterozygous A1783V missense mutation were used to investigate numerous behavioural traits, comorbidities and hippocampal phenotypes (Fadila et al., 2020; Kuo et al., 2019; Ricobaraza et al., 2019; Styr et al., 2019). Particularly, developmental changes in the CA1 hippocampal circuit were investigated. This study found that the intrinsic excitability of interneurons within this network was reduced throughout all disease stages, with the greatest impairment observed during the severe stage. In contrast, excitatory neurons displayed a transient increase in excitability during the pre-epileptic stage, followed by reduced excitability during the severe stage (Almog et al., 2021). A summary of the main findings, including global disease phenotype as well as cell type-specific phenotypes, is reported for each mouse model in Table 1.1.

Several conditional knock-out mouse models have also been generated. Conditional heterozygous deletion of *Scn1a* in forebrain GABAergic interneurons was proved sufficient to cause epilepsy and premature death around P18-22 (Cheah et al., 2012). This mouse model was also shown to exhibit autistic-like behaviours (S. Han et al., 2012). Both these studies, however, did not investigate the contribution of pyramidal neurons. Two other studies, instead, performed conditional *Scn1a* heterozygous inactivation only in inhibitory interneurons or only in

excitatory neurons to assess the contribution of the different mutated populations to the epileptic phenotype (Dutton et al., 2013; Ogiwara et al., 2013). One study found that conditional *Scn1a* inactivation in hippocampal interneurons, but not excitatory neurons, was sufficient to increase the susceptibility to drug- and hyperthermia-induced seizures. Furthermore, reduced *Scn1a* expression in interneurons resulted in the generation of spontaneous seizures (Dutton et al., 2013). Similarly, PV-interneuron specific *Scn1a* inactivation was found to be sufficient to cause spontaneous epileptic seizures and ataxia. Interestingly, when *Scn1a* was inactivated in excitatory neurons, additionally to PV interneurons, this had a beneficial effect on the severe epileptic phenotype (Ogiwara et al., 2013). However, the presence of spontaneous epileptic activity in animals with selective inactivation of *Scn1a* in excitatory neurons only was not investigated in either study. Further studies on conditional knock-out mouse models revealed important insights into DS comorbidities. Conditional heterozygous deletion of *Scn1a* in PV interneurons was shown to lead to an increased susceptibility to hyperthermia-induced seizures accompanied by autistic like-behaviour with no hyperactivity. *Scn1a* inactivation in SST interneurons, instead, resulted in increased susceptibility to hyperthermia-induced seizures and hyperactivity, without autistic-like behaviour. When *Scn1a* was inactivated in both PV and SST interneurons, the mice displayed impaired cognition, assessed as the impairment of long-term spatial memory in context-dependant fear conditioning (Rubinstein 2015). A similar study confirmed the presence of epileptic and behavioural phenotypes in a PV interneuron-specific *Scn1a* knock-out model. These mice displayed spontaneous epileptic seizures as well as hyperactivity, impaired social novelty recognition and altered spatial memory. SST-interneuron specific *Scn1a* inactivation, instead, did not lead to either spontaneous epileptic activity nor behavioural abnormalities (Tatsukawa 2018). A summary of the main disease phenotype, including behavioural phenotypes, is reported for each conditional mouse model in Table 1.2.

Importantly, most of the described mouse models recapitulate the typical disease progression observed in DS patients, presenting with pre-epileptic, severe and stabilisation stages (Almog et al., 2021; Miller, Hawkins, McCollom, et al., 2014; Mistry et al., 2014; Oakley et al., 2009a; Ogiwara et al., 2007a; Tsai et al., 2015; F. H. Yu et al., 2006a). Moreover, many of these models also recapitulate hyperthermia-induced seizures, a phenotype typical of DS (Almog et al., 2021; Cheah et al., 2012; Dutton et al., 2013; Kalume et al., 2013; M. S. Martin et al., 2010; Oakley et al., 2009a; Ogiwara et al., 2007a; Tsai et al., 2015). However, numerous studies have also demonstrated that the presence and severity of seizure phenotypes as well as survival rates are highly dependent on the background strain of the mice (Kalume et al., 2013; Ogiwara et al.,

2007a; Rubinstein, Westenbroek, et al., 2015; F. H. Yu et al., 2006a). One study in particular has shown that impairment of Na^+ current densities and correlated severity of the phenotype were both age- and strain-dependant (Mistry et al., 2014). These differences have been attributed to strain-specific genetic modifier genes (Miller, Hawkins, McCollom, et al., 2014).

Collectively, work performed in mouse models largely supports the interneuron hypothesis. However, most studies only demonstrate that *Scn1a* loss-of-function in inhibitory interneurons is sufficient to produce seizures. In itself, the observation that targeted deletion of an important sodium channel in GABAergic neurons results in network hyperexcitability is not surprising. Furthermore, reduced interneuron excitability has been almost exclusively characterised during the second and third post-natal week (P10-21), because this period coincides with the start of NaV1.1 expression. This stage is the equivalent of 2/3 years of age in humans, corresponding to the severe stage of DS progression (Griffin et al., 2018). Phenotypes of pre-epileptic and stabilisation stages have not been thoroughly characterised and may reveal more complex pathophysiological mechanisms.

Mouse model	Disease phenotype	Approach	GABAergic interneurons phenotype	Pyramidal neurons phenotype	Study (citation)
Scn1a exon 26 heterozygous deletion	Spontaneous seizures and sporadic death after P21	*Ex vivo* (dissociated neurons)	Reduced Na^+ current density and reduced intrinsic excitability (hippocampus P14-16)	No phenotype	(F. H. Yu et al., 2006b)
		Ex vivo (brain slices)	Reduced intrinsic excitability of PV and SST interneurons (cortical layer V P21)	No phenotype	(Tai et al., 2014)
		In vivo	Unaltered firing of PV and SST interneurons during spontaneous dynamics (neocortex P15-18)	No phenotype	(De Stasi et al., 2016)
Scn1a exon 1 heterozygous deletion	Spontaneous and temperature-induced seizures, sudden death, hyperactivity and deficits in social behaviour. Severity of disease phenotypes was shown to be strain-dependant.	*Ex vivo* (dissociated neurons)	Reduced Na^+ current density only in the mouse strain with more severe epileptic phenotype (hippocampus P21)	Increased Na^+ current density and higher spontaneous firing frequency independently of the strain (hippocampus >P21)	(Mistry et al., 2014)
		Ex vivo (brain slices)	Reduced Na^+ current density and reduced intrinsic excitability of PV interneurons (somatosensory cortex P18-21) Restored Na^+ current density and intrinsic excitability of PV interneurons (somatosensory cortex P35-56)	No phenotype	(Favero et al., 2018)
		Ex vivo (brain slices)	Reduced intrinsic excitability of VIP interneurons (somatosensory cortex P18-21, P30-55)	Not investigated	(Goff & Goldberg, 2019)

		In vivo	Higher mean activity at baseline but decreased synchrony of PV interneurons immediately before seizure onset (neocortex P90)	Higher mean activity at baseline (neocortex P90)	(Tran et al., 2020a)
Heterozygous R1407X truncation mutation	Spontaneous seizures and sudden death after P18	*Ex vivo* (brain slices)	Impaired fast-spiking of putative PV interneurons (neocortex P25-29)	No phenotype	(Ogiwara et al., 2007b)
Heterozygous R1848H missense mutations	Infrequent spontaneous seizures but higher susceptibility to drug- and hyperthermia-induced seizures	*Ex vivo* (dissociated neurons)	Reduced Na^+ current density but normal intrinsic excitability (cortex P13-15)	Tendency towards increased Na^+ current densities (cortex P13-15)	(M. S. Martin et al., 2010)
Heterozygous E1099X truncation mutation	Early-onset spontaneous seizures and higher susceptibility to hyperthermia-induced seizures	*Ex vivo* (brain slices)	Reduced number of NaV1.1 expressing interneurons. Reduced intrinsic excitability and lower action potential amplitudes of PV interneurons. (hippocampal dentate gyrus P21-28)	Not investigated	(Tsai et al., 2015)
Heterozygous A1783V missense mutation	Frequent spontaneous seizures and susceptibility to hyperthermia-induced seizures	*Ex vivo* (brain slices)	Reduced intrinsic excitability throughout all disease stages, with the greatest impairment observed during the severe stage (hippocampus P14, P21, P35)	Transient increase in excitability during the pre-epileptic stage, followed by reduced excitability during the severe stage (hippocampus P14, P21, P35)	(Almog et al., 2021)

Table 1.1 – Summary of the main findings in DS mouse model studies.

Mouse model	**Behavioural phenotype**	**Study (citation)**
Conditional heterozygous deletion of *Scn1a* in forebrain **GABAergic interneurons**	Spontaneous seizures, susceptibility to hyperthermia-induced seizures and sudden death after P18-22	(Cheah et al., 2012)
Conditional heterozygous deletion of *Scn1a* in **PV interneurons**	Spontaneous generalised seizures and increased susceptibility to drug- and hyperthermia-induced seizures	(Dutton et al., 2013)
Conditional heterozygous deletion of *Scn1a* in **pyramidal neurons**	No alteration of susceptibility to drug- and hyperthermia-induced seizures	
Conditional heterozygous deletion of *Scn1a* in **PV interneurons**	Spontaneous epileptic seizures and ataxia	(Ogiwara et al., 2013)
Conditional heterozygous deletion of *Scn1a* in **PV interneurons and pyramidal neurons**	Amelioration of severe epileptic phenotype	
Conditional heterozygous deletion of *Scn1a* in **PV interneurons**	Increased susceptibility to hyperthermia-induced seizures, autistic like-behaviour	(Rubinstein, Han, et al., 2015)
Conditional heterozygous deletion of *Scn1a* in **SST interneurons**	Increased susceptibility to hyperthermia-induced seizures, hyperactivity	
Conditional heterozygous deletion of *Scn1a* in **PV interneurons**	Spontaneous epileptic seizures, hyperactivity, impaired social novelty recognition, and altered spatial memory	(Tatsukawa et al., 2018)
Conditional heterozygous deletion of *Scn1a* in **SST interneurons**	No spontaneous seizures, only increased susceptibility to hyperthermia-induced seizures, no behavioural abnormalities	

Table 1.2 – Summary of the main findings in DS conditional knock-out models.

1.3.2 In vitro human models of Dravet syndrome

Alongside well-established animal models, in an attempt to further understand the mechanisms involved in DS pathology, human *in vitro* models have also been employed. Before the advent of hiPSCs, *in vitro* human models of DS mainly consisted of artificial expression systems, typically involving cancer cell lines which expressed exogenously transfected human genes harbouring DS mutations (Mantegazza, 2011). While these systems are relatively cheap and provide good recording conditions for whole-cell patch clamping, they also have important intrinsic disadvantages. Standard expression systems lack a neuronal cell background, are not able to form neuronal circuits, and the protein of interest is normally overexpressed at non-physiological levels (Mantegazza, 2011). In order to develop more representative human models of DS, recent work has used hiPSCs derived from Dravet patients to generate cortical neurons. hiPSCs have many advantages: they possess an unlimited capability for self-renewal, can be differentiated into diverse and specific neuronal populations and, by retaining their genotype, allow for the generation of disease models that recapitulate the exact genetic background of Dravet patients. The number of studies performed on hiPSC-based DS models represent a small fraction compared to mouse model studies. Nonetheless, in the past decade, Dravet patient-derived hiPSCs have been used to study the effect of specific mutations (Higurashi et al., 2013a; Y. Sun et al., 2016), uncover novel disease mechanisms (Y. Liu, Lopez-Santiago, et al., 2013) and characterise disease phenotypes (Jiao et al., 2013a; van Hugte et al., 2023). Several of these studies have focused exclusively on patient-derived GABAergic inhibitory interneurons. The investigation of disease phenotypes in particular interneuron subtypes is limited by the lack of specificity of current differentiation protocols, however, cultures of mixed GABAergic interneurons can be obtained through various differentiation strategies.

hiPSC-derived interneurons (primarily SST and calretinin - CR) carrying the c.4933C>T truncation mutation displayed reduced intrinsic excitability, characterised by lower AP firing frequency (Higurashi et al., 2013a). Similarly, the missense mutation c.5768A>G was shown to cause decreased excitability of GABAergic interneurons, with reduced Na^+ current densities, reduced AP amplitude and frequency. Furthermore, these neuronal cultures were found to display a lower frequency of sIPSCs and a higher frequency of sEPSCs (J. Liu et al., 2016a). Another study characterised the effect of two different mutations, missense c.4261G > T and frameshift c.3576_3580. Both mutations resulted in decreased intrinsic excitability of

interneurons (mainly SST), characterised by reduced Na^+ currents and lower AP firing frequency. Interestingly, the severity of the phenotype observed matched the symptomatic severity of the donors (H. W. Kim et al., 2018).

Additional patient-derived hiPSC studies have investigated disease phenotypes in both excitatory and inhibitory neurons. Phenotypes inferred by the missense mutation S1328P were characterised in telencephalic excitatory and inhibitory neurons (mainly SST and CR) separately derived. While excitatory neurons displayed normal Na^+ currents and firing properties, GABAergic interneurons were found to display reduced excitability, characterised by reduced Na^+ current densities and firing frequency (Y. Sun et al., 2016). The IVS14+3A>T splice donor site mutation and the c.975T>A truncation mutations were investigated in mixed neuronal cultures containing forebrain pyramidal neurons and calbindin (CB), CR, SST and PV interneurons. Interestingly, both mutations were found to confer hyperexcitability to both excitatory and inhibitory neurons. Indeed, both types of neurons displayed increased Na^+ current densities, increased repetitive firing frequency and spontaneous bursting activity (Y. Liu, Lopez-Santiago, et al., 2013). However, it is important to note that neuronal identity was only assessed based on morphology (pyramidal vs. bipolar). hiPSC-derived neurons in culture can assume morphologies that differ substantially from the pyramidal or bipolar morphology that is considered typical of excitatory or inhibitory neurons, respectively. Therefore, a classification based solely on morphology cannot be considered at all accurate. In this case, a bias towards the most abundant neuronal identity present in culture (80-90% inhibitory interneurons) should be taken into consideration (Y. Liu, Lopez-Santiago, et al., 2013).

Finally, two studies investigated the effects of various *SCN1A* mutations on cultures containing only cortical glutamatergic excitatory neurons. The Q1923R and F1415I missense mutations were both found to increase the excitability of glutamatergic neurons, causing increased Na^+ currents, higher AP amplitudes and firing frequency (Jiao et al., 2013a). Hyperexcitability of glutamatergic neurons was also consistently observed across 5 different patient lines and 2 CRISPR-mutated lines, all harbouring different *SCN1A* mutations. Interestingly, excitatory networks displayed increased rates of high frequency bursts that were aggravated by fever-like temperatures (van Hugte et al., 2023).

Overall, research in hiPSC-based DS models is in agreement with previous observations on the reduced excitability of inhibitory interneurons. However, several studies have also consistently reported hyperexcitability of glutamatergic neurons, suggesting that these neurons might also

play a role in DS pathology. Importantly, the characterisation of DS phenotypes within these models was mainly performed in isolated cultures of either inhibitory or excitatory neurons. While these models offer important new insights into the pathophysiology of DS, the lack of interactions between the excitatory and inhibitory components of neural networks does not allow for a comprehensive study of disease phenotypes.

1.4 Hypothesis and project aims

While the majority of Dravet syndrome (DS) research has historically been carried out using animal models, more recently, an increasing number of studies have used patient-derived hiPSCs to generate neuronal models that recapitulate the exact genetic background of Dravet patients. However, characterisation of DS phenotypes within these models was performed in isolated cultures of either inhibitory or excitatory neurons. These models offered important new insights into DS disease mechanisms, suggesting that excitatory neurons might play an active role in the pathophysiology of DS. However, in these studies, the lack of an interacting network composed of both excitatory and inhibitory neurons does not allow for a comprehensive study of disease phenotypes. Our central hypothesis is that Dravet syndrome occurs as the result of a complex pathoetiology emerging from the active contribution of both excitatory and inhibitory neurons. We predict that network disinhibition is not the only pathological mechanism in DS, but instead, innate excitatory hyperactivity acts synergically with disinhibition to generate the epileptic phenotype. Thus, the generation of an *in vitro* model composed of inhibitory *and* excitatory neurons forming functional, ratio-defined networks, could provide a more powerful tool for the study of DS pathology and uncover novel disease mechanisms.

Therefore, the principal aim of this work was to generate a novel *in vitro* human model of cortical circuits with physiological excitation/inhibition balance, and apply it to the study of DS disease mechanisms inferred by the *SCN1A*$^{\text{IVS 14+3A>T}}$ loss-of-function mutation.

The individual aims of this projects were to:

- Generate separately derived populations of cortical excitatory neurons, inhibitory interneurons and astrocytes from hiPSCs.
    - Test dorsal and ventral directed differentiation protocols.
    - Generate hiPSC subclone lines suitable for forward programming.
    - Test forward programming strategies for the generation of excitatory and inhibitory neurons and astrocytes.
- Generate an *in vitro* model of cortical circuits with physiological cell type ratio suitable for the study of disease phenotypes.

- Establish a co-culture comprising 70% excitatory neurons, 30% inhibitory interneurons and astrocytes to resemble the human cortex E/I ratio.
- Generate co-culture models from wildtype, Dravet and CRISPR-corrected hiPSC lines.
- Functionalise excitatory and inhibitory neurons with distinct genetically encoded calcium indicators for monitoring of network activity with distinguishable neuronal population contribution.

- Characterise inhibitory and excitatory neuron-specific phenotypes in inhibitory and excitatory monocultures over time.
  - Assess neuronal activity.
  - Characterise intrinsic excitability.
  - Investigate AIS phenotypes.

- Characterise disease phenotypes and assess neuronal population contribution in co-culture over time.
  - Characterise network activity and individual neuronal population contribution.
  - Assess the relative contribution of Dravet excitatory and inhibitory neurons to the overall disease phenotype using mixed-genotype cultures.
  - Investigate AIS phenotypes and activity-dependant plasticity.

Chapter 2

Materials and Methods

2.1 Human induced Pluripotent Stem Cell (hiPSC) maintenance culture

The wildtype PAMV1 hiPSC line used in this study was obtained from the human induced pluripotent stem cell initiative (HiPSCi - https://www.hipsci.org/lines/#/lines/HPSI1013i-pamv_1). The DS1 patient-derived hiPSC line included in this study, previously described in Yu Liu et al. (Y. Liu, Lopez-Santiago, et al., 2013), was kindly provided by Prof. Jack Parent (University of Michigan). This line harbours the *SCN1A*$^{\text{IVS 14+3A>T}}$ splice donor site mutation. This mutation results in *SCN1A* abnormal transcript missing exon 14 and was classified as a loss-of-function mutation (Y. Liu, Lopez-Santiago, et al., 2013). Finally, the DS1 Corrected line was generated in our lab, using CRISPR Cas9 technology to correct the IVS 14+3A>T mutation present in the DS1 line, as described below.

All lines were maintained on tissue culture (TC)-treated plates coated with 1:30 Laminin-521 (BioLamina, LN521) at 37°C, 5% CO_2, 20% O_2 in StemMACS iPS-Brew XF (Miltenyi Biotec, 130-104-368) supplemented with 1% PenStrep (Gibco, 15140122). Medium was replaced every 1-2 days and cells were passaged at 70-80% confluency. To passage the cells, colonies were dissociated to a single cell suspension by incubating in TrypLE Express (Gibco, 12605010) at 37°C for 5 minutes. The cells were then centrifuged at 1200 RPM for 4 minutes and re-suspended in fresh iPS-Brew. Rock inhibitor Y-27632 (ROCKi) (Tocris, 1254) 10µM was added to the medium for 24h after passaging.

2.2 CRISPR correction of the DS1 line

Targeted gene editing of the DS1 line to correct the endogenous *SCN1A*$^{\text{IVS 14+3A>T}}$ mutation (genome coordinates NC_000002.11[166,039,420]) was achieved using CRISPR/Cas9 mediated Homology-Directed Repair (HDR). The single guide RNA (sgRNA) (CRISPR ID: 941482857) (Table 2.1) was designed using the online tool provided by the Wellcome Sanger Institute Genome Editing (WGE). The sgRNA was chosen based on its proximity to the

mutation and its off-target score (Mismatch score: MM1:0 – MM2:0 – MM3:0). The double strand oligonucleotide (dsOligo) (Sigma-Aldrich – Table 2.1) donor template was designed according to the wildtype sequence and it was modified to introduce a silent MspI restriction site in the seed region of the sgRNA binding site of the CRISPR edited cells. The sgRNA was cloned into the pSpCas9(BB)-2A-Puro (PX459) V2.0 plasmid (Addgene #62988) following the procedure described in section *2.3.1 (Molecular cloning)* below. For hiPSC transfection, 5 µg of the resulting SpCas9-2A-Puro_sgRNA(DS1) plasmid were pre-mixed with 5 µl of dsOligo template (100 µM) at room temperature. $1x10^6$ DS1 cells were electroporated with the plasmid/dsOligo mix following the procedure described in section *2.3.3 (Electroporation of hiPSCs)* below. The day after electroporation, the cells were treated with 0.5µg/ml puromycin (Gibco, A1113803) for 24h then maintained in culture with fresh iPS-Brew provided daily. When the cells reached 80% confluency, they were dissociated with TrypLE Express and divided in 2. Half of the cells were re-plated in a LN521-coated dish for future single-cell sorting while the other half was used to extract bulk genomic DNA (gDNA) to assess CRISPR-editing success and efficiency. gDNA was extracted using DNeasy Blood & Tissue kit (Qiagen, 69504) and used for PCR amplification using Q5® High-Fidelity 2X Master Mix (NEB, M0492S) and primers SCN1A-14/13_2F and SCN1A-14/13_3R (Sigma-Aldrich - Table 2.1) according to the manufacturer's protocol. The resulting PCR product was digested using the restriction enzyme MspI (NEB, R0106S) for 1h at RT and subsequently run on a 1% agarose gel to confirm the presence of a digested fragment. After confirming successful CRISPR-editing, the remaining cells in culture were single-cell sorted using FACS as described in the section *2.3.5 (FACS sample preparation and sorting)* below. Single-cell clones were grown up to 24-well plate format then screened for the presence of the MspI restriction site. gDNA was extracted from individual clones using QuickExtract solution (Epicenter - QE09050) according to the manufacturer's protocol and PCR-based genotyping was performed as described above. Positive clones were then sequenced using sanger sequencing (SourceBioscience) to confirm successful correction as well as the integrity of the genomic sequence around the editing site (~1000 bp upstream and downstream of the mutation). The top 5 off-target sites were also sequenced to confirm the absence of off-target editing (Table 2.1). Finally, we carried out g-banding to confirm a normal karyotype (CellGuidanceSystems).

Name	Sequence (5'-3')	Ta	Genome coordinates
sgRNA (CRISPR ID: 941482857)	TGTTCTCCGTTCATTTCGAT		2: 166,039,422 – 166,039,444
dsOligo	TGACATTGCTATGCAAGAACCCTGAT TGTTAGAAAGGTTTTTGAATTTGGTG CTTTTTTTTTTTTTTTTTTACCAACCGGA ATGAACGGAGAACAGATAATCCTTCC ACATTGGCGAGTCCAAGTTCTACCAG GCTAAGCG		2: 166,039,350 – 166,039,490
SCN1A-14/13_1F	CCTCCCAGGTTAAAGTGATC	59°C	2: 166,894,918 – 166,894,938
SCN1A-14/13_1R	GCTTCTAGAGACTACTACAG	59°C	2: 166,895,668 - 166,895,688
SCN1A-14/13_2F	TCTCTCCTTTGACTTTCGCA	64°C	2: 166,895,487 - 166,895,507
SCN1A-14/13_2R	GAAGGCTGGAATATCTTTGACG	64°C	2: 166,896,014 - 166,896,034
SCN1A-14/13_3F	GCTAATGGTTGTGTGGCAAA	65°C	2: 166,895,835 - 166,895,855
SCN1A-14/13_3R	ATTTCACCCATCTGAAGACCTC	65°C	2: 166,896,340 - 166,896,360
SCN1A-14/13_4F	GCTTATGCTATTTTCCCACA	57°C	2: 166,896,185 - 166,896,205
SCN1A-14/13_4R	CATGTGCATAACAAAGAATG	57°C	2: 166,896,915 - 166,896,935
OT-1_F	CCCATTTTGCATGTTGTCTC	59°C	11: 25,288,027 – 25,288,047
OT-1_R	GCCTAGGAATCAATTTAACC	59°C	11: 25,288,807 – 25,288,827
OT-2_F	TTGCAATGGCTACGTAGGAA	60°C	9: 74,161,353 – 74,161,373
OT-2_R	GTCGATAGTTTGTTTTGCTG	60°C	9: 74,162,124 – 74,162,144
OT-3_F	GCTGTGCAGAAGCTTGTTAG	65°C	1: 59,490,498 – 59,490,518
OT-3_R	GCAAGCAAGCAAGCAAGCAG	65°C	1: 59,490,977 – 59,490,997
OT-4_F	TTGGCATGATGAAATTCTAT	53°C	1: 72,723,460 – 72,723,480
OT-4_R	CTACCTAGGAATAAATGTAA	53°C	1: 72,724,231 – 72,724,251
OT-5_F	TCGTTTCAATTGAAAGAGGA	59°C	21: 32,954,014 – 32,954,034
OT-5_R	TATAACGCATAAACTCAGCA	59°C	21: 32,954,767 – 32,954,787

Table 2.1. sgRNA, dsOligo and primer sequences used for the CRISPR-correction of the DS1 line. Red ink in the dsOligo sequence highlights the SCN1A$^{IVS\ 14+3A>T}$ mutation and blue ink highlights the silent MspI restriction site.

2.3 Generation of hiPSC transgenic lines

Wildtype, DS1 and Corrected hiPSC lines were genetically modified to generate subclonal lines suitable for forward programming differentiation into cortical excitatory neurons (iGlut),

inhibitory interneurons (iGABA) and astrocytes (iAstro). For each genetic background, iGlut and iGABA lines were further modified to express the genetically encoded calcium indicator (GECI) GCaMP6f and jrGECO1a, respectively.

A summary of the transgenic hiPSC lines produced for this project is given in Table 2.2.

Cell line	Transgene 1	Transgene 2	Cell line name
Wildtype	(AAVS1)TetO-NGN2 (**iGlut**)		WT-iGlut
Wildtype	(AAVS1)TetO-ASCL1-T2A-DLX2 (**iGABA**)		WT-iGABA
Wildtype	(AAVS1)TetO-NF1B-T2A-SOX9 (**iAstro**)		WT-iAstro
Wildtype	(AAVS1)TetO-NGN2 (**iGlut**)	(PB)CAG-GCaMP6F	WT-iGlut-6F
Wildtype	(AAVS1)TetO-ASCL1-T2A-DLX2 (**iGABA**)	(PB)CAG-jrGECO1a	WT-iGABA-1a
DS1	(AAVS1)TetO-NGN2 (**iGlut**)		DS1-iGlut
DS1	(AAVS1)TetO-ASCL1-T2A-DLX2 (**iGABA**)		DS1-iGABA
DS1	(AAVS1)TetO-NF1B-T2A-SOX9 (**iAstro**)		DS1-iAstro
DS1	(AAVS1)TetO-NGN2 (**iGlut**)	(PB)CAG-GCaMP6F	DS1-iGlut-6F
DS1	(AAVS1)TetO-ASCL1-T2A-DLX2 (**iGABA**)	(PB)CAG-jrGECO1a	DS1-iGABA-1a
Corrected	(AAVS1)TetO-NGN2 (**iGlut**)		Corr-iGlut
Corrected	(AAVS1)TetO-ASCL1-T2A-DLX2 (**iGABA**)		Corr-iGABA
Corrected	(AAVS1)TetO-NGN2 (**iGlut**)	(PB)CAG-GCaMP6F	Corr-iGlut-6F
Corrected	(AAVS1)TetO-ASCL1-T2A-DLX2 (**iGABA**)	(PB)CAG-jrGECO1a	Corr-iGABA-1a

Table 2.2. List of the transgenic hiPSC lines generated and used for this project.

2.3.1 Molecular cloning

- *SpCas9-T2A-Puro_sgRNA(DS1)* – PCR primers were designed to contain the entire sgRNA sequence as well as to have compatible ends for ligation with BbsI digested DNA. Forward and reverse primers were annealed by incubating in a thermocycler at 95°C for 5 minutes with the temperature subsequently decreased to 25°C at a rate of 5°C/min. Plasmid pSpCas9(BB)-2A-Puro (PX459) V2.0 (Addgene #62988) was digested with BbsI (NEB, R3539S) enzyme to allow for insertion of the annealed primers, which were ligated using T4 DNA Ligase (NEB, M0202S) according to the manufacturer's protocol.
- *(AAVS1)TetO-hNGN2 (**iGlut**)* – The plasmid (AAVS1)TO-hNGN2 (Addgene #105840) was digested with PmeI (NEB, R0560S) and KpnI (NEB, R3142S) enzymes to remove the fragment '*EF1a-mCherry'* and ligated using T4 DNA Ligase. The resulting

(AAVS1)TetO-hNGN2 (**iGlut**) plasmid was used as a backbone to build the other two AAVS1 integrating plasmids.

- *(AAVS1)TetO-hASCL1-T2A-hDLX2 (**iGABA**)* – TetO-mAscl1-puro (Addgene #97329) and hDLX2-N174 (Addegene #60860) were PCR amplified and assembled to replace the puromycin resistance gene with the hDLX2 gene, generating the TetO-mAscl1-T2A-hDlx2 plasmid. A PacI restriction site was included in the hDLX2 forward primer sequence in order to insert a PacI site between the T2A and hDLX2 sequences. Next, (AAVS1)TetO-hNGN2 (iGlut) was digested with PacI (NEB, R0547S) and NotI (NEB, R3189S) enzymes to remove the hNGN2 gene. The resulting fragment was assembled with hASCL1, PCR-amplified from hASCL1-N106 (#31781) including BstBI restriction sites at either side of hASCL1, and T2A-hDLX2, PCR-amplified from TetO-mAscl1-T2A-hDlx2 including an AgeI restriction site after the hDLX2 gene. This assembly generated the (AAVS1)TetO-hASCL1-T2A-hDLX2 (**iGABA**) plasmid.
- *(AAVS1)TetO-hNF1B-T2A-hSOX9 (**iAstro)*** – (AAVS1)TetO-hASCL1-T2A-hDLX2 (iGABA) was first digested with BstBI (NEB, R0519S) to replace the hASCL1 gene with hNF1B, which was PCR-amplified from TetO-NF1B-Hygro (Addgene #117271). Finally, resulting plasmid (AAVS1)TetO-hNF1B-T2A-hDLX2 was digested with PacI and AgeI (NEB, R3552S) to remove hDLX2 and replace it with hSOX9, PCR-amplified from AAVS1-TRE3G-NF1A+SOX9 (Addgene #129455). This assembly generated the (AAVS1)TetO-hNF1B-T2A-hSOX9 (**iAstro**) plasmid.

A graphical explanation of the cloning steps to generate iGlut, iGABA and iAstro plasmids is given in Figure 2.1.

- *(PB)CAG-GCaMP6f* – GCaMP6f was PCR amplified from pGP-CMV-GCaMP6f (Addgene #40755) and assembled in the PiggyBAC (PB)-CAG expression vector digested with AscI (NEB, R0558S) and PacI enzymes.
- *(PB)CAG-jrGECO1a* – jrGECO1a was PCR amplified from pGP-CMV-NES-jRGECO1a (Addgene #61563) and assembled in the PiggyBAC (PB)-CAG expression vector digested with AscI and PacI enzymes.

PCR amplification of fragments of interest was performed using Q5® High-Fidelity 2X Master Mix (NEB, M0492S) and primers (Sigma-Aldrich – Table 2.3) according to the manufacturer's protocol. Enzymatic digestion was performed for 1h at 37°C except otherwise specified by the

manufacturer and assembly of PCR products and digested fragments was performed using Gibson Assembly® Master Mix (NEB, E2611S) according to the manufacturer's protocol.

Target (Plasmid #)	Forward Primer (5'-3')	Reverse Primer (5'-3')	Ta
SpCas9-T2A-Puro_sgRNA(DS1)	*CACCG*TGTTCTCCGTTCATTTCGAT	*AAAC*ATCGAAATGAACGGAGAACA*C*	95°C
TetO-Ascl1-puro (#97329)	GCTAGCTAATTCGATATCAAGCTTATCG	TGGGCCGGGATTTTCCTC	66°C
hDLX2 (#60860)	tggaggaaaatcccggccca*ttaattaat*A T GACTGGAGTCTTTGAC	ttgatatcgaattagctagcTTAGAAAATCGTCCCCGC	59°C
hASCL1 (#31781)	aagacttcccctgccctctt*cgaa*GAACCAGTTGGTGAAGTCG	cgtaaacttaaggttaattt*cgaa*GCCACCATGGAAAGCTCTG	64.2°C
T2A-hDLX2	tggggtgggcgatcgattgcaccggtTTAGAAAATCGTCCCCGCG	gaaaatcccggcccattaat*taat*ATGACTGGAGTCTTTGAC	59°C
hNFIB (#117271)	aagacttcccctgccctctt*cgaa*GCCCAGGTACCAGGACTG	taaacttaaggttaattt*cgaagccacc*ATGATGTATTCTCCCATCTGTCT	64.2°C
hSOX9 (#129455)	ggggtgggcgatcgattgca*ccggt*TCA A GGTCGAGTGAGCTG	gaaaatcccggcccattaat*taat*AATCTCCTGGACCCCTTC	64.4°C
GCaMP6f (#40755)	cattttggcaaagaattcgg*cgcgcc*ACCGGACTCAGATCTCGC	ctccatggtagcccttaat*taa*CGCCTTAAGATACATTGATGAGTTTG	64.4°C
jRGECO1a (#61563)	cattttggcaaagaattcgg*cgcgcc*ACCGGACTCAGATCTCGC	ctccatggtagcccttaat*taa*CGCCTTAAGATACATTGATGAGTTTG	64.4°C

Table 2.3. List of plasmids and respective Addgene numbers (in brackets) and corresponding forward and reverse primers used for PCR cloning. *Italic* indicates DNA sequences recognised by restriction enzymes. Blue ink in the first set of primers highlights the 20 nucleotide sequence of the sgRNA.

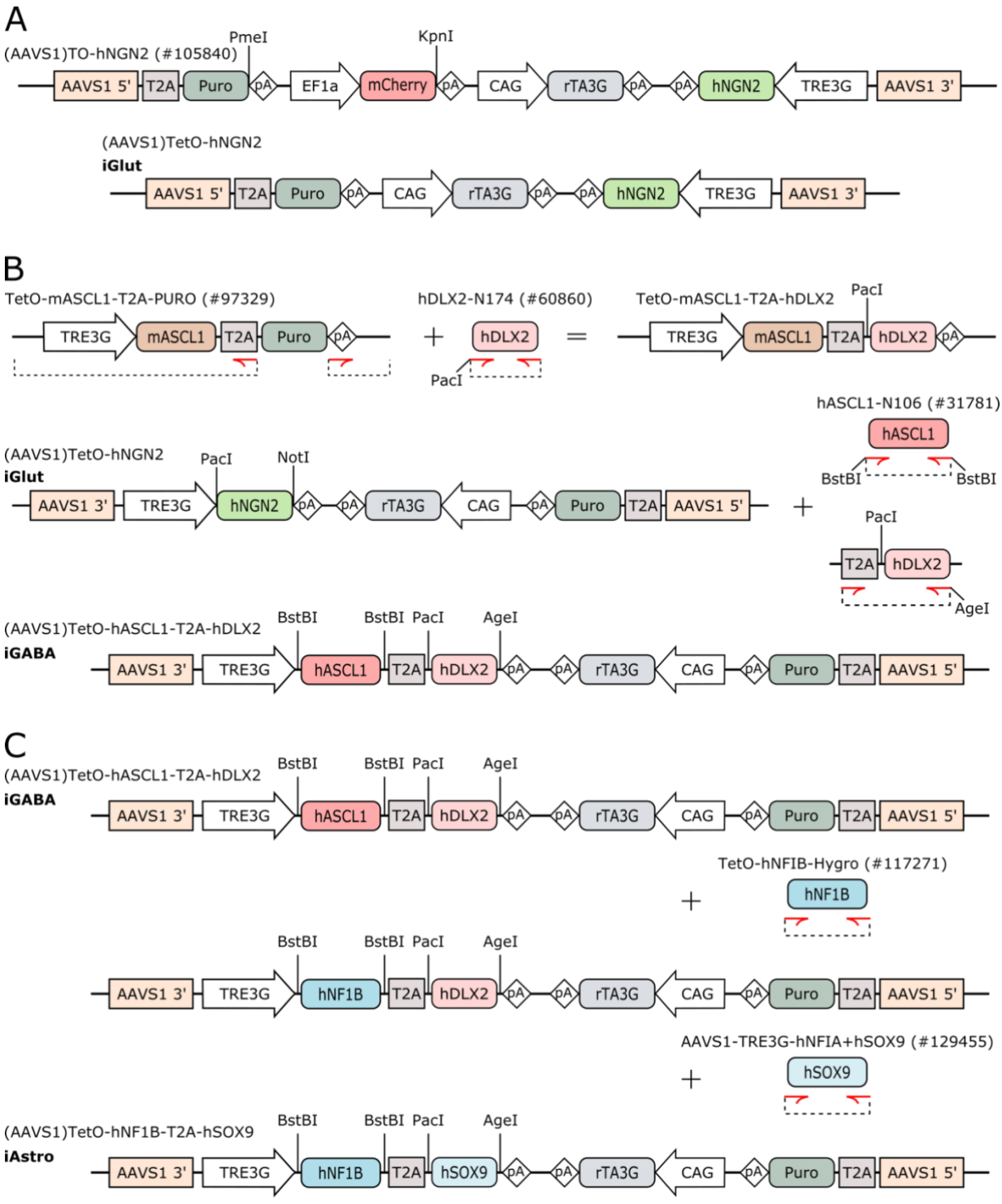
A
(AAVS1)TO-hNGN2 (#105840)
PmeI
KpnI
AAVS1 5'
T2A
Puro
pA
EF1a
mCherry
CAG
rTA3G
hNGN2
TRE3G
AAVS1 3'
(AAVS1)TetO-hNGN2
iGlut
B
TetO-mASCL1-T2A-PURO (#97329)
hDLX2-N174 (#60860)
TetO-mASCL1-T2A-hDLX2
PacI
mASCL1
hDLX2
hASCL1-N106 (#31781)
hASCL1
BstBI
NotI
AgeI
(AAVS1)TetO-hASCL1-T2A-hDLX2
iGABA
C
TetO-hNFIB-Hygro (#117271)
hNF1B
AAVS1-TRE3G-hNFIA+hSOX9 (#129455)
hSOX9
(AAVS1)TetO-hNF1B-T2A-hSOX9
iAstro

Figure 2.1. *Schematic representation of the cloning strategy*. **A –** The plasmid (AAVS1)TO-hNGN2 (Addegene #105840) was digested with PmeI and KpnI enzymes to remove the fragment '*polyA-EF1a-mCherry'* to generate (AAVS1)TetO-hNGN2 (**iGlut**). **B –**TetO-mAscl1-puro (Addgene #97329) and hDLX2-N174 (Addegene #60860) were PCR amplified and assembled to replace the puromycin resistance gene with the hDLX2 gene, generating TetO-mAscl1-T2A-hDlx2. A PacI restriction site was included in the sequence of the hDLX2 forward primer in order to insert a PacI site between the T2A and hDLX2 sequences. iGlut plasmid was then digested with PacI and NotI enzymes to remove the hNGN2 gene and replace it with hASCL1, PCR-amplified from hASCL1-N106 (#31781) including BstBI restriction sites at either side of hASCL1, and T2A-hDLX2, PCR-amplified from TetO-mAscl1-T2A-hDlx2 including an AgeI restriction site after the hDLX2 gene. This assembly generated the (AAVS1)TetO-hASCL1-T2A-hDLX2 (**iGABA**) plasmid. **C –** iGABA was first digested with BstBI to replace hASCL1 with hNF1B, which was PCR-amplified from TetO-NF1B-Hygro (Addgene #117271). The resulting plasmid (AAVS1)TetO-hNF1B-T2A-hDLX2 was digested with PacI and AgeI to remove hDLX2 and replace it with hSOX9, PCR-amplified from AAVS1-TRE3G-NF1A+SOX9 (Addgene #129455). This assembly generated the (AAVS1)TetO-hNF1B-T2A-hSOX9 (**iAstro**) plasmid.

2.3.2 Plasmid production and purification

All plasmids were transformed in 5-alpha Competent E. coli (NEB, C2987H) or Stable Competent E. coli (NEB, C3040H) according to the manufacturer's protocol. Bacterial colonies were picked and cultured in antibiotic-supplemented LB broth in a bacterial shaker at 215 RPM, at 37°C, overnight. A Qiagen Plasmid Midi kit (Qiagen, 12143) was used to extract the plasmid DNA. All constructs were verified by DNA sequencing.

Preceding transfection, plasmid DNA was purified by ethanol precipitation. 50µg of plasmid DNA were combined with 1/10 volume of 3M sodium acetate and 2.5 volume of 100% ethanol. The solution was centrifuged at 20 000 RPM for 30 min at 4°C. The supernatant was removed and the pellet was washed with 100% ethanol for 5 min at 20000 RPM. Following the wash, the ethanol was removed and the pellet left to air-dry inside the hood. Finally, the DNA pellet was resuspended in OptiMEM Reduced-Serum Medium (Gibco, 11058021) at a concentration of 1 µg/µl.

2.3.3 Electroporation of hiPSCs

hiPSCs were dissociated using TrypLE Express and resuspended at $1x10^6$ cells in 90µl OptiMEM Reduced-Serum Medium. For AAVS1 integration, 5µg of (AAVS1)TetO expression vector + 2.5 µg TALEN-Left (Addgene #52341) + 2.5 µg TALEN-Right (Addgene #52342) were added to the cells. For piggyBAC integration, 5µg of (PB)CAG expression vector + 5µg (PB)transposase were added to the cell suspension. For CRISPR editing, 5µg of SpCas9-T2A-Puro_sgRNA(DS1) plasmid + 5µl of dsOligo template (100 µM) were added to the cells. The cell suspensions were transferred into 2mm electroporation cuvettes (GeneFlow, E6-0062) and transfection was performed using a NEPA21 electroporator (Sonidel) with settings as reported in Table 2.4. Cells were retrieved from the cuvettes and plated into LN521-coated 10cm-dishes containing warm iPS-Brew + 10µM ROCKi.

For Dlx5/6 expression analysis, PAMV1-derived dorsal and ventral progenitors at day 22 were disassociated using TrypLE Express and resuspended at $5x10^6$ cells in 90µl OptiMEM. 8µg of Dlx5/6-GFP plasmid were added to the cells and electroporation was performed as above. Progenitors were retrieved from the cuvettes and plated into 10cm-dishes coated with 1:50 Growth Factor Reduced-Matrigel (MG) (Corning, 354230) and containing warm Neural Maintenance Medium (details in the *2.4.1 Dorsal differentiation* section) supplemented with 10µM ROCKi.

Poring Pulse							Transfer Pulse				
V	Length (ms)	Interval (ms)	No.	D. Rate (%)	Polarity	V	Length (ms)	Interval (ms)	No.	D. Rate (%)	Polarity
150	5	50	2	10	+	20	50	50	5	40	+/-

Table 2.4. Electroporation settings.

2.3.4 Monoclonal colonies selection and screening

For AAVS1 integration, 48h after electroporation cells were treated with 0.5 µg/mL puromycin for three to five days, until all non-transfected cells have died. Following drug selection, surviving cells were grown until they form small visible colonies. For each cell line, 10 monoclonal colonies were picked by manually scraping and aspirating each colony using a 200µl pipette tip. Individual colonies were transferred to a LN521-coated 96-well plate containing warm iPS-Brew + 10µM ROCKi. Colonies were grown up to 24-well plate format then screened for homozygous integration. The correct integration of the transgene was determined by PCR analysis of isolated genomic DNA (gDNA) as described by Fernandopoulle and colleagues (Fernandopulle et al., 2018). Briefly, gDNA was extracted from individual clones using QuickExtract solution and PCR-based clone genotyping was performed using 1µl of extracted gDNA, Taq 2X Master Mix (NEB, M0270L) and primer combinations according to Table 2.5.

Name	Primer sequence (5'-3')	Primer combination
A1	GGAATCTGCCTAACAGGAGGT	Used with A2 for detection of WT alleles – 0.16 kb
A2	CGGTTAATGTGGCTCTGGTT	
A3	CCCCCAGAATAGAATGACACC	Used with A2 for detection of modified alleles – 1 kb

Table 2.5. List of primers used for AAVS1 integration screening.

2.3.5 FACS sample preparation and sorting

For CRISPR correction and piggyBAC integration, cells were sorted when they reached ~80% confluency, but a minimum of 5 days after electroporation. For Dlx5/6 expression analysis, samples were sorted the day after electroporation. Each sample was disassociated using TrypLE Express and resuspended in FACS Buffer (0.5% BSA (Roche, 10735078001), 10 U/ml DNase-I (Roche, 4714728001) in DPBS (Gibco, 14190094)). The cell suspension was passed through a 40µm nylon cell strainer (BD Falcon, 10737821), resuspended in 0.5-1ml FACS Buffer and

collected into Test Tubes with Cell Strainer Snap Cap (Corning, 352235). For piggyBAC integration and Dlx5/6 expression analysis, samples were labelled with DAPI (Thermo Fisher, D1306) and sorted for the fluorescent protein of interest. For CRISPR correction, the sample was labelled with DAPI and live cells were single cell-sorted directly into LN521-coated 96-well plates containing iPS-Brew + 10μM ROCKi. FACS sorting was performed by the staff of the NIHR Guy's and St Thomas BRC Flow Core using a BD FACSAria™ Cell Sorter (BD Biosciences).

2.4 Directed neuronal differentiation

In the first part of this study, we tried to optimise directed differentiation protocols for the generation of cortical neurons from hiPSCs. We tested two different versions of dorsal differentiation for the generation of excitatory glutamatergic neurons (based on (Y. Shi, Kirwan, & Livesey, 2012)) and two ventral differentiation protocols for the generation of inhibitory GABAergic interneurons (based on (Maroof et al., 2013) and (Y. Shi, Kirwan, & Livesey, 2012)).

2.4.1 Dorsal differentiation

The following protocols are based on Y. Shi, Kirwan and Livesey (Y. Shi, Kirwan, & Livesey, 2012). Complete medium compositions are reported in Table 2.6.

- *Dorsal differentiation Version 1 (D-V1):* confluent hiPSC cells from 5 wells of a 6-well plate were dissociated with Versene, combined, resuspended in iPS-Brew + 10μM ROCKi and plated into 1 well of a 6-well plate coated with MG 1:50 The next day, iPS-Brew was replaced by dorsal Neural Induction Medium-1 (dNIM-1) following one DPBS wash. dNIM-1 was refreshed daily for 8 days after which the cells were split using Collagenase IV (Invitrogen, 17104019) and manually scraped into large, detached sheets. The sheets were resuspended in dNIM-1 + 10μM ROCKi and re-plated into MG-coated plates at a 1:1 split ratio. From the following day, dNIM-1 was replaced by Neural Maintenance Medium-1 (NMM-1). NMM-1 was changed daily and supplemented with FGF2 at 20ng/ml (Peprotech, 100-18B) between day 12 and 16. At day 18 of differentiation, cells were split with Collagenase IV into MG-coated plates at a 1:3 split ratio. Cells were maintained in NMM-1 until day 30 when they were processed for analysis.

- *Dorsal differentiation Version 2 (D-V2):* confluent hiPSC cells from 2 wells of a 6-well plate were dissociated with 0.5mM EDTA (Invitrogen, 15575020), combined, resuspended in iPS-

Brew + 10µM ROCKi and plated into 1 well of a 6-well plate coated with 1:50 MG. The next day, iPS-Brew was replaced by dNIM-2 following two DPBS washes. dNIM-2 was refreshed daily for 12 days after which the cell sheet was detached as a whole, using 1mg/ml Dispase (Stem Cell Technologies, 07923). The detached sheet was resuspended in dNIM-2 + 10µM ROCKi and re-plated into a MG-coated 10cm-dish. From the following day, dNIM-2 was replaced by NMM-2 supplemented with FGF2 at 20ng/ml for 4 days. At day 17 of differentiation, cells were passaged with Dispase into a MG-coated 10cm-dish at a 1:1 split ratio. Cells were maintained in NMM-2 and passaged with Dispase at a 1:2 ratio every 3-4 days until day 30 when they were processed for analysis.

2.4.2 Ventral differentiation

Complete medium compositions are reported in Table 2.6.

- *Ventral differentiation Version 1 (V-V1):* The following protocol is based on Maroof et al. (Maroof et al., 2013). Confluent hiPSC cells were dissociated with TrypLE Express, resuspended in iPS-Brew + 10µM ROCKi and plated into MG-coated dishes at 18.000 cells/cm^2. The next day, ROCKi was removed and cells were grown in iPS-Brew until 100% confluent. When completely confluent, iPS-Brew was replaced by ventral Neural Induction Medium-1 (vNIM-1) following one DPBS wash. vNIM-1 was refreshed daily for 10 days, after which the cells were split using Collagenase IV and manually scraped into large, detached sheets. The sheets were resuspended in vNIM-1 + 10µM ROCKi and re-plated into MG-coated plates at a 1:1 split ratio. The following day, ROCKi was removed and vNIM-1 was refreshed daily for 8 days. At day 18, cells were passaged with Collagenase IV into a MG-coated 10cm-dish at a 1:1 split ratio and vNIM-1 was replaced by NMM-1 supplemented with FGF2 at 20ng/ml for 2 days. From day 20, cells were maintained in NMM-1 until day 30 when they were processed for analysis.

- *Ventral differentiation Version 2 (V-V2):* Adapted from Y. Shi, Kirwan and Livesey (Y. Shi, Kirwan, & Livesey, 2012). The protocol is the same as D-V2, with dNIM-2 replaced by vNIM-2.

Component	Concentration	Supplier	Cat. #
Coating and Dissociation reagents			
Matrigel Basement Membrane, GFR	1:50/1:100	Corning	354230
Versene	1X	Gibco	15040066
TrypLE Express	1X	Gibco	12605010
Collagenese IV	1 mg/ml	Invitrogen	17104019
Neuronal Maintenance Medium-1 (NMM-1)			
DMEM/F12 Medium (1X)	1X	Gibco	21331020
Neurobasal Medium (1X)	1X	Gibco	21103049
200 mM L-Glutamine	2 mM	Gibco	25030024
Penicillin-Streptomycin, 100X	1X	Gibco	15140122
MEM Non-Essential Amino Acids Solution, 100X	1X	Gibco	11140050
N2 Supplement, 100X	1X	Gibco	17502001
MACS NeuroBrew-21 w/o Vit A, 50X	1X	Miltenyi Biotec	130-097-263
Insulin Transferrin-Selenium, 100X	1X	Gibco	41400045
55 mM 2-Mercaptoethanol	50 μM	Sigma	21985023
Dorsal Neuronal Induction Medium-1 (dNIM-1)			
Neuronal Maintenance Medium-1 (NMM-1) (1X)	1X		
Dorsomorphin	1 μM	Tocris	3093
SB431542	10 μM	Tocris	1614
XAV939	2 μM	CaymanChemical	13596
Ventral Neuronal Induction Medium-1 (vNIM-1)			
Neuronal Maintenance Medium-1 (NMM-1) (1X)	1X		
Purmorphamine	1 μM	Tocris	4551
SAG	1 μM	Tocris	566660
Neuronal Maintenance Medium-2 (NMM-2)			
DMEM/F12 GlutaMAX Medium (1X)	1X	Gibco	10565018
Neurobasal Medium (1X)	1X	Gibco	21103049
200 mM L-Glutamine	2 mM	Gibco	25030024
Penicillin-Streptomycin, 100X	1X	Gibco	15140122
MEM Non-Essential Amino Acids Solution, 100X	1X	Gibco	11140050
100 mM Sodium Pyruvate	1 mM	Gibco	11360070
N2 Supplement, 100X	1X	Gibco	17502001
B27 Supplement, 50X	1X	Gibco	17504044
Insulin Transferrin-Selenium, 100X	1X	Gibco	41400045
55 mM 2-Mercaptoethanol	50 μM	Sigma	21985023
Dorsal Neuronal Induction Medium-2 (dNIM-2)			
Neuronal Maintenance Medium-2 (NMM-2) (1X)	1X		
Dorsomorphin	1 μM	Tocris	3093
SB431542	10 μM	Tocris	1614
Ventral Neuronal Induction Medium-2 (vNIM-2)			
Neuronal Maintenance Medium-1 (NMM-1) (1X)	1X		
Dorsomorphin	1 μM	Tocris	3093
SB431542	10 μM	Tocirs	1614
Purmorphamine	1 μM	Tocris	4551

Table 2.6. List of directed differentiation reagents and their working concentration, supplier and cat. #.

2.5 Forward programming differentiation

To generate glutamatergic neurons, GABAergic interneurons and astrocytes using forward programming differentiation of hiPSCs, we generated engineered hiPSC lines as described above (details in section *2.3 Generation of hiPSC transgenic lines*). Each cell line was then differentiated using the respective protocol described below. Complete medium compositions are reported in Table 2.7.

2.5.1 iGlut forward programming differentiation

The following protocol is based on Fernandopulle et al. (Fernandopulle et al., 2018). On Day 0, 70% confluent iGlut-hiPSCs were dissociated with TrypLE Express, resuspended in iGlut Induction Medium + 2 µg/ml Doxycycline (Dox) (Sigma, D9891) + 10 µM ROCKi and plated at 100.000 cells/cm^2 into dishes coated with Geltrex 1:100 (Gibco, A1413201). After 24h ROCKi was removed and the Dox-supplemented medium was changed daily until Day 3, when the cells were dissociated with Accumax (Millipore, SCR006), resuspended in Cortical Neuron Maturation Medium + 10µM ROCKi and plated at the appropriate density for their final application (plating densities for each specific application are reported in Table 2.9). At this stage, the glutamatergic neuron precursors are plated on 0.1 mg/ml Poly-L-Ornithine (PLO) (Sigma, P3655) and 1 µg/ml Laminin (Gibco, 23017015) coated plates or on a monolayer of either human iAstro or mouse ESC-derived astrocytes. On Day 3, the precursors can be frozen in Recovery™ Cell Culture Freezing Medium (Invitrogen, 12648010) at variable densities. On Day 4, the day after the cells were split or thawed, half the culture medium is replaced by an equal volume of fresh Cortical Neuron Maturation Medium supplemented with 10µM Ara-C (final concentration 5µM) (Sigma, C1768). From Day 7 onwards, half medium changes with fresh Cortical Neuron Maturation Medium were performed once a week, for low density cultures, or twice a week, for high density cultures.

2.5.2 iGABA forward programming differentiation

The following protocol is adapted from Yang et al. (Yang et al., 2017). On Day -2, 70% confluent iGABA-hiPSCs were dissociated with TrypLE Express, resuspended in iPS-Brew and plated into Geltrex-coated dishes at 40.000 cells/cm^2. The medium was supplemented with 10 µM ROCKi for 24h after plating. On Day 0, the medium was replaced with iGABA Induction Medium + 2 µg/ml Doxycycline following two DPBS washes. Dox-supplemented medium was changed daily until Day 4, when the cells are dissociated with Accumax, resuspended in

Cortical Neuron Maturation Medium + 2 µg/ml Doxycycline + 10 µM ROCKi and plated at the appropriate density for their final application. GABAergic interneuron precursors are plated in 50% excess to account for the number of cells that will die following the Ara-C treatment (plating densities for each specific application are reported in Table 2.9). At this stage, the induced cells are plated on PLO/Laminin-coated plates or on a monolayer of either human iAstro or mouse ESC-derived astrocytes. On Day 4, the precursors can also be frozen in Recovery™ Cell Culture Freezing Medium at variable densities. On Day 5, the day after the cells were split or thawed, half the culture medium was replaced by an equal volume of Dox-supplemented Cortical Neuron Maturation Medium + 10 µM Ara-C (final concentration 5µM). From Day 7 onwards, half medium changes with fresh Cortical Neuron Maturation Medium were performed once a week, for low density cultures, or twice a week, for high density cultures. Cortical Neuron Maturation Medium is supplemented with Dox until Day 14.

2.5.3 iAstro forward programming differentiation

The following protocol is adapted from Canals et al. (Canals et al., 2018). On Day 0, 70% confluent iAstro-hiPSCs were dissociated with TrypLE Express, resuspended in iPS-Brew + 2 µg/ml Doxycycline + 10 µM ROCKi and plated into Geltrex-coated dishes at 20'000 cells/cm^2. The day after, the medium was replaced with iAstro Expansion Medium + 2 µg/ml Doxycycline following two DPBS washes. Medium was changed daily until Day 3, when the medium was changed to ¾ Dox-supplemented Expansion Medium – ¼ Dox-supplemented FGF Medium. On Day 4, the medium was changed to ½ Dox-supplemented Expansion Medium – ½ Dox-supplemented FGF Medium. On Day 5 the medium was changed to ¼ Dox-supplemented Expansion Medium – ¾ Dox-supplemented FGF Medium. Cells were then maintained in Dox-supplemented FGF Medium until Day 7, when they were dissociated with Accumax, resuspended in iAstro Maturation Medium + 2 µg/ml Doxycycline + 10 µM ROCKi and plated at 100'000 cell/cm^2 in MG-coated plates. On Day 7, the astrocytes precursors can be frozen in Recovery™ Cell Culture Freezing Medium at variable densities. From Day 8 onwards, half medium changes with fresh iAstro Maturation Medium were performed twice a week. iAstro Maturation Medium is supplemented with Dox until Day 21.

Component	Concentration	Supplier	Cat. #
Coating and Dissociation reagents			
Matrigel Basement Membrane, GFR	1:50/1:100	Corning	354230
Geltrex™ RGF Basement Membrane	1:100	Gibco	A1413201
Poly-L-Ornithine (PLO)	0.1 mg/ml	Sigma	P3655
Laminin Mouse Protein	1 μg/ml	Gibco	23017015
TrypLE Express	1X	Gibco	12605010
AccuMAX	1X	Millipore	SCR006
iGlut Induction Medium			
DMEM/F12 Hepes Medium (1X)	1X	Gibco	11330032
200 mM L-Glutamine	2 mM	Gibco	25030024
MEM Non-Essential Amino Acids, 100X	1X	Gibco	11140050
N2 Supplement, 100X	1X	Gibco	17502001
Doxycycline hyclate	2 μg/ml	Sigma	D9891
iGABA Induction Medium			
DMEM/F12 Medium (1X)	1X	Gibco	21331020
N2 Supplement, 100X	1X	Gibco	17502001
Doxycycline hyclate	2 μg/ml	Sigma	D9891
Cortical Neuron Maturation Medium			
BrainPhys Neuronal Medium (1X)	1X	STEMCELL	05790
B27 Supplement, 50X	1X	Gibco	17504044
BDNF	10 ng/ml	PeproTech	450-02
NT-3	10 ng/ml	PeproTech	450-03
Laminin Mouse Protein	1 μg/ml	Gibco	23017015
iAstro Expansion Medium			
DMEM/F12 Medium (1X)	1X	Gibco	21331020
Fetal Bovine Serum	10%	Sigma	F7524
200 mM L-Glutamine	2 mM	Gibco	25030024
N2 Supplement, 100X	1X	Gibco	17502001
Doxycycline hyclate	2 μg/ml	Sigma	D9891
iAstro FGF Medium			
Neurobasal Medium (1X)	1X	Gibco	21103049
B27 Supplement, 50X	1X	Gibco	17504044
MEM Non-Essential Amino Acids, 100X	1X	Gibco	11140050
200 mM L-Glutamine	2 mM	Gibco	25030024
Fetal Bovine Serum	10%	Sigma	F7524
FGF2	8 ng/ml	PeproTech	100-18B
CNTF	5 ng/ml	PeproTech	450-13
BMP4	10 ng/ml	PeproTech	120-05ET
Doxycycline hyclate	2 μg/ml	Sigma	D9891
iAstro Maturation Medium			
DMEM/F12 Medium (1X)	1X	Gibco	21331020
Neurobasal Medium (1X)	1X	Gibco	21103049
200 mM L-Glutamine	2 mM	Gibco	25030024
100 mM Sodium Pyruvate	1 mM	Gibco	11360070
N2 Supplement, 100X	1X	Gibco	17502001
N-acetyl-cysteine	1X	Sigma	A8199
Heparin-binding EGF-like growth factor	1X	Sigma	E4643

CNTF	10 ng/ml	PeproTech	450-13
BMP4	10 ng/ml	PeproTech	120-05ET
dbcAMP	500 µg/ml	Sigma	D0627
Other reagents			
Y-27632 dihydrochloride (ROCKi)	10 µM	Tocris	1254
Ara-C	5 µM	Sigma	C1768
Recovery™ Cell Culture Freezing Medium	1X	Invitrogen	12648010
Trypan Blue Solution, 0.4%	0.5X	Gibco	15250061

Table 2.7. List of forward programming differentiation reagents and their working concentration, supplier and catalogue number.

2.6 Human astrocytes and neurons co-culture

Day 7 iAstro precursors were split (or thawed if frozen) and counted with Trypan Blue Solution (Gibco, 15250061) to assess cell viability. The cells were then resuspended in iAstro Maturation Medium + 2 µg/ml Doxycycline + 10 µM ROCKi and plated at 100'000 cell/cm^2 in MG-coated plates. On Day 8, half the medium was replaced by fresh, Dox-supplemented iAstro Maturation Medium. On Day 14, iGlut and iGABA precursors were split or thawed, counted with Trypan Blue Solution, resuspended in 1:1 Maturation Medium (iAstro Maturation Medium/Cortical Neuron Maturation Medium) + 2 µg/ml Doxycycline + 10 µM ROCKi and plated at the appropriate density for their final application on the iAstro monolayer. The day after, Day 1 of co-culture, half the medium was replaced by an equal volume of 1:1 Maturation Medium + 2 µg/ml Doxycycline + 10 µM Ara-C (final concentration 5µM). From co-culture Day 4 onwards, half medium changes with fresh 1:1 Maturation Medium were performed twice a week. 1:1 Maturation Medium was supplemented with Dox until co-culture Day 10.

2.7 Mouse Embryonic Stem Cell (mESC) maintenance, differentiation and sorting

E14-IB10 mESCs (Casola et al., 2006) were maintained on TC-treated plates coated with 1:100 Laminin-521 at 37°C, 5% CO_2, 20% O_2 in 2iLIF medium (complete medium compositions are reported in Table 2.8). The medium was replaced every 1-2 days and the cells were passaged at 70-80% confluency. To passage the cells, colonies were dissociated to a single cell suspension by incubating in 0.25% Trypsin-EDTA (Invitrogen, 25200056) at 37°C for 5 minutes. The cells were then centrifuged at 260 g for 4 minutes and re-suspended in fresh 2iLIF medium supplemented with 10µM ROCKi. 24h after passaging ROCKi was removed from the cell culture medium.

2.7.1 Mouse Astrocyte differentiation

The E14-IB10 subclone G6, expressing GFAP::CD14/CAG::GDNF, was previously generated by Carolina Machado and used in this study for astrocyte differentiation according to Machado et al. (Machado et al., 2019). Briefly, on Day 0, 80% confluent G6 mESCs were dissociated into single cells using 0.25% Trypsin-EDTA and 0.5-1x10^6 cells were plated into 10 cm^2 untreated suspension culture dishes (Corning, 430591) in ADFNB medium (Table 2.8) to form embryoid bodies (EBs). On Day 2, each dish of EBs was divided into 4 fresh 10 cm^2 dishes and maintained in ADFNB supplemented with 0.5 µM SAG and 1 µM Retinoic Acid for neural induction. On Day 5, the EBs from all 4 dishes were pooled and plated onto Geltrex-coated flasks and cultured in ADFNB medium until Day 12, when they were MACS sorted.

2.7.2 Magnetic-Activated Cell Sorting (MACS)

Mouse astrocytes (mAstro) were isolated from astrocyte differentiation cultures using magnetic-activated cell sorting (MACS, Miltenyi Biotec) according to (Bryson et al., 2014). On Day 12 of the mouse astrocyte differentiation protocol, adherent EBs were dissociated to single cells using 0.25% Trypsin-EDTA + 10 U/ml DNaseI (Roche, 4714728001) for 15 minutes at 37°C. The dissociated cells were washed 3 times with DMEM + 10 U/ml DNaseI and passed through a 40 µm nylon cell strainer (BD Falcon, 10737821). Cells were then re-suspended in MACS buffer (0.5% BSA, 10 U/ml DNase-I in DPBS – Table 2.8) and incubated with 3 µg/ml α-CD14 antibody (DSHB, clone 26ic) for 15 min at 4°C using a MACSmix tube rotator (Miltenyi Biotec, 130-090-753). Following primary antibody incubation, the cells were washed in MACS buffer and incubated with 1:10 α-mouse IgG MACS beads (Miltenyi Biotec, 130-042-201) for 20 min at 4°C using a MACSmix tube rotator. The cells were then washed, re-suspended in 1 ml MACS buffer and applied to a magnetic MS-column (Miltenyi Biotec, 130-042-201) that was pre-washed with 0.5 ml MACS buffer and mounted on an OctoMACS magnetic separator (Miltenyi Biotec, 130-042-108). Following 3 column washes with 0.5 ml MACS buffer, the column was removed from the magnetic separator and the cells were eluted with 1 ml MACS buffer. MACS-sorted astrocytes were re-suspended in ADFNB medium and plated at 30-60’000 cell/cm^2.

Component	Concentration	Supplier	Cat. #
Coating and Dissociation reagents			
Laminin-521	1:200	BioLamina	LN521
Matrigel Basement Membrane, GFR	1:100	Corning	354230
Geltrex™ LDEV-Free RGF Basement Membrane	1:100	Gibco	A1413201
0.25% Trypsin, 2mM EDTA	1X	Invitrogen	25200-056
2iLIF Medium			
DMEM/F12 Medium (1X)	1X	Gibco	21331020
Neurobasal Medium (1X)	1X	Gibco	21103049
Penicillin-Streptomycin, 100X	1X	Gibco	15140122
200 mM L-Glutamine	2 mM	Gibco	25030024
MACS NeuroBrew-21 w/o Vit A, 50X	1X	Miltenyi Biotec	130-097-263
N2 Supplement, 100X	1X	Gibco	17502001
55 mM 2-Mercaptoethanol	50 μM	Sigma	21985023
PD0325901	1 μM	Tocris	4192
CHIR99021	3 μM	Tocris	4423
Plasmocin Prophylactic (25mg/ml)	5 μg/ml	InvivoGen	ant-mpp
LIF supernatant (COS7/pCAGGS::LIF)	10 μl/ml	-	-
ESC-qualified Fetal Bovine Serum	20 μl/ml	Hyclone	HYC001331G
5% Sterile Bovine Serum Albumin	10%	Roche	10735078001
ADFNB Medium			
Advanced DMEM/F12 Medium (1X)	1X	Gibco	12634010
Neurobasal Medium (1X)	1X	Gibco	21103049
Penicillin-Streptomycin, 100X	1X	Gibco	15140122
200 mM L-Glutamine	2 mM	Gibco	25030024
MACS NeuroBrew-21, 50X	0.5X	Miltenyi Biotec	130-093-566
N2 Supplement, 100X	0.5X	Gibco	17502001
55 mM 2-Mercaptoethanol	50 μM	Sigma	21985023
5% Sterile Bovine Serum Albumin	10%	Roche	10735078001
MACS Buffer			
DPBS (1X)	1X	Gibco	14190094
5% Sterile Bovine Serum Albumin	10%	Roche	10735078001
DNase-I, recombinant	10 U/ml	Roche	4714728001
Other reagents			
Y-27632 dihydrochloride (ROCKi)	10 μM	Tocris	1254
SAG	0.5 μM	Calbiochem	566660
Retinoic Acid (RA)	1 μM	Sigma	R2625

Table 2.8. List of mouse astrocyte differentiation reagents and their working concentration, supplier and catalogue number.

2.8 Mouse astrocytes and human neurons co-culture

After MACS, mAstro were maintained in culture for a week until they formed a monolayer. Fresh ADFNB medium was provided every other day. After a week, iGlut and iGABA precursors were split or thawed, counted with Trypan Blue Solution, resuspended in 1:1 ADFNB/Cortical Maturation Medium + 2 µg/ml Doxycycline + 10 µM ROCKi and plated at the appropriate density for their final application on the mAstro monolayer (plating densities for each specific application are reported in Table 2.9). The day after, Day 1 of co-culture, half the medium was replaced by an equal volume of 1:1 ADFNB/Cortical Maturation Medium + 2 µg/ml Doxycycline + 10 µM Ara-C (final concentration 5µM). From co-culture Day 4 onwards, half medium changes with fresh 1:1 ADFNB/Cortical Maturation Medium were performed twice a week. Medium was supplemented with Dox until co-culture Day 10.

Application	iGlut (cell/cm^2)	iGABA (cell/cm^2)	iGlut + iGABA co-culture (cell/cm^2)
RT-qPCR	200'000	280'000	
ICC	30'000	45'000	22'000 iGlut + 19'000 iGABA
Electrophysiology	35'000	50'000	20'000 iGlut + 17'000 iGABA
Calcium imaging	50'000	80'000	37'000 iGlut + 31'000 iGABA

Table 2.9. List of cell plating densities for iGlut and iGABA lines for different applications. To note: iGABA cells are plated in 50% excess to account for the number of cells that will die following the Ara-C treatment.

2.9 Real-Time quantitative PCR (RT-qPCR)

Total RNA was isolated using RNeasy Mini Kit (Qiagen, 74104) according to the manufacturer's protocol. RNA was quantified spectrophotometrically using the NanoDrop 2000 (Thermo Fisher Scientific). First-strand cDNA for each sample was obtained from retro transcription of RNA using the GoScript^{TM} Reverse Transcription System (Promega, A5001) according to the manufacturer's protocol. Quantitative RT-PCR was carried out in 10µl reaction mixtures containing 10-20 ng cDNA, oligonucleotide primers (Sigma-Aldrich – Table 3) and Fast SYBR Green PCR Master Mix (Thermo Fischer Scientific, 4385612). RT-qPCR was performed using a CFX384 Touch Real-Time PCR Detection System (Bio-Rad) at the following settings: 95°C 10 min, 40 cycles of 95°C for 30 s and 60°C for 1 min, 75°C for 10 s, 95°C for 10 s. Gene expression levels were normalised to housekeeping gene TBP and the normalised data was analysed either by -ΔCt or Comparative CT Method (Livak & Schmittgen, 2001).

For *SCN1A* transcript analysis (Figure 3.11), SCN1A_13/15 forward and reverse primers (Sigma-Aldrich – Table 2.10) were used to amplify the portion of the transcript comprised between exon 13 and 15. cDNA from 3-week-old iGlut or iGABA cultures was used as a template for PCR amplification using Q5® High-Fidelity 2X Master Mix and primers (Sigma-Aldrich - Table 2.10) according to the manufacturer's protocol. The resulting PCR products were run on a 1.5% agarose gel and the gel was imaged using a Bio-Rad Gel Dock XR+ Molecular Imager (Bio-Rad).

Target Gene	**Forward Primer (5'-3')**	**Reverse Primer (5'-3')**
ALDH1L1	GGATGCCTTTGAGAATGGACGG	TCCTGGTGCTGCTCCATGAGAT
ALDOC	CATTCTGGCTGCGGATGAGTCT	CACACGGTCATCAGCACTGAAC
ANK2	AGCACTCTTTCCCCAAACTC	TCTCTGATGTTTCTGTTCCTGG
ANK3	AAAGGACTGCCTCAAACAGCGG	CTAAGGATGCGAAGCTCTGTCG
AQP4	GCCATCATTGGAGCAGGAATCC	ACTCAACCAGGAGACCATGACC
ASCL1	CGACTTCACCAACTGGTTCTG	ATGCAGGTTGTGCGATCA
ATP1A2	CGCTCGACAAGGAGATGCAAGA	CCGAGGAAACTTTCCAGATGGC
CACNA1A	CTGGTAGCCTTTGCCTTCACTG	ACACAGCCTTGAGCTTTGGCAG
CALB1	TTTCCTGCTGCTCTTCCGATGC	GCTCCTCAGTTTCTATGAAGCCA
CALB2	GATCCTGCCAACCGAAGAGAAC	CGATGTAGCCACTCCTGTCTGT
CAM2KA	CAGTTCCAGCGTTCAGTTAATG	TTCGTGTAGGACTCAAAATCTCC
CASPR2	CTGTGAGCATGGTGGAAAGTGC	GCTTCACAGGAAGGCTCGTAGA
CD11b	GGAACGCCATTGTCTGCTTTCG	ATGCTGAGGTCATCCTGGCAGA
CD44	CCAGAAGGAACAGTGGTTTGGC	ACTGTCCTCTGGGCTTGGTGTT
CUX1	TCACCTCTTCATAGTCAGCCT	CAGCCAGATCTCACAGCTTG
CX30	GAAACCACTCGCAAGTTCAGGC	AGGCTGCTTCAAAGATGATTCGG
DCX	TCAGGGAGTGCGTTACATTTAC	GTTGGGATTGACATTCTTGGTG
DLG2	TGCTTCTCCCAGGCACTATTCC	CTGACGAGTTGCGGTGCTATGT
DLX1	CATCAGTTCGGTGCAGTCCTAC	CCTTGCCATTGAAGCGCACTTC
DLX2	AGCAGCTATGACCTGGGCTA	GCTCAAGGTCCTCCTTCTCA
DLX5	TACCCAGCCAAAGCTTATGCCG	GCCATTCACCATTCTCACCTCG
DLX6	CCTCGGACCATTTATTCCAG	TTGTTCTGAAACCATATCTTCACC
EZR	ATCGAGGTGCAGCAGATGAAGG	CGCAGCATCAACTCCTCCTTCT
FOXG1	CGTTCAGCTACAACGCGCTCAT	CAGATTGTGGCGGATGGAGTTC
GABRA2	TTAGCCAGCACCAACCTG	TCGTCAAGATCAGGGCAAAAG
GABRB1	TGCTGGAAATACATGGTGAGTG	AGTGGACAGATTGCTCAAAGG
GABRG2	GCACACTCATTGTCGTCCTATCC	CAATGGTGCTGAGGGTGGTCAT
GAD65	CACCATCTCATATCCTTCTCGG	AAACTATGGCTGATGTGGAGG
GAD67	ATGGTGATGGGATATTTTCTCC	GCCATGCCCTTTGTCTTAAC

GAT1	AACACAGACCGCTGCTTCTCCA	AGCGGATCTGACCTGGCTTATC
GAT2	GCTGCTACCATGAGTGGAACAC	CGATGACAGGAGAGGTGGCATT
GFAP	GAAGCTCCAAGATGAAACCAAC	CCTCCAGCGATTCAACCTTT
GJA1	GGAGATGAGCAGTCTGCCTTTC	TGAGCCAGGTACAAGAGTGTGG
GLAST	GGTTGCTGCAAGCACTCATCAC	CACGCCATTGTTCTCTTCCAGG
GLT1	TGCCAACAGAGGACATCAGCCT	CAGCTCAGACTTGGAGAGGTGA
GLUL	CTGCCATACCAACTTCAGCACC	ATAGGCACGGATGTGGTACTGG
GLUR1	TGATGGAAAATACGGAGCCC	CTTCCCGGACCAAAGTGATAG
GLUR2	TCTCTGGTTTTCCTTGGGTG	CAGTCAGGAAGGCAGCTAAG
GRIA3	GTCTTTGGTTTTCCTTGGGTG	CAGCGAGATTGGCAGTATAGG
GRIA4	CAAGGAGAGGAAATGCTGGG	ACGTCCATAGTGGTCAAACTG
KCNA1	CATCTTTTGCCTGGAGACGCTC	GGAGAACCAGATGATACACAGCG
KCNC3	GACAAGAGCCCCATCACG	GCTTACGCCAGTCTTGGG
KCNQ2	TCATCGGTGTCTCCTTCTTCGC	GAGAGGTTGGTGGCGTAGAATC
KCNQ3	CGTCTGATTGCCGCCACCTTTT	TTCTGACGGTGTTGCTCCTGCA
LHX6	CTGTCCGACGACATCCACTA	GCCCGCACTGTACCTGAC
LIFR	CACCTTCCAAAATAGCGAGTATGG	ATGGTTCCGACCGAGACGAGTT
MAP2	CAGGAGACAGAGATGAGAATTCC	CAGGAGTGATGGCAGTAGAC
MBP	TCCTCTCCCCTTTCCCTG	CCCAAGATGAAAACCCCGTAG
MYT1L	AGGCACAGGAAAAGCACCAGAG	TTGGAACGCGGCGTAGTTGTGG
NANOG	TTTGTGGGCCTGAAGAAAACT	AGGGCTGTCCTGAATAAGCAG
NCAM1	GACATCACCTGCTACTTCCTG	GGCTCCTTGGACTCATCTTTC
NDRG2	CACTCTGTGGAGACACCATACG	CTGAAACAGTGGCTGGAAGCAAG
NESTIN	TGCGGGCTACTGAAAAGTTC	GGCTGAGGGACATCTTGAG
NF1B	GGAACCAAGTCCTACAGGAGAC	GAATCCTGTGGAGATGCAGAGC
NFASC	GGCAAAGCTGAAAACCAAGTCCG	TTCAGCCAGGAGACGGTGAGTT
NGN2	TACCTCCTCTTCCTCCTTCA	GACATTCCCGGACACACAC
NKX2.1	TCATTTGTTGGCGACTGG	TGCTTTGGACTCATCGACAT
NPY	GCTGCGACACTACATCAACCTC	CTGTGCTTTCTCTCATCAAGAGG
NR1	GAGAAGGAGAACATCACCGAC	GTCCCCATCCTCATTGAACTC
NR2B	CGTGGCTGTCTTTGTCTTTG	ACCCCAGAGCAACCAAATAG
NRCAM	TGTGGCTGAAGGACAACAGGGA	AGACGCTGTCCAGAGTGGTGTT
OCT3/4	AACCTGGAGTTTGTGCCAGGGTTT	TGAACTTCACCTTCCCTCCAACCA
OLIG2	AGATAGTCGTCGCAGCTTTC	GTTCTCCCCTGAGGCTTTTC
PAX6	GCACACACACATTAACACACTTG	GGTGTGTGAGAGCAATTCTCAG
PSD95	AGTCAGAAATACCGCTACCAAG	CCGTTCACCTGCAACTCATATC
PVALB	CTGATGGCTGCTGGAGACAAAG	GAGATTGGGTGTTCAGGGCAGA
S100B	GAAGAAATCCGAACTGAAGGAGC	TCCTGGAAGTCACATTCGCCGT
SCN10A	TGGCAGATGACCTGGAAGAACC	CGATACGGTAGCAAGTCTTGCG

SCN11A	CATCACACAACCTGAGCCTGAAC	CCTGTATGGTCAGATGAGGCTC
SCN1A	CGCATCAATCTGGTGTTCATTGTGC	TCGGGTGGCTTACTGTTGAGAATG
SCN1A_13/15	GCCATCACCATCTGTATTGTCT	CGGAATTGCCGATGATCTTTA
SCN1B	AACGCTGAGACCTTCACCGAGT	TCATCCTCCTCCAGCTGCAACA
SCN2A	CTAGCCTCACTGTGACAGTACC	TCAACCGTGCTGCCTTCAGATG
SCN2B	CTGGACTTACCAGGAGTGCAAC	CACCGACACATCGTACTTGCTG
SCN3A	CGTCACCTACTGGACAACTTCC	TCACGGCTCTTTGCCTTCCAGA
SCN3B	TCTGGTCTTCCTCACCTTGTGG	TGGGATGGCAAGGTAGTCAGAC
SCN4A	GCCTGCTTCAAGATTGTCGAGC	TAGGATGGTGCGAATGACTCGC
SCN4B	GTGGACCTACAACAGCAGTGAC	CCTACCAGAGTGATGCGGTCAT
SCN5A	CAAGACCTGCTACCACATCGTG	GTCGGCATACTCAAGCAGAACC
SCN8A	GGATTGAGACCATGTGGGACTG	ATCTGTGGCAGCCAGGTTGTCT
SCN9A	GTGGAAGGATTGTCAGTTCTGCG	GCCAACACTAAGGTGAGGTTACC
SLC12A2	CCTCTACACAAGCCCTGACTTAC	CGTGAGTTTGGAGCACCTGTCA
SNTA1	CCAGGACATCAAGCAGATTGGC	GAGACAAGTAGAGGAGCAGTTCC
SOX9	AGGAAGCTCGCGGACCAGTAC	GGTGGTCCTTCTTGTGCTGCAC
SPTBN4	CGCACATCTACCAGCTCTTCCT	AGTCACGGTGCTGTTTCAAGGC
SST	CCAGACTCCGTCAGTTTCTGCA	TTCCAGGGCATCATTCTCCGTC
SYN1	CCCCAATCACAAAGAAATGCTC	ATGTCCTGGAAGTCATGCTG
TNC	ATGTCCTCCTGACAGCCGAGAA	AGTCACGGTGAGGTTTTCCAGC
TUBA1A	CGGGCAGTGTTTGTAGACTTGG	CTCCTTGCCAATGGTGTAGTGC
TUBB3	TTTGGACATCTCTTCAGGCC	TTTCACACTCCTTCCGCAC
VGAT	AGGCTGGAACGTGACCAA	GGATGGCGTAGGGTAGGC
VGLUT1	TCAATAACAGCACGACCCAC	TCCTGGAATCTGAGTGACAATG
VGLUT2	TGGTCGTTGGCTATTCTCATAC	ATACTGGCATATCTTGGAGCG
VIM	AGGCAAAGCAGGAGTCCACTGA	ATCTGGCGTTCCAGGGACTCAT
VIP	CCAGTCAAACGTCACTCAGATGC	CTGGAAAGTCGGGAGATTCTCC

Table 2.10. List of forward and reverse primers used for RT-qPCR analysis, in alphabetical order.

2.10 Immunocytochemistry (ICC)

All samples for immunocytochemistry were fixed with 4% w/v PFA (Thermo Fisher Scientific, 11586711) for 10 min and, following three DPBS washes, were permeabilised and blocked for 30 min with 3% Horse Serum (Sigma-Aldrich) in DPBS-T (0.1% Triton X-100 (Thermo Fisher Scientific) in DPBS). Primary antibodies, appropriately diluted in block buffer (Table 2.11), were applied overnight at 4°C and, after three 10min DPBS-T washes, secondary antibodies were applied for 1h at RT. Following three 10min DPBS washes, samples were imaged using

the confocal laser scanning microscope Leica TCS SP8 (Leica Microsystems). Imaging analysis was performed using FiJi (NIH).

For AIS morphology analysis, the Ankyrin-G staining was imaged using the same laser intensity across all comparable conditions. Using FIJI, Ankyrin-G fluorescence was uniformly thresholded to assess AIS length, distance from the soma and fluorescence intensity. Distance from the soma was measured relative to the MAP2 counter stain. For AIS analysis in iGlut/iGABA co-cultures, Ankyrin-G staining analysis was performed relatively to the anti-GFP/anti-RFP staining used to distinguish between GCaMP6f-expressing iGlut and jrGECO1a-expressing iGABA, respectively.

Target	**Species / Fluorophore**	**Concentration**	**Manufacturer (Cat #)**
Primary Antibodies			
Ankyrin-G	Mouse IgG2a	1:200	Merck Millipore (MABN466)
GDNF	Goat IgG	1:500	R&D Systems (AF-212-NA)
GFAP	Rat IgG	1:500	Invitrogen (13-0300)
GFP	Rabbit IgG	1:500	Invitrogen (A11122)
GluN1	Mouse IgG2b	1:200	Synaptic Systems (114011)
MAP2	Rabbit IgG	1:1000	Antibodies-Online (ABIN1742387)
Nkx2.1	Rabbit IgG	1:500	Provided by the Burrone lab
Oct4	Mouse IgG2b	1:500	Santa Cruz (sc-5279)
PSD95	Mouse IgG2a	1:200	NeuroMabs (75-028)
RFP	Rabbit IgG	1:500	Abcam (ab62341)
S100b	Rabbit IgG	1:500	Abcam (ab52642)
Sox2	Rabbit IgG	1:500	Stemgent (09-0024)
SSEA-4	Mouse IgG	1:500	Abcam (ab16287)
Syn1	Mouse IgG	1:500	Synaptic Systems (106 001)
Tau	Sheep IgG	1:200	Abcam (ab62639)
TUBB3	Mouse IgG2a	1:1000	R&D Systems (MAB1195)
Vimentin	Mouse IgG	1:200	Merk (MABT121)
Secondary Antibodies			
Goat	Donkey – AF647	1:1000	Invitrogen (A11057)
Mouse IgG2a	Goat – AF488	1:1000	Invitrogen (A21143)

Mouse IgG2a	Donkey – AF647	1:1000	Invitrogen (A21123)
Mouse IgG	Donkey – AF488	1:1000	Invitrogen (A21206)
Mouse IgG	Donkey – AF568	1:1000	Invitrogen (A21208)
Mouse IgG	Donkey – AF647	1:1000	Invitrogen (A21043)
Rabbit IgG	Donkey – AF488	1:1000	Invitrogen (A21126)
Rabbit IgG	Donkey – AF568	1:1000	Invitrogen (A12379)
Rabbit IgG	Donkey – AF647	1:1000	Invitrogen (A21050)
DNA	DAPI 405	1:1000	Thermo Fisher (D1306)

Table 2.11. List of primary and secondary antibodies used in the immunocytochemistry analysis.

2.11 Calcium imaging (Ca^{2+} imaging)

For calcium imaging, MACS-sorted mAstro and iGlut/iGABA precursors were plated onto 1:100 MG-coated 13mm glass coverslips (cell densities according to Table 2.9) and maintained in culture until analysis (see section *2.3 Mouse astrocytes and human neurons co-culture*). At the desired time-point, coverslips were gently washed twice in warm Modified Tyrode Solution (buffer composition modified from Sun & Sudof (Z. Sun & Südhof, 2021a) – Table 2.12) and transferred into a 24-well glass bottom plate (Cellvis, P24-1.5H-N) containing either warm Modified Tyrode Solution, for the analysis of spontaneous activity, or warm Ca^{2+} Imaging Buffer, for the analysis of synchronous activity (buffer composition modified from Sun & Sudof (Z. Sun & Südhof, 2021a) – Table 2.12). After 1-2 min equilibration, Ca^{2+} imaging was performed at room temperature using either a Nikon Eclipse Ti-2 inverted microscope equipped with 2 x Photometrics Prime 95B sCMOS cameras or an inverted epifluorescent microscope (Olympus IX71). GCaMP6f fluorescence was recorder using a 488 nm filter while jrGECO1a fluorescence was recorder using a 568 nm filter. Time-lapse recordings were acquired using a 20x objective, at a 1x digital zoom, for 2 minutes at a frame rate of 10-20 frames/sec. For 2-colour imaging, the dual-camera mode was used and time-lapse recordings were acquired using a 20x objective - 1x digital zoom, with 488-568 sequential/alternate frame acquisition at a frame rate of 9 frames/sec. An average of 3 fields of view per coverslip were imaged and a minimum of 3 coverslip per biological sample were included in the analysis. All images were acquired using the same laser intensity and exposure time.

Time-lapses were analysed using a series of published MATLAB script (Z. Sun & Südhof, 2021a). The script "mmc3_REVISED" was used to automatically detect ROIs and calculate the raw fluorescent intensity over time for each ROI. The script "mmc6" was used to detect calcium spikes and calculate the spike rate and average spike amplitude for each ROI, as well as to calculate the normalised fluorescence intensity over time ($\Delta F/F_0$) for each ROI. Finally, the script "mmc5" was used to calculate the synchronous firing rate and amplitude from the average intensity of all ROIs in one field of view.

Component	**Modified Tyrode Solution**	**Ca^{2+} Imaging Buffer**
NaCl	136 mM	136 mM
HEPES	10 mM	10 mM
Glucose	10 mM	10 mM
$MgCl_2$	1 mM	1 mM
KCl	5 mM	8 mM
$CaCl_2$	2 mM	4 mM

Table 2.12. Details of Ca^{2+} imaging buffers composition.

2.12 Whole-cell patch clamp electrophysiology

For patch clamp recordings, MACS-sorted mAstro and iGlut/iGABA precursors were plated onto 1:100 MG-coated 18mm glass coverslips (cell densities according to Table 2.9) and maintained in culture until analysis (see section *2.3 Mouse astrocytes and human neurons co-culture*). At the desired time-point, coverslips were transferred to an open bath chamber (Warner Instruments, RC-41LP) containing extracellular solution at pH 7.3 and osmolarity at ~305 mOsm (solution composition detailed in Table 2.13). The chamber was mounted on an inverted epifluorescent microscope (Olympus IX71) fitted with a 60x oil objective. Glass pipettes were pulled from borosilicate glass (O.D. 1.5 mm, I.D. 0.86 mm, Sutter Instruments, B150-86-10) to have a resistance between 3 and 5 MΩ and were filled with 10 µl of intracellular solution (Table 2.13) at pH 7.4 and osmolarity 290 mOsm. Whole-cell patch clamp was performed at the soma of neurons using a Multiclamp 700B amplifier (Molecular Devices) and recorded using a Digidata 1440A digitizer (Molecular Devices). All recordings were carried out at room temperature and the data was acquired with Clampex software (Molecular Devices) and Axon Multiclamp Commander Software (Molecular Devices). Current-clamp data was sampled at a rate of 50 kHz and filtered at 10 kHz while voltage-clamp data was sampled at 20 kHz and

filtered at 10 kHz. Whole-cell currents used to estimate the conductance of Na^+ and K^+ were recorded in voltage-clamp mode using 50 msec voltage steps from -80 mV to +50 mV. Resting membrane potential and spontaneous action potential (AP) spiking were recorded, within the first 2 minutes after whole-cell patch was achieved, for 1 minute in current-clamp mode in the absence of current injection. Intrinsic excitability measurements and AP properties were recorded in current-clamp mode, using a steady current injection to maintain the membrane potential at -60 mV. Input-Output measurements were performed using 500 msec current injections from -50 pA to 300 pA (50 pA steps) while AP properties were assessed using 10 msec current injections from -20pA – 170pA (10 pA steps).

Electrophysiological measurements were analysed using custom MATLAB scripts written by Guilherme Neves (Burrone Lab). Inward Na^+ currents in voltage-clamp were measured as the minimum value of a current trace, while steady state outward K^+ currents were measured by averaging values over a 15 msec window acquired 25 msec after the voltage step. Values were corrected for baseline current offset before stimulation and normalised to the membrane capacitance to obtain an estimate of the amount of current flowing through the cell membrane per unit area (current density). Action potential (AP) properties in current-clamp were measured using sequential injection of 10 msec current steps of increasing amplitude (10 pA increments). Only the measurements of the first AP at the current threshold (first step to elicit an AP) were considered. AP waveforms were extracted using the MATLAB's findpeaks function with minimum peak Amplitude 0 mV. For each cell we extracted the following parameters: Amplitude (Max amplitude – average Vm at the end of stimulus 50 msec window excluding APs), Voltage Threshold (Voltage at the time the speed of Vm rise is above 0.15 mV/ms), Half-width. Input-Output curves were obtained using sequential injection of 500 msec current steps of increasing amplitude (50 pA increments). The location of the AP was extracted using MATLAB's findpeaks function with minimum peak Amplitude set at 0 mV. Cells with access resistance greater than 30 MΩ or a holding current lower than -100 pA were excluded from the analysis.

Extracellular solution	Intracellular solution
NaCl – 136 mM	$KMeSO_4$ – 125 mM
KCl – 2.5 mM	$MgCl_2$ – 5 mM
HEPES – 10 mM	EGTA – 10 mM
$MgCl_2$ – 1.3 mM	HEPES – 10 mM
$CaCl_2$ – 2 mM	NaGTP – 0.5 mM
Glucose – 10 mM	Na_2ATP – 5mM

Table 2.13. Details of intracellular/extracellular patch clamping solutions composition.

2.13 Statistical Analysis

All data are presented as mean ± standard error of the mean (SEM). The nature and size of the samples, specific statistical methods carried out and exact P-values are detailed in the figure legends and in supplementary tables for each chapter. Briefly, a series of normality tests (Anderson-Darling, D'Agostino & Pearson, Shapiro-Wilk, Kolmogorov-Smirnov) were performed to determine if parametric or non-parametric approaches were appropriate.

For normally distributed datasets:

- Unpaired parametric t-test was performed when comparing the effect of one variable across two datasets.
- Ordinary One-Way ANOVA with Tukey's multiple comparisons test was performed when comparing the effect of one variable across three or more datasets.

For non-normally distributed datasets:

- Unpaired non-parametric Mann-Whitney test was performed when comparing the effect of one variable across two datasets.
- Kruskal-Wallis with Dunn's multiple comparisons test was performed when comparing the effect of one variable across three or more datasets.
- Two-Way ANOVA with multiple comparison was performed when comparing the effect of two variables across three or more datasets.

P-values < 0.05 were considered to be statistically significant and in figures and figure legends are denoted by asterisks * (* $p < 0.05$, ** $p < 0.01$, *** $p < 0.001$). Data presentation and statistical analyses were performed using Graphpad Prism, Version 9.4.1 (458) (Graphpad Software, San Diego, California USA, www.graphpad.com).

Chapter 3

Engineering hiPSC-derived cortical neurons to model Dravet syndrome

3.1 Introduction

The first aim of this project was to establish a robust and reproducible method for the generation of cortical excitatory neurons, inhibitory interneurons and astrocytes from hiPSCs. As discussed in *Chapter 1 section 1.3*, several protocols already exist in the literature, typically directed differentiation protocols using small molecules and growth factors, but also forward programming strategies using the expression of lineage-specific transcription factors. While directed differentiation may more closely model *in vivo* developmental pathways, these protocols are typically very lengthy, poorly reproducible and tend to generate mixed cell populations (S. M. Ho et al., 2015; B. Y. Hu et al., 2010). A key aspect of our proposed *in vitro* model of cortical circuits is the defined composition of exclusively excitatory and inhibitory neurons at a consistent ratio of 70:30 to resemble the human cortex E/I ratio. For this purpose, reproducible protocols which could yield mature and homogenous neuronal subtype populations are required. Forward programming approaches are known to enable scalable and rapid generation of homogenous cell populations, however, they are considered less suitable for developmental studies. In order to find the best performing differentiation strategy, in the first part of this project we explored both directed differentiation and forward programming methods to generate excitatory and inhibitory neurons from hiPSCs. In this chapter, two versions of dorsal directed differentiation (D-V1 and D-V2) into excitatory neurons (Y. Shi, Kirwan, & Livesey, 2012) and two versions of ventral directed differentiation (V-V1 and V-V2) into inhibitory interneurons (Maroof et al., 2013) were first compared. Results from the best directed differentiation protocols were then compared with forward programming strategies for the generation of either excitatory neurons (iGlut) (C. Wang et al., 2017) or inhibitory interneurons (iGABA) (Yang et al., 2017). Together with neuronal differentiation, in this chapter, a forward programming approach for the generation of inducible astrocytes (iAstro) (Canals et al., 2018) was established, and the cells generated characterised for their identity and differentiation profile.

After generating forwards programming lines for the generation of iGlut, iGABA and iAstro, we attempt to combine the differentiation of these three cell types to generate a fully human *in vitro* model of cortical circuits. Unforeseen technical issues with the use of inducible astrocytes forced us to find an alternative strategy to include this important cell type in our system. We elected to use mouse Embryonic Stem Cell (mESC)-derived astrocytes, a well-established model already in use in the lab. Herein, we describe the ability of these astrocytes to support long-term neuronal survival and promote neuronal maturation.

Alongside the establishment and optimisation of our co-culture system, we designed a CRISPR/Cas9-mediated gene editing strategy to correct the *SCN1A*$^{IVS14+3A>T}$ pathogenic mutation harboured by the DS1 line and generate a corrected isogenic control line. Finally in this chapter, we describe the functionalisation of our neuronal lines with spectrally distinct Genetically Encoded Calcium Indicators (GECIs) to allow for monitoring of neuronal network activity with single cell resolution and distinguishable neuronal population contribution. We use these calcium probes to confirm the successful generation of a co-culture system composed of ratio-defined excitatory and inhibitory neurons to resemble the human cortex E/I ratio of 70:30.

3.2 Results

3.2.1 Directed differentiation of hiPSCs into glutamatergic cortical neurons

In order to generate glutamatergic cortical neurons by directed differentiation of hiPSCs, two different versions of the Shi et al. dorsal differentiation protocol were tested (Y. Shi, Kirwan, & Livesey, 2012). Starting from a monolayer of hiPSCs, version 1 (D-V1) involves: (i) dual SMAD inhibition to induce neural forebrain specification (Day1-8); (ii) a short maintenance period (Day8-12); (iii) an expansion phase to form neural rosettes (Day12-14) and (iv) a maturation period until cells have reached the progenitor stage (Day14-35) (Fig. 3.1-A). Dorsal differentiation version 2 (D-V2) is characterised by: (i) a longer neuroectoderm induction phase with dual SMAD inhibition (Day1-12); (ii) a longer expansion phase for the formation of rosettes (Day 12-16) and (iii) maturation to progenitors (Day16-35) (Fig. 3.1-B). At day 35 of differentiation, we performed a pilot characterisation to assess the quality of the neuronal progenitor populations obtained with the two versions of the dorsal differentiation protocol. All the results discussed below are relative to 1 biological replicate, therefore, statistical analysis was not performed on any of these datasets. First, ICC was performed on the progenitor populations obtained to analyse protein expression levels of specific markers (Fig. 3.1-C). First, general cell identity and maturation stage of the cultures was evaluated. MAP2, a protein found in the soma and dendrites of neurons, was positively detected in both progenitor populations, with lower expression levels observed in the D-V2 progenitors (Fig. 3.1-C). Expression of β3-Tubulin (TUBB3), a marker of post-mitotic neurons, was also detected in both progenitor samples. While DV-1 progenitors were mainly composed of cells with low TUBB3 expression levels, typical of the progenitor stage, D-V2 progenitors showed increasing abundance of cells with higher TUBB3 expression levels (Fig. 3.1-C). When observing neuronal morphology, it was apparent that the lower MAP2 and higher TUBB3 fluorescent intensity observed in D-V2 progenitors were a result of a more mature neuronal morphology displayed by these cells. In fact, D-V1 progenitors were mainly characterised by big cell bodies, with fewer and shorter processes. The D-V2 progenitor population instead, generally exhibited smaller cell bodies and more defined, longer neuronal processes, indicative of a more mature morphology. Finally, post-synaptic marker PSD95 was detected in a small number of cells in both dorsal progenitor populations, with higher abundance in D-V2 progenitors (Fig. 3.1-C). However, at this stage, PSD95 had not yet assumed the characteristic punctate distribution typical of synapses.

Based on this preliminary ICC characterisation, the D-V2 protocol seemed to generate a population of progenitors at a more advanced developmental stage compared to D-V1. For this reason, D-V2 progenitors were further characterised to assess the efficiency of neuronal fate specification inferred by this differentiation protocol. Gene expression profile analysis showed that D-V2 progenitors expressed *PAX6*, a marker of glutamatergic progenitors (Götz et al., 1998), *ASCL1*, a marker of GABAergic progenitors (Marín et al., 2000), and *ISL1*, a marker of GABAergic and cholinergic progenitors (Siddiqi et al., 2021) (Fig. 3.1-D). While *PAX6* was the most abundantly expressed progenitor marker, suggesting that glutamatergic neurons were the prevalent identity, the presence of *ASCL1* and *ISL1* indicated that the analysed population contained a mix of different progenitor cells. *NEUROD1* marker of immature neurons (Hevner et al., 2006) was also detected, alongside pan-neuronal markers *MAP2* and *TUBB3* (Fig. 3.1-D). Cortical identity genes such as *LHX2*, *CUX1* and *NR2F1* (Leung et al., 2022) were all found to be expressed at high levels, while markers of mature glutamatergic identity such as *NR1*, *NR2B* (P. Singh et al., 2011), *vGLUT1/2* (Vigneault et al., 2015) and *CAMK2A* (E. G. Jones et al., 1994) were either not detected or detected at very low levels (Fig. 3.1-D). Finally, markers of mature GABAergic identity such as *GAD67* (Modi et al., 2015) and *vGAT* (McIntire et al., 1997) were not expressed (Fig. 3.1-D).

Overall, the analysis of D-V2 cells showed that after 35 days of differentiation the generated neurons were at progenitor stage, as indicated by the MAP2/TUBB3 stainings, the expression of *PAX6* and lack of mature neuronal markers. These progenitors were of cortical identity, as suggested by the expression of *LHX2*, *CUX1* and *NR2F1*. However, the expression of GABAergic progenitor markers *ASCL1* and *ISL1* suggested that this differentiation protocol had low fate specification efficiency and the resulting cell population was likely to contain mixed progenitors of glutamatergic and GABAergic identity. In order to obtain a pure population of glutamatergic progenitors, an additional step to enrich the differentiated culture for the desired cell type would be required.

3.2.2 Directed differentiation of hiPSCs into GABAergic cortical interneurons

For the directed differentiation of hiPSCs into GABAergic inhibitory interneurons, two different ventral differentiation protocols were tested. Version 1 (V-V1), based on Maroof et al. (Maroof et al., 2013), involves: (i) combined dual SMAD and Wnt inhibition to achieve neural induction with enhanced forebrain specification (Day1-10); (ii) SHH signalling activation to induce ventralisation of forebrain progenitors (Day10-18); (iii) a short expansion phase (Day18-

20) and (iv) maturation until cells have reached the progenitor stage (Day21-35) (Fig. 3.2-A). Using this protocol, differentiating cells failed to form neural rosettes and did not survive past this stage (Fig. 3.2-A). Version 2 of ventral differentiation (V-V2) is adapted from Shi et al. (Y. Shi, Kirwan, & Livesey, 2012). This protocol is characterised by: (i) combined neural induction and ventralisation with simultaneous dual SMAD inhibition and SHH activation (Day1-12); (ii) a longer expansion phase for neural rosettes formation (Day12-16) and (iii) maturation to progenitors (Day16-35) (Fig. 3.2-B). Using this protocol, differentiating cells were able to form neural rosettes and further develop to ventral progenitors (Fig. 3.2-B). At day 35 of differentiation, we performed a pilot characterisation to assess the quality of the neuronal progenitor population obtained with the version 2 of the ventral differentiation protocol. All the results discussed below are relative to 1 biological replicate, therefore, statistical analysis was not performed on any of these datasets. At day 35 of differentiation, ICC was performed on the obtained progenitor population to assess neuronal morphology and identity (Fig. 3.2-C). MAP2 and TUBB3 were both positively detected and depicted a neuronal morphology comprising cells with small cell bodies and numerous neuronal processes, as well as bigger cells with no or shorter processes (Fig. 3.2-C). The ventral forebrain marker NKX2.1 (Q. Xu et al., 2004) was found to be present in only 22.9 ± 2.3% of cells (Fig. 3.2-C and D), suggesting low fate specification efficiency. According to the published protocol, around 80% of progenitor cells should be $NKX2.1^+$ at this stage, however, this assessment was performed using a NKX2.1-GFP knock-in hESC line, not immunolabelling (Maroof et al., 2013). To further investigate the efficiency of neuronal fate specification, gene expression profile analysis was performed on the ventral progenitor population obtained with V-V2. It was found that these progenitors express *PAX6* as well as *ASCL1* and *ISL1*. Ventral forebrain marker *NKX2.1* and ganglionic eminence marker *LHX6* (Du et al., 2008) were expressed at very low levels, together with *NEUROD1* (Fig. 3.2-E). Pan-neuronal markers *MAP2* and *TUBB3* were found to be highly expressed, while markers of mature GABAergic identity (*DLX2/6* (Anderson et al., 1997), *GAD67*, *GAT1* (Scimemi, 2014) and *vGAT*) were detected at very low levels (Fig. 3.2-E). Variable levels of different GABAergic interneuron subtype markers (Q. Xu et al., 2004) were detected, with somatostatin (*SST*) and calbindin (*CALB1*) being more abundant over calretinin (*CALB2*) and parvalbumin (*PVALB*) (Fig. 3.2-E). Finally, markers of mature glutamatergic identity such as *vGLUT1* and *vGLUT2* were not expressed (Fig. 3.2-E).

Overall, the analysis of V-V2 cells showed that after 35 days of differentiation the generated culture is likely to contain neuronal progenitors of various identities. Only ~20% of cells

expressed the ventral forebrain marker NKX2.1 and, while the bulk population was positive for the GABAergic progenitor markers *ASCL1* and *ISL1*, it was also found that they express high levels of *PAX6*, a marker of dorsal progenitors. These observations suggest that, similarly to D-V2, this differentiation protocol has low fate specification efficiency and the resulting cell population is likely to contain mixed progenitors of glutamatergic and GABAergic identity. As previously discussed for D-V2, in order to obtain a pure population of GABAergic progenitors, an additional step to enrich the differentiated culture for our desired cell type would be required.

3.2.3 Neuronal type-specific Magnetic-Activated Cell Sorting (MACS)

As reported in the literature (S. M. Ho et al., 2015; B. Y. Hu et al., 2010), and confirmed by our analysis, both ventral- and dorsal-type differentiations produce populations of cells of heterogenous identity and developmental stage. For our experimental model, pure populations of glutamatergic and GABAergic neurons are required, so we designed and tested a MACS-based purification strategy aimed at enriching the differentiated cultures for our desired cell types. This strategy, successfully used in the Lieberam lab to purify homogenous populations of motor neurons (Bryson et al., 2014) and astrocytes (Machado et al., 2019), relies on the use of a cell type-specific promoter to drive the expression of the membrane surface marker CD14. Cells expressing CD14 can then be live labelled using a mouse anti-human CD14 primary antibody, followed by an anti-mouse IgG magnetic beads-conjugated secondary antibody and the labelled cells can be sorted using Miltenyi Biotech magnetic separation columns (Fig.3.3-A). Using the same approach, we investigated the use of GABAergic-specific promoter Dlx5/6 (Anderson et al., 1997) to allow for efficient isolation of our desired cell populations. As a proof of concept for this approach, a plasmid encoding GFP under the transcriptional control of the Dlx5/6 promoter (Fig. 3.3-B) was transfected into ventral progenitors at day 22 of differentiation, with cells FACS sorted at day 24 to isolate the GFP^+ population (Fig. 3.3-B). Gene expression levels of selected GABAergic interneuron markers were analysed in the $Dlx5/6^+$-enriched ventral progenitor population in comparison with the unsorted ventral population and with dorsal progenitors. The investigated ventral forebrain markers *DLX2*, *DLX6* and *NKX2.1*, as well as GABAergic markers *GAD67*, *LHX6* and *vGAT*, were all found to be expressed at higher levels in the enriched $Dlx5/6^+$ ventral progenitor population (Fig. 3.3-C). Contrarily, higher levels of the dorsal progenitor marker *PAX6* were detected in the dorsal and unsorted ventral progenitor populations (Fig.3.3-C). Although this experiment was only

performed once, the observed results support the feasibility of a Dlx5/6 MACS-sorting step in the differentiation protocol to isolate inhibitory GABAergic interneuron precursors.

3.2.4 Generation of hiPSC lines suitable for forward programming differentiation

Alongside directed differentiation of hiPSCs into cortical neurons, we investigated the use of published forward programming strategies to derive glutamatergic excitatory neurons, GABAergic interneurons and astrocytes. As discussed in *Chapter 1 Section 1.3.2*, forward programming relies on the induced expression of lineage-specific transcription factors to directly convert hiPSCs into the desired cell type. The transgene expression is typically regulated by a Tet-ON system, where the reverse tetracycline trans-activator (rtTA) protein, after binding to doxycycline, interacts with the tetracycline response element (TRE) in the transgene promoter region, causing initiation of transcription (Das et al., 2016) (Chapter 1 Fig. 1.4-B). To achieve stable and reproducible integration of the rtTA and TRE-regulated transgenes into hiPSC lines, we used transcription activator-like effector nucleases (TALENs) to target the integration at the adeno-associated virus integration site 1 (AAVS1) safe-harbour locus (Fig. 3.4-A). Contrarily to lentiviral-mediated integration, characterised by low efficiency and random genomic insertion, safe-harbour loci provide defined integration sites for exogenous DNA with minimal impact on neighbouring endogenous gene structures or functions (Pavani & Amendola, 2021). Additionally, while integration achieved by lentiviral transduction can result in variability of expression levels and transgene silencing, AAVS1 integration ensures active and robust expression of exogenous DNA in many cell types, including stem cells (J. R. Smith et al., 2008b). For this purpose, constructs compatible with AAVS1 integration, encoding for a puromycin resistance gene (for cell line selection), rtTA and TRE-regulated transgenes (Fig. 3.4-A), were cloned as described in *Chapter 2 section 2.3.1*. Specifically, three vectors were made, one encoding NGN2 for the induction of glutamatergic neurons (iGlut), one encoding ASCL1-DLX2 for the generation of GABAergic interneurons (iGABA) and one encoding NF1B-SOX9 to derive astrocytes (iAstro) (Fig. 3.4-B). Transfection of these vectors in hiPSCs was performed via electroporation and, following monoclonal selection, the correct and homozygous integration of the transgene was confirmed using a PCR-based screen composed of two reactions, one to detect the presence of WT alleles (Reaction #1) and one to detect the presence of modified alleles (Reaction #2) (Fig.3.4-A). Homozygous modified clones are therefore negative for reaction #1 and positive for #2 (Fig.

3.4-C). Using this strategy, we generated three sub-clonal lines suitable for forward programming differentiation (iGlut, iGABA and iAstro – Fig. 3.4-C + Supplementary Fig. 3.1-A) from wildtype and DS1 hiPSCs.

3.2.5 Forward programming differentiation into excitatory cortical neurons

Using forward programming, the differentiation of hiPSCs into cortical excitatory neurons is mediated by the doxycycline-induced expression of the transcription factor NGN2. Following a published protocol (Fernandopulle et al., 2018), hiPSCs undergo only 3 days of doxycycline induction before they are frozen or re-plated into their final format. Induced cells quickly assume neuronal morphology and develop long neuronal processes (Day 7), such that re-plating later than Day 3 would cause substantial axonal damage (Fig. 3.5-A). Induced iGlut cells are then maintained in Dox-free medium supplemented with BDNF and NT3 to promote maturation and Laminin to maintain cell adherence (Fig. 3.5-A). Occasionally, differentiating cultures contained contaminating cobblestone-shaped cells (Supplementary Fig. 3.1-B), likely undifferentiated hiPSCs or differentiating cells stuck in a progenitor-like stage. While the maturing neurons quickly became post-mitotic, these cells maintained proliferative capacities and, long-term, they would overgrow the neuronal culture (Supplementary Fig. 3.1-B). To remove any undifferentiated or contaminating cell types, the differentiation protocol was modified to include a preventative 3-day treatment with cytarabine (Ara-C), an anti-mitotic agent commonly used to induce cell death of rapidly proliferating non-neuronal cells in culture (Calderón-Martínez et al., 2002; Kidambi et al., 2008; Maňáková et al., 2003). Ara-C treatment successfully killed any unwanted proliferating cells and resulted in a homogenous population of post-mitotic neurons (Fig. 3.5-A, Day 7-Day25 + Supplementary Fig. 3.1-B). ICC evaluation at Day 10 showed that, at this early stage, iGlut differentiating neurons have already assumed a more mature neuronal morphology compared to D-V1/2 progenitors, characterised by small $MAP2^+$ cell bodies and fully formed $TUBB3^+$ axons (Fig. 3.5-B). By Day 25 of differentiation (3 weeks after sub-plating), iGlut displayed an even more intricate neuronal morphology, with expanded cell bodies and multiple long processes per cell (Fig. 3.5-C). At this stage, iGlut expressed TAU, a microtubule-associated protein present in mature neurons of the cerebral cortex (Y. Wang & Mandelkow, 2015), as well as pre-synaptic protein SYN1 (Rosahl et al., 1995) and post-synaptic proteins PSD-95 (E. Kim & Sheng, 2004) and GluN1 (Hansen et al., 2014). Importantly, synaptic proteins were found to adopt a characteristic punctate distribution along the $MAP2^+$ dendrites, suggesting the synaptic maturity of the neurons (Fig. 3.5-C +

Supplementary Fig. 3.1-C). 4-week-old iGlut neurons (Day 35) were further characterised to assess the efficiency of neuronal fate specification resulting from NGN2-mediated differentiation. Both WT and DS1 iGlut populations were investigated and, for both lines, gene expression profile analysis confirmed a population of mature cortical neurons of glutamatergic identity (Fig.3.5-D). Specifically, we found that pluripotency genes *NANOG* and *OCT3/4* (Seymour et al., 2015), as well as dorsal progenitor genes *PAX6* and *NESTIN* were not expressed. Contrarily, pan-neuronal markers such as *TUBB3, MAP2, MYT1L, ANK2, NCAM1* and *DCX* were found to be abundantly expressed (Fig.3.5-D). The investigated markers of telencephalic and cortical glutamatergic identity were also positively expressed, specifically *CUX1* and *LHX2*. Multiple glutamate and GABA receptors were detected, including *GLUR1*, *GLUR2*, *GRIA4*, *NR1*, *GABRA2* and *GABRB1* (Olsen & DeLorey, 1999; Traynelis et al., 2010), together with glutamate transporter genes *VGLUT1* and *VGLUT2*, while additional receptor genes such as *GRIA3* and *NR2B* (Traynelis et al., 2010) were found to be less expressed (Fig.3.5-D). Similarly, low expression levels were detected for *CAMK2A*, a kinase specific to glutamatergic neurons, and for the post-synaptic protein *PSD95*. Contrarily, higher expression levels were observed for the pre-synaptic protein *SYN1*. Finally, the expression of GABAergic identity genes *GAD65* (Modi et al., 2015) and *GAD67* was not detected (Fig.3.5-D). Considering some degree of variability across differentiation batches, these results were found to be consistent across different samples derived from the same hiPSC line, as well across different lines (WT and DS1) (Fig.3.5-D).

Overall, the characterisation of forward programming differentiated glutamatergic neurons is consistent with the published literature (Frega et al., 2017; Nehme et al., 2018; Y. Zhang et al., 2013), and seem to indicate rapid and homogenous development towards the desired neuronal identity. When compared to dorsal progenitors derived using directed differentiation (D-V2, previously discussed in this chapter, *section 3.2.1*), it is noticeable how these two populations differ in developmental stage (Fig. 3.5-E). Both types of differentiation produced neurons of cortical identity, indicated by the expression of *LHX2* and *CUX1*. However, D-V2 neurons still expressed progenitor genes such as *PAX6*, *NEUROD1* and *TBR1*, which were not detected in the iGlut population. Contrarily, iGlut neurons expressed a range of more mature genes, including *NR1*, *VGLUT1* and 2 and *SYN1* which were not yet expressed in D-V2 progenitors (Fig.3.5-E). Additionally, in terms of developmental timing, iGlut neurons reach a more mature stage in the same time that is required by directed differentiation to generate progenitor cells (35 days). Considering these observations, forward programming differentiation was

considered the most suitable strategy to derive homogenous populations of mature excitatory cortical neurons.

3.2.6 Forward programming differentiation into GABAergic inhibitory interneurons

Using forward programming, the differentiation of hiPSCs into GABAergic inhibitory interneurons is mediated by the doxycycline-induced expression of the transcription factors ASCL1 and DLX2. Starting from a published protocol (Yang et al., 2017), we adapted the differentiation process to include a sub-plating/freezing step following 4 days of doxycycline induction (Fig. 3.6-A). Similarly to iGlut, induced iGABA cells quickly assume neuronal morphology and develop long neuronal processes (Fig. 3.6-A, Day 7). Induced iGABA cells are then maintained in medium supplemented with BDNF, NT3 and Laminin to promote maturation and adhesion (Fig. 3.6-A), and doxycycline is withdrawn after 14 days (as in the original protocol). Interestingly, during the initial 4 days of induction, iGABA cells organise into "polarised" colonies, with cells at one end of the colony clustering in a tight three-dimensional structure and cells on the opposite end assuming a two-dimensional, flat and spread-out morphology (highlighted by a white dashed line in Supplementary Fig. 3.1-D). This "polarised" colony morphology was observed in all iGABA cell lines, independently of genotype, suggesting this is a characteristic of the differentiation protocol, rather than a cell line-specific behaviour (Supplementary Fig. 3.1-D). If left untreated, cells populating the "flat" end of the colony rapidly proliferate and, by Day 10, take over the entire culture (Supplementary Fig. 3.1-D). Similarly to the iGlut differentiation protocol, a 3-day Ara-C treatment after the sub-plating step was sufficient to successfully kill these unwanted proliferating cells, resulting in cultures that contain a homogenous population of post-mitotic neurons (Fig. 3.6-A, Day 7-Day 25). ICC evaluation at Day 10 showed that, at this stage, iGABA differentiating neurons have already assumed a more mature neuronal morphology compared with V-V2 progenitors, characterised by $MAP2^+$ cell bodies and fully formed $TUBB3^+$ axons (Fig. 3.6-B). By Day 25 of differentiation (3 weeks after sub-plating), iGABA neurons, like iGlut neurons, expressed microtubule-associated protein TAU, as well as pre-synaptic protein SYN1 and post-synaptic proteins PSD-95 and GLUN1. Synaptic proteins were all observed in a characteristic punctate distribution along the $MAP2^+$ dendrites, suggesting the synaptic maturity of the neurons (Fig. 3.6-C + Supplementary Fig. 3.1-E). 4-week-old iGABA neurons (Day 35) were further characterised to assess the efficiency of neuronal fate specification inferred by ASCL1/DLX2-

mediated differentiation. Both WT and DS1 iGABA populations were investigated and, for both lines, gene expression profile analysis seemed to define a population of mature GABAergic cortical interneurons (Fig.3.6-D). Specifically, we found that pluripotency genes *NANOG* and *OCT3/4*, as well as dorsal progenitor genes *PAX6* and *NESTIN* were not expressed. Of the interneuron progenitor markers investigated, *NKX2.1* and *LHX6* were not detected, while *ASCL1* was only detected in iGABA derived from the DS1 line (Fig.3.6-D). Pan-neuronal markers *TUBB3*, *MAP2*, *MYT1L*, *ANK2*, *NCAM1* and *DCX* were all found to be abundantly expressed, together with mature GABAergic identity genes. Particularly, interneuron-specific transcription factors *DLX1*, *DLX2*, *DLX5* and *DLX6*, GABA producing enzymes *GAD65* and *GAD67* and GABA transporters *GAT1* and *vGAT* were all highly expressed, while transporter *GAT2* (Scimemi, 2014) was detected at lower levels (Fig.3.6-D). Pre-synaptic protein *SYN1* was also abundantly expressed. Variable levels of different GABAergic interneuron subtype markers (Wonders & Anderson, 2006) were detected, with somatostatin (*SST*) being the most abundant over calbindin (*CALB1*), calretinin (*CALB2*), parvalbumin (*PVALB*) and Neuropeptide Y (*NPY*), while Vasoactive Intestinal Peptide (*VIP*) was not detected (Fig. 3.6-D). Finally, markers of mature glutamatergic identity *vGLUT1* and *vGLUT2* were not expressed. With minor variability across differentiation batches, these results were found to be consistent across independent samples derived from the same hiPSC line, as well across different lines (WT and DS1) (Fig.3.6-D).

Consistently with the published literature (Yang et al., 2017)(Barretto et al., 2020), the characterisation of forward programming differentiated GABAergic interneurons seem to indicate rapid and homogenous development towards the desired neuronal identity. When compared to V-V2 progenitors derived using directed ventral differentiation, iGABA neurons clearly emerged as the more mature, fate-defined, population (Fig.3.6-E). As previously discussed in this chapter (section 3.2.2), V-V2 differentiation likely generates a mixed population of dorsal and ventral progenitors, indicated by the expression of both *PAX6* and *ASCL1*. The expression of progenitor markers was not detected in the iGABA population which, by contrast, expressed multiple mature GABAergic identity genes, including *DLX2*, *DLX6*, *GAD67*, *GAT1* and *vGAT* (Fig.3.6-E). The expression of these genes shows that iGABA neurons matured much faster than V-V2 progenitors, reaching a more mature stage in the same time that was required by directed differentiation to generate progenitor cells. Considering these observations, forward programming differentiation was considered the most suitable strategy to derive homogenous populations of mature GABAergic inhibitory interneurons.

3.2.7 Forward programming differentiation into astrocytes

Using forward programming, the differentiation of hiPSCs into astrocytes is defined by the doxycycline-induced expression of the transcription factors NF1B and SOX9. The differentiation process was optimised from a published protocol (Canals et al., 2018). Briefly, hiPSC colonies undergo 3 days of doxycycline induction followed by 4 days of FGF-mediated expansion. At Day 7, astrocytes are frozen down or sub-plated into their final format and are maintained in CNTF and BMP4 supplemented medium to promote maturation. Doxycycline is withdrawn after 14 days (Fig. 3.7-A). At different time points during the differentiation, we performed a pilot ICC characterisation to assess the quality of the astrocyte population obtained with forward programming differentiation. The ICC results discussed below are relative to 1 biological replicate, therefore, statistical analysis was not performed on this dataset. The expression of key astrocytic markers over time was evaluated using ICC at Day 7, Day 14 and Day 21 of differentiation (Fig. 3.7-B and C). This characterisation was performed in collaboration with Lieberam lab PhD student Sofia Syntaka. The calcium-binding protein S100b, expressed in various types of astrocytes (Bramanti et al., 2010), was positively detected in 83±% of cells as early as Day 7. Its expression was maintained in ~86% of cells at the two successive time-points (Fig. 3.7-C). The glial fibrillary acidic protein (GFAP), commonly used as a marker of astrocytic identity (Jurga et al., 2021), was detected in 41% of cells at Day 7 and increased in abundance over the next two time-points, respectively 61% at Day 14 and 73% at Day 21 (Fig. 3.7-C). Vimentin, another intermediate filament protein found in both immature and post-mitotic astrocytes (Bramanti et al., 2010), was also found to increase its abundance over time. Starting from 26% of cells expressing Vimentin at Day 7, the number of positive cells increased to 38% at Day 14 and 69% at Day 21 (Fig. 3.7-C). Finally, the proliferation properties of iAstro were investigated by staining against Ki67, a common marker of cell proliferation (Gerdes et al., 1984). Ki67 was detected in the nucleus of 45% of cells at Day 7, however, the number of proliferative cells was substantially reduced at Day 14 (18%) and, by Day 21, only 10% of cells were positive for Ki67 (Fig. 3.7-C). The robust expression of S100b and increasing abundance of GFAP and Vimentin indicated the successful differentiation of iAstro over the 21-day period we analysed. Similarly, an increasing number of post-mitotic cells, suggested by the decrease of $Ki67^{+}$ cells over time, suggested progressive maturation of iAstro over the analysed timeframe.

iAstro were further characterised to assess the identity imposed by NF1B/SOX9-mediated differentiation. The gene expression profile of both WT and DS1 iAstro populations were investigated at Day 21 of differentiation (Fig.3.7-D). We found that pluripotency genes *NANOG* and *OCT3/4*, as well neuronal genes *NGN2* and *MYT1L* were not expressed. Similarly, oligodendrocyte markers *OLIG2* and *MBP* (Wegner, 2001), as well as microglia marker *CD11b* (Jurga et al., 2020) were not detected (Fig.3.7-D), suggesting the absence of other types of glial cells in the culture. Of all the investigated markers of mature astrocytic identity, the expression of some key genes was not detected. Astrocyte-specific glutamate transporter *GLT1*(Jia et al., 2020), water channel *AQP4* (Tang et al., 2013), gap-junction protein *CX30* (Liebmann et al., 2013), aldehyde dehydrogenase *ALDH1L1* (Cahoy et al., 2008), glycoprotein *CD44* (Akiyama et al., 1993) and astrogliosis gene *NDRG2* (X. L. Hu et al., 2006) were all found not to be expressed in iAstro. At the same time, other astrocyte-specific structural protein genes like gap-junction protein *GJA1* (Liebmann et al., 2013), vimentin (*VIM*), cytoskeleton protein *EZR* and extra-cellular matrix glycoprotein *TNC* (Wiese et al., 2012) were all abundantly expressed. Similarly, astrocytic functional proteins such as glutamine synthetase *GLUL* (Baek et al., 2019), glutamate transporter *GLAST* (Jia et al., 2020), cytokine receptor *LIFR* and aldolase-C enzyme *ALDOC* (Cahoy et al., 2008) were also highly expressed. Finally, transcription factors *NF1B* and *SOX9* were still detected after doxycycline had been interrupted (Fig.3.7-D). Though there was some degree of variability between differentiation batches, these results were found to be consistent across different samples derived from the same hiPSC line, as well across different lines (WT and DS1) (Fig.3.7-D).

Overall, our characterisation of forward programming differentiated astrocytes is consistent with the published literature (Canals et al., 2018; X. Li et al., 2018a) and seem to indicate rapid and homogenous development towards astrocytic identity. After one week of induction, iAstro cells started to display glia-like morphology and were found immunoreactive for S100B, VIM and GFAP, markers known to be robustly expressed by primary astrocytes (Brozzi et al., 2009; O'Leary et al., 2020). The absence of neuronal and non-astrocytic glial cell markers, together with the abundant expression of many astrocyte-specific genes suggests high specification efficiency towards astrocytic identity. However, at 3 weeks post-induction (Day 21) iAstro did not express some of the most common markers of astrocyte maturation, including *GLT1* and *ALDH1L1*, suggesting that further maturation might be needed in order to obtain functionally mature astrocytes. Nevertheless, forward programming differentiation allowed us to generate astrocyte-like cells in a third of the time (60-70 days) required by standard directed

differentiation protocols and therefore was considered a suitable strategy to quickly derive homogenous populations of mature astrocytes.

3.2.8 Neuronal co-culture with iAstro

To assemble our *in vitro* model of cortical circuits we combined the differentiation of iAstro, iGlut and iGABA. Briefly, iAstro hiPSCs were differentiated as previously described in *section 3.2.7.* At Day 14 of iAstro differentiation, when the cells have arranged in a flat and dense monolayer (Fig. 3.7-A), the desired number of pre-differentiated iGlut (Day 3) and/or iGABA (Day 4) were plated on the iAstro monolayer (Day 1 of co-culture). The culture was then treated with Ara-C for 3 days and maintained in growth factors supplemented co-culture medium for maturation (Fig. 3.8-A). Despite all 3 types of differentiation (iGlut, iGABA and iAstro) performing well individually, after only 2 weeks of co-culture with iAstro, both iGlut and iGABA neurons started to clump and assumed an unhealthy morphology (Fig. 3.8-B), while the underlying iAstro monolayer was clearly still present and appeared healthy. By comparison, when the neurons were matured on their own, without iAstro, they still appeared healthy after 3 weeks of culture (Fig. 3.8-C).

In recent publications, the transcription factor-mediated differentiation of multiple cell types was pooled, using a so called "cell-autonomous approach" to combine and promote their maturation and functionalisation (Ng et al., 2020; Skylar-Scott et al., 2022). Inspired by these publications, we tested an alternative approach for the co-differentiation of our neurons and astrocytes. Rather than pre-differentiate iAstro and iGlut individually before combining them into a co-culture system for maturation, we combined iAstro and iGlut hiPSCs in a 2:1 ratio and added Doxycycline directly to the pooled hiPSC culture. Interestingly, the two cell types differentiated and autonomously organised with a monolayer of iAstro underneath and iGlut on top (Fig. 3.8-D). However, after 2 weeks of pooled differentiation, the results were the same as with our original co-culture method, with the iGlut neurons clumping and looking unhealthy (Fig. 3.8-D). Alongside a pooled culture of iAstro:iGlut with a 2:1 ratio we also tested a 1:1 ratio, obtaining the same negative results (Supplementary Fig. 3.2-A).

Using mouse Embryonic Stem Cell (mESC)-derived astrocytes, the Lieberam lab has previously demonstrated that astrocytes engineered to express the growth factor GDNF performed much better than wildtype astrocytes in supporting the survival of spinal-like motor neurons derived from mESC and hiPSCs in co-culture. GDNF-expressing astrocytes supported

mESC-motor neuron survival better than wildtype astrocytes supplemented with recombinant GDNF (Machado et al., 2019). In an attempt to improve the performance of human iAstro, post-doc Lea R'Bibo (Lieberam Lab) used a PiggyBAC/transposase-mediated integration strategy (later described) to generate a sub-clonal iAstro line stably expressing GDNF (Fig. 3.8-E and F – ICC image generated by Lieberam Lab PhD student Peter Harley). In collaboration with Sofia Syntaka and Peter Harley, we assessed the ability of iAstro to support neuronal survival (in this case hiPSC-derived motor neurons) using a High Content Imaging (HCI)-based screen. Neuronal cell number was automatically quantified at defined time intervals using an operetta CLS HCI system and normalised to the original starting population. The percentage of surviving neurons after 1, 4 and 7 days of culture was assessed in 3 conditions: (i) Neurons only, (ii) Neurons + WT iAstro and (iii) Neurons + $GDNF^+$ iAstro (Fig. 3.8-G). After only 4 days of culture, neuronal survival was reduced to 31.0% (SEM ± 1.7) in the co-culture with WT iAstro and to 51.3% (SEM ± 3.4) in the co-culture with $GDNF^+$ iAstro, while the population of neurons in the neurons only condition actually increased to 111.4% (SEM ± 15.0) (Fig. 3.8-H and I – Table 3.1). After 7 days, the survival of neurons dropped dramatically to 2.0% (SEM ± 0.4) in the co-culture with WT iAstro and to 10.6% (SEM ± 2.6) in the co-culture with $GDNF^+$ iAstro, while 75.4% (SEM ± 5.2) of neurons survived in the neuronal monoculture (Fig. 3.8-H and J – Table 3.1). Overall, $GDNF^+$ iAstro performed slightly better than their WT counterpart however, their presence was still severely detrimental to the survival of neurons in co-culture.

An additional problem we encountered using iAstro was that, while they survived and appeared completely healthy when cultured on Matrigel-coated tissue culture plastic and imaging-grade plastic polymers, they died within a few days of being cultured on Matrigel-coated glass coverslips, the standard culture surface for patch-clamp recording (Supplementary Fig. 3.2-B). When cultured on other types of coating commonly used in astrocytic and neuronal cultures, such as Poly-L-Ornithine (PLO) or Poly-D-Lysine (PDL), iAstro detached and died within a few days, independently of the underlaying material they were plated on (TC plastic, glass-like plastic polymer or standard glass) (Supplementary Fig. 3.2-B). This unexpected phenotype didn't emerge during the initial characterisation of the iAstro line because the plates used in any of the assays, including imaging, were made of either polystyrene plastic or a imaging-grade plastic polymer. While we don't have a good explanation for why this happens, this phenotype would be extremely problematic for experiments requiring the use of glass coverslips (e.g., electrophysiology and calcium imaging) and, more in general, it raised and additional alarm bell on the functionality of these cells.

Taken together, this characterisation showed that this iAstro line is not suitable for neuronal co-culture. The presence of WT iAstro, as well as GDNF^{+} iAstro, appeared to have a toxic effect on the survival of iGlut, iGABA and motor neurons. In the original publication using the transcription factor combination NF1B-SOX9 to generate inducible astrocytes (Canals et al., 2018), the resulting cells are successfully used in co-culture with inducible neurons obtained through NGN2 overexpression (like our iGlut). More specifically, the co-culture was maintained for up to 5 weeks where the astrocytes were shown to support the survival and maturation of the neurons, promoting synapse formation and function. We were not able to replicate these results and a possible explanation for the discrepancies between our results and those within Canals et al. is their use of hESCs to derive inducible astrocytes and neurons, which are widely known to outperform hiPSCs in terms of differentiation potential (Narsinh et al., 2011; Puri & Nagy, 2012). Further characterisation will be necessary in order to understand why iAstro exert this negative effect on neuronal survival but, since the use of human astrocytes was not a fundamental requirement for the generation of our *in vitro* model, we decided to drop this approach and seek an alternative strategy to incorporate astrocytes in our culture system.

3.2.9 mouse Embryonic Stem Cell-derived astrocytes

Mouse Embryonic Stem Cell (mESC)-derived astrocytes have been routinely used in the Lieberam Lab to generate different mouse and human disease models, including ALS (Machado et al., 2019), Duchenne muscular dystrophy (Paredes-Redondo et al., 2021) and spinal cord injury (Berzanskyte et al., 2023). This being a well-established technology already in use in the Lieberam Lab, we chose it as the alternative strategy to produce the astrocytic component of our *in vitro* model. mESCs are differentiated and sorted into a pure population of functional astrocytes using a small molecule-based directed differentiation approach combined with magnetic-activated cell sorting (MACS). The cell line and differentiation protocol used for this study were originally developed by the Lieberam Lab postdoc Carolina Barcellos-Machado (Machado et al., 2019). To use a similar MACS approach to that described in *Section 3.2.3* of this chapter, a mESC line was genetically engineered to express the human cell surface antigen hCD14 under the transcriptional regulation of the astrocyte-specific GFAP minimal promoter (Fig. 3.9-A). As discussed in the section above, to improve the supportive performance of the astrocytes, this line was also modified to express GDNF under the control of the constitutive CAG promoter (Fig 3.8-E). For astrocyte differentiation, mESCs were plated in suspension dishes to form embryoid bodies (EBs) for 2 days, before adding Retinoic Acid

(RA) and Sonic Agonist (SAG) to induce neuroectoderm differentiation for 3 days (Fig. 3.9-B). Following a 7-day expansion phase on adherent plates to facilitate astrocyte differentiation, MACS was performed to enrich the final population of $GFAP^+$ astrocytes. Finally, sorted mouse astrocytes (mAstro) were matured in culture for a week before neurons were plated on top (Fig. 3.9-B). The inclusion of a MACS step in this differentiation protocol is fundamental to obtain a nearly pure population of astrocytes. As previously described, through the use of an anti-hCD14 primary antibody and a magnetic beads-conjugated secondary antibody, the $hCD14^+$ labelled cells can be sorted using Miltenyi Biotech magnetic separation columns (Fig.3.3-A). As a proof of concept, following MACS, pre-sort, flow through (FT) and eluate populations were fixed and stained for GFAP and neuronal marker TUBB3 (Fig. 3.9-C). GFAP and TUBB3 positive cells were quantified relatively to the total number of DAPI stained nuclei – data from PhD student Peter Harley. The $GFAP^+$ population was found to be enriched from 26.0% (SEM ± 4) in the pre-sort population to 91.6% (SEM ± 0.84) in the final eluted population. At the same time, the $TUBB3^+$ population was completely depleted from 12.4% (SEM ± 4) in the pre-sort to 0.2% (SEM ± 0.2) in the eluted population (Fig. 3.9-D – Table 3.2).

The ability of wildtype and $GDNF^+$ mAstro to support mouse neuronal survival had been previously documented (Machado et al., 2019). Similarly, their ability to support human neuronal survival had been previously tested in the lab (Berzanskyte et al., 2023; Harley et al., 2022) – data from PhD student Peter Harley. Using the same HCI-based screen mentioned in the section above, neuronal cell number was automatically quantified at defined time intervals and normalised to the original starting population. The percentage of surviving neurons after 1, 2 and 3 days was assessed in co-culture with WT mAstro and with $GDNF^+$ mAstro (Fig. 3.9-E). It was found that in as little as 3 days, GDNF expressing mAstro had a remarkable effect on preserving neuronal survival to 92.7% (SEM ± 5.1) compared to only 52.4% (SEM ± 2.7) of neurons surviving in culture with WT mAstro (Fig. 3.9-F – Table 3.3). At a comparable time-point, WT mAstro performed similarly to human $GDNF^+$ iAstro, which supported the survival of only 51.3% (SEM ± 3.4) of neurons after 4 days of culture (Fig. 3.9-F – Table 3.3).

Given the relative ease of production and excellent performance of $GDNF^+$ mAstro, this approach was considered the most suitable strategy to derive homogenous populations of astrocytes (from now on referred to simply as mAstro) that will support the survival and maturation of our neuronal model of cortical circuits.

3.2.10 Neuronal co-culture with mAstro

To establish our co-culture model, we derived mAstro as described above. On Day 19 of mAstro differentiation, when the cells have arranged in a flat and dense monolayer (Fig. 3.9-B), the desired number of pre-differentiated iGlut (Day 3) and/or iGABA (Day 4) were plated on the mAstro monolayer (Day 1 of co-culture). The culture was then maintained in growth factors supplemented co-culture medium for maturation. Contrarily to what was observed in cultures with iAstro, in long-term cultures with mAstro the neurons displayed a healthy morphology and did not form clumps (Fig. 3.10-A). When cultured with mAstro, neurons could be maintained in culture for up to 10 weeks.

It is widely known that culturing neurons with astrocytes promotes functional and synaptic maturation, both in primary cultures (Nakajima & Kunugi, 2020; Shan et al., 2021) as well as in hiPSC-derived cultures (Hedegaard et al., 2020; Sloan et al., 2017b). To evaluate the effect of mAstro on neuronal maturation, we compared the gene expression profile of iGlut and iGABA cultured on their own or in co-culture with mAstro. This comparison was made possible by the use of human specific primers that recognise the human transcripts (neuronal) but not mouse transcripts (astrocytic). For both neuronal types, we found that multiple genes typically expressed by mature neurons were expressed at higher levels in co-culture with mAstro. Specifically, when in culture with mAstro, iGlut neurons expressed statistically higher levels of glutamate receptors *GLUR2* and *NR1*, as well as vesicular glutamate transporters *VGLUT1* and *VGLUT2*, excitatory neuron specific kinase *CAMK2A* and pre-synaptic protein *SYN1* (Fig. 3.10-B – Table 3.4). Similarly, when cultured with mAstro, iGABA expressed statistically higher levels of interneuron-specific transcription factors *DLX2* and *DLX5*, and GABA transporters *GAT1* and *GAT2* (Fig. 3.10-C – Table 3.5). Interestingly, co-culture with mAstro also increased the expression levels of multiple interneuron subtype specific markers, specifically *CALB1*, *CALB2* and *STT* (Fig. 3.10-C – Table 3.5), suggesting that mAstro promote interneuron maturation and associated subtype specification. The same increase in specific interneuron subtypes was observed in DS1 iGABA when they are cultured with mAstro (Table 3.6).

Finally, we analysed the profile of *SCN1A* expression over time in iGlut and iGABA neurons cultured on mAstro. In both neuronal types we observed a progressive increase in *SCN1A* expression across the 50-day time period analysed (Fig. 3.10-D and E). The observed expression pattern is in line with the early stages of *SCN1A* expression observed in human and mouse, where the mRNA levels progressively increase throughout developmental age, from

embryonic stage to adulthood (Heighway et al., 2022; Helbig & Goldberg, 2021; Voskobiynyk et al., 2021). Based on the observed expression profile, we selected an early (3 weeks) and a late (6 weeks) timepoint to conduct our future experiments (dotted lines in Fig. 3.10-D and E). Although *SCN1A* expression was already abundantly detectable at 3 weeks, based on published literature the neuronal cultures have yet to reach maturity so they might not present a significant Dravet-related phenotype (Lam et al., 2017; C. Wang et al., 2017; Yang et al., 2017). As such, a later time point was also selected, at which point the neurons are more mature and more likely to exhibit disease phenotypes.

3.2.11 CRISPR/Cas9-mediated correction of the SCN1A$^{IVS14+3A>T}$ mutation in the DS1 Dravet patient-derived human iPSC line

Targeted gene editing of the DS1 line to correct the endogenous *SCN1A*$^{\text{IVS 14+3A>T}}$ mutation was achieved using CRISPR/Cas9-mediated Homology-Directed Repair (HDR). A single guide RNA (sgRNA) was designed using the online tool provided by the Wellcome Sanger Institute Genome Editing (WGE) and chosen based on its proximity to the mutation and its off-target score (Supplementary Fig. 3.3-A). The sgRNA was cloned into a Cas9 expressing vector and used in conjunction with a donor template. The donor template was designed based on the wildtype sequence and modified to contain two silent mutations in the sgRNA seed region exerting two functions: i) prevent the Cas9 enzyme from cleaving template DNA that had already been integrated into the genome; ii) introduce a MspI enzymatic cut site to facilitate clonal selection of CRISPR-edited cells (Fig. 3.11-A). Following transfection, we confirmed successful CRISPR-editing in the cell population by bulk DNA analysis (Fig. 3.11-B). The genomic sequence covering *SCN1A* intron 13, exon 14 and intron 14 (black arrows, Fig. 3.11-A) was PCR amplified from bulk DNA and digested with MspI restriction enzyme to confirm the integration of the MspI site in a sub-population of cells (Fig. 3.11-B). Following clonal selection, 8.6% of the screened clones were found positive for the integration of the MspI cut site (5/58 clones), all clones were homozygous. Positive clones were further investigated by Sanger sequencing to show that only 1 homozygous clone (Supplementary Fig. 3.3-B) had clean sequencing reads 1000bp upstream and downstream of the Cas9 cut site (Fig. 3.11-C) – an overall efficiency of 1.7%. Finally, the top 5 predicted off-target sites were sequenced to check for unintended off-target editing (Supplementary Fig. 3.3-A) and all sites were found unmodified. The successfully corrected clone was further characterised to assess its genomic integrity and stemness. G-banding analysis revealed a normal karyotype for the corrected line

(Fig. 3.11-D), while a normal karyotype for the DS1 line has previously been reported (Y. Liu, Lopez-Santiago, et al., 2013). Immunocytochemical analysis of common stemness markers confirmed the expression of OCT4, SOX2 and SSEA-4 in both the corrected line and the DS1 line (Fig. 3.11-E). Successful correction of the *SCN1A*$^{IVS\ 14+3A>T}$ mutation was further confirmed by *SCN1A* transcript analysis. As previously mentioned, this heterozygous mutation results in 50% abnormal transcripts that skip the *SCN1A* exon 14 (Y. Liu, Lopez-Santiago, et al., 2013). Electrophoresis analysis showed that when the region of transcript including *SCN1A* intron 13, exon 14 and intron 14 was PCR amplified from wildtype cDNA, a fragment of 340bp was obtained, while from DS1 cDNA two fragments were obtained, one of 340bp and one of 170bp, lacking exon 14 (Fig. 3.11-F). When the same region was amplified from the corrected cDNA, only the full-size fragment of 340bp was obtained (Fig. 3.11-F).

Following characterisation of the corrected DS1 line, we used this clone to generate sub-clonal lines suitable for forward programming into iGlut and iGABA using the methods previously discussed in this chapter *sections 3.2.4, 3.2.5 and 3.2.6* (Supplementary Fig. 3.3-C). After 3 weeks of differentiation, we did not observe any differences in the expression levels of *SCN1A* in iGlut and iGABA neurons derived from wildtype, DS1 and corrected lines (Fig 3.11-G – Table 3.7).

Together, our characterisation shows the successful generation of a DS1 corrected cell line. This line retained genomic integrity and stemness and, after forward programming, was capable of generating glutamatergic and GABAergic neurons that could be used as isogenic controls for our following experiments.

3.2.12 Neuronal functionalisation for two-colour calcium imaging

The final step in the generation of our *in vitro* model of cortical circuits for the study of Dravet syndrome was the introduction of functional probes to assess epileptic phenotypes. Calcium imaging has been classically used to study epileptiform activity *in vivo,* especially in mice and zebrafish (Khan et al., 2021; Rosch et al., 2018; Somarowthu et al., 2021; Wenzel et al., 2019; X. Zhang et al., 2019), and *in vitro,* mainly in primary neuronal cultures (Jablonski et al., 2021; Kiese et al., 2017; Pacico & Meur, 2014; D. A. Sun et al., 2001), and some hiPSC-derived neuronal models (Negraes et al., 2021). Typically, these studies were performed using membrane permeable calcium dyes, which are acutely applied to the culture and internalised by all the cells in culture (Paredes et al., 2008). Our *in vitro* system contains 3 distinct cell types

(excitatory neurons, inhibitory interneurons and astrocytes), all of which would be indiscriminately labelled by traditional calcium dyes, introducing a significant confounding factor in the signal read-out and interpretation of the data. With the advent of Genetically Encoded Calcium Indicators (GECIs) the targeted introduction of calcium sensors into specific cell populations was made possible (Oh et al., 2019). Using GECIs, we were able to individually target excitatory and inhibitory neurons with probes of different fluorescent wavelengths, allowing us to perform "two-colour" calcium imaging by conferring cell type specificity to the recorded calcium signal. Specifically, we selected a GFP-based probe (GCaMP6f) and a mApple-based probe (jrGECO1a) with comparable kinetics (Dana et al., 2016), to be introduced in excitatory neurons and inhibitory interneurons respectively.

To introduce the selected GECIs in our cell lines, we used a PiggyBAC/transposase-mediated integration strategy. PiggyBac (PB) transposon vectors are designed to contain the expression cassette surrounded by transposon-specific inverted terminal repeat sequences (ITRs). Stable integration of exogenous DNA is achieved via non-homologous recombination using a transposase, which recognises the ITRs and integrates the DNA enclosed in between them at TTAA genomic sites (Chen et al., 2020; Grabundzija et al., 2010). To use this strategy, we designed PiggyBac transposon vectors containing GCaMP6f or jrGECO1a downstream of a CAG promoter (Fig. 3.12-A). iGlut hiPSCs of all 3 genetic backgrounds (wildtype, DS1 and corrected) were transfected with PB-GCaMP6f while all iGABA hiPSC lines were transfected with PB-jrGECO1a. The transfected lines were then FACS sorted based on the GFP (Fig. 3.12-B) or mApple (Fig. 3.12-C) fluorescence to isolate a stably integrated polyclonal population expressing medium-high levels of probe.

The integration of two spectrally distinct probes in our co-culture system also allowed us to distinguish between excitatory and inhibitory neurons in fixed cultures stained for GFP and RFP (Fig. 3.12-D). Using GCaMP6f and jrGECO1a as identity signatures we were able to confirm that the desired cell-type ratio of 70:30 excitatory to inhibitory neurons could be consistently obtained in our co-culture system with mAstro (Fig. 3.12-E). This ratio was also reliably maintained in long-term cultures (Fig. 3.12-F).

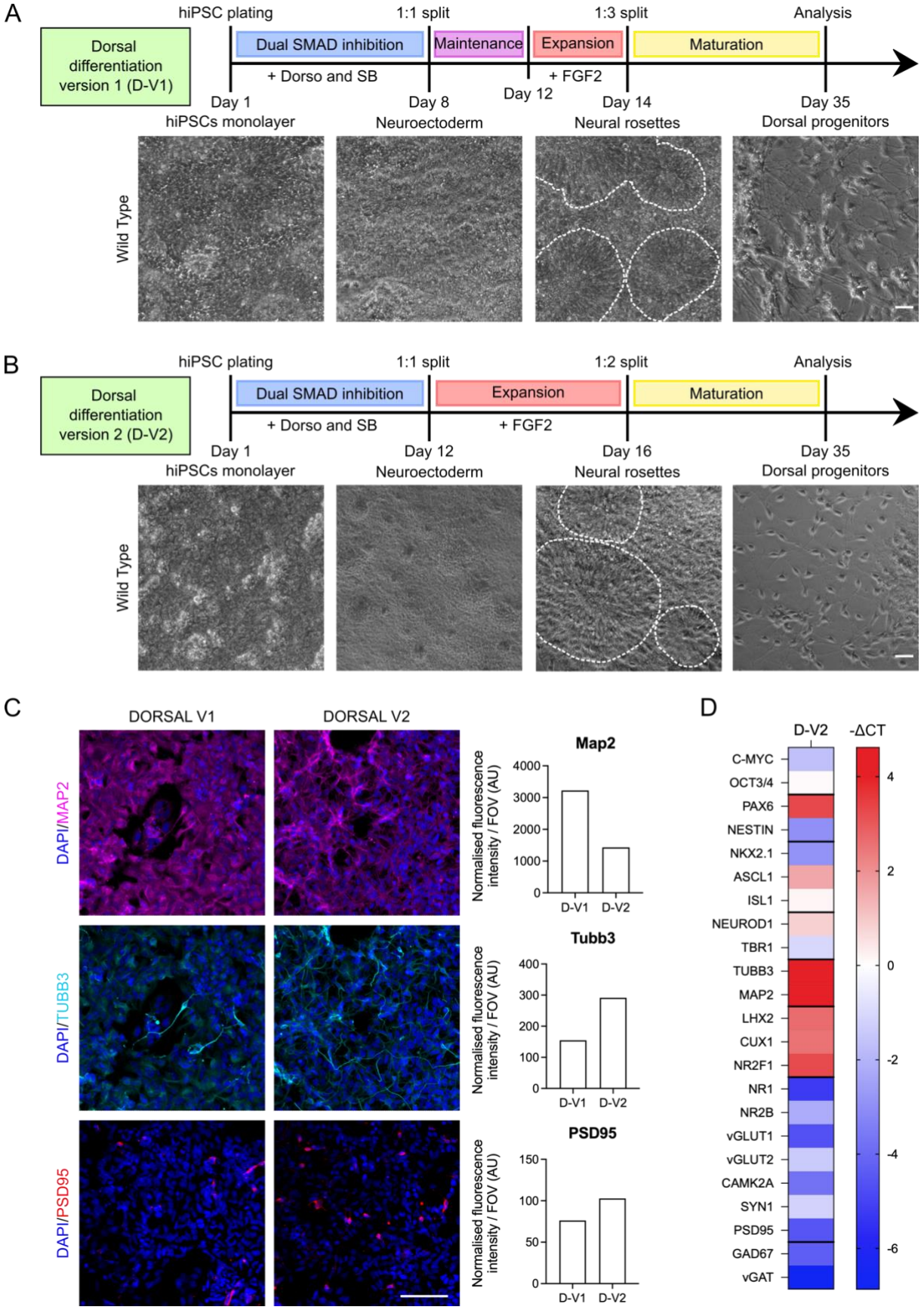
A
hiPSC plating
1:1 split
1:3 split
Analysis
Dorsal differentiation version 1 (D-V1)
Dual SMAD inhibition
Maintenance
Expansion
Maturation
+ Dorso and SB
+ FGF2
Day 1
Day 8
Day 12
Day 14
Day 35
hiPSCs monolayer
Neuroectoderm
Neural rosettes
Dorsal progenitors
Wild Type
B
hiPSC plating
1:1 split
1:2 split
Analysis
Dorsal differentiation version 2 (D-V2)
Dual SMAD inhibition
Expansion
Maturation
+ Dorso and SB
+ FGF2
Day 1
Day 12
Day 16
Day 35
hiPSCs monolayer
Neuroectoderm
Neural rosettes
Dorsal progenitors
Wild Type
C
DORSAL V1
DORSAL V2
DAPI/MAP2
DAPI/TUBB3
DAPI/PSD95
Map2
Tubb3
PSD95
Normalised fluorescence intensity / FOV (AU)
D-V1
D-V2
D
D-V2
-ΔCT
C-MYC
OCT3/4
PAX6
NESTIN
NKX2.1
ASCL1
ISL1
NEUROD1
TBR1
TUBB3
MAP2
LHX2
CUX1
NR2F1
NR1
NR2B
vGLUT1
vGLUT2
CAMK2A
SYN1
PSD95
GAD67
vGAT

Figure 3.1. *hiPSC directed dorsal differentiation.* **A –** Top, schematic of the dorsal differentiation protocol version 1 (D-V1). Starting from a hiPSC monolayer, Dorsomorphin and SB431542 are applied for 8 days to achieve dual SMAD inhibition and induce neuroectoderm formation. Following 4 days of maintenance, FGF2 is used to induce expansion of neural precursors and rosette formation (highlighted by a white dotted line) from day 12 to day 14. After, cells are maintained in small molecule-free medium for maturation. Cells reach the progenitor stage at around day 35 of differentiation. Protocol based on Shi et al (Y. Shi, Kirwan, & Livesey, 2012). Bottom, phase contrast images of the main differentiation stages for the wildtype hiPSC line. Scale bar = 100µm. **B –** Top, schematic of the dorsal differentiation protocol version 2 (D-V2). Dorsomorphin and SB431542 are applied for 12 days to induce dual SMAD inhibition and neuroectoderm formation. Following 4 days of expansion with FGF2 to induce rosette formation (highlighted by a white dotted line), from day 16 cells are maintained in small molecule-free medium for maturation. Cells reach the progenitor stage around day 35 of differentiation. Protocol based on Shi et al (Y. Shi, Kirwan, & Livesey, 2012). Bottom, phase contrast images of the main differentiation stages for the wildtype hiPSC line. Scale bar = 100µm. **C** – Left, Immunofluorescence images of Day 35 D-V1 and D-V2 progenitor populations stained for Map2 (magenta), Tubb3 (cyan), PSD95 (red) and DAPI (blue). Scale bar = 100µm. Right, quantification of the mean fluorescence intensity per FOV (field of view) normalised to the number of nuclei. AU = arbitrary unit. N=1 biological replicate with n=5 FOV per condition. **D** – Heatmap representation of RT-qPCR analysis of D-V2 progenitors at Day 35. Gene expression levels are normalised to the housekeeping gene TBP and expressed as -ΔCT. N=1 biological replicate with n=3 technical replicates per condition.

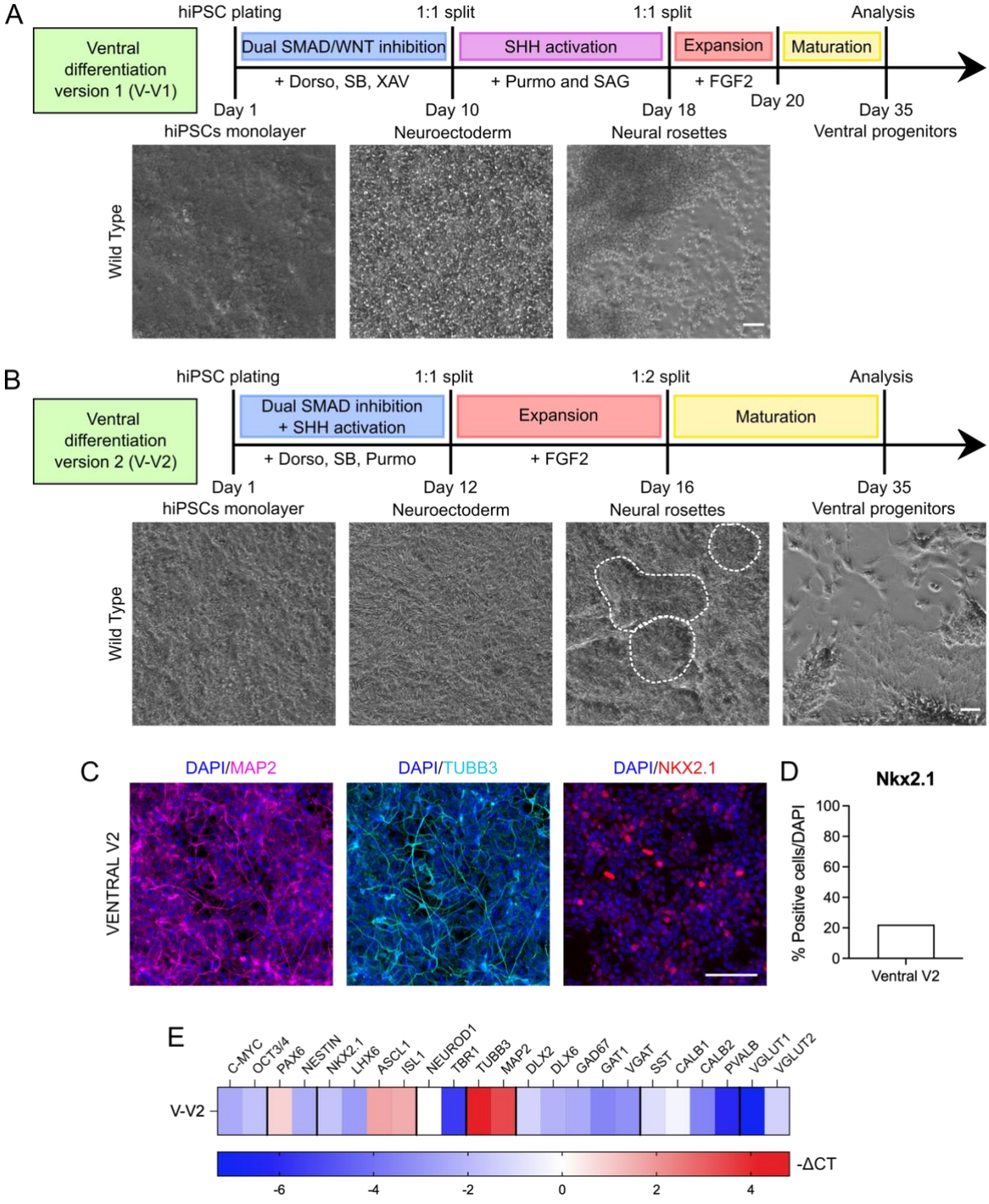

Figure 3.2. *hiPSC directed ventral differentiation.* **A** – Top, schematic of the ventral differentiation protocol version 1 (V-V1). Starting from a hiPSC monolayer, Dorsomorphin and SB431542 are applied, together with XAV939, for 10 days to combine dual SMAD and Wnt inhibition to induce neuroectoderm formation with enhanced forebrain specification. Subsequently, Purmorphamine and SAG are applied for 8 days to activate SHH signalling, inducing ventralisation of neural precursors. Next, FGF2 is used from day 18 to day 20 to induce precursors expansion and rosette formation. Finally, cells are maintained in small molecule-free medium for maturation, reaching the progenitor stage around day 35 of differentiation. Protocol based on Maroof et al. (Maroof et al., 2013). Bottom, phase contrast images of the main

differentiation stages for the wildtype hiPSC line. Scale bar = 100µm. **B –** Top, schematic of the ventral differentiation protocol version 2 (V-V2). Dorsomorphin, SB431542 and Purmorphamine are applied for 12 days to induce simultaneous dual SMAD inhibition and SHH signalling activation to achieve neuroectoderm formation. Following 4 days of expansion with FGF2 to induce rosette formation (highlighted by a white dotted line), cells are maintained from day 16 in small molecule-free medium for maturation. Cells reach the progenitor stage around day 35 of differentiation. Protocol based on Shi et al. (Y. Shi, Kirwan, & Livesey, 2012). Bottom, phase contrast images of the main differentiation stages for the wildtype hiPSC line. Scale bar = 100µm. **C** –Immunofluorescence images of Day 35 V-V2 progenitors stained for Map2 (magenta), Tubb3 (cyan), Nkx2.1 (red) and DAPI (blue). Scale bar = 100µm. **D** – Quantification of $Nkx2.1^{+}$ cells (%) relative to the total nuclear count (DAPI). N=1 biological replicate with n=5 FOV per condition. **E** – Heatmap representation of RT-qPCR analysis of V-V2 progenitors at Day 35. Gene expression levels are normalised to the housekeeping gene TBP and expressed as -ΔCT. N=1 biological replicate with n=3 technical replicates per condition.

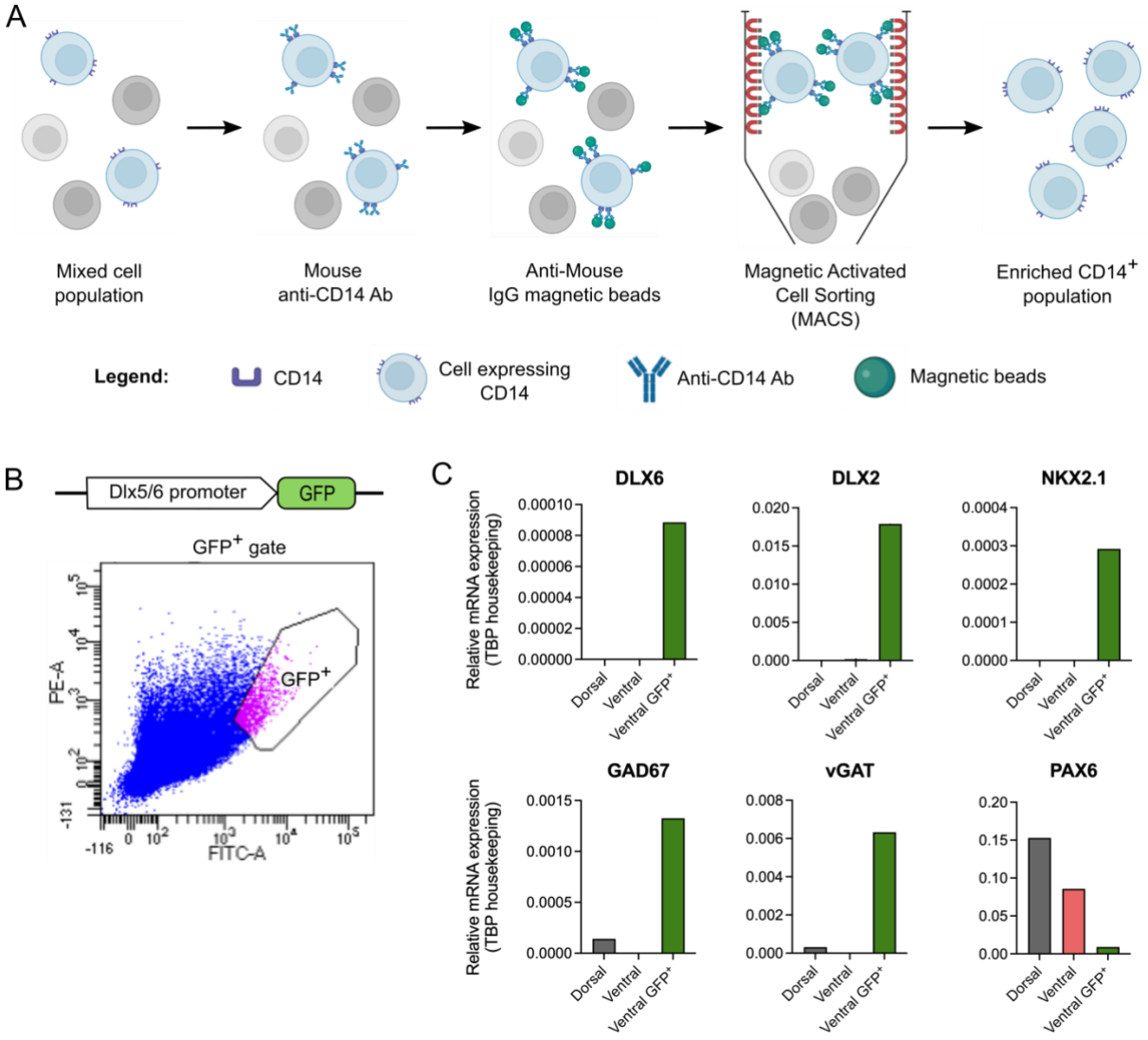

Figure 3.3. *Neuronal type-specific Magnetic-Activated Cell Sorting (MACS).* **A –** MACS sorting process illustrative scheme. A mixed cell population, containing CD14-expressing cells, is labelled with a mouse anti-CD14 primary antibody, followed by an anti-mouse IgG magnetic beads-conjugated secondary antibody. Labelled cells are then passed through a magnetic separation column that retains the beads-labelled cells which are subsequently eluted to obtain an enriched $CD14^+$ population. **B –** Top, schematic representation of the DLX5/6-GFP expression vector. Bottom, FACS sorting GFP gate set to isolate GFP^+ ventral progenitors. **C –** Gene expression analysis of unsorted dorsal and ventral progenitors and Dlx5/6-GFP^+ ventral progenitors. mRNA expression relative to TBP housekeeping gene was measured for ventral interneuron markers DLX6, DLX2, NKX2.1, GAD67 and vGAT and for dorsal progenitor marker PAX6. N=1 biological replicate with n=3 technical replicates per condition.

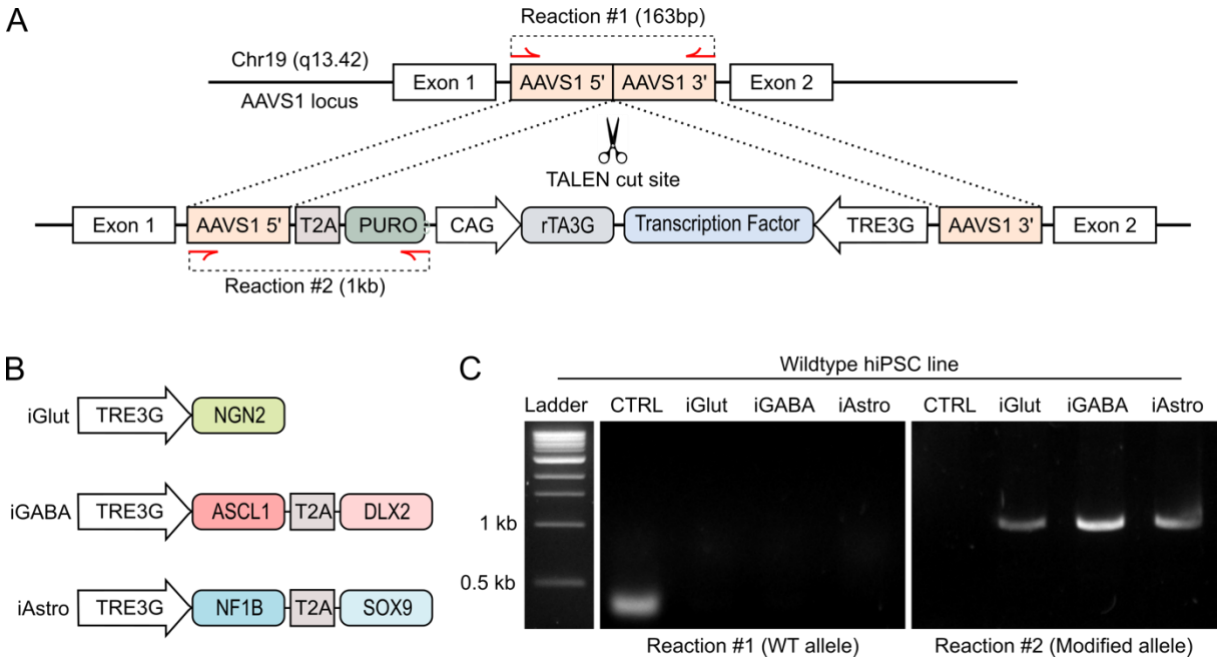

Figure 3.4. *Generation of hiPSC lines suitable for forward programming differentiation.* **A** – Schematic representation of the TALEN-mediated integration of the coding region of interest at the AAVS1 safe harbor locus, located on chromosome 19 (q13.42). The AAVS1 vector contains, in between the 5' and 3' homology sequences, the puromycin resistance gene downstream of a T2A sequence, followed by a CAG promoter upstream of the rtTA3G. From the 3' end, the TRE3G promoter regulates the expression of the desired transcription factors. Site-specific TALENs recognise the AAVS1 5' and 3' sequences and allow for homologous recombination between the genome and the vector plasmid. Successful integrations are identified using two PCR reactions. Reaction #1 is designed to test for the presence of a WT allele, while reaction #2 tests for the presence of a modified allele. Clones that are positive for reaction #1 and negative for #2 are homozygous WT, clones that are positive for reaction #1 and #2 are heterozygous and finally, clones that are negative for reaction #1 and positive for #2 are homozygous modified. **B** – Schematic representation of the iGlut vector, encoding for NGN2, the iGABA vector, encoding for ASCL1 and DLX2 and iAstro vector, encoding for NF1B and SOX9. **C** – Gel electrophoresis of PCR reactions #1 and #2 performed on the iGlut, iGABA and iAstro monoclonal lines derived from wildtype hiPSCs. Non-transfected wildtype hiPSCs are used as a control.

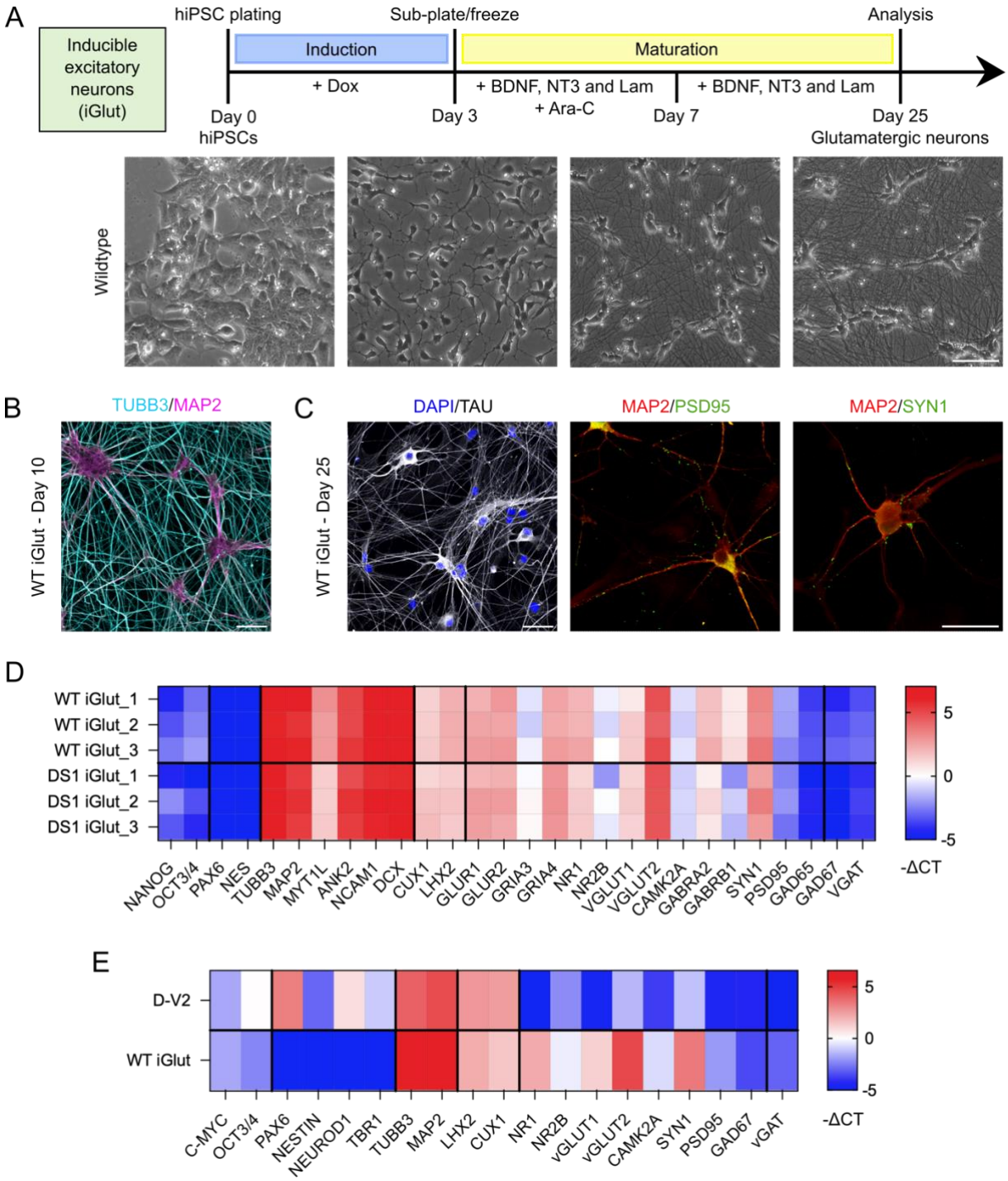

Figure 3.5. *Forward programming differentiation into excitatory cortical neurons.* **A –** Top, schematic of the iGlut differentiation protocol. Starting from hiPSCs, Doxycycline is applied for 3 days before the cells are sub-plated or frozen. Differentiating cells are then maintained in BDNF, NT3 and Laminin supplemented medium for maturation, with Ara-C applied for 3 days after Dox-induction to eliminate proliferating cells. Protocol based on Fernandopulle et al. (Fernandopulle et al., 2018). Bottom, phase contrast images of the main differentiation stages for the wildtype hiPSC line. Scale bar = 100µm. **B –** Immunofluorescence image of Day 10 WT iGlut stained for Map2 (magenta) and Tubb3 (cyan). Scale bar = 100µm. **C** – Immunofluorescence images of Day 25 WT iGlut neurons stained for Tau (grey) and DAPI (blue) with a scale bar = 100µm, and Map2 (red), PDS95 and Syn1 (green) with a scale bar =

50µm. **D** – Heatmap representation of RT-qPCR analysis of WT and DS1 iGlut neurons at Day 30. Gene expression levels are normalised to the housekeeping gene TBP and expressed as -ΔCT. N=3 biological replicates with n=3 technical replicates per sample. **E** – Heatmap representation of RT-qPCR analysis of D-V2 progenitors at Day 35 and WT iGlut neurons at Day 30. Gene expression levels are normalised to the housekeeping gene TBP and expressed as -ΔCT. N=1 biological replicate with n=3 technical replicates for D-V2; N=3 biological replicates with n=3 technical replicates per for WT-iGlut.

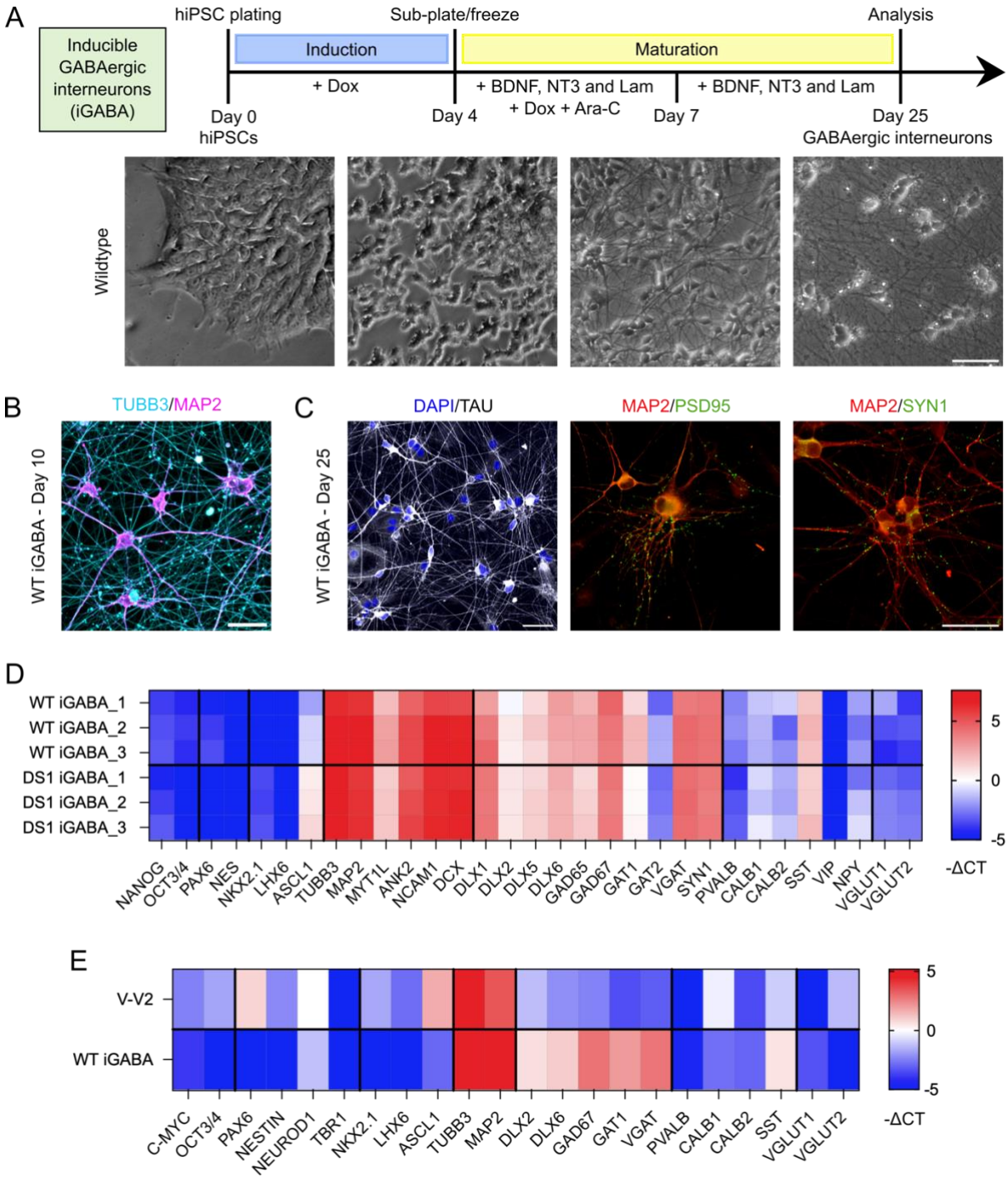

Figure 3.6. *Forward programming differentiation into GABAergic inhibitory interneurons.* **A –** Top, schematic of the iGABA differentiation protocol. Starting from hiPSCs, Doxycycline is applied for 4 days before the cells are sub-plated or frozen. Differentiating cells are then maintained in BDNF, NT3 and Laminin supplemented medium for maturation, with Ara-C applied for 3 days after Dox-induction to eliminate proliferating cells. Protocol based on Yang et al. (Yang et al., 2017). Bottom, phase contrast images of the main differentiation stages for the wildtype hiPSC line. Scale bar = 100µm. **B –** Immunofluorescence image of Day 10 WT iGABA stained for Map2 (magenta) and Tubb3 (cyan). Scale bar = 100µm. **C** – Immunofluorescence images of Day 25 WT iGABA neurons stained for Tau (grey) and DAPI

(blue) with a scale bar = 100μm, and Map2 (red), PDS95 and Syn1 (green) with a scale bar = 50μm. **D** – Heatmap representation of RT-qPCR analysis of WT and DS1 iGABA neurons at Day 30. Gene expression levels are normalised to the housekeeping gene TBP and expressed as -ΔCT. N=3 biological replicates with n=3 technical replicates per sample. **E** – Heatmap representation of RT-qPCR analysis of V-V2 progenitors at Day 35 and WT iGABA neurons at Day 30. Gene expression levels are normalised to the housekeeping gene TBP and expressed as -ΔCT. N=1 biological replicate with n=3 technical replicates for V-V2; N=3 biological replicates with n=3 technical replicates for WT-iGABA.

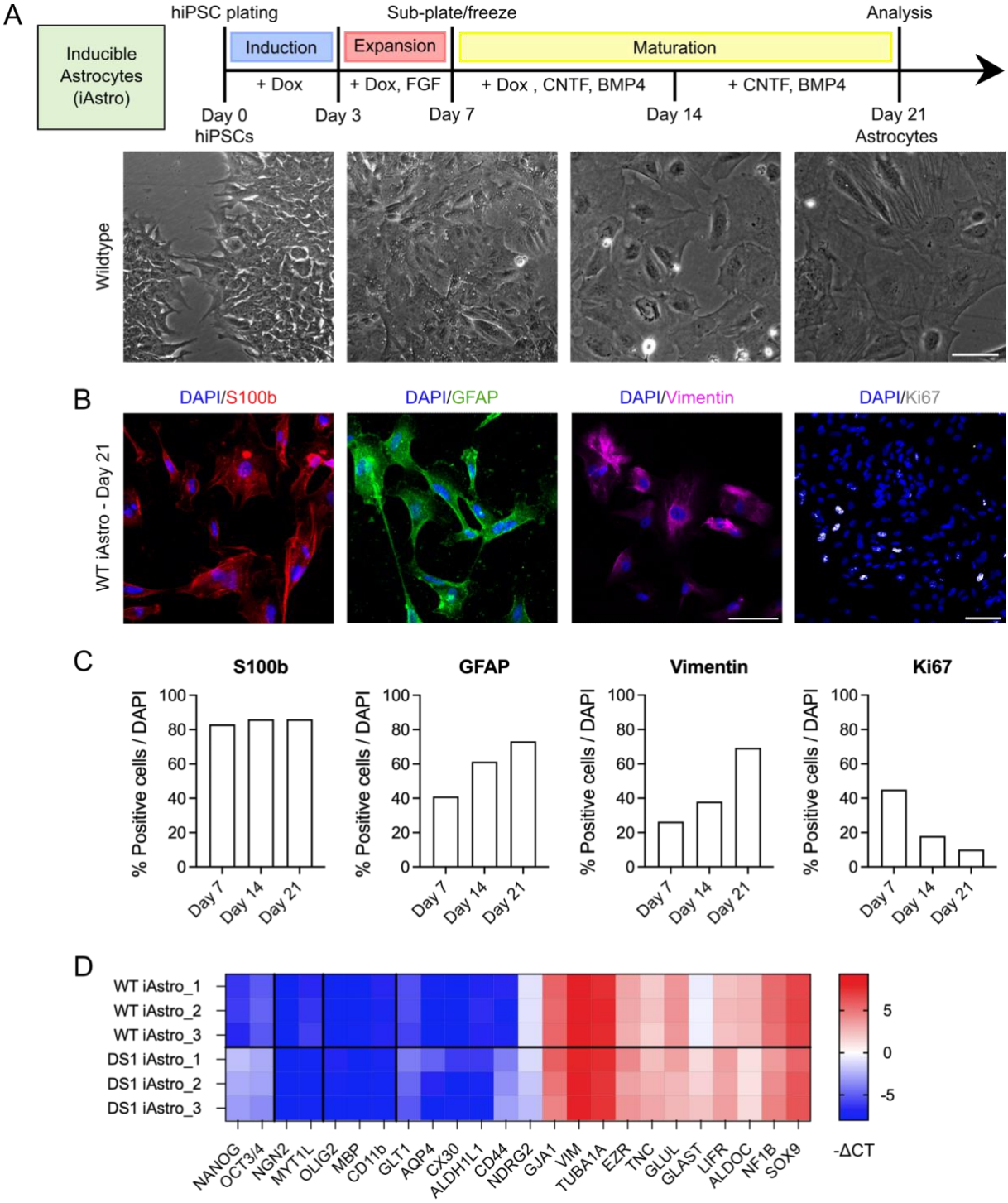

Figure 3.7. *Forward programming differentiation into astrocytes.* **A –** Top, schematic of the iAstro differentiation protocol. hiPSC colonies undergo 3 days of doxycycline induction followed by 4 days of FGF-mediated expansion. At Day 7, astrocytes are frozen down or sub-plated then maintained in CNTF and BMP4 supplemented medium for maturation. Doxycycline is withdrawn after 14 days. Protocol based on Canals et al. (Canals et al., 2018). Bottom, phase contrast images of the main differentiation stages for the wildtype hiPSC line. Scale bar = 100µm. **B –** Representative immunofluorescence images of Day 21 WT iAstro stained for S100b (red), GFAP (green), Vimentin (magenta), Ki67 (grey) and DAPI (blue). Scale bar = 100µm. **C** – Quantification of cells positive for the investigated markers (%) relative to the total

nuclear count (DAPI). N=1 biological replicate with n=3 technical replicates per condition. **D** – Heatmap representation of RT-qPCR analysis of WT and DS1 iAstro at Day 21. Gene expression levels are normalised to the housekeeping gene TBP and expressed as -ΔCT. N=3 biological replicates with n=3 technical replicates per sample.

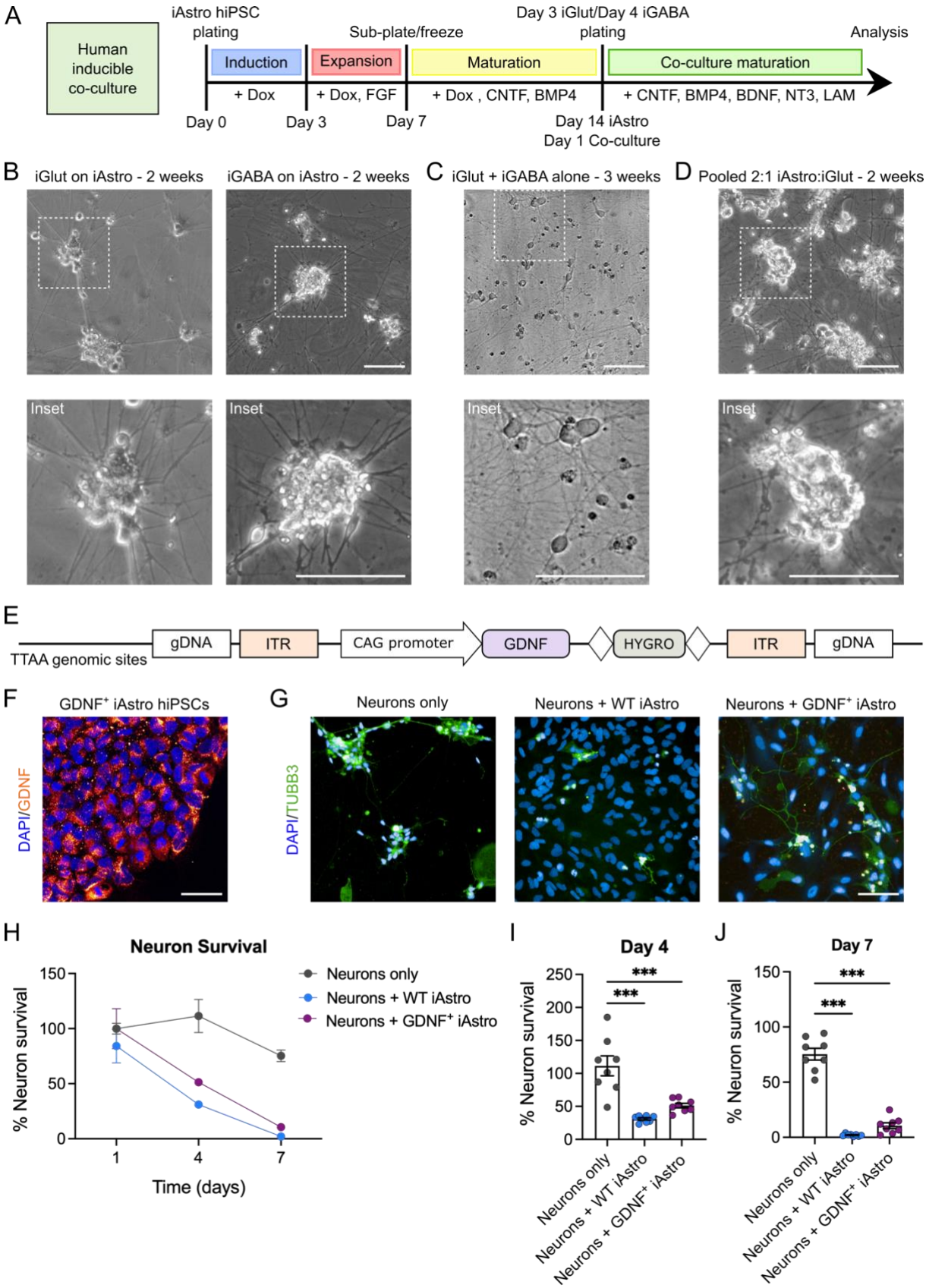
A
Human inducible co-culture
iAstro hiPSC plating
Induction
+ Dox
Day 0
Expansion
+ Dox, FGF
Day 3
Sub-plate/freeze
Maturation
+ Dox , CNTF, BMP4
Day 7
Day 3 iGlut/Day 4 iGABA plating
Co-culture maturation
+ CNTF, BMP4, BDNF, NT3, LAM
Day 14 iAstro
Day 1 Co-culture
Analysis
B iGlut on iAstro - 2 weeks
iGABA on iAstro - 2 weeks
C iGlut + iGABA alone - 3 weeks
D Pooled 2:1 iAstro:iGlut - 2 weeks
Inset
E
TTAA genomic sites
gDNA
ITR
CAG promoter
GDNF
HYGRO
ITR
gDNA
F GDNF+ iAstro hiPSCs
DAPI/GDNF
G
Neurons only
Neurons + WT iAstro
Neurons + GDNF+ iAstro
DAPI/TUBB3
H
Neuron Survival
% Neuron survival
Time (days)
Neurons only
Neurons + WT iAstro
Neurons + GDNF+ iAstro
I
Day 4
% Neuron survival
***
J
Day 7
% Neuron survival
***

Figure 3.8. *Neuronal co-culture with iAstro.* **A –** Schematic of the human inducible co-culture protocol. iAstro are differentiated as previously described until Day 14, when Day 3 iGlut and/or Day 4 iGABA are plated on the astrocytic monolayer. The co-culture is maintained in growth factor-supplemented maturation medium until analysis. **B –** Phase contrast images of iGlut and iGABA in co-culture with iAstro after 2 weeks. Scale bar = 100µm. **C –** Phase contrast images of iGlut and iGABA in co-culture without iAstro after 3 weeks. Scale bar = 100µm. **D –** Phase contrast images of a pooled culture of iAstro and iGlut (2:1 ratio) after 2 weeks of differentiation. Scale bar = 100µm. **E –** Schematic representation of the PiggyBac vector containing GDNF downstream of a CAG promoter, followed by a hygromycin resistance cassette. The open reading frame is flanked by transposon-specific inverted terminal repeat sequences (ITRs). Transposase-mediated integration is targeted at TTAA genomic sites. **F –** Immunofluorescence image of the $GDNF^+$ iAstro hiPSC line stained for GDNF (orange) and DAPI (blue). Scale bar = 20 µm. **G –** Representative immunofluorescence images of Day 7 of the survival assay for neurons only, neurons + WT iAstro and neurons + $GDNF^+$ iAstro stained for Tubb3 (green) and DAPI (blue). Scale bar = 100 µm. **H –** The percentage of neuron survival over 7 days is plotted for neurons only, neurons + WT iAstro and neurons + $GDNF^+$ iAstro. **I-J –** The percentage of neuron survival at Day 4 or Day 7 is plotted for neurons only, neurons + WT iAstro and neurons + $GDNF^+$ iAstro. N=3 biological replicates with n=8 wells per condition. Error bars represent the SEM, Ordinary One-way ANOVA + Tukey's multiple comparison, *** = $p<0.001$.

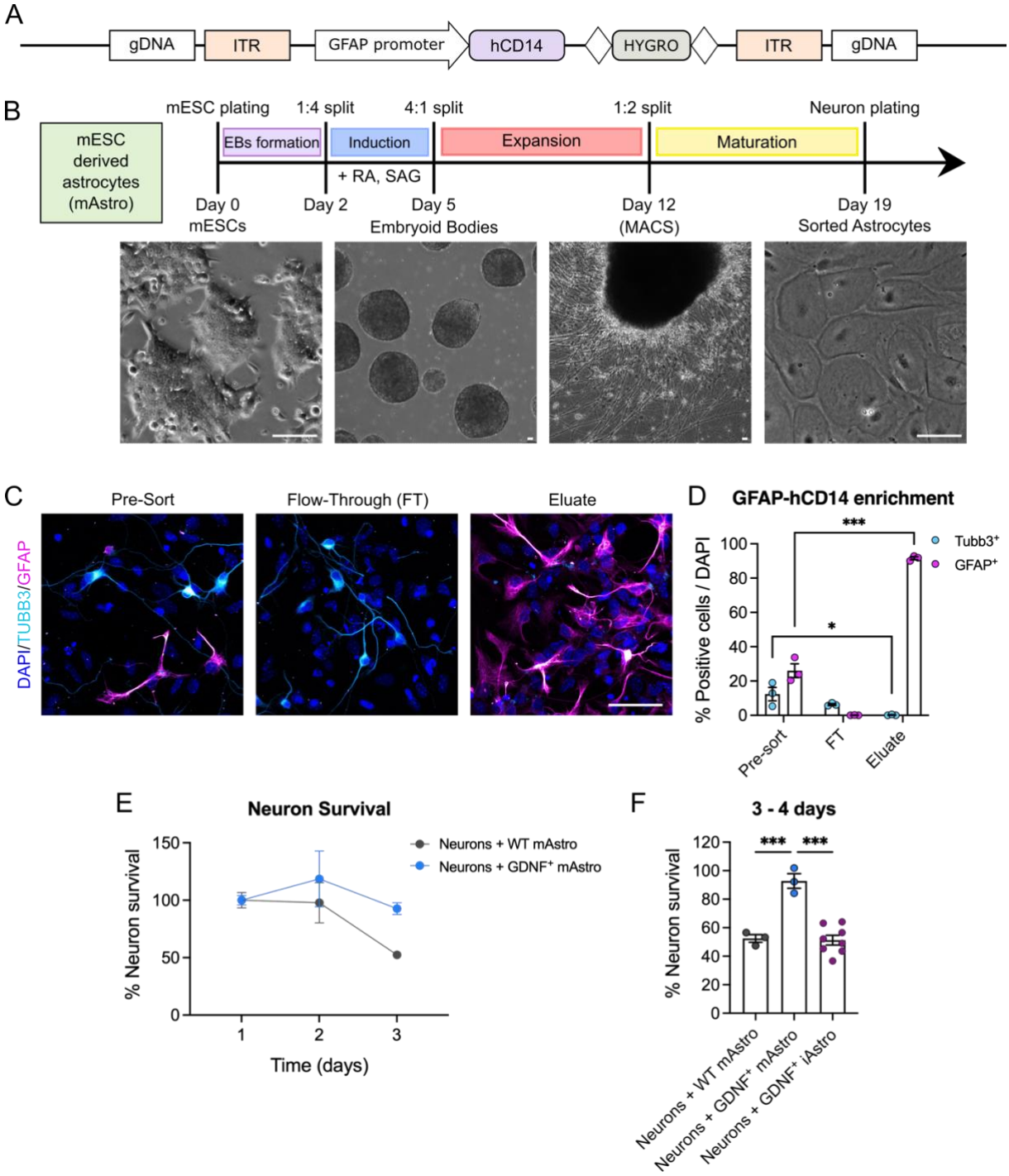

Figure 3.9. *Mouse ESC-derived astrocytes differentiation and sorting.* **A** – Schematic representation of the Tol2 vector containing hCD14 downstream of the GFAP minimal promoter, followed by a hygromycin resistance cassette. The open reading frame is flanked by transposon-specific inverted terminal repeat sequences (ITRs) for transposase-mediated genomic integration. **B** – Top, schematic of the mouse astrocytes differentiation protocol. mESCs are plated in suspension plates to form embryoid bodies (EBs) for 2 days before RA and SAG are applied for 3 days to achieve neuroectoderm induction. EBs are then expanded on MG-coated plates for 7 days until they are MACS sorted. Finally, sorted astrocytes are matured for a week before neurons are plated on top. Bottom, phase contrast images of the main differentiation stages. Scale bar = 100µm. **C** – Representative immunofluorescence images of

pre-sort, flow-through and eluate populations from a GFAP-CD14 MACS stained for Tubb3 (cyan), GFAP (magenta) and DAPI (blue). Scale bar = 50 μm. **D –** The percentage of $Tubb3^+$ and $GFAP^+$ cells is plotted for pre-sort, flow-through and eluate populations. N=3 biological replicates with n=3 wells per sample. Error bars represent the SEM, unpaired t test, * = $p<0.05$, *** = $p<0.001$. **E –** The percentage of neuron survival over 3 days is plotted for neurons + WT mAstro and neurons + $GDNF^+$ mAstro. **F –** The percentage of neuron survival at Day 3 – 4 days is plotted for neurons + WT mAstro, neurons + $GDNF^+$ mAstro and neurons + $GDNF^+$ iAstro. N=3 biological replicates with n=3-8 wells per condition. Error bars represent the SEM, Ordinary One-way ANOVA + Tukey's multiple comparison, *** = $p<0.001$.

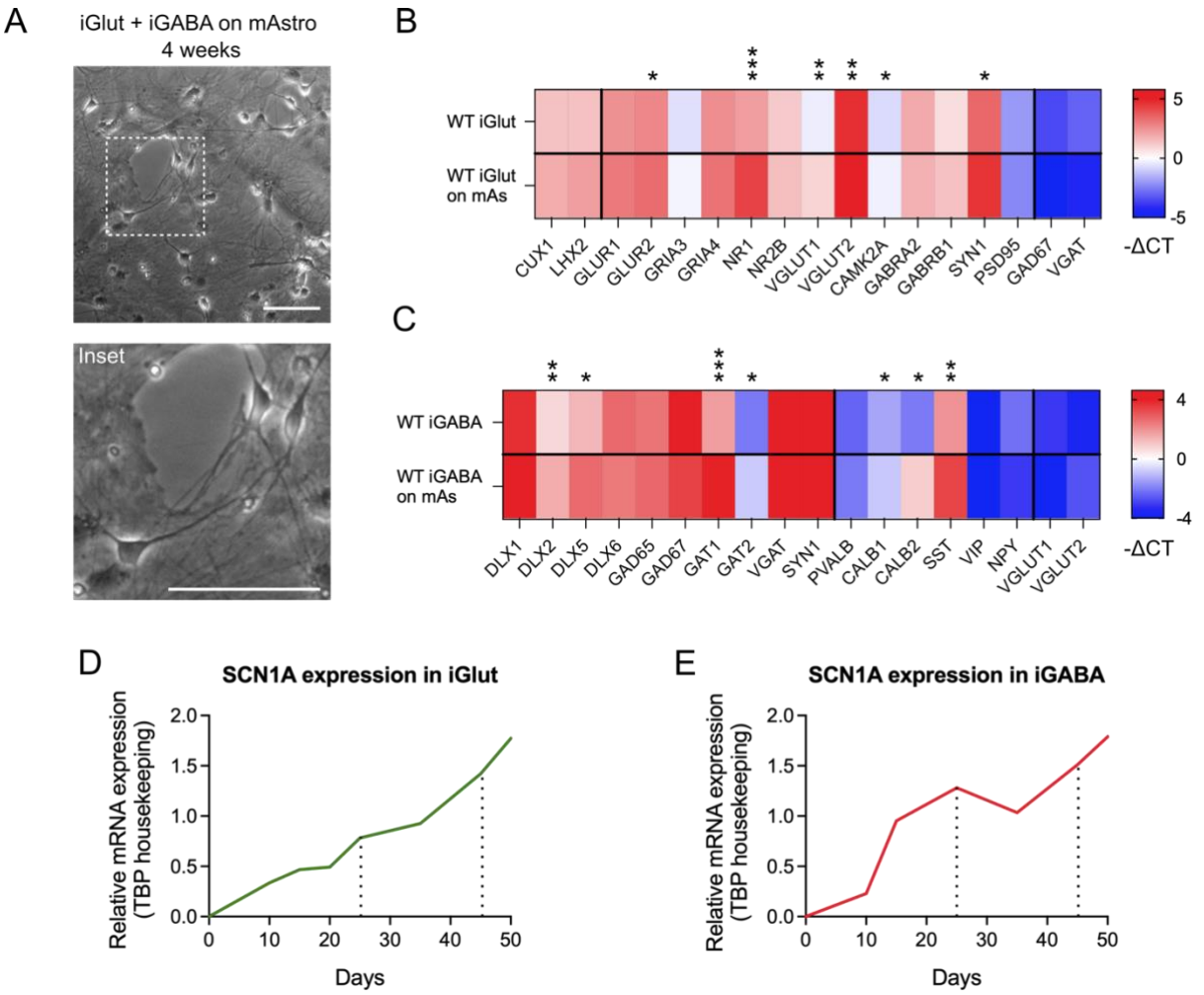

Figure 3.10. *Neuronal co-culture with mAstro.* **A –** Phase contrast images of a 4-week-old co-culture of iGlut and iGABA on mAstro. Scale bar = 100µm. **B-C** – Heatmap representation of RT-qPCR analysis of WT iGlut and WT iGlut on mAstro at Day 30 or WT iGABA and WT iGABA on mAstro at Day 30. Gene expression levels are normalised to the housekeeping gene TBP and expressed as -ΔCT. N=3 biological replicates with n=3 technical replicates per sample. Unpaired t test with Welch's correction, * = $p<0.05$, ** = $p<0.01$, *** = $p<0.001$. **D-E –** mRNA expression, relative to the housekeeping gene TBP, of *SCN1A* over the course of 50 days in iGlut or iGABA neurons cultured on mAstro. Dotted lines indicate the 3 and 6 weeks experimental timepoints.

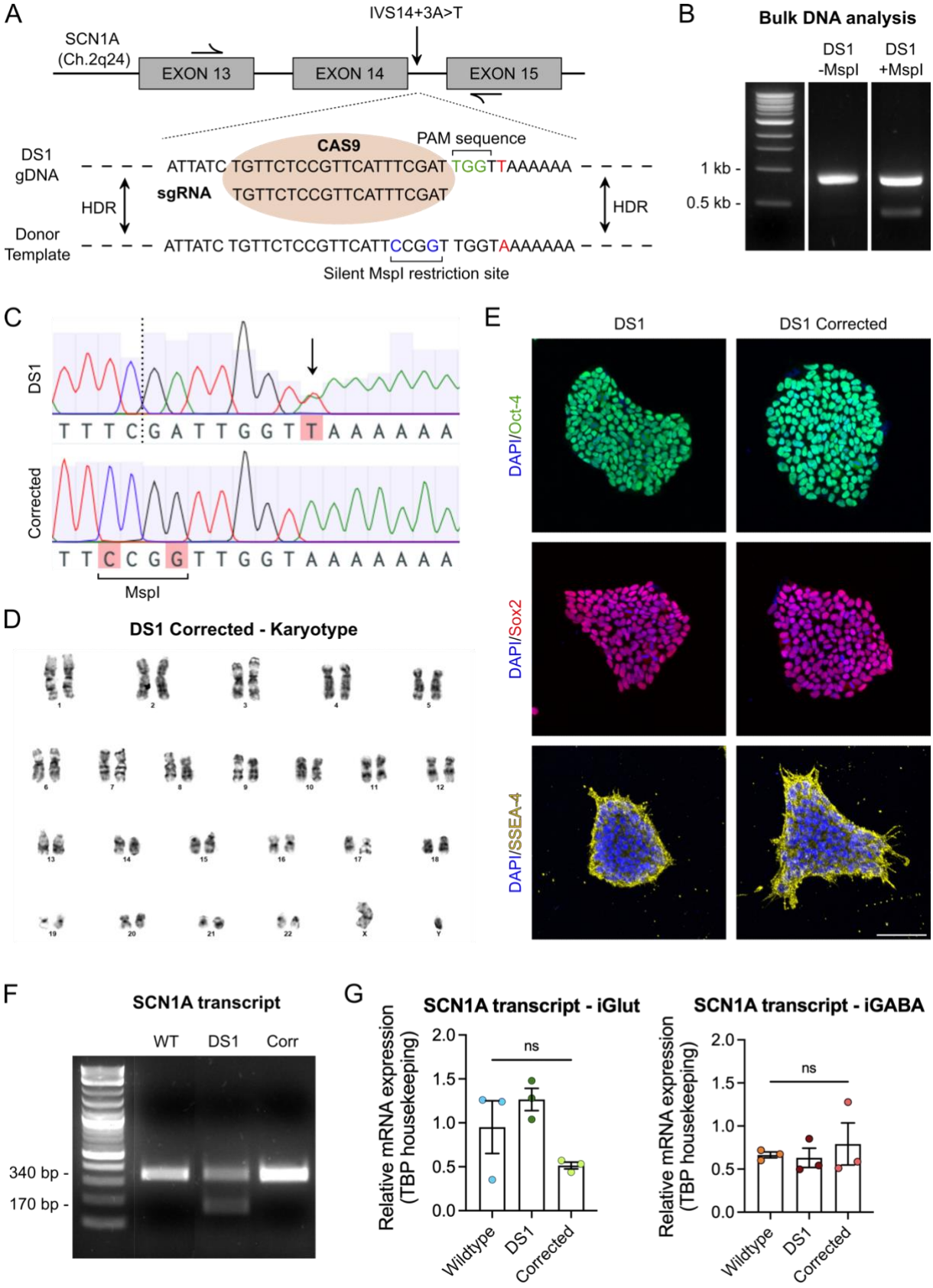
A
IVS14+3A>T
SCN1A
(Ch.2q24)
EXON 13
EXON 14
EXON 15
CAS9
PAM sequence
DS1
gDNA
ATTATC TGTTCTCCGTTCATTTCGAT TGGTTAAAAAA
sgRNA
TGTTCTCCGTTCATTTCGAT
HDR
HDR
Donor
Template
ATTATC TGTTCTCCGTTCATTCCGGT TGGTAAAAAAA
Silent MspI restriction site
B
Bulk DNA analysis
DS1
-MspI
DS1
+MspI
1 kb -
0.5 kb -
C
DS1
T T T C G A T T G G T T A A A A A A A
Corrected
T T C C G G T T G G T A A A A A A A A
MspI
D
DS1 Corrected - Karyotype
E
DS1
DS1 Corrected
DAPI/Oct-4
DAPI/Sox2
DAPI/SSEA-4
F
SCN1A transcript
WT
DS1
Corr
340 bp -
170 bp -
G
SCN1A transcript - iGlut
Relative mRNA expression
(TBP housekeeping)
2.0
1.5
1.0
0.5
0.0
ns
Wildtype
DS1
Corrected
SCN1A transcript - iGABA
Relative mRNA expression
(TBP housekeeping)
2.0
1.5
1.0
0.5
0.0
ns
Wildtype
DS1
Corrected

Figure 3.11. *CRISPR/Cas9-mediated correction of Dravet SCN1A$^{IVS14+3A>T}$ mutation in the DS1 patient derived hiPSC line.* **A –** Schematic showing the CRISPR/Cas9 mediated genome editing strategy to correct the endogenous *SCN1A*$^{IVS14+3A>T}$ mutation in the DS1 line. Black arrows on exon 13 and 15 indicate the primers used for PCR amplification of the genomic region for sequencing purposes. Highlighted in red is the mutated nucleotide, in green the PAM sequence and in blue the silent mutations inserted in the donor template to introduce a MspI restriction site. **B –** MspI restriction digestion confirming successful CRISPR editing within the targeted hiPSC population. **C –** Sanger sequencing of the genomic region of interest showing correction of the *SCN1A*$^{IVS14+3A>T}$ mutation (black arrow) and homozygous integration of the donor template harbouring the silent MspI restriction site. The dotted line indicates the Cas9 cut site. **D –** G-banding analysis showing normal karyotype for the DS1 corrected hiPSC line. **E –** Immunofluorescence images of DS1 and DS1 corrected hiPSCs stained for the pluripotency markers Oct-4 (green), Sox2 (red) and SSEA-4 (yellow) and DAPI (blue). Scale bar = 100 μm. **F –** Electrophoresis analysis of *SCN1A* transcript showing the full-size amplification of intron 13, exon 14 and intron 14 from WT cDNA (340 bp), the presence of 50% aberrant transcript missing exon 14 amplified from DS1 cDNA (170 bp) and the full-size amplification of the transcript fragment from corrected cDNA (340 bp). **G –** RT-qPCR analysis of *SCN1A* mRNA expression, relative to the housekeeping gene TBP, performed in iGlut and iGABA derived from wildtype, DS1 and corrected lines. N=3 biological replicates with n=3 technical replicates per sample. Error bars represent the SEM, One-way ANOVA Kruskal-Wallis test + Dunn's multiple comparison, ns = $p>0.05$.

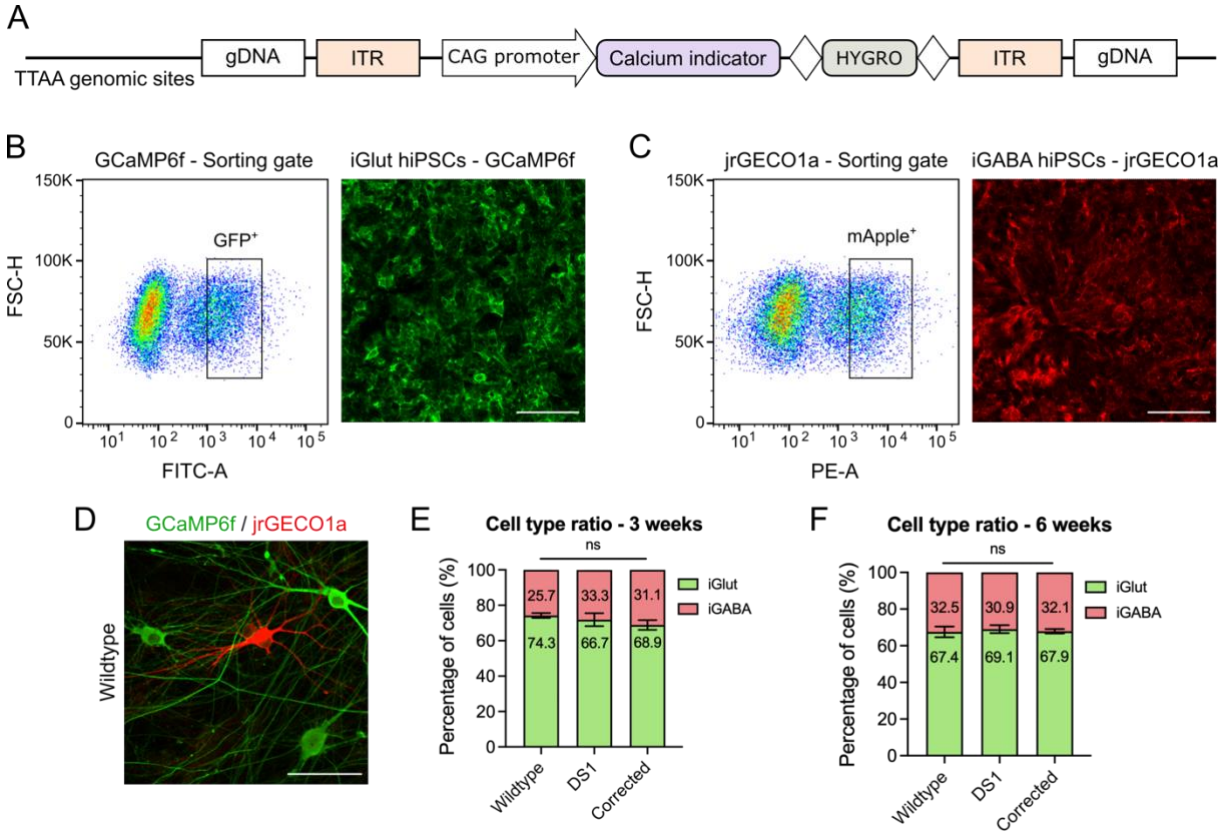

Figure 3.12. *Stable integration of spectrally distinct Genetically Encoded Calcium Indicators (GECIs) in iGlut and iGABA lines.* **A –** Schematic representation of the PiggyBac vector containing the calcium indicator downstream of a CAG promoter, followed by a hygromycin resistance cassette. The open reading frame is flanked by transposon-specific inverted terminal repeat sequences (ITRs). Transposase-mediated integration is targeted at TTAA genomic sites. **B-C –** Left, FACS sorting of GCaMP6f or jrGECO1a transfected cells. The gate was set to isolate medium/high GFP^+ or $mApple^+$ cells. Right, fluorescence images of sorted WT iGlut stably expressing GCaMP6f or WT iGABA stably expressing jrGECO1a. Scale bar = 100µm. **D –** Fluorescence image showing a wildtype co-culture of GCaMP6f-expressing iGlut and jrGECO1a-expressing iGABA stained for GFP (green) and RFP (red). **E-F –** Cell type ratio at 3 and 6 weeks plotted as the percentage of iGlut and iGABA cells in wildtype, DS1 and corrected co-cultures. N=3 biological replicates with n=4 FOW per sample. Error bars represent the SEM, Two-way ANOVA with multiple comparison, ns = $p>0.05$.

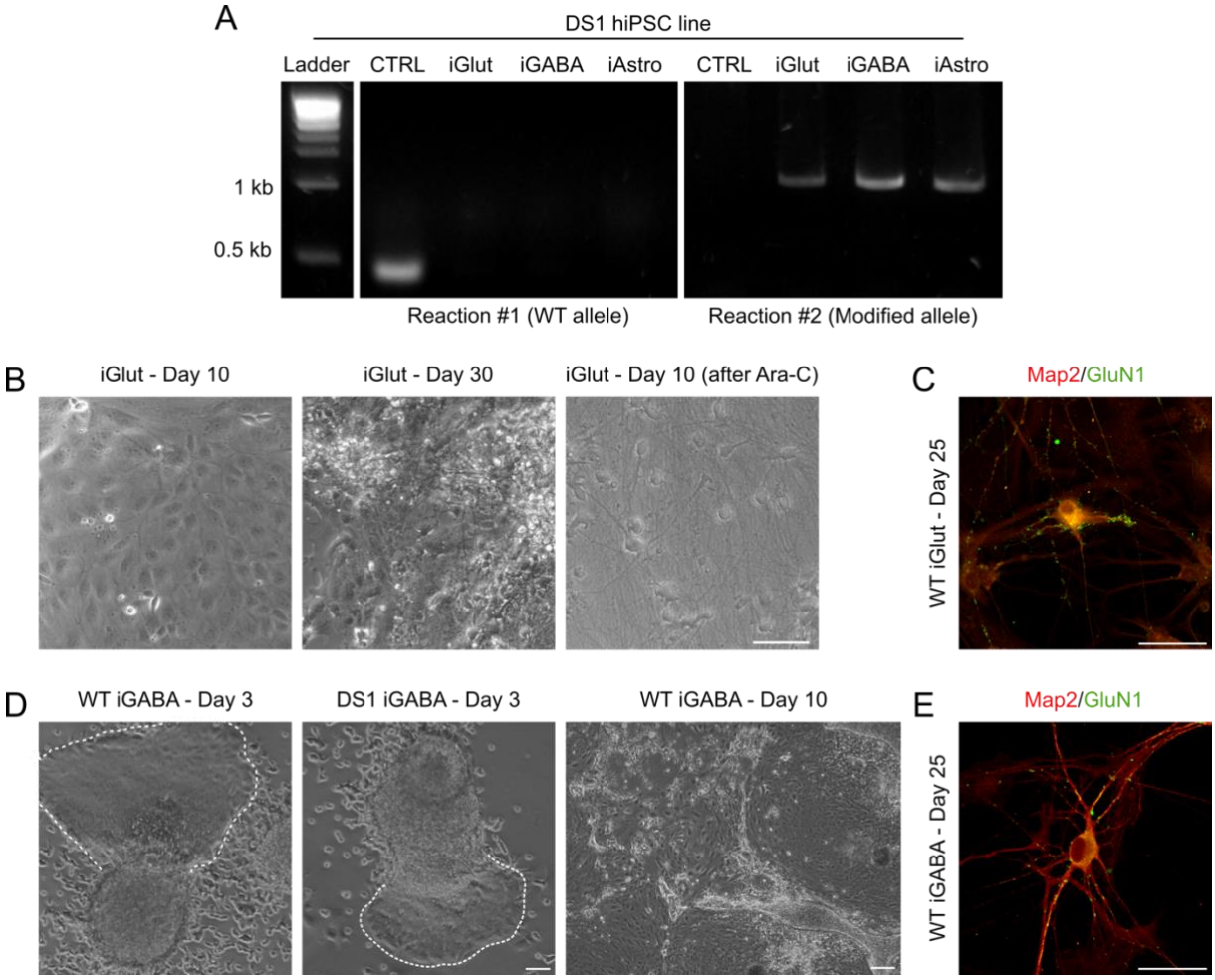

Supplementary Figure 3.1. A – Gel electrophoresis of PCR reactions #1 and #2 performed on the iGlut, iGABA and iAstro monoclonal lines derived from DS1 hiPSCs. Non-transfected DS1 hiPSCs are used as a control. **B –** Representative phase contrast images of an iGlut culture overgrown by proliferative cells at Day 10 and Day 30 and an iGlut culture at Day 10 after treatment with Ara-C to remove proliferative cells. Scale bar = 100µm. **C** – Immunofluorescence image of Day 25 WT iGlut neurons stained for Map2 (red) and GluN1 (green). Scale bar = 50µm. **D –** Representative phase contrast images of the iGABA "polarised" colony morphology observed at Day 3 in WT and DS1 iGABA differentiation – the white dashed line highlights proliferative cells. At Day 10, the culture is overgrown by the proliferative cells. Scale bar = 100µm. **E** – Immunofluorescence image of Day 25 WT iGABA neurons stained for Map2 (red) and GluN1 (green). Scale bar = 50µm.

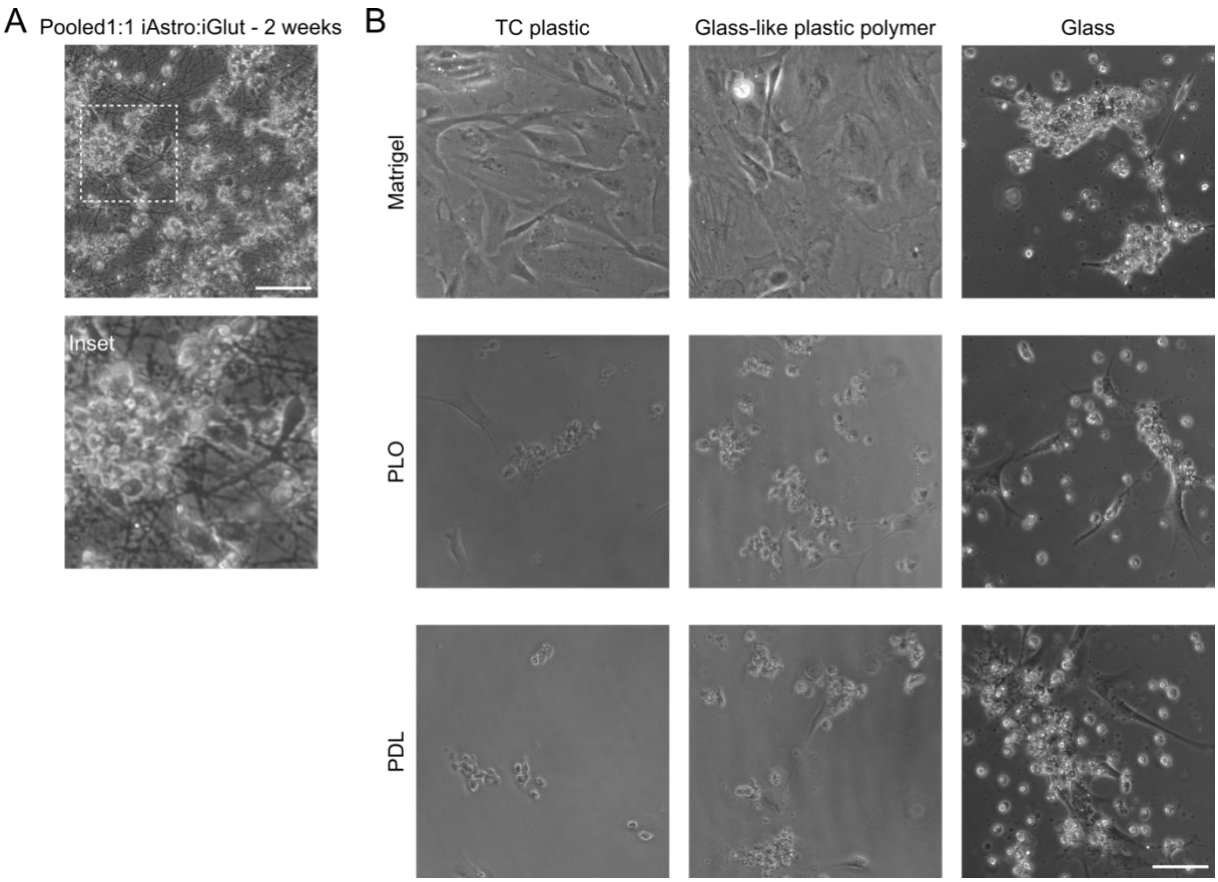

Supplementary Figure 3.2. A – Phase contrast images of a pooled culture of iAstro and iGlut (1:1 ratio) after 2 weeks of differentiation. Scale bar = 100µm. **B –** Phase contrast images of iAstro cultured on tissue culture (TC) plastic, glass-like plastic polymer or glass coated with either Matrigel, PLO or PDL. Scale bar = 100µm.

A

sgRNA ID: 941482857 Sequence: TGTTCTCCGTTCATTTCGAT TGG Location: 2:166039422-166039444 Strand: (-)

Off-Target Counts	All	Exonic	Intronic	Intergenic
Total	127	4	53	70
Summary	{0:1, 1:0, 2:0, 3:5, 4:121}	{0:1, 1:0, 2:0, 3:0, 4:3}	{0:0, 1:0, 2:0, 3:1, 4:52}	{0:0, 1:0, 2:0, 3:4, 4:66}

Top 5 off-target sites:

WGE ID	Location	Sequence	Mismatches	Strand	Type
941482857	Original CRISPR	TGTTCTCCGTTCATTTCGAT TGG (reversed)			Exonic
941482857	2:166039422-166039444	TGTTCTCCGTTCATTTCGAT TGG	0	-	Exonic
1079832671	11:25288419-25288441	TGTTCTCCATTAATTTCCAT TGG	3	+	Intergenic
1055239019	9:74161751-74161773	GGTTCTCCGTTCTTTTCCAT TGG	3	-	Intergenic
907981890	1:59490855-59490877	TGTTCTCTGTTCTTTTCCAT TGG	3	+	Intronic
909203402	1:72723847-72723869	TGTTCTCTGTTCAGTTCAAT TGG	3	+	Intergenic
1178477966	21:32954379-32954401	TGTTCCCCGTTCATTGCGAA AGG	3	-	Intergenic

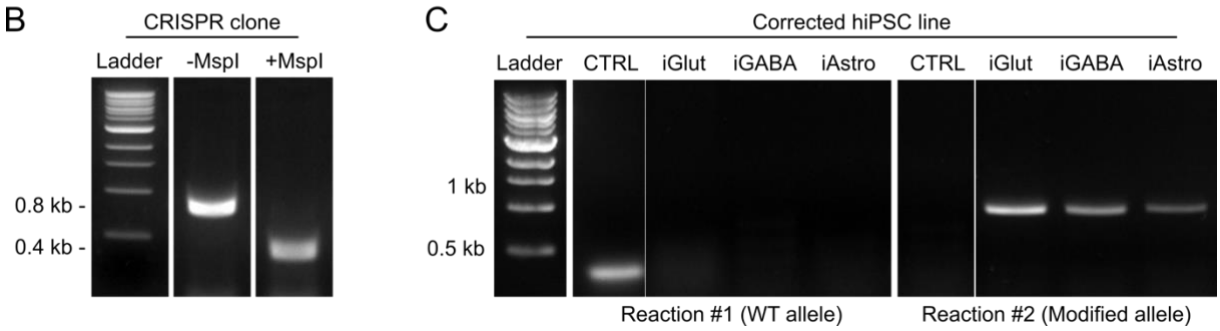

Supplementary Figure 3.3. A – Details of the sgRNA used for CRISPR/Cas9-mediated genome editing, including CRISPR ID, sequence, genome location, strand and off-target score. **B –** MspI restriction digest of CRISPR-edited hiPSC clone showing homozygous integration of the donor template harbouring the silent MspI restriction site. **C** – Gel electrophoresis of PCR reactions #1 and #2 performed on the iGlut, iGABA and iAstro monoclonal lines derived from corrected hiPSCs. Non-transfected corrected hiPSCs are used as a control.

Experiment: Neuronal survival assay on iAstro

Dataset analysed	Sample size	Normality	Statistical test	P Value (Significance)
Neuronal survival on iAstro – Day 4	Neurons only N = 8 Neurons + WT iAstro N = 8 Neurons + GDNF^{+} iAstro N = 8 N = FOV from 8 separate wells	YES YES YES	Ordinary One-way ANOVA + Tukey's multiple comparison Alpha 0.05	Neurons only vs. Neurons + WT iAstro = <0.001 (***) Neurons only vs. Neurons + GDNF^{+} iAstro = <0.001 (***) Neurons + WT iAstro vs. Neurons + GDNF^{+} iAstro = 0.2683 (ns)
Neuronal survival on iAstro – Day 7	Neurons only N = 8 Neurons + WT iAstro N = 8 Neurons + GDNF^{+} iAstro N = 8 N = FOV from 8 separate wells	YES YES YES	Ordinary One-way ANOVA + Tukey's multiple comparison Alpha 0.05	Neurons only vs. Neurons + WT iAstro = <0.001 (***) Neurons only vs. Neurons + GDNF^{+} iAstro = <0.001 (***) Neurons + WT iAstro vs. Neurons + GDNF^{+} iAstro = 0.1997 (ns)

Table 3.1. Statistical details of neuronal survival assay on iAstro.

Experiment: GFAP-CD14 enrichment quantification

Dataset analysed	Sample size	Normality	Statistical test	P Value (Significance)
% $GFAP^+$ cells	Pre-sort N = 3 Eluate N = 3 N = FOV from 3 separate wells	YES YES	Unpaired t test	Pre-sort vs. Eluate = <0.001 (***)
% $Tubb3^+$ cells	Pre-sort N = 3 Eluate N = 3 N = FOV from 3 separate wells	YES YES	Unpaired t test	Pre-sort vs. Eluate = 0.0366 (*)

Table 3.2. Statistical details on GFAP-CD14 enrichment quantification.

Experiment: Neuronal survival assay on mAstro

Dataset analysed	Sample size	Normality	Statistical test	P Value (Significance)
Neuronal survival on mAstro – 3-4 days	Neurons + WT mAstro N = 3 Neurons + $GDNF^+$mAstro N = 3 Neurons + $GDNF^+$ iAstro N = 8 N = FOV from 3 or 8 separate wells	YES YES YES	Ordinary One-way ANOVA + Tukey's multiple comparison Alpha 0.05	Neurons + WT mAstro vs. Neurons + $GDNF^+$ mAstro = <0.001 (***) Neurons + WT mAstro vs. Neurons + $GDNF^+$ iAstro = 0.9809 (ns) Neurons + $GDNF^+$ mAstro vs. Neurons + $GDNF^+$ iAstro = <0.001 (***)

Table 3.3. Statistical details on neuronal survival assay on mAstro.

Experiment: iGlut maturation on mAstro
Samples: WT iGlut vs. WT iGlut on mAstro
Sample size: N = 3 biological replicates for both samples and all datasets
Normality: Normal distribution for all datasets
Test: Unpaired t test with Welch's correction for all datasets

Dataset analysed	**P Value (Significance)**	**Dataset analysed**	**P Value (Significance)**
CUX1	0.1168 (ns)	GABRB1	0.1477 (ns)
LHX2	0.1303 (ns)	SYN1	0.0101 (*)
GLUR1	0.0634 (ns)	PSD95	0.1902 (ns)
GLUR2	0.0193 (*)	GAD67	0.0786 (ns)
GRIA3	0.1613 (ns)	vGAT	0.0730 (ns)
GRIA4	0.1225 (ns)		
NR1	0.0003 (***)		
NR2B	0.4361 (ns)		
vGLUT1	0.0029 (**)		
vGLUT2	0.0038 (**)		
CAMK2A	0.0366 (*)		
GABRA2	0.4527 (ns)		

Table 3.4. Statistical details on iGlut maturation on mAstro.

Experiment: iGABA maturation on mAstro
Samples: WT iGABA vs. WT iGABA on mAstro
Sample size: N = 3 biological replicates for both samples and all datasets
Normality: Normal distribution for all datasets
Test: Unpaired t test with Welch's correction for all datasets

Dataset analysed	**P Value (Significance)**	**Dataset analysed**	**P Value (Significance)**
DLX1	0.0748 (ns)	CALB2	0.0199 (*)
DLX2	0.0048 (**)	SST	0.0026 (**)
DLX5	0.0277 (*)	VIP	0.0514 (ns)
DLX6	0.2140 (ns)	NPY	0.1336 (ns)
GAD65	0.1018 (ns)	vGLUT1	0.4051 (ns)
GAD67	0.0810 (ns)	vGLUT2	0.0636 (ns)
GAT1	0.0005 (***)		
GAT2	0.0424 (*)		
vGAT	0.6212 (ns)		
SYN1	0.0820 (ns)		
PVALB	0.1101 (ns)		
CALB1	0.0244 (*)		

Table 3.5. Statistical details on iGABA maturation on mAstro.

Experiment: Interneuron subtype specification in iGABA
Samples: DS1 iGABA vs. DS1 iGABA on mAstro
Sample size: N = 3 biological replicates for all samples and all datasets
Normality: Normal distribution for all datasets
Test: Unpaired parametric t test with Welch's correction for all datasets

Sample	Dataset	P Value (Significance)
DS1 iGABA vs. DS1 iGABA on mAstro	Parvalbumin	0.0564 (ns)
	Calbindin	0.0245 (*)
	Calretinin	0.0068 (**)
	Somatostatin	0.0748 (ns)
	VIP	0.7808 (ns)
	NPY	0.2199 (ns)

Table 3.6. Statistical details on interneuron subtype specification on mAstro.

Experiment: SCN1A transcript quantification

Dataset analysed	Sample size	Normality	Statistical test	P Value (Significance)
SCN1A transcript quantification in iGlut	Wildtype N = 3 DS1 N = 3 Corrected = 3 N = independent cultures	NO YES YES	One-way ANOVA Kruskal-Wallis test + Dunn's multiple comparison Alpha 0.05	Wildtype vs DS1 = 0.6991 (ns) Wildtype vs Corrected = >0.9999 (ns) DS1 vs Corrected = 0.1579 (ns)
SCN1A transcript quantification in iGABA	Wildtype N = 3 DS1 N = 3 Corrected = 3 N = independent cultures	YES YES YES	Ordinary One-way ANOVA + Tukey's multiple comparison Alpha 0.05	Wildtype vs DS1 = 0.9869 (ns) Wildtype vs Corrected = 0.8385 (ns) DS1 vs Corrected = 0.7567 (ns)

Table 3.7. Statistical details on SCN1A transcript quantification.

3.3 Conclusions

- Both versions of hiPSC dorsal directed differentiation (D-V1 and D-V2) into excitatory cortical neurons generated neuronal progenitor cells after 35 days of differentiation.
    - The generated cells express neuronal markers MAP2, TUBB3 and PSD95 at variable levels. D-V2 progenitors express lower levels of MAP2 and higher levels of TUBB3 and PSD95, suggesting a more mature phenotype compared to D-V1 progenitors.
    - D-V2 progenitors express markers of cortical identity and neuronal progenitor markers of both dorsal and ventral identity, suggesting inefficient fate specification to dorsal progenitors.
- hiPSC ventral directed differentiation Version 1 (V-V1) failed to produce progenitor cells, while ventral directed differentiation Version 2 (V-V2) generated neuronal progenitor cells after 35 days of differentiation.
    - V-V2 progenitors express neuronal markers MAP2 and TUBB3 but only ~23% of progenitor cells express the ventral forebrain marker NKX2.1.
    - V-V2 progenitors express markers of both dorsal and ventral identity, suggesting inefficient fate specification to ventral progenitors.
- Magnetic-Activated Cell Sorting (MACS) can be used to isolate progenitors of defined identity from a mixed population of differentiating cells.
    - The interneuron-specific minimal promoter DLX5/6 was successfully used to label and isolate GABAergic interneuron progenitors from the mixed progenitor population generated with V-V2.
- hiPSC lines suitable for forward programming differentiation were successfully generated using TALEN-mediated integration of doxycycline-inducible transcription factors into the AAVS1 safe harbour locus.
- Forward programming differentiation into excitatory neurons (iGlut) generates neuronal cells after 10 days.

- iGlut neurons display a mature neuronal morphology and express neuronal markers MAP2 and TUBB3 by day 10 of differentiation. By day 25, iGlut neurons express mature pre- and post-synaptic markers Synapsin-1 and PSD95.

- At day 35 of differentiation, iGlut neurons express mature markers of glutamatergic identity and have a more mature gene expression profile compared to progenitors derived with D-V2 at day 35.

- iGlut neurons don't express markers of GABAergic identity, suggesting homogenous cell specification towards excitatory neurons.

- Forward programming differentiation into GABAergic inhibitory interneurons (iGABA) generates neuronal cells after 10 days.

  - iGABA neurons display a mature neuronal morphology and express neuronal markers MAP2 and TUBB3 by day 10 of differentiation. By day 25, iGABA neurons express mature pre- and post-synaptic markers, Synapsin-1 and PSD95.

  - At day 35 of differentiation, iGABA neurons express mature markers of GABAergic identity and have a more mature gene expression profile compared to progenitors derived with V-V2 at day 35.

  - iGABA neurons don't express markers of glutamatergic identity, suggesting homogenous cell specification towards inhibitory interneurons.

- Forward programming differentiation into astrocytes (iAstro) generates astrocyte cells after 7 days.

  - iAstro already express astrocyte markers S100b, Vimentin and GFAP by day 7 of differentiation. By day 21, 70-80% of iAstro cells express these markers.

  - At Day 21, iAstro express many astrocyte-specific genes, suggesting high specification efficiency towards astrocytic identity, but they lack expression of some common markers of functional maturation.

- Co-culture with iAstro doesn't support neuronal survival in long-term cultures.

  - After 2 weeks of co-culture with iAstro, both iGlut and iGABA neurons form clumps and display an unhealthy morphology compared to neurons cultured without iAstro.

- The iAstro line was modified to constitutively express the neurotrophic factor GDNF in an attempt to improve its performance.

- An imaging-based survival assay showed that only 2% of neurons survived after 7 days of co-culture with iAstro. $GDNF^+$ iAstro performed slightly better, with 10% of neurons surviving after 7 days, however, their presence was still detrimental to the survival of neurons in co-culture.

- mESC-derived astrocytes (mAstro) support neuronal survival more efficiently than iAstro.

  - Directed differentiation of mESCs combined with magnetic-activated cell sorting of $GFAP^+$ cells generate pure populations of astrocytes (92% $GFAP^+$ cells) suitable for neuronal co-culture in only 20 days.

  - $GDNF^+$ mAstro support the survival of 92% of neurons after 3 days, compared to 52% for WT mAstro and 51% for $GDNF^+$ iAstro.

- $GDNF^+$ mAstro support the survival and promote the maturation of iGlut and iGABA in long-term cultures.

  - After 4 weeks of co-culture with $GDNF^+$ mAstro, both iGlut and iGABA are still healthy and gene expression analysis indicates improved neuronal maturation compared to astrocyte-free cultures.

  - iGlut and iGABA cultured on mAstro express increasing levels of *SCN1A* over 50 days of culture.

- The $SCN1A^{IVS14+3A>T}$ mutation in the DS1 line was successfully corrected using CRISPR/Cas9-mediated genome editing.

  - The karyotype and stemness properties of the corrected line were not affected by the genome editing process.

  - Upon correction, the *SCN1A* transcript was restored to its full size and no differences in expression levels were observed between wildtype, DS1 and corrected lines.

- $GDNF^+$ mAstro, iGlut and iGABA can be assembled into long-term co-culture models of cortical circuits with a stable ratio of 70% excitatory neurons and 30% inhibitory interneurons.

- iGlut and iGABA hiPSC lines from WT, DS1 and corrected background were successfully modified to express spectrally distinct genetically encoded calcium indicators. GFP-based GCaMP6f was introduced in the iGlut lines and mApple-based jrGECO1a in the iGABA lines.

- Using GCaMP6f and jrGECO1a as identity signatures we confirmed that iGlut:iGABA co-cultures maintain a ratio of 70% to 30% after 3 and 6 weeks of co-culture.

Chapter 4

Pathogenic SCN1A$^{IVS14+3A>T}$ impairs inhibitory interneuron activity

4.1 Introduction

In the previous chapter we described the generation of a ratio-defined *in vitro* model of cortical circuits suitable for the study of Dravet syndrome (DS). However, prior to investigating disease phenotypes within this co-culture model, we first sought to functionally characterise the effect of the *SCN1A*$^{IVS14+3A>T}$ Dravet mutation in the individual neuronal populations in monoculture. As previously discussed, the epileptic phenotype in DS is thought to be caused by a lack of inhibition associated with the compromised function of inhibitory interneurons. Studies on Dravet patient hiPSC-derived neurons have also reported **impaired** activity of inhibitory interneurons (Higurashi et al., 2013a; J. Liu et al., 2016b; Y. Sun et al., 2016). However, not all published reports on *in vitro* Dravet models support this consensus view: one study by Liu et al. found that hiPSC-derived interneurons generated from two independent patients with DS (one of them carrying the *SCN1A*$^{IVS14+3A>T}$ mutation), displayed **increased** excitability and therefore, increased inhibitory activity (Y. Liu, Lopez-Santiago, et al., 2013). To characterise the Dravet-related phenotype in our neuronal model, in this chapter, we investigate interneuron-specific phenotypes in iGABA monocultures. Specifically, we determined structural and electrophysiological properties of early (3 weeks) and late (6 weeks) iGABA neurons derived from wildtype, DS1 and corrected hiPSC lines.

4.2 Results

4.2.1 Pathogenic *SCN1A*$^{IVS14+3A>T}$ causes increased activity in early inhibitory interneurons (3 weeks)

iGABA neurons expressing the genetically encoded calcium indicator jrGECO1a were derived from hiPSCs as previously described and matured on mAstro for 3 weeks before experiments were performed. Calcium imaging experiments were conducted according to Sun & Südhof (Z. Sun & Südhof, 2021b). This publication provides a simple protocol to induce and analyse neuronal activity in human iPSC-derived neurons. Since these neurons are generally less mature than neurons in primary cultures and exhibit less spontaneous activity, this protocol uses a specific imaging buffer containing higher concentrations of Ca^{2+} and K^{+} designed to stimulate neuronal activity. To this end, iGABA at 3 weeks were first equilibrated in Modified Tyrode Solution (2 mM Ca^{2+}, 5 mM K^{+}), and then incubated in Ca^{2+} imaging buffer (4 mM Ca^{2+}, 8 mM K^{+}) for the recordings. Full buffer compositions are listed in *Chapter 2, Table 2.12*. Time-lapse recordings were carried out over 120 sec at a frame rate of 10-20 frames/sec and the fluorescence intensity profile was analysed for the active cells within the field of view (Fig. 4.1-A). The jrGECO1a signal intensity for each neuron was normalised by calculating the ratio ($\Delta F/F_0$) of the increase in fluorescence (ΔF) to the baseline (F_0) and plotted over time (Fig. 4.1-B). Single-neuron Ca^{2+} dynamics were analysed in terms of their amplitude and frequency. The Ca^{2+} signal amplitude was comparable across conditions (Fig. 4.1-C – Table 4.1). However, we found that DS1 iGABA neurons displayed an almost doubled Ca^{2+} signal frequency (2.24 ± 0.29 spikes/min), compared to wildtype (1.14 ± 0.16 spikes/min) and corrected (1.35 ± 0.19 spikes/min) lines (Fig. 4.1-D – Table 4.1). The higher Ca^{2+} signal frequency observed in DS1 iGABA suggests an increase in neuronal activity, which, although in contrast with the main literature, is in line with previous observations from Liu et al. (Y. Liu, Lopez-Santiago, et al., 2013).

4.2.2 Pathogenic *SCN1A*$^{IVS14+3A>T}$ causes increased sodium and potassium currents in early inhibitory interneurons (3 weeks).

Voltage clamp recordings performed on iGABA neurons at 3 weeks revealed that DS1 interneurons have significantly increased Na^{+} and K^{+} current densities compared to wildtype and corrected interneurons (Fig. 4.2-A and B – Table 4.2). Putative currents were measured as

the minimum fast inward currents (Na^+ currents) and average steady state outward currents (K^+ currents) – highlighted in blue and pink respectively in Fig. 4.2-B. Membrane capacitance is directly proportional to the membrane surface area and it can be used experimentally to determine the cell area. Current values were normalised to the membrane capacitance to extrapolate an estimate of the amount of current flowing through the cell membrane per unit area (current density). Measurements of membrane capacitance (Cm), as well as other passive properties like membrane resistance (Rm) and access resistance (Rs) were comparable across conditions (Table 4.2). Interestingly, the increase in Na^+ and K^+ current densities did not translate into differences in AP properties. Current clamp recordings revealed no differences across conditions in AP amplitude, half-width, maximum rate of depolarisation and repolarisation, nor in the current and voltage membrane (Vm) thresholds required to elicit an AP (Fig. 4.2-C and Supplementary Fig. 4.1-A – Table 4.2). The observed AP profiles, characterised by low amplitude and large width, were indicative of neurons at a relatively immature stage (Supplementary Fig. 4.1-C). The relationship between injected current and AP firing frequency (input-output curve) was also consistent with an immature phenotype. Indeed, all iGABA populations were found to fire only a few AP (typically one or two) in response to increasing amounts of injected currents (Fig. 4.2-D – Table 4.2). No differences were observed in the maximum firing frequency (Fig. 4.2-E – Table 4.2) nor the spontaneous firing frequency (Supplementary Fig. 4.1-B – Table 4.2). However, the resting membrane potential was found to be more hyperpolarised in DS1 iGABA neurons (-30.74 ± 1.51 mV) compared to wildtype (-23.37 ± 1.36 mV) and corrected (-24.65 ± 1.75 mV) lines (Fig. 4.2-F – Table 4.2). A more hyperpolarised resting potential is typically associated with reduced membrane excitability, where a higher amount of current is needed in order to drive AP initiation. Interestingly, in particular circumstances, a more hyperpolarised membrane potential can have the opposite effect and lead to hyperexcitability. Indeed, at more negative membrane potentials, more Na^+ channels are available for activation, causing a greater influx of Na^+ into the cell and leading to greater depolarisation amplitudes that are more likely to reach the threshold for AP initiation (Bodi et al., 2005).

4.2.3 Pathogenic SCN1A$^{IVS14+3A>T}$ causes proximal shift of the AIS in early inhibitory interneurons (3 weeks)

Studies in rodents have previously demonstrated that NaV1.1, the channel encoded by *SCN1A*, is primarily localised at the AIS of interneurons, particularly SST and PV-positive interneurons

(T. Li et al., 2014; Lorincz & Nusser, 2008; Ogiwara et al., 2007b). Similarly, in human brain tissue, NaV1.1 was mainly found at the AIS of inhibitory interneurons (Tian et al., 2014). Moreover, morphological characteristics and structural changes of the axon initial segment have been shown to modulate intrinsic neuronal excitability (discussed in *Chapter 1, section 1.1.4*). Despite the strong association between NaV1.1 and the AIS, the effects of Dravet-related NaV1.1 mutations on the properties of the AIS have not been previously investigated. To address this, we assessed the structural properties of the AIS, based on Ankyrin-G (Ank-G) staining, in 3-week-old iGABA neurons cultured on mAstro (Fig. 4.3-A). While the length of the AIS was comparable across all conditions (Fig. 4.3-B – Table 4.3), the AIS distance from the soma was found to be reduced in DS1 iGABA neurons (4.95 ± 0.97 μm) compared to wildtype (9.90 ± 1.22 μm) and corrected (10.39 ± 1.17 μm) lines (Fig. 4.3-C – Table 4.3). Finally, Ank-G fluorescence intensity along the AIS was comparable across all conditions (Fig. 4.3-D – Table 4.3).

The proximity of the AIS to the soma is thought to be directly correlated with neuronal excitability and AP properties. A shorter distance between the soma and the start of the AIS reduces the dissipation of charges during propagation from the soma (Yamada & Kuba, 2016). Thus, functionally, a more proximal AIS is associated with increased neuronal excitability, characterised by a lower current threshold and higher AP firing frequencies (Grubb et al., 2011; Grubb & Burrone, 2010). Specific differences in current threshold and AP frequency were not observed in DS1 iGABA neurons (Fig. 4.1-C-D-E). However, the electrophysiological recordings of early inhibitory interneurons were characterised by high variability which, together with the relatively low number of cells analysed, might be concealing subtle differences. Indeed, when neuronal activity was investigated using calcium imaging (a higher-throughput technique compared to patch-clamping), DS1 iGABA displayed a higher frequency of events, consistent with neuronal hyperexcitability.

4.2.4 Hyperexcitability in early DS1 interneurons is not caused by transcriptional upregulation of other sodium channels (3 weeks)

Overall, early DS1 interneurons showed several indications of hyperexcitability, characterised by increased Na^+ current density, increased neuronal activity and a more proximal AIS. As mentioned, a similar phenotype has been previously observed in the same DS cell line used in this project (Y. Liu, Lopez-Santiago, et al., 2013). We speculated that such a phenotype could

be mediated by a compensational mechanism implemented by DS1 interneurons in response to the loss of function of NaV1.1. Specifically, this might include overexpression of a different NaV channel. To test this hypothesis, the expression levels of all the different types of NaV channels were compared in early wildtype, DS1 and corrected iGABA (Fig. 4.4-A). Since the β-subunits of NaV channels can modulate the voltage-gate and kinetics of the channel pore (Bouza & Isom, 2018), their expression was also analysed. Interestingly, no differences were observed in the expression levels of these genes across populations. The expression levels of voltage-gated calcium channels (CaV) and Kv channels was also analysed. Similarly, we did not observe any significant difference in the expression of these genes across populations (Fig. 4.4-B). Unfortunately, the analysis of the majority of Kv channels was unsuccessful and it will need to be repeated with newly designed primer sets to confirm whether they are involved in a possible compensational mechanism. Finally, the expression of some AIS resident proteins was also investigated but, once again, no differences were observed in the expression levels of these genes across populations (Fig. 4.4-C).

None of the investigated targets seemed responsible for the hyperexcitable phenotype of early DS1 interneurons suggesting that, if a compensation mechanism is at play, it's either mediated by genes not included in this study or through post-transcriptional mechanisms.

4.2.5 Pathogenic SCN1A$^{IVS14+3A>T}$ causes reduced activity in late inhibitory interneurons (6 weeks)

We next characterised our iGABA lines at a later time point (6 week). Calcium imaging recordings were collected as described above for the 3 week timepoint. Thus, iGABA neurons at 6 weeks were imaged while incubated in Ca^{2+} imaging buffer (4 mM Ca^{2+}, 8 mM K^{+}) to induce neuronal activity (Fig. 4.5-A). The jrGECO1a $\Delta F/F_0$ was calculated and plotted over time (Fig.4.5-B) for wildtype, DS1 and corrected iGABA neurons. Unfortunately, due to the protracted unavailability of the microscope used for the acquisition of wildtype and DS1 samples, corrected iGABA neurons were imaged using a different imaging system. For this reason, the Ca^{2+} signal amplitude detected for the corrected iGABA line could not be compared with the one detected for wildtype and DS1 iGABA lines. However, since Ca^{2+} signal frequency is not dependent on the light source, this parameter could be compared across all conditions.

DS1 iGABA neurons at 6 weeks were found to have a lower calcium signal amplitude (0.023 ± 0.006 $\Delta F/F_0$) compared to the wildtype line (0.038 ± 0.006 $\Delta F/F_0$) (Fig. 4.5-C – Table 4.5).

DS1 iGABA neurons also displayed a significantly lower calcium signal frequency (4.07 ± 0.60 spikes/min) compared to wildtype (6.86 ± 0.77 spikes/min) and corrected (7.98 ± 0.64 spikes/min) lines (Fig. 4.5-D – Table 4.5). Over time, there was a significant increase in spike frequency in all iGABA populations, consistent with neuronal maturation. However, the increase observed in DS1 iGABA neurons was substantially smaller compared to wildtype and corrected lines (Fig. 4.5-D – Table 4.5). A lower Ca^{2+} signal amplitude, and therefore lower neuronal depolarisation (Akerboom et al., 2012; Shidara et al., 2013), together with a lower Ca^{2+} signal frequency suggests reduced neuronal excitability of late DS1 iGABA. These observations are in contrast with the phenotype observed in early interneurons but in agreement with the expected reduced functionality of inhibitory interneurons generally reported in DS.

4.2.6 Pathogenic SCN1A$^{IVS14+3A>T}$ might cause reduced intrinsic excitability in late inhibitory interneurons (6 weeks)

Voltage clamp recordings revealed that, at this later time point, Na^+ and K^+ current densities were comparable across all neuronal populations (Fig. 4.6-A and B – Table 4.6a). Similarly, the membrane capacitance (Cm) was comparable across conditions (Table 4.6a). Unsurprisingly, the Cm was universally increased across all populations compared with the 3 week timepoint (Supplementary Fig. 4.1-D) in accordance with increasing cell size and thus membrane surface area. This means that Na^+ currents per unit area (current density) significantly increased over time in the wildtype and corrected iGABA populations while they remained unchanged in DS1 interneurons (Fig. 4.6-A – Table 4.6b). K^+ current densities, instead, were unchanged over time in wildtype and corrected lines, while they were significantly decreased in DS1 iGABA neurons (Fig. 4.5-6 – Table 4.6b).

Current clamp recordings revealed no differences across conditions in AP amplitude, half-width, maximum rate of depolarisation or repolarisation, nor in the current and voltage membrane (Vm) thresholds required to elicit an AP (Fig. 4.6-C and Supplementary Fig. 4.1-E – Table 4.6a). At this later time point, the observed AP profiles, characterised by higher amplitude and smaller width, were indicative of neurons at a more mature stage (Supplementary Fig. 4.1-F). Indeed, over time, an increase in AP amplitude and rate of rise, together with a decrease in AP half-width was observed in all populations, consistent with progressive neuronal maturation (Supplementary Fig. 4.1-G – Table 4.6b). On average, DS1 iGABA neurons displayed a lower AP frequency in response to increasing amounts of injected current (input-output curve), compared to wildtype and corrected lines (Fig. 4.6-D). Indeed, DS1 iGABA

neurons typically fired only one or two AP in response to high amounts of current, compared to five or six AP fired by wildtype and corrected iGABA neurons. However, all iGABA populations still displayed a prevalently immature firing capacity, characterised by adaptive rather than repetitive firing (Fig. 4.6-E). Similarly, DS1 iGABA neurons displayed a lower maximum frequency (3.87 ± 0.68 Hz) compared to wildtype (6.58 ± 1.51 Hz) and corrected (8.23 ± 1.49 Hz) lines (Fig. 4.6-F – Table 4.6a). Consistent with neuronal maturation, the maximum frequency over time was found to significantly increase in wildtype and corrected iGABA lines, but it did not increase in DS1 neurons (Fig. 4.6-F – Table 4.6b). Decreased current-induced firing and lower AP maximum frequency are consistent with the lower Ca^{2+} signal frequency observed in late DS1 iGABA neurons by calcium imaging (Fig. 4.5-D). Both the lower AP firing frequency and Ca^{2+} signal frequency were observed under stimulating conditions (i.e. current-induced firing and K^{+}-induced activity respectively), while no differences across populations were observed in spontaneous AP frequency (Supplementary Fig. 4.1-H – Table 4.6a). Together, these data indicate a potentially compromised capacity of DS1 inhibitory interneurons to fire high frequency action potentials in response to functional stimulation.

Finally, similarly to the 3 week time point, the resting membrane potential was found to be more hyperpolarised in the DS1 iGABA line (-47.75 ± 2.87 mV), compared to wildtype (-34.75 ± 3.19 mV) and corrected (-38.41 ± 1.75 mV) lines (Fig. 4.6-G – Table 4.6a). Over time, the resting membrane potential became significantly more hyperpolarised in all populations, with a higher decrement observed in the DS1 line (Fig. 4.6-G – Table 4.6b). As previously mentioned, a more negative resting potential is typically associated with reduced membrane excitability which, in this case, is consistent with the overall electrophysiological phenotype observed in late DS1 interneurons.

4.2.7 Pathogenic SCN1A$^{IVS14+3A>T}$ causes lower Ank-G availability at the AIS

Structural properties of the AIS were next investigated, based on Ankyrin-G staining (Fig. 4.7-A). The length of the AIS at 6 weeks was comparable across all lines and, consistent with maturation, was found to increase compared with the 3 week time point (Fig. 4.7-B – Table 4.7). At 6 weeks the AIS was found to be equally distant from the soma across all three lines. This indicates that, over time, the AIS moved proximally in wildtype and corrected lines, while shifting distally in the DS1 line (Fig. 4.7-C – Table 4.7). Finally, the average Ank-G fluorescence intensity at 6 weeks was found to be lower in DS1 iGABA neurons (25.16 ± 0.60

AU), compared to wildtype (27.38 ± 0.62 AU) and corrected (28.15 ± 0.63 AU) lines (Fig. 4.7-D – Table 4.7). The change in Ank-G fluorescence intensity over time could not be calculated due to the replacement of the confocal light source between the 3 and 6 week time points. Since Ank-G is a scaffolding protein essential for the clustering of NaV channels at the AIS, a lower availability of Ank-G might reduce the density of NaV channels at the AIS and contribute towards reduced neuronal excitability.

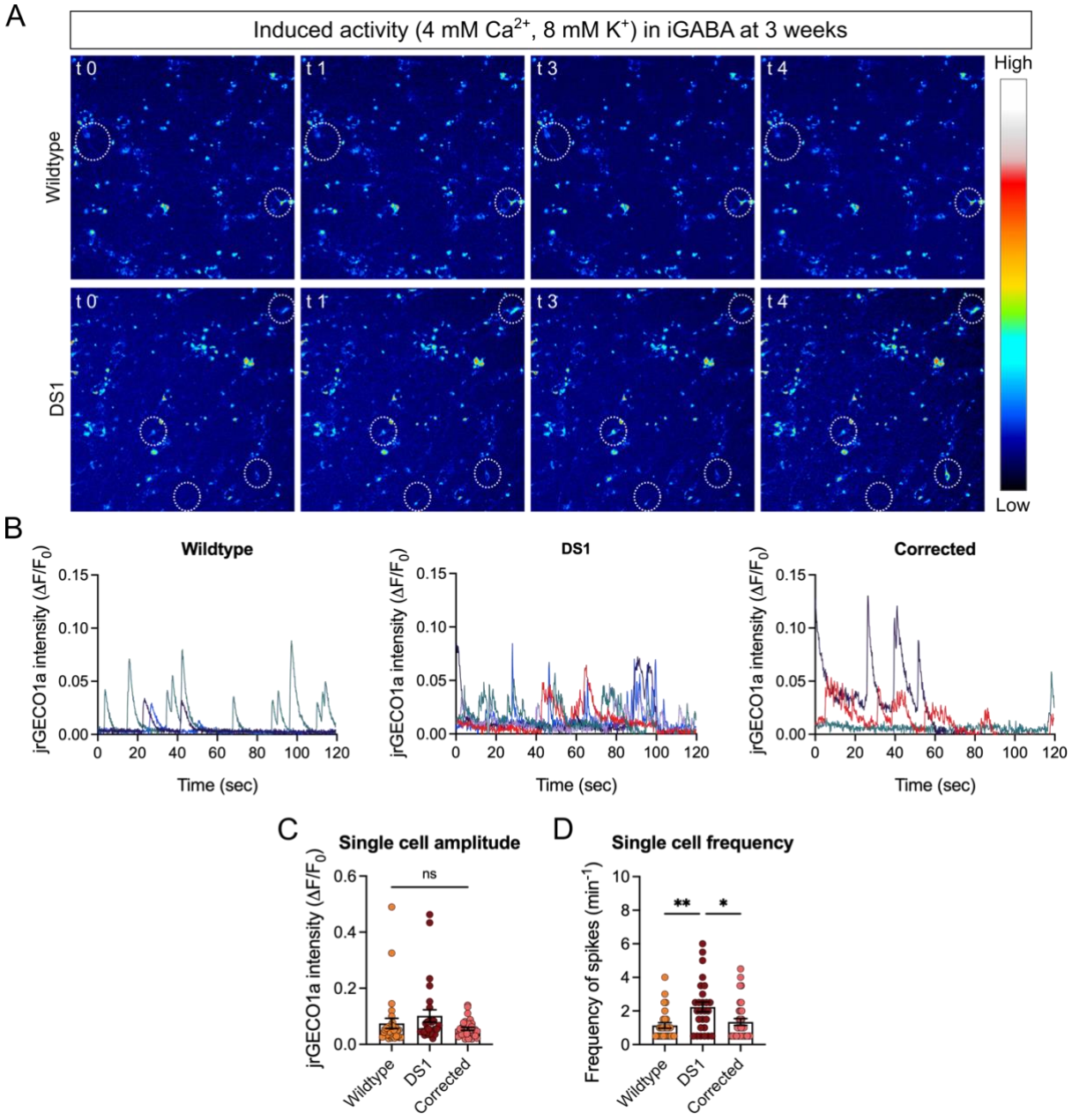

Figure 4.1. *Pathogenic SCN1A$^{IVS14+3A>T}$ causes increased activity in early inhibitory interneurons (3 weeks).* **A –** Representative time-lapse images of the induced activity of 3 weeks iGABA expressing jrGECO1a monitored in calcium imaging buffer with an increased Ca^{2+} (4 mM) and K^+ concentration (8 mM). Scale bar = 100 µm. **B –** Representative calcium traces plotted as the jrGECO1a $\Delta F/F_0$ over time for wildtype, DS1 and corrected iGABA at 3 weeks. **C-D –** Quantification of single-cell calcium signal amplitude and frequency recorded in iGABA at 3 weeks. N=3 biological replicates, n = 27-33 cells. Error bars represent the SEM, One-way ANOVA Kruskal-Wallis test + Dunn's multiple comparison, ns = $p>0.05$, * = $p<0.05$, ** = $p<0.01$.

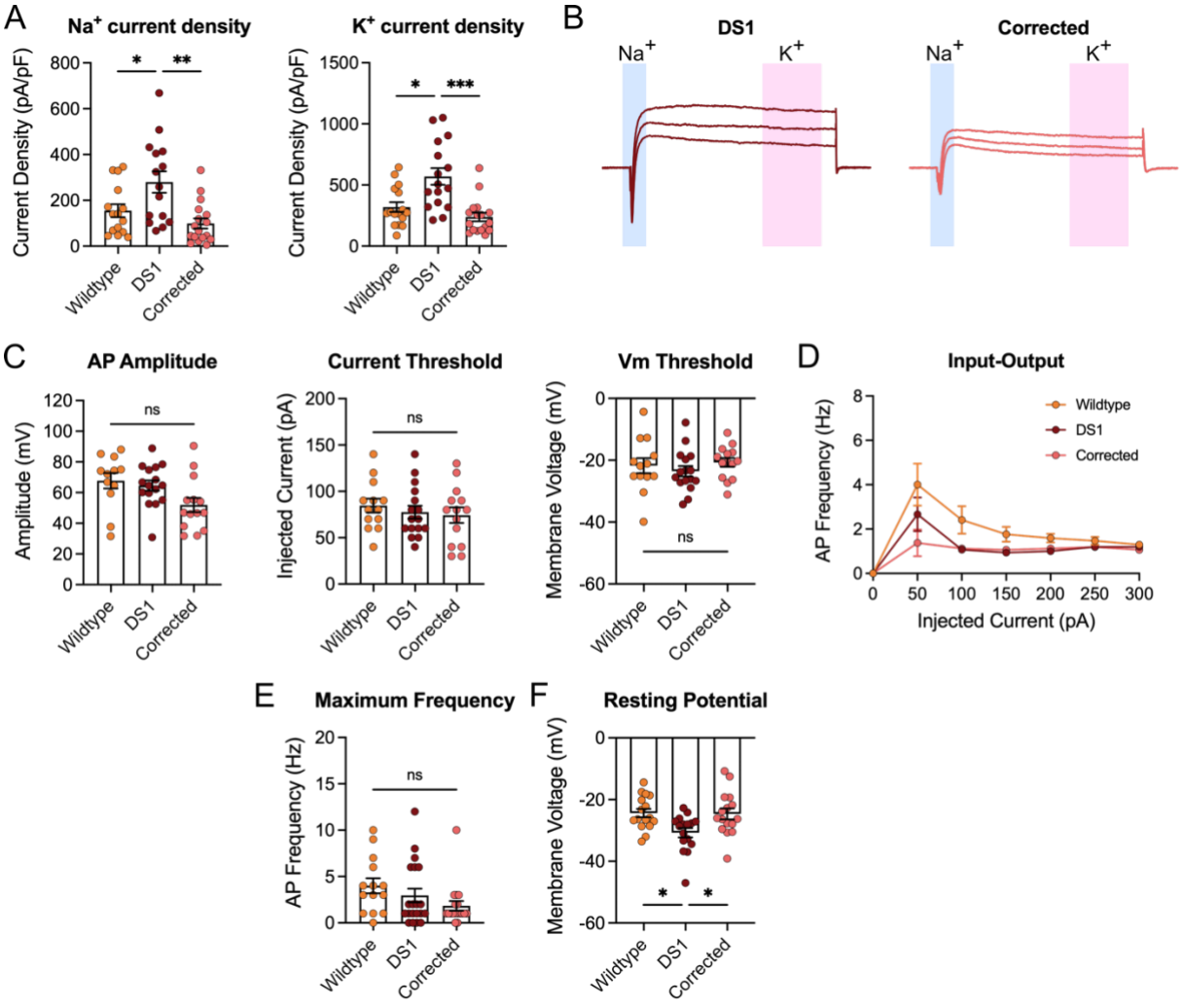

Figure 4.2. *Pathogenic SCN1A$^{IVS14+3A>T}$ causes increased sodium and potassium currents in early inhibitory interneurons (3 weeks).* **A –** Quantification of Na^+ and K^+ currents normalised to the capacitance (current densities) in iGABA at 3 weeks. N=4 biological replicates, n = 15-17 cells. Error bars represent the SEM, Ordinary One-way ANOVA + Tukey's multiple comparison, * = $p<0.05$, ** = $p<0.01$. **B –** Representative inward (Na^+) and outward (K^+) current traces recorded at 0, 10, and 20mV pulses from DS1 and corrected iGABA at 3 weeks. **C –** Quantification of action potential properties including amplitude, current threshold and membrane voltage (Vm) threshold recorded in iGABA at 3 weeks. N=4 biological replicates, n = 12-16 cells. Error bars represent the SEM, Ordinary One-way ANOVA + Tukey's multiple comparison, ns = $p>0.05$. **D –** AP frequency in relationship to injected current recorded in iGABA at 3 weeks. N=4 biological replicates, n = 14-20 cells. Error bars represent the SEM. **E –** Quantification of the maximum evoked AP frequency recorded in iGABA at 3 weeks. N=4 biological replicates, n = 14-20 cells. Error bars represent the SEM, Ordinary One-way ANOVA + Tukey's multiple comparison, ns = $p>0.05$. **F –** Quantification of the resting membrane potential recorded in iGABA at 3 weeks. N=4 biological replicates, n = 16 cells. Error bars represent the SEM, Ordinary One-way ANOVA + Tukey's multiple comparison, * = $p<0.05$.

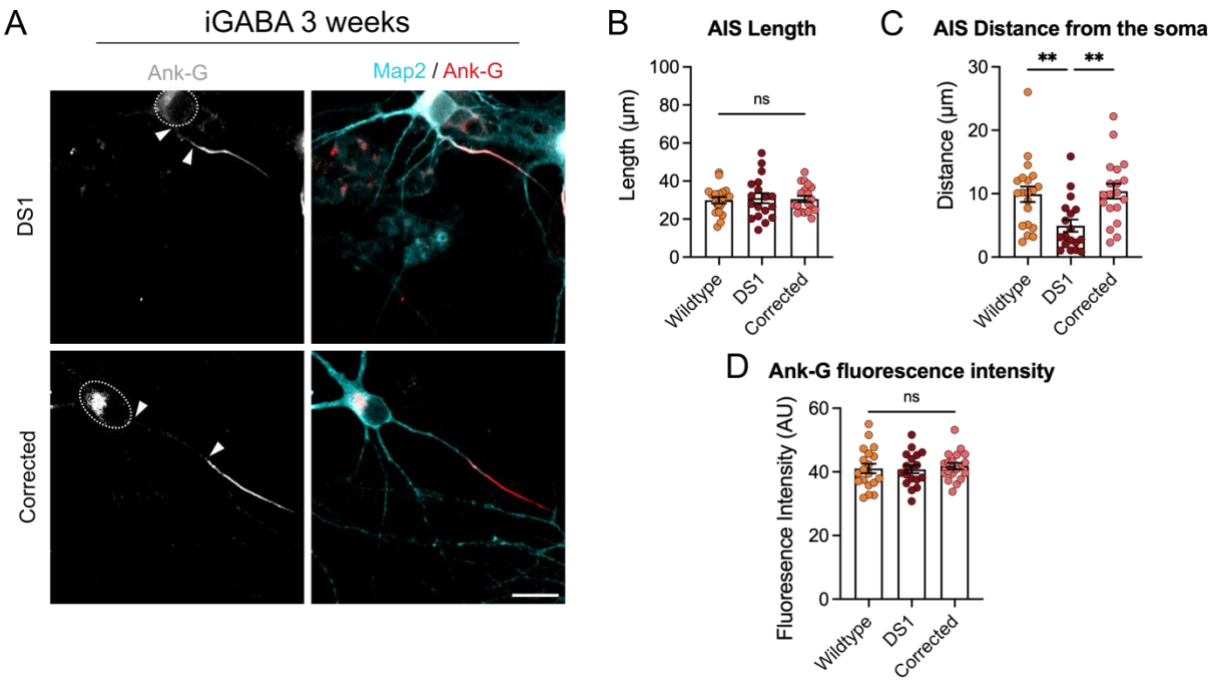

Figure 4.3. *Pathogenic SCN1A$^{IVS14+3A>T}$ causes proximal shift of the AIS in early inhibitory interneurons (3 weeks).* **A –** Representative immunofluorescence images of DS1 and corrected iGABA neurons at 3 weeks stained for Ank-G (grey on the left and red on the right) and Map2 (cyan). Scale bar = 20 µm. **B-C –** Quantification of AIS length and distance from the soma based on Ank-G staining (AIS) relative to Map2 staining (soma) in iGABA at 3 weeks. N=3 biological replicates, n = 18-19 cells. Error bars represent the SEM, Ordinary One-way ANOVA + Tukey's multiple comparison or One-way ANOVA Kruskal-Wallis test + Dunn's multiple comparison, ns = $p>0.05$, ** = $p<0.01$. **D –** Quantification of Ank-G fluorescence intensity in iGABA at 3 weeks. AU = arbitrary unit. N=3 biological replicates, n = 18-19 cells. Error bars represent the SEM, Ordinary One-way ANOVA + Tukey's multiple comparison, ns = $p>0.05$.

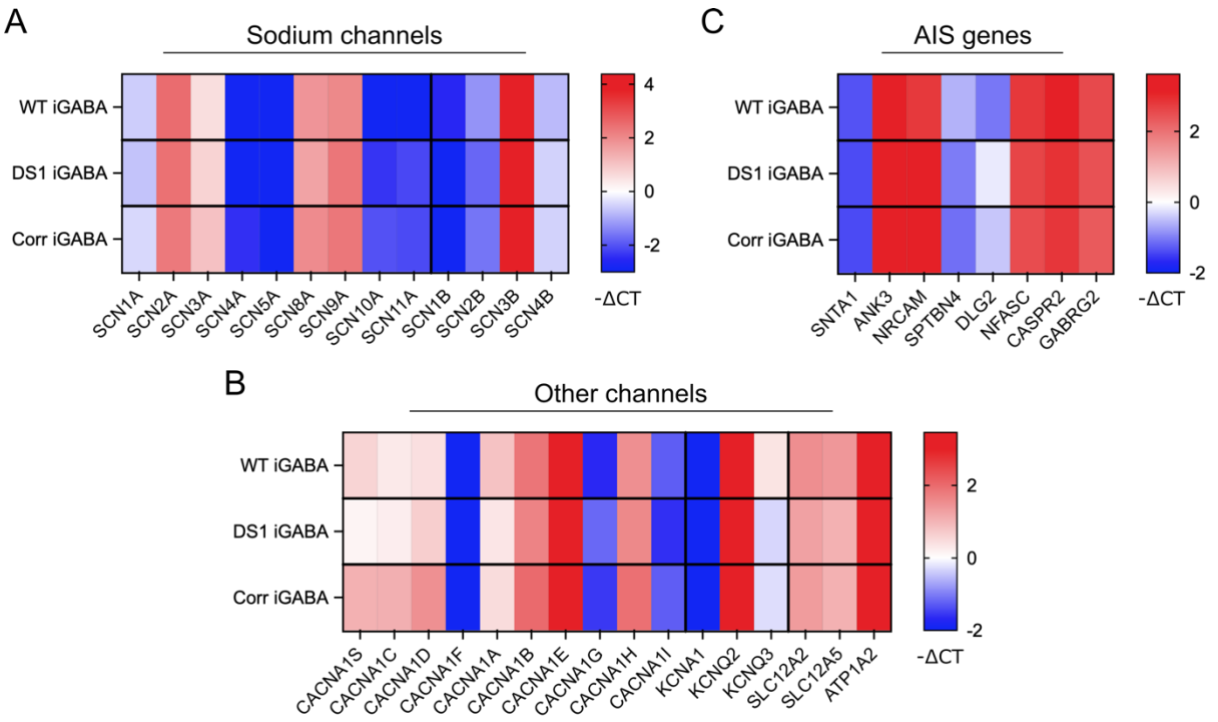

Figure 4.4. *Hyperexcitability in early DS1 interneurons is not caused by transcriptional upregulation of other sodium channels (3 weeks).* **A –** Heatmap representation of RT-qPCR analysis of sodium channels α and β subunits in wildtype, DS1 and corrected iGABA neurons at 3 weeks. Gene expression levels are normalised to the housekeeping gene TBP and expressed as -ΔCT. N=3 biological replicates with n=3 technical replicates per sample. **B –** Heatmap representation of RT-qPCR analysis of different ion channels in wildtype, DS1 and corrected iGABA neurons at 3 weeks. Gene expression levels are normalised to the housekeeping gene TBP and expressed as -ΔCT. N=3 biological replicates with n=3 technical replicates per sample. **C –** Heatmap representation of RT-qPCR analysis of AIS genes in wildtype, DS1 and corrected iGABA neurons at 3 weeks. Gene expression levels are normalised to the housekeeping gene TBP and expressed as -ΔCT. N=3 biological replicates with n=3 technical replicates per sample.

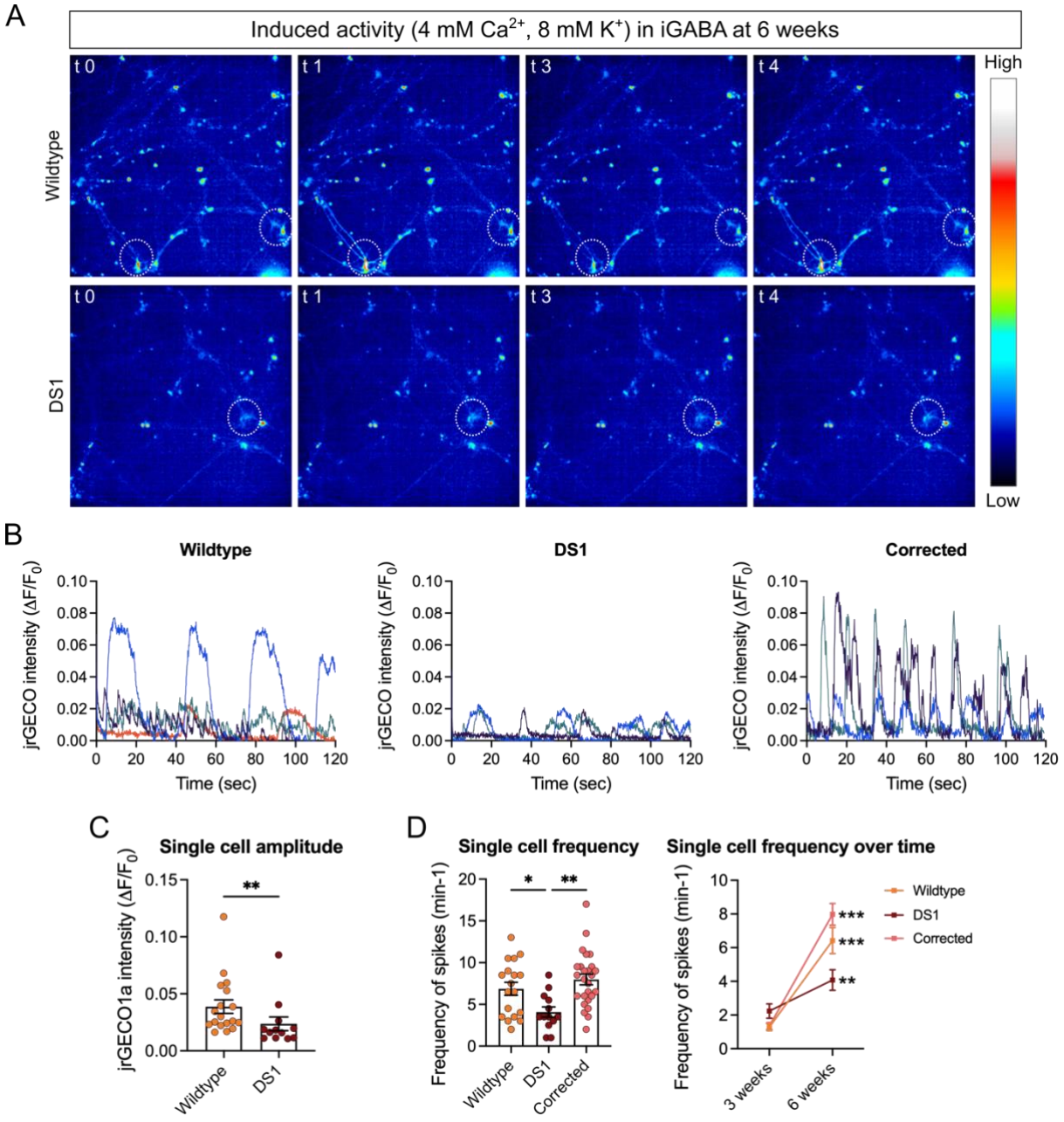

Figure 4.5. *Pathogenic SCN1A$^{IVS14+3A>T}$ causes reduced activity in late inhibitory interneurons (6 weeks).* **A –** Representative time-lapse images of the induced activity of 6 weeks iGABA expressing jrGECO1a monitored in calcium imaging buffer with an increased Ca^{2+} (4 mM) and K^+ concentration (8 mM). Scale bar = 100 µm. **B –** Representative calcium traces plotted as the jrGECO1a $\Delta F/F_0$ over time for wildtype, DS1 and corrected iGABA at 6 weeks. **C –** Quantification of single-cell calcium signal amplitude ($\Delta F/F_0$) recorded in iGABA at 6 weeks. N=3 biological replicates, n = 13-19 cells. Error bars represent the SEM, One-way ANOVA Kruskal-Wallis test + Dunn's multiple comparison, * = $p<0.05$, ** = $p<0.01$. **D –** Left, quantification of single-cell calcium signal frequency (spikes/min) recorded in iGABA at 6 weeks. N=3 biological replicates, n = 13-26 cells. Error bars represent the SEM, Ordinary One-way ANOVA + Tukey's multiple comparison, * = $p<0.05$, ** = $p<0.01$. Right, quantification of single-cell calcium signal frequency over time. N=3 biological replicates, n = 13-30 cells. Error bars represent the SEM, Unpaired nonparametric t test + Mann-Whitney test, ** = $p<0.01$, *** = $p<0.001$.

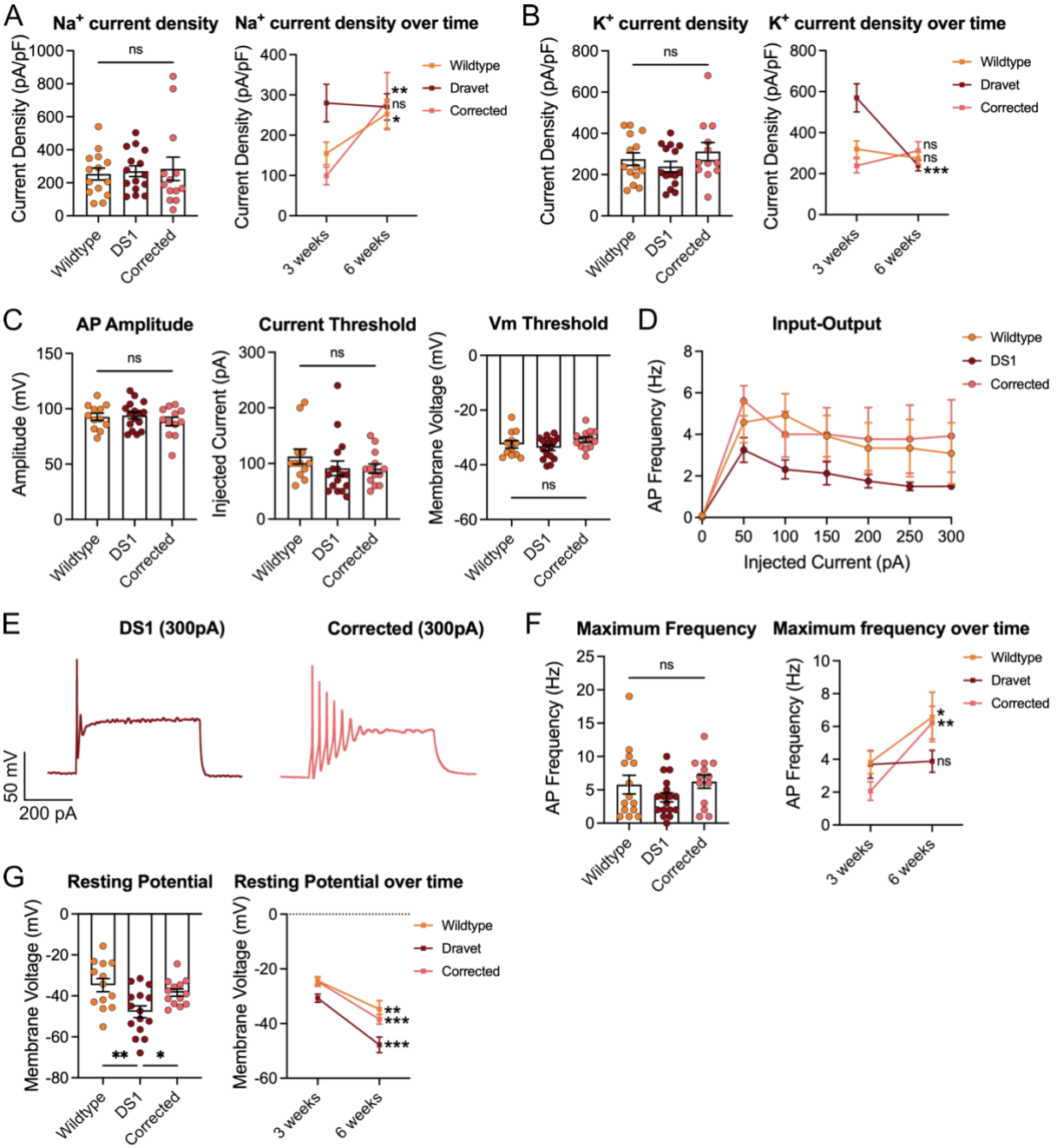

Figure 4.6. *Pathogenic SCN1A$^{IVS14+3A>T}$ might cause reduced intrinsic excitability in late inhibitory interneurons (6 weeks).* **A –** Left, quantification of Na^+ currents normalised to the capacitance (current density) in iGABA at 6 weeks. N=3 biological replicates, n = 13-15 cells. Error bars represent the SEM, One-way ANOVA Kruskal-Wallis test + Dunn's multiple comparison, ns = p>0.05. Right, quantification of iGABA Na^+ current density over time. N=3 biological replicates, n = 13-17 cells. Error bars represent the SEM, Unpaired parametric t test or Unpaired nonparametric t test + Mann-Whitney test, * = p<0.05, ** = p<0.01. **B –** Left, quantification of K^+ currents normalised to the capacitance (current density) in iGABA at 6 weeks. N=3 biological replicates, n = 13-15 cells. Error bars represent the SEM, Ordinary One-way ANOVA + Tukey's multiple comparison, ns = p>0.05. Right, quantification of iGABA K^+ current density over time. N=3 biological replicates, n = 13-17 cells. Error bars represent the SEM, Unpaired parametric t test, *** = p<0.001. **C –** Quantification of action potential

amplitude, current and membrane voltage (Vm) threshold recorded in iGABA at 6 weeks. N=3 biological replicates, n = 12/16 cells. Error bars represent the SEM, Ordinary One-way ANOVA + Tukey's multiple comparison or One-way ANOVA Kruskal-Wallis test + Dunn's multiple comparison, ns = $p>0.05$. **D –** AP frequency in relation to injected current recorded in iGABA at 6 weeks. n = 13-17 cells. Error bars represent the SEM. **E –** Representative traces of AP fired in response to 300pA of injected current from DS1 and corrected iGABA at 6 weeks. **F –** Left, quantification of the maximum evoked AP frequency recorded in iGABA at 6 weeks. N=3 biological replicates, n = 13-17 cells. Error bars represent the SEM, One-way ANOVA Kruskal-Wallis test + Dunn's multiple comparison, ns = $p>0.05$. Right, quantification of maximum AP frequency over time. N=3 biological replicates, n = 12-16 cells. Error bars represent the SEM, Unpaired nonparametric t test + Mann-Whitney test, * = $p<0.05$, ** = $p<0.01$. **G –** Left, quantification of the resting membrane potential recorded in iGABA at 6 weeks. N=3 biological replicates, n = 13-16 cells. Error bars represent the SEM, Ordinary One-way ANOVA + Tukey's multiple comparison, * = $p<0.05$, ** = $p<0.01$. Right, quantification of resting membrane potential over time. N=3 biological replicates, n = 13-16 cells. Error bars represent the SEM, Unpaired parametric t test, ** = $p<0.01$, *** = $p<0.001$.

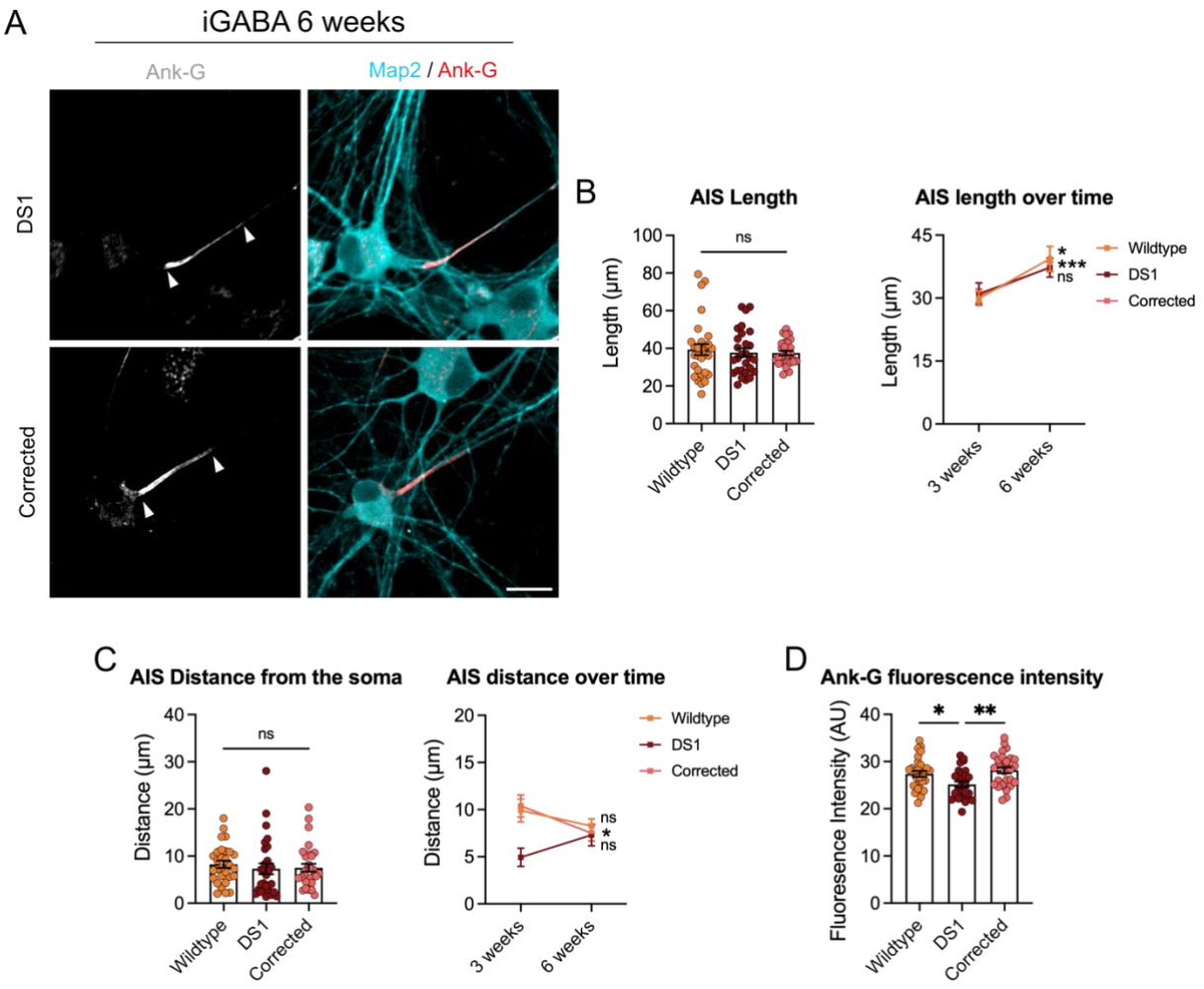

Figure 4.7. *Pathogenic SCN1A$^{IVS14+3A>T}$ causes impaired AIS development.* **A –** Representative immunofluorescence images of DS1 and corrected iGABA neurons at 6 weeks stained for Ank-G (grey on the left and red on the right) and Map2 (cyan). Scale bar = 20 µm. **B –** Left, quantification of AIS length based on Ank-G staining in iGABA at 6 weeks. N=3 biological replicates, n = 29-30 cells. Error bars represent the SEM, One-way ANOVA Kruskal-Wallis test + Dunn's multiple comparison, ns = $p>0.05$. Right, quantification of AIS length over time. N=3 biological replicates, n = 19-30 cells. Error bars represent the SEM, Unpaired parametric t test or Unpaired nonparametric t test + Mann-Whitney test, * = $p<0.05$, *** = $p<0.001$. **C –** Left, quantification of AIS distance from the soma based on Ank-G staining (AIS) relative to Map2 staining (soma) in iGABA at 6 weeks. N=3 biological replicates, n = 29-30 cells. Error bars represent the SEM, One-way ANOVA Kruskal-Wallis test + Dunn's multiple comparison, ns = $p>0.05$. Right, quantification of AIS distance over time. N=3 biological replicates, n = 19-30 cells. Error bars represent the SEM, Unpaired nonparametric t test + Mann-Whitney test, ns = $p>0.05$, * = $p<0.05$. **D –** Quantification of Ank-G fluorescence intensity in iGABA at 6 weeks. AU = arbitrary unit. N=3 biological replicates, n = 29-30 cells. Error bars represent the SEM, Ordinary One-way ANOVA + Tukey's multiple comparison, * = $p<0.05$, ** = $p<0.01$.

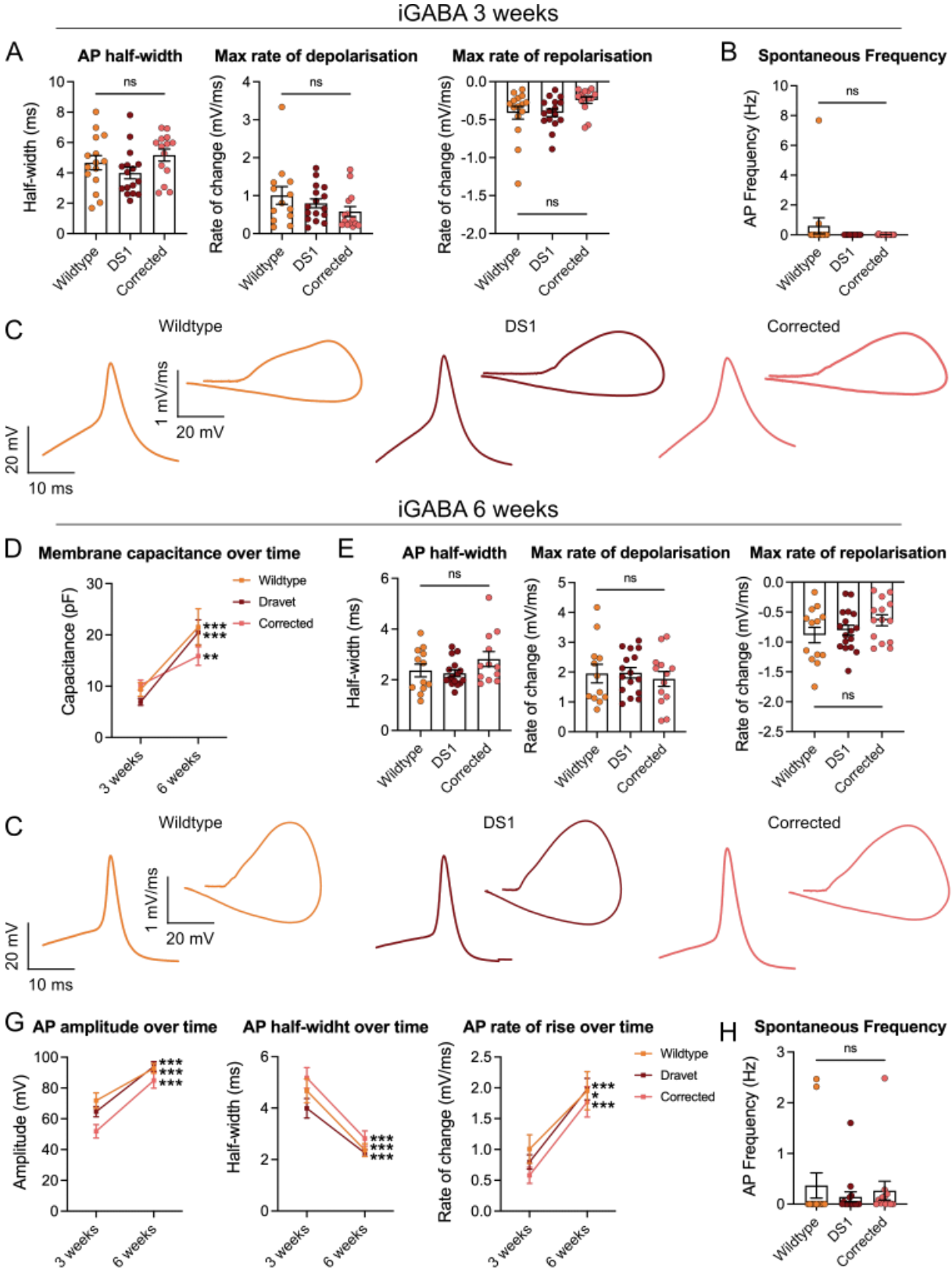
iGABA 3 weeks
A
AP half-width
Max rate of depolarisation
Max rate of repolarisation
B
Spontaneous Frequency
Half-width (ms)
Rate of change (mV/ms)
AP Frequency (Hz)
ns
Wildtype
DS1
Corrected
C
1 mV/ms
20 mV
10 ms
iGABA 6 weeks
D
Membrane capacitance over time
Capacitance (pF)
Dravet
3 weeks
6 weeks
E
G
AP amplitude over time
AP half-widht over time
AP rate of rise over time
Amplitude (mV)
H

Supplementary Figure 4.1. **A –** Quantification of action potential half-width, maximum rate of depolarisation and repolarisation recorded in iGABA at 3 weeks. N=3 biological replicates, n = 12-16 cells. Error bars represent the SEM, Ordinary One-way ANOVA + Tukey's multiple comparison, ns = $p>0.05$. **B –** Quantification of spontaneous action potential frequency recorded in iGABA at 3 weeks. N=3 biological replicates, n=16 cells. Error bars represent the SEM, One-way ANOVA Kruskal-Wallis test + Dunn's multiple comparison, ns = $p>0.05$. **C –** Average single AP traces and phase plots from wildtype, DS1 and corrected iGABA at 3 weeks. **D –** Quantification of the membrane capacitance recorded in iGABA over time. N=3 biological replicates, n=16-17 cells. Unpaired parametric t test, ** = $p<0.01$, *** = $p<0.001$. **E –** Quantification of action potential half-width, maximum rate of depolarisation and repolarisation recorded in iGABA at 6 weeks. N=3 biological replicates, n=12-15 cells. Error bars represent the SEM, Ordinary One-way ANOVA + Tukey's multiple comparison, ns = $p>0.05$. **F –** Average single AP traces and phase plots from wildtype, DS1 and corrected iGABA at 6 weeks. **G –** Quantification of action potential amplitude, half-width and rate of rise in iGABA over time. N=3 biological replicates, n=12-16 cells. Error bars represent the SEM, Unpaired parametric t test or Unpaired nonparametric t test + Mann-Whitney test, * = $p<0.05$, *** = $p<0.001$. **H –** Quantification of spontaneous action potential frequency recorded in iGABA at 6 weeks. N=3 biological replicates, n = 13-16 cells. Error bars represent the SEM, One-way ANOVA Kruskal-Wallis test + Dunn's multiple comparison, ns = $p>0.05$.

Experiment: iGABA Ca^{2+} imaging at 3 weeks. For all samples, N = cells from multiple coverslips.

Dataset analysed	Sample size	Normality	Statistical test	P Value (Significance)
Calcium signal Amplitude	Wildtype N = 30 DS1 N = 27 Corrected N = 33	WT = NO DS1 = NO Corr = NO	One-way ANOVA Kruskal-Wallis test + Dunn's multiple comparison	Wildtype vs. DS1 = 0.2159 (ns) Wildtype vs. Corrected = >0.9999 (ns) DS1 vs. Corrected = 0.3106 (ns)
Calcium signal Frequency	Wildtype N = 30 DS1 N = 27 Corrected N = 33	WT = NO DS1 = NO Corr = NO	One-way ANOVA Kruskal-Wallis test + Dunn's multiple comparison	Wildtype vs. DS1 = 0.0099 (**) Wildtype vs. Corrected = >0.9999 (ns) DS1 vs. Corrected = 0.0292 (*)

Table 4.1. Statistical details of iGABA Ca^{2+} imaging at 3 weeks.

Experiment: iGABA electrophysiological characterisation at 3 weeks. For all samples, N = cells from multiple coverslips.

Dataset analysed	Sample size	Normality	Statistical test	P Value (Significance)
Na^+ current density	Wildtype N = 15 DS1 N = 15 Corrected N = 17	WT = YES DS1 = YES Corr = YES	Ordinary One-way ANOVA + Tukey's multiple comparison	Wildtype vs. DS1 = 0.0330 (*) Wildtype vs. Corrected = 0.4654 (ns) DS1 vs. Corrected = 0.0010 (**)
K^+ current density	Wildtype N = 15 DS1 N = 15 Corrected N = 17	WT = YES DS1 = YES Corr = NO	One-way ANOVA Kruskal-Wallis test + Dunn's multiple comparison	Wildtype vs. DS1 = 0.0262 (*) Wildtype vs. Corrected = 0.4995 (ns) DS1 vs. Corrected = <0.001 (***)
AP Amplitude	Wildtype N = 12 DS1 N = 16 Corrected N = 14	WT = YES DS1 = YES Corr = YES	Ordinary One-way ANOVA + Tukey's multiple comparison	Wildtype vs. DS1 = 0.9395 (ns) Wildtype vs. Corrected = 0.0885 (ns) DS1 vs. Corrected = 0.1045 (ns)
AP Half-width	Wildtype N = 12 DS1 N = 16 Corrected N = 14	WT = YES DS1 = YES Corr = YES	Ordinary One-way ANOVA + Tukey's multiple comparison	Wildtype vs. DS1 = 0.4797 (ns) Wildtype vs. Corrected = 0.6811 (ns) DS1 vs. Corrected = 0.1254 (ns)
AP Rate of rise	Wildtype N = 12 DS1 N = 16 Corrected N = 14	WT = YES DS1 = YES Corr = YES	Ordinary One-way ANOVA + Tukey's multiple comparison	Wildtype vs. DS1 = 0.6334 (ns) Wildtype vs. Corrected = 0.1787 (ns) DS1 vs. Corrected = 0.5984 (ns)
Current threshold	Wildtype N = 12 DS1 N = 16 Corrected N = 14	WT = YES DS1 = YES Corr = YES	Ordinary One-way ANOVA + Tukey's multiple comparison	Wildtype vs. DS1 = 0.7879 (ns) Wildtype vs. Corrected = 0.6256 (ns) DS1 vs. Corrected = 0.9504 (ns)
Vm Threshold	Wildtype N = 12 DS1 N = 16 Corrected N = 14	WT = YES DS1 = YES Corr = YES	Ordinary One-way ANOVA + Tukey's multiple comparison	Wildtype vs. DS1 = 0.9007 (ns) Wildtype vs. Corrected = 0.7797 (ns) DS1 vs. Corrected = 0.5116 (ns)

Maximum Frequency	Wildtype N = 14 DS1 N = 20 Corrected N = 18	WT = YES DS1 = NO Corr = NO	One-way ANOVA Kruskal-Wallis test + Dunn's multiple comparison	Wildtype vs. DS1 = 0.3586 (ns) Wildtype vs. Corrected = 0.0755 (ns) DS1 vs. Corrected = >0.9999 (ns)
Spontaneous Frequency	Wildtype N = 16 DS1 N = 16 Corrected N = 16	WT = NO DS1 = NO Corr = NO	One-way ANOVA Kruskal-Wallis test + Dunn's multiple comparison	Wildtype vs. DS1 = 0.4651 (ns) Wildtype vs. Corrected = >0.9999 (ns) DS1 vs. Corrected = >0.9999 (ns)
Resting potential	Wildtype N = 16 DS1 N = 16 Corrected N = 16	WT = YES DS1 = YES Corr = YES	Ordinary One-way ANOVA + Tukey's multiple comparison	Wildtype vs. DS1 = 0.0154 (*) Wildtype vs. Corrected = 0.9908 (ns) DS1 vs. Corrected = 0.0215 (*)
Membrane capacitance (Cm)	WT N = 17 (9.359 ± 1.320 pF) DS1 N = 16 (6.942 ± 0.6807 pF) Corr N = 17 (10.24 ± 0.9572 pF)	WT = YES DS1 = YES Corr = YES	Ordinary One-way ANOVA + Tukey's multiple comparison	Wildtype vs. DS1 = 0.2365 (ns) Wildtype vs. Corrected = 0.8145 (ns) DS1 vs. Corrected = 0.0734 (ns)
Membrane resistance (Rm)	WT N = 17 (1931 ± 347.1 MΩ) DS1 N = 16 (1796 ± 420.3 MΩ) Corr N = 17 (1962 ± 292.3 MΩ)	WT = YES DS1 = NO Corr = YES	One-way ANOVA Kruskal-Wallis test + Dunn's multiple comparison	Wildtype vs. DS1 = >0.9999 (ns) Wildtype vs. Corrected = >0.9999 (ns) DS1 vs. Corrected = >0.9999 (ns)
Access resistance (Rs)	WT N = 17 (19.78 ± 1.744 MΩ) DS1 N = 16 (27.88 ± 4.517 MΩ) Corr N = 17 (31.08 ± 3.909 MΩ)	WT = NO DS1 = NO Corr = YES	One-way ANOVA Kruskal-Wallis test + Dunn's multiple comparison	Wildtype vs. DS1 = >0.9999 (ns) Wildtype vs. Corrected = 0.1049 (ns) DS1 vs. Corrected = 0.6619 (ns)

Table 4.2. Statistical details of iGABA electrophysiological characterisation at 3 weeks.

Experiment: iGABA AIS characterisation at 3 weeks. For all samples, N = cells from multiple wells.

Dataset analysed	Sample size	Normality	Statistical test	P Value (Significance)
AIS length	Wildtype N = 19 DS1 N = 18 Corrected N = 19	WT = YES DS1 = YES Corr = YES	Ordinary One-way ANOVA + Tukey's multiple comparison	Wildtype vs. DS1 = 0.9224 (ns) Wildtype vs. Corrected = 0.9726 (ns) DS1 vs. Corrected = 0.9857 (ns)
AIS distance	Wildtype N = 19 DS1 N = 18 Corrected N = 19	WT = NO DS1 = NO Corr = YES	One-way ANOVA Kruskal-Wallis test + Dunn's multiple comparison	Wildtype vs. DS1 = 0.0044 (**) Wildtype vs. Corrected = >0.9999 (ns) DS1 vs. Corrected = 0.0030 (**)
Ank-G intensity	Wildtype N = 19 DS1 N = 18 Corrected N = 19	WT = YES DS1 = YES Corr = YES	Ordinary One-way ANOVA + Tukey's multiple comparison	Wildtype vs. DS1 = 0.9891 (ns) Wildtype vs. Corrected = 0.9011 (ns) DS1 vs. Corrected = 0.8365 (ns)

Table 4.3. Statistical details of iGABA AIS characterisation at 3 weeks.

Experiment: iGABA Ca^{2+} imaging at 6 weeks and over time. For all samples, N = cells from multiple coverslips.

Dataset analysed	Sample size	Normality	Statistical test	P Value (Significance)
Calcium signal Amplitude	Wildtype N = 19 DS1 N = 13	WT = NO DS1 = NO	Unpaired nonparametric t test + Mann-Whitney test	Wildtype vs. DS1 = 0.0077 (**)
Calcium signal Frequency	Wildtype N = 18 DS1 N = 13 Corrected N = 26	WT = YES DS1 = YES Corr = YES	Ordinary One-way ANOVA + Tukey's multiple comparison	Wildtype vs. DS1 = 0.0416 (*) Wildtype vs. Corrected = 0.4657 (ns) DS1 vs. Corrected = 0.0013 (**)
Calcium signal Frequency over time – Wildtype	3 weeks N = 30 6 weeks N = 19	3 weeks = NO 6 weeks = YES	Unpaired nonparametric t test + Mann-Whitney test	3 weeks vs. 6 weeks = <0.001 (***)
Calcium signal Frequency over time – DS1	3 weeks N = 27 6 weeks N = 13	3 weeks = NO 6 weeks = YES	Unpaired nonparametric t test + Mann-Whitney test	3 weeks vs. 6 weeks = 0.0051 (**)
Calcium signal Frequency over time – Corrected	3 weeks N = 33 6 weeks N = 26	3 weeks = NO 6 weeks = YES	Unpaired nonparametric t test + Mann-Whitney test	3 weeks vs. 6 weeks = <0.001 (***)

Table 4.5. Statistical details of iGABA Ca^{2+} imaging at 6 weeks and over time.

Experiment: iGABA electrophysiological characterisation at 6 weeks. For all samples, N = cells from multiple coverslips.

Dataset analysed	Sample size	Normality	Statistical test	P Value (Significance)
Na^+ current density	Wildtype N = 14 DS1 N = 15 Corrected N = 13	WT = YES DS1 = YES Corr = NO	One-way ANOVA Kruskal-Wallis test + Dunn's multiple comparison	Wildtype vs. DS1 = >0.9999 (ns) Wildtype vs. Corrected = >0.9999 (ns) DS1 vs. Corrected = >0.9999 (ns)
K^+ current density	Wildtype N = 14 DS1 N = 15 Corrected N = 13	WT = YES DS1 = YES Corr = YES	Ordinary One-way ANOVA + Tukey's multiple comparison	Wildtype vs. DS1 = 0.6723 (ns) Wildtype vs. Corrected = 0.6723 (ns) DS1 vs. Corrected = 0.3450 (ns)
AP Amplitude	Wildtype N = 12 DS1 N = 16 Corrected N = 12	WT = YES DS1 = YES Corr = YES	Ordinary One-way ANOVA + Tukey's multiple comparison	Wildtype vs. DS1 = 0.7935 (ns) Wildtype vs. Corrected = 0.6435 (ns) DS1 vs. Corrected = 0.5785 (ns)
AP Half-width	Wildtype N = 12 DS1 N = 16 Corrected N = 12	WT = YES DS1 = YES Corr = YES	Ordinary One-way ANOVA + Tukey's multiple comparison	Wildtype vs. DS1 = 0.9223 (ns) Wildtype vs. Corrected = 0.3650 (ns) DS1 vs. Corrected = 0.1673 (ns)
AP Rate of rise	Wildtype N = 12 DS1 N = 16 Corrected N = 12	WT = YES DS1 = YES Corr = YES	Ordinary One-way ANOVA + Tukey's multiple comparison	Wildtype vs. DS1 = 0.9964 (ns) Wildtype vs. Corrected = 0.8668 (ns) DS1 vs. Corrected = 0.8045 (ns)
Current threshold	Wildtype N = 12 DS1 N = 16 Corrected N = 12	WT = NO DS1 = NO Corr = YES	One-way ANOVA Kruskal-Wallis test + Dunn's multiple comparison	Wildtype vs. DS1 = 0.1657 (ns) Wildtype vs. Corrected = 0.6649 (ns) DS1 vs. Corrected = >0.9999 (ns)
Vm Threshold	Wildtype N = 12 DS1 N = 16 Corrected N = 12	WT = YES DS1 = YES Corr = YES	Ordinary One-way ANOVA + Tukey's multiple comparison	Wildtype vs. DS1 = 0.7012 (ns) Wildtype vs. Corrected = 0.1280 (ns) DS1 vs. Corrected = 0.1420 (ns)
Maximum Frequency	Wildtype N = 14 DS1 N = 17 Corrected N = 13	WT = NO DS1 = YES Corr = YES	One-way ANOVA Kruskal-Wallis test + Dunn's multiple comparison	Wildtype vs. DS1 = >0.9999 (ns) Wildtype vs. Corrected = >0.9999 (ns) DS1 vs. Corrected = 0.3593 (ns)
Spontaneous Frequency	Wildtype N = 13 DS1 N = 16 Corrected N = 13	WT = NO DS1 = NO Corr = NO	One-way ANOVA Kruskal-Wallis test + Dunn's multiple comparison	Wildtype vs. DS1 = >0.9999 (ns) Wildtype vs. Corrected = 0.0767 (ns) DS1 vs. Corrected = 0.2520 (ns)
Resting potential	Wildtype N = 13 DS1 N = 16 Corrected N = 13	WT = YES DS1 = YES Corr = YES	Ordinary One-way ANOVA + Tukey's multiple comparison	Wildtype vs. DS1 = 0.0042 (**) Wildtype vs. Corrected = 0.6227 (ns) DS1 vs. Corrected = 0.0478 (*)
Membrane capacitance (Cm)	WT N = 17 (21.50 ± 3.590 pF) DS1 N = 16 (20.49 ± 2.426 pF) Corr N = 17 (15.85 ± 1.820 pF)	WT = NO DS1 = YES Corr = YES	One-way ANOVA Kruskal-Wallis test + Dunn's multiple comparison	Wildtype vs. DS1 = 0.9937 (ns) Wildtype vs. Corrected = 0.4295 (ns) DS1 vs. Corrected = 0.3541 (ns)

Membrane resistance (Rm)	WT N = 15 (638.1 ± 87.26 MΩ) DS1 N = 15 (694.0 ± 149.4 MΩ) Corr N = 13 (725.8 ± 202.6 MΩ)	WT = YES DS1 = NO Corr = NO	One-way ANOVA Kruskal-Wallis test + Dunn's multiple comparison	Wildtype vs. DS1 = >0.9999 (ns) Wildtype vs. Corrected = >0.9999 (ns) DS1 vs. Corrected = >0.9999 (ns)
Access resistance (Rs)	WT N = 17 (13.93 ± 2.005 MΩ) DS1 N = 16 (14.91 ± 1.914 MΩ) Corr N = 17 (12.60 ± 1.429 MΩ)	WT = NO DS1 = NO Corr = NO	One-way ANOVA Kruskal-Wallis test + Dunn's multiple comparison	Wildtype vs. DS1 = >0.9999 (ns) Wildtype vs. Corrected = >0.9999 (ns) DS1 vs. Corrected = >0.9999 (ns)

Table 4.6a. Statistical details of iGABA electrophysiological characterisation at 6 weeks.

Experiment: iGABA electrophysiological parameters over time. For all samples, N = cells from multiple coverslips.

Dataset analysed	**Sample size**	**Normality**	**Statistical test**	**P Value (Significance)**
Na^+ current density over time – Wildtype	3 weeks N = 15 6 weeks N = 14	3 weeks = YES 6 weeks = YES	Unpaired parametric t test	3 weeks vs. 6 weeks = 0.0390 (*)
Na^+ current density over time – DS1	3 weeks N = 15 6 weeks N = 15	3 weeks = YES 6 weeks = YES	Unpaired parametric t test	3 weeks vs. 6 weeks = 0.8701 (ns)
Na^+ current density over time – Corrected	3 weeks N = 17 6 weeks N = 13	3 weeks = NO 6 weeks = NO	Unpaired nonparametric t test + Mann-Whitney test	3 weeks vs. 6 weeks = 0.0052 (**)
K^+ current density over time – Wildtype	3 weeks N = 16 6 weeks N = 14	3 weeks = YES 6 weeks = YES	Unpaired parametric t test	3 weeks vs. 6 weeks = 0.3997 (ns)
K^+ current density over time – DS1	3 weeks N = 16 6 weeks N = 15	3 weeks = YES 6 weeks = YES	Unpaired parametric t test	3 weeks vs. 6 weeks = <0.001 (***)
K^+ current density over time – Corrected	3 weeks N = 16 6 weeks N = 13	3 weeks = YES 6 weeks = YES	Unpaired parametric t test	3 weeks vs. 6 weeks = 0.3997 (ns)
AP amplitude over time – Wildtype	3 weeks N = 15 6 weeks N = 12	3 weeks = YES 6 weeks = NO	Unpaired nonparametric t test + Mann-Whitney test	3 weeks vs. 6 weeks = 0.0342 (*)
AP amplitude over time – DS1	3 weeks N = 16 6 weeks N = 16	3 weeks = YES 6 weeks = YES	Unpaired parametric t test	3 weeks vs. 6 weeks = <0.001 (***)
AP amplitude over time – Corrected	3 weeks N = 14 6 weeks N = 13	3 weeks = YES 6 weeks = YES	Unpaired parametric t test	3 weeks vs. 6 weeks = <0.001 (***)
AP half-width over time – Wildtype	3 weeks N = 15 6 weeks N = 12	3 weeks = YES 6 weeks = YES	Unpaired parametric t test	3 weeks vs. 6 weeks = <0.001 (***)
AP half-width over time – DS1	3 weeks N = 16 6 weeks N = 16	3 weeks = YES 6 weeks = YES	Unpaired parametric t test	3 weeks vs. 6 weeks = <0.001 (***)
AP half-width over time – Corrected	3 weeks N = 14 6 weeks N = 13	3 weeks = YES 6 weeks = NO	Unpaired nonparametric t test + Mann-Whitney test	3 weeks vs. 6 weeks = <0.001 (***)

AP rate of rise over time – Wildtype	3 weeks N = 15 6 weeks N = 12	3 weeks = NO 6 weeks = YES	Unpaired nonparametric t test + Mann-Whitney test	3 weeks vs. 6 weeks = 0.0188 (*)
AP rate of rise over time – DS1	3 weeks N = 16 6 weeks N = 16	3 weeks = YES 6 weeks = YES	Unpaired parametric t test	3 weeks vs. 6 weeks = <0.01 (****)
AP rate of rise over time – Corrected	3 weeks N = 14 6 weeks N = 13	3 weeks = NO 6 weeks = YES	Unpaired nonparametric t test + Mann-Whitney test	3 weeks vs. 6 weeks = <0.001 (***)
Maximum frequency over time – Wildtype	3 weeks N = 16 6 weeks N = 12	3 weeks = NO 6 weeks = YES	Unpaired nonparametric t test + Mann-Whitney test	3 weeks vs. 6 weeks = 0.0458 (*)
Maximum frequency over time – DS1	3 weeks N = 16 6 weeks N = 16	3 weeks = NO 6 weeks = NO	Unpaired nonparametric t test + Mann-Whitney test	3 weeks vs. 6 weeks = 0. 4170 (ns)
Maximum frequency over time – Corrected	3 weeks N = 16 6 weeks N = 13	3 weeks = NO 6 weeks = YES	Unpaired nonparametric t test + Mann-Whitney test	3 weeks vs. 6 weeks = 0.0017 (**)
Resting potential over time – Wildtype	3 weeks N = 16 6 weeks N = 13	3 weeks = YES 6 weeks = YES	Unpaired parametric t test	3 weeks vs. 6 weeks = 0.0078 (**)
Resting potential over time – DS1	3 weeks N = 16 6 weeks N = 15	3 weeks = YES 6 weeks = YES	Unpaired parametric t test	3 weeks vs. 6 weeks = <0.001 (***)
Resting potential over time – Corrected	3 weeks N = 16 6 weeks N = 13	3 weeks = YES 6 weeks = YES	Unpaired parametric t test	3 weeks vs. 6 weeks = <0.001 (***)

Table 4.6b. Statistical details of iGABA electrophysiological parameters overtime.

Experiment: iGABA AIS characterisation at 6 weeks and over time. For all samples, N = cells from multiple wells.

Dataset analysed	Sample size	Normality	Statistical test	P Value (Significance)
AIS length	Wildtype N = 29 DS1 N = 29 Corrected N = 30	WT = NO DS1 = YES Corr = YES	One-way ANOVA Kruskal-Wallis test + Dunn's multiple comparison	Wildtype vs. DS1 = >0.9999 (ns) Wildtype vs. Corrected = >0.9999 (ns) DS1 vs. Corrected = >0.9999 (ns)
AIS length over time – Wildtype	3 weeks N = 19 6 weeks N = 29	3 weeks = YES 6 weeks = NO	Unpaired nonparametric t test + Mann-Whitney test	3 weeks vs. 6 weeks = 0.0258 (*)
AIS length over time – DS1	3 weeks N = 19 6 weeks N = 29	3 weeks = YES 6 weeks = YES	Unpaired parametric t test	3 weeks vs. 6 weeks = 0.0650 (ns)
AIS length over time – Corrected	3 weeks N = 19 6 weeks N = 30	3 weeks = YES 6 weeks = YES	Unpaired parametric t test	3 weeks vs. 6 weeks = <0.001 (***)
AIS distance	Wildtype N = 29 DS1 N = 29 Corrected N = 30	WT = YES DS1 = NO Corr = NO	One-way ANOVA Kruskal-Wallis test + Dunn's multiple comparison	Wildtype vs. DS1 = 0.3097 (ns) Wildtype vs. Corrected = >0.9999 (ns) DS1 vs. Corrected = >0.9999 (ns)
AIS Distance over time – Wildtype	3 weeks N = 19 6 weeks N = 29	3 weeks = NO 6 weeks = YES	Unpaired nonparametric t test + Mann-Whitney test	3 weeks vs. 6 weeks = 0.2426 (ns)
AIS Distance over time – DS1	3 weeks N = 19 6 weeks N = 29	3 weeks = NO 6 weeks = NO	Unpaired nonparametric t test + Mann-Whitney test	3 weeks vs. 6 weeks = 0.1469 (ns)
AIS Distance over time – Corrected	3 weeks N = 19 6 weeks N = 30	3 weeks = YES 6 weeks = NO	Unpaired nonparametric t test + Mann-Whitney test	3 weeks vs. 6 weeks = 0.0358 (*)
Ank-G intensity	Wildtype N = 29 DS1 N = 29 Corrected N = 30	WT = YES DS1 = YES Corr = YES	Ordinary One-way ANOVA + Tukey's multiple comparison	Wildtype vs. DS1 = 0.0352 (*) Wildtype vs. Corrected = 0.6522 (ns) DS1 vs. Corrected = 0.0029 (**)

Table 4.7. Statistical details of iGABA AIS characterisation at 6 weeks.

4.3 Conclusions

- Pathogenic *SCN1A*$^{IVS14+3A>T}$ causes **hyperexcitability** in inhibitory interneurons at 3 weeks.
    - Early DS1 iGABA neurons exhibit increased calcium spike frequency when activity is induced by elevated Ca^{2+} and K^{+} concentrations.
    - Early DS1 iGABA neurons display increased Na^{+} and K^{+} current densities compared to wildtype and corrected iGABA lines.
    - Consistent with neuronal hyperexcitability, the axon initial segment (AIS) of early DS1 iGABA neurons is closer to the cell soma compared with wildtype and corrected iGABA lines.
    - Hyperexcitability of early DS1 iGABA is not mediated by transcriptional upregulation of any of the ion channels or AIS genes investigated.
- Pathogenic *SCN1A*$^{IVS14+3A>T}$ causes **hypoexcitability** in inhibitory interneurons at 6 weeks.
    - Late DS1 iGABA neurons exhibit lower calcium spike amplitude and frequency when activity is induced by elevated Ca^{2+} and K^{+} concentrations.
    - Late DS1 iGABA neurons display decreased current-induced repetitive firing and lower action potential maximum frequency compared to wildtype and corrected iGABA lines.
    - Consistent with neuronal hypoexcitability, late DS1 iGABA neurons display lower availability of Ank-G at the AIS, which might contribute towards reduced neuronal excitability by reducing the density of NaV channels at the AIS.

Chapter 5

Pathogenic SCN1A$^{IVS14+3A>T}$ causes hyperactivity of excitatory neurons

5.1 Introduction

In the previous chapter we described the effect of the Dravet-related *SCN1A*$^{IVS14+3A>T}$ mutation on patient-derived inhibitory interneurons. Interestingly, we found that early interneurons exhibited a hyperexcitable phenotype, while late interneurons displayed reduced neuronal excitability consistent with the literature. While interneuron disfunction is regarded as the leading neurophysiological cause of Dravet syndrome (DS), reduced inhibitory activity in animal models was shown to be transient and limited only to the severe stage of the disease (Favero et al., 2018; Tran et al., 2020b), suggesting that the pathological mechanism of DS may be more complex. Recent studies are starting to challenge the 'interneuron hypothesis' and growing interest is arising concerning the role played by excitatory neurons in the pathophysiology of DS. So far however, both *in vivo* and *in vitro* studies have produced inconsistent results. In some mouse models, increased Na^+ currents (Mistry et al., 2014) and hyperexcitability during the pre-epileptic stage (Almog et al., 2021) were observed in pyramidal hippocampal neurons. Conversely, the interneuron-specific deletion of *SCN1A* was found to produce a more severe epileptic phenotype compared to deletion in both excitatory and inhibitory neurons, suggesting that loss of *SCN1A* in pyramidal cells might be partially protective (Ogiwara et al., 2013). Furthermore, studies in hiPSC-derived Dravet models (including *SCN1A*$^{IVS14+3A>T}$ mutation) have also reported increased Na^+ current densities and generalised **hyperexcitability** in pyramidal neurons (Jiao et al., 2013b; Y. Liu, Lopez-Santiago, et al., 2013). One recent study in particular, has shown that cultures of *SCN1A*-deficient excitatory neurons are sufficient to recapitulate mutation-specific phenotypes (van Hugte et al., 2023). However, other studies have observed **normal** activity of Dravet patients hiPSC-derived pyramidal neurons (Y. Sun et al., 2016). To assess the presence of a Dravet-related phenotype in our neuronal model, in this chapter, we investigate pyramidal neuron-specific phenotypes in iGlut monocultures. Specifically, we investigated structural and electrophysiological properties

of early (3 weeks) and late (6 weeks) iGlut excitatory neurons derived from wildtype, DS1 and corrected hiPSC lines.

5.2 Results

5.2.1 Pathogenic *SCN1A*$^{IVS14+3A>T}$ does not affect the activity of early excitatory neurons (3 weeks)

iGlut neurons expressing the genetically encoded calcium indicator GCaMP6f were derived from hiPSCs as previously described and matured on mAstro for 3 weeks before experiments were performed. Calcium imaging experiments were conducted as previously described for iGABA, using a calcium imaging buffer containing higher concentrations of Ca^{2+} and K^{+} designed to stimulate neuronal activity (Z. Sun & Südhof, 2021b). To this end, iGlut at 3 weeks were first equilibrated in Modified Tyrode Solution (2 mM Ca^{2+}, 5 mM K^{+}), then incubated in Ca^{2+} imaging buffer (4 mM Ca^{2+}, 8 mM K^{+}) for the recordings – full buffer compositions in *Chapter 2, Table 2.12*. Time-lapse recordings were carried out over 120 sec at a frame rate of 10-20 frames/sec and the fluorescence intensity profile was analysed for the active cells within the field of view (Fig. 5.1-A). The GCaMP6f signal intensity for each neuron was normalised by calculating the ratio ($\Delta F/F_0$) of the increase in fluorescence (ΔF) to the baseline (F_0) and plotted over time (Fig. 5.1-B). The analysis of single-neuron Ca^{2+} dynamics revealed that both the amplitude and frequency of Ca^{2+} events were comparable across all neuronal populations (Fig. 5.1-C – Table 5.1). Contrarily to inhibitory interneurons, excitatory neurons in culture exhibit network activity characterised by synchronous neuronal firing. At 3 weeks, synchronous activity was found to be relatively sparse, with comparable frequency across conditions (Fig. 5.1-D – Table 5.1). Overall, calcium imaging data seemed to indicate that the *SCN1A*$^{IVS14+3A>T}$ Dravet-related mutation has no effect on the activity of early excitatory neurons.

5.2.2 Pathogenic *SCN1A*$^{IVS14+3A>T}$ does not affect the intrinsic properties of early excitatory neurons (3 weeks)

Voltage clamp recordings performed on iGlut neurons at 3 weeks revealed that early DS1 iGlut neurons have normal Na^{+} and K^{+} current densities (Fig. 5.2-A – Table 5.2), comparable to wildtype and corrected neurons. Current densities were derived as previously described for iGABA. Briefly, putative currents were measured as the minimum fast inward current (Na^{+} currents) and average steady state outward current (K^{+} currents). Current values were then normalised to the membrane capacitance to extrapolate an estimate of the amount of current flowing through the cell membrane per unit area (current density). Measurements of membrane capacitance (Cm), as well as other passive properties like membrane resistance (Rm) and access

resistance (Rs) were comparable across populations (Table 5.2). Current clamp recordings revealed no differences across conditions in AP amplitude, half-width, maximum rate of depolarisation and repolarisation, as well as in the current and voltage membrane (Vm) thresholds required to elicit an AP (Fig. 5.2-B and C and Supplementary Fig. 5.1-A – Table 5.2). The observed AP profiles were characterised by relatively low amplitude and large width, indicating that at 3 weeks, iGlut neurons still have immature electrophysiological properties (Supplementary Fig. 5.1-C). No differences were observed in the AP firing frequency in response to increasing amounts of injected currents (input-output curve) nor in the maximum firing frequency (Fig. 5.2-D and E – Table 5.2) and spontaneous firing frequency (Supplementary Fig. 5.1-B – Table 5.2). Finally, the resting membrane potential was also found to be comparable across all conditions (Fig. 5.2-F – Table 5.2). Overall, consistently with Ca^{+} imaging data, early DS1 iGlut neurons seemed to display normal intrinsic properties.

5.2.3 Pathogenic SCN1A$^{IVS14+3A>T}$ does not affect the AIS of early excitatory neurons (3 weeks)

Unlike inhibitory interneurons, where NaV1.1 channels localise at the AIS, in pyramidal neurons, these channels were shown to be expressed on the soma (Ogiwara et al., 2013; Tian et al., 2014; W. Wang et al., 2011). Nonetheless, properties of the AIS have direct influence on neuronal excitability and, vice versa, alterations in neuronal activity can trigger AIS-mediated plasticity mechanism (Gründemann & Häusser, 2010). For these reasons, structural properties of the AIS were investigated, based on Ank-G staining, in 3-week-old iGlut neurons cultured on mAstro (Fig. 5.3-A). The AIS length and distance from the soma were found to be comparable across all iGlut populations (Fig. 5.3-B and C – Table 5.3). Similarly, no differences were observed in average Ank-G fluorescence intensity across conditions (Fig. 5.3-D – Table 5.3).

This data indicates that the *SCN1A*$^{IVS14+3A>T}$ Dravet-related mutation has no effect on the structural properties of the AIS in early excitatory neurons.

5.2.4 Pathogenic SCN1A$^{IVS14+3A>T}$ causes induced hyperactivity in late excitatory neurons (6 weeks)

We next characterised iGlut neurons at a later time point (6 weeks). Calcium imaging recordings were carried out as previously described. Thus, iGlut neurons at 6 weeks were imaged while

incubating in Ca^{2+} imaging buffer (4 mM Ca^{2+}, 8 mM K^{+}) to induce neuronal activity (Fig. 5.5-A). The GCaMP6f $\Delta F/F_0$ was calculated and plotted over time (Fig.5.4-B) for wildtype, DS1 and corrected iGlut. As previously mentioned for iGABA at 6 weeks, due to the protracted unavailability of the microscope used for the acquisition of wildtype and DS1 samples, corrected iGlut were imaged using a different imaging system. For this reason, the Ca^{2+} signal amplitude detected for corrected iGlut neurons could not be compared with the one detected for wildtype and DS1 iGlut lines. However, since Ca^{2+} signal frequency is not dependent on the light source, this parameter could be compared across all conditions.

Similarly to what was observed for late DS1 iGABA neurons, DS1 iGlut neurons at 6 weeks also displayed a much lower single-cell Ca^{2+} signal amplitude (0.47 ± 0.03 $\Delta F/F_0$) compared to wildtype neurons ($1.11 \pm 0.09 \Delta F/F_0$). Consistent with neuronal maturation, Ca^{2+} signal amplitude increased over time in both populations, however, it increased substantially less in DS1 iGlut neurons (Fig. 5.4-C – Table 5.4). On the other hand, single-cell Ca^{2+} signal frequency was found to be significantly higher in DS1 iGlut neurons (7.30 ± 0.34 spikes/min), compared to wildtype (2.33 ± 0.22 spikes/min), and corrected lines (1.59 ± 0.10 spikes/min). Over time, there is a significant increase in Ca^{2+} signal frequency in all iGlut populations, consistent with neuronal maturation, however, the increase observed in DS1 neurons is substantially higher compared to wildtype and corrected neurons (Fig. 5.4-D – Table 5.4). At 6 weeks, synchronous "network-like" activity was consistently observed in all iGlut neuronal cultures. Synchronous Ca^{2+} signal amplitude was also observed to be reduced in DS1 iGlut cultures (0.51 ± 0.09 $\Delta F/F_0$), compared to wildtype cultures (1.13 ± 0.18 $\Delta F/F_0$). Over time, synchronous Ca^{2+} signal amplitude was found to be significantly increased in wildtype but not in DS1 cultures (Fig. 5.4-E – Table 5.4). Alongside single-cell frequency, synchronous Ca^{2+} signal frequency was also found to be significantly higher in DS1 cultures (6.75 ± 1.33 spikes/min), compared to wildtype (2.35 ± 0.55 spikes/min) and corrected cultures (1.59 ± 0.23 spikes/min). Consistent with neuronal maturation, a significant increase in synchronous Ca^{2+} signal frequency over time was observed in all neuronal lines, however, the increase observed in DS1 iGlut neurons was substantially higher compared to wildtype and corrected cultures (Fig. 5.4-F – Table 5.4).

Both at single cell and network level, late DS1 cultures display lower Ca^{2+} signal amplitude but substantially increased Ca^{2+} signal frequency. Ca^{2+} signals are a direct representation of calcium transients mediated by CaV, therefore, a lower Ca^{2+} signal amplitude suggests lower Ca^{2+} influx into the cell. Such a phenotype could result from alterations in the expression or conductance

of CaV and further investigation should be performed to assess if CaV play a role in mediating this phenotype.

5.2.5 Pathogenic SCN1A$^{IVS14+3A>T}$ causes spontaneous hyperactivity in late excitatory neurons (6 weeks)

For the analysis of spontaneous neuronal activity, iGlut were cultured on mAstro and imaged at 6 weeks while incubating in Modified Tyrode Solution containing physiological concentrations of Ca^{2+} (2 mM) and K^+ (5 mM) (Fig. 5.5-A). The GCaMP6f $\Delta F/F_0$ was calculated and plotted over time (Fig.5.5-B) for wildtype, DS1 and corrected iGlut.

The analysis of spontaneous calcium dynamics revealed that single-cell Ca^{2+} signal amplitude was once again reduced in late DS1 iGlut neurons (0.80 ± 0.04 $\Delta F/F_0$) compared to wildtype (1.45 ± 0.14 $\Delta F/F_0$). As discussed in the previous section, due to the protracted unavailability of the microscope, the Ca^{2+} signal amplitude detected for corrected iGlut could not be compared with wildtype and DS1 iGlut. Similarly to stimulated cultures, spontaneous single-cell Ca^{2+} signal frequency was also found substantially increased in DS1 iGlut neurons (6.20 ± 0.25 spikes/min) compared to wildtype (4.13 ± 0.11 spikes/min) and corrected neurons (2.53 ± 0.16 spikes/min) (Fig. 5.5-C – Table 5.5). Spontaneous synchronous activity was also consistently observed in all excitatory neuronal cultures at 6 weeks. Synchronous Ca^{2+} signal amplitude was reduced in DS1 iGlut cultures (0.83 ± 0.05 $\Delta F/F_0$) compared to wildtype (1.40 ± 0.22 $\Delta F/F_0$). Synchronous frequency instead was found to be significantly higher in DS1 cultures (7.00 ± 0.82 spikes/min) compared to wildtype (4.12 ± 0.29 spikes/min) and corrected cultures (2.62 ± 0.43 spikes/min) (Fig. 5.5-D – Table 5.5).

Overall, the profile of spontaneous activity observed in physiological conditions closely resembled the profile observed when neuronal activity was induced by high K^+/Ca^{2+} buffer. In both conditions, DS1 iGlut neurons displayed a reduced Ca^{2+} signal amplitude and a greatly increased Ca^{2+} signal frequency compared to wildtype and corrected neurons. Interestingly, when we compared the Ca^{2+} signal frequency observed in spontaneous and induced conditions, we found that in wildtype and corrected cultures, both single-cell and synchronous frequency were significantly reduced when neuronal activity was induced. DS1 cultures, on the other hand, displayed a similar, or even increased frequency in induced compared to spontaneous conditions (Fig. 5.5-E and F – Table 5.5). To induce neuronal activity, the concentrations of extracellular Ca^{2+} and K^+ were increased. Increasing extracellular Ca^{2+} concentrations has been

widely reported to acutely decrease neuronal intrinsic excitability (B. L. Jones & Smith, 2016; Lu et al., 2010; Martiszus et al., 2021; Penn et al., 2016; Yue et al., 2008), however, how this mechanism is exerted is not fully understood. Ca^{2+}-mediated inactivation of the Na^{+}-leak channel NALCN (Lu et al., 2010) and the depolarising shift in voltage-dependence of NaV channels (Martiszus et al., 2021) have both been proposed as possible mechanisms. The observation that the excitability of DS1 iGlut neurons is unaffected, or even enhanced, by higher extracellular Ca^{2+} concentrations could imply a role for NaV1.1 in mediating this mechanism.

5.2.6 Pathogenic SCN1A$^{IVS14+3A>T}$ might cause intrinsic hyperexcitability in late excitatory neurons (6 weeks)

For the analysis of late excitatory neurons, iGlut were derived and matured on mAstro for 6 weeks before whole-cell patch clamp recordings were performed. Voltage clamp recordings showed that, similarly to the 3 weeks time point, Na^{+} and K^{+} current densities at 6 weeks were comparable across all conditions (Fig. 5.6-A – Table 5.6a). Similarly, measurements of membrane capacitance (Cm), as well as other passive properties like membrane resistance (Rm) and access resistance (Rs) were also comparable across conditions (Table 5.5a). Current clamp recordings revealed no differences in AP amplitude, half-width, maximum rate of depolarisation and repolarisation, as well as in the current and voltage threshold required to elicit an AP (Fig. 5.6-B and Supplementary Fig. 5.1-D and E – Table 5.6a). The AP profiles observed at 6 weeks, characterised by higher amplitude and smaller width compared to the earlier time point, were indicative of neurons at a more mature stage (Supplementary Fig. 5.1-G). Indeed, over time, an increase in AP amplitude and rate of rise, together with a decrease in AP half-width were observed in all populations, consistent with neuronal maturation (Supplementary Fig. 5.1-H – Table 5.6b). When analysing the relationship between injected current and AP firing frequency (input-output curve), DS1 iGlut neurons displayed a trend towards higher AP frequency in response to injected currents, with the greatest difference observed at 300pA (Fig. 5.6-D). At this later time point, all iGlut populations displayed a more mature firing capacity, mainly characterised by repetitive firing (Fig. 5.6-D). Similarly, DS1 iGlut neurons displayed a trend to a higher maximum frequency (12.19 ± 1.32 Hz) compared to wildtype (8.77 ± 0.97 Hz) and corrected lines (8.68 ± 1.73 Hz), however, this difference was not statistically significant (Fig. 5.6-E – Table 5.6a). Over time, the AP maximum frequency was increased in all neuronal populations, however, the increase was significantly observed only in DS1 neurons. (Fig. 5.6-E – Table 5.6b). Finally, no differences were observed in the

resting membrane potential and spontaneous AP frequency (Supplementary Fig. 5.1-F and I – Table 5.6a).

Contrarily to a previous study conducted on this disease line (Y. Liu, Lopez-Santiago, et al., 2013), we did not observe a substantial increase in Na^+ currents or intrinsic excitability of DS1 excitatory neurons. However, it is important to note that the currents measured in this study were not isolated from families of inward and outward currents and therefore, their measurement is not entirely accurate. Furthermore, the trends towards an increased current-induced repetitive firing and higher AP maximum frequency observed in DS1 iGlut, although not significant, are consistent with the higher Ca^{2+} signal frequency observed by calcium imaging in late DS1 iGlut neurons (Fig. 5.4 and 5.5) and, together, could indicate an increase in excitability of DS1 pyramidal neurons.

5.2.7 Pathogenic SCN1A$^{IVS14+3A>T}$ causes decreased AIS length in late excitatory neurons (6 weeks)

Structural properties of the AIS were investigated, based on Ank-G staining, in 6-week-old iGlut neurons cultured on mAstro (Fig. 5.7-A). Surprisingly, the AIS was found to be significantly shorter in DS1 iGlut neurons (36.63 ± 2.35 μm) compared to wildtype (48.87 ± 2.81 μm) and corrected lines (52.28 ± 2.02 μm). Consistent with maturation, the AIS length increased over time in wildtype and corrected iGlut neurons, but it did not increase in the DS1 line (Fig. 5.7-B – Table 5.7). At 6 weeks the AIS was found to be equally distant from the soma in all neuronal populations (Fig. 5.7-C – Table 5.7). Overtime, the AIS was observed to significantly shift its position only in wildtype iGlut, where the AIS moved proximally to the soma (Fig. 5.7-C – Table 5.7). Finally, the average fluorescence intensity of Ank-G at 6 weeks was found to be comparable across all lines (Fig. 5.7-D – Table 5.7). As for the AIS characterisation in iGABA, the change in Ank-G fluorescence intensity over time could not be calculated due to the replacement of the confocal light source between the 3 and 6 weeks time points.

A shorter AIS has been consistently associated, both theoretically and empirically, with reduced intrinsic excitability (Chand et al., 2015; Evans et al., 2015; Gulledge & Bravo, 2016; Jamann et al., 2021a; Telenczuk et al., 2017). Contrarily, late DS1 excitatory neurons showed signs of increased excitability. Interestingly, structural AIS studies in animal models of epilepsy have also reported shortening of the AIS of pyramidal neurons associated with increased neuronal

excitability (T. T. Liu et al., 2017; Y. Wang et al., 2016). The authors speculate that AIS length reduction is caused by irreversible calpain-mediated proteolysis of Ank-G and βIV spectrin (another structural component of the AIS). Calpain is a calcium-dependant cysteine protease that is activated in the context of neuronal injury (Schafer et al., 2009), such as, as hypothesised by the authors, seizure-induced hypoxia. However, in these studies, the concomitant AIS shortening and increased neuronal excitability are either not addressed or attributed to a proximal shift of the AIS towards the soma. Such a shift is not observed in our neuronal model. Furthermore, our *in vitro* cultures could not have experienced seizure-induced hypoxia. Therefore, we speculate that, despite the fact that shortening the AIS should reduce excitability, this is not sufficient to counterbalance the primary cause of increased neuronal excitability.

5.2.8 Hyperexcitability in late DS1 excitatory neurons might be caused by transcriptional upregulation of sodium and calcium channels (6 weeks)

Overall, late DS1 excitatory neurons showed consistent signs of hyperexcitability. The fact that increased excitability (gain-of-function) can arise from a loss-of-function mutation within a sodium channel, raises interesting mechanistic questions. We speculated that such phenotype could be mediated by a compensational mechanism implemented by DS1 excitatory neurons in response to the loss of function of NaV1.1. Specifically, this might include overexpression of a different NaV channel. To test this hypothesis, the expression levels of all the different types of NaV channels were compared in late wildtype, DS1 and corrected iGlut (Fig. 5.8-A). Since the β subunits of NaV channels can modulate the voltage-gate and kinetics of the channel pore (Bouza & Isom, 2018), their expression was also analysed. Interestingly, the expression of multiple sodium channels, including NaV1.2 (*SCN2A*), NaV1.3 (*SCN3A*), NaV1.6 (*SCN8A*) and NaV1.7 (*SCN9A*) appeared to be increased in DS1 iGlut neurons, however the difference did not reach statistical significance (Supplementary Fig. 5.2-A – Table 5.8). A similar trend towards upregulation has been previously observed for NaV1.2 and NaV1.8 in animal models of DS (Mistry et al., 2014). Interestingly, the expression of NaV1.1 (*SCN1A*) was also observed to be increased in the DS1 line (Supplementary Fig. 5.2-A – Table 5.8), suggesting that DS1 iGlut neurons might be upregulating *SCN1A* transcription in an attempt to compensate for the reduced NaV1.1 protein levels (Y. Liu, Lopez-Santiago, et al., 2013). The expression of the sodium channel β subunit *SCN2B* also appeared to be increased, although not significantly, in DS1 iGlut neurons (Supplementary Fig. 5.2-B – Table 5.8). The expression levels of CaV and Kv channels were also analysed (Fig. 5.8-B). Similarly, a trend towards upregulation was

observed for the calcium channels CaV1.1 (*CACNA1S*) and CaV2.2 (*CACNA1B*) in DS1 iGlut neurons (Supplementary Fig. 5.2-C – Table 5.8). Contrarily, the expression of calcium channel CaV3.1 (*CACNA1G*) was observed to be significantly reduced in both DS1 and corrected iGlut. Interestingly, this gene has been previously identified as a genetic modifier of epilepsy in a mouse model of DS (Calhoun et al., 2017). The presence of a *CACNA1G* modifier mutation in the DS1 line could explain why the expression of this gene is altered in both DS1 and corrected neurons. Sequencing of the *CACNA1G* gene in the DS1 line will be necessary to confirm this hypothesis. Finally, the expression of some AIS resident proteins was also investigated but no differences were observed in the expression levels of these genes across populations (Fig. 5.8-C).

Overall, the differential expression profile of late DS1 iGlut revealed a trend of increased expression of multiple sodium and calcium channels. While this characterisation doesn't paint a clear mechanistic picture to justify hyperexcitability of pyramidal neurons in the DS1 line, it suggests that an array of different genes may be involved in regulating this phenotype.

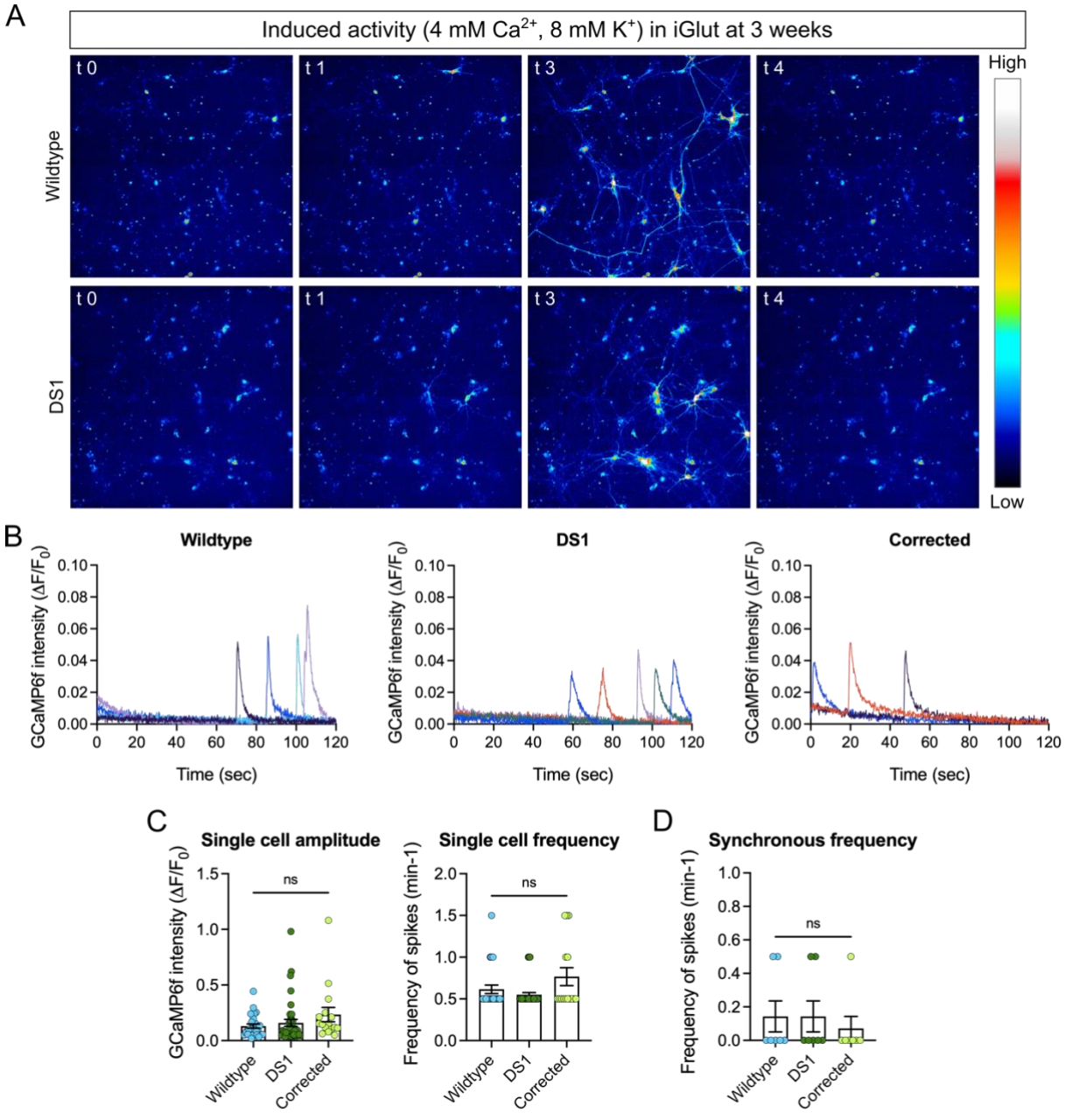

Figure 5.1. *Pathogenic SCN1A$^{IVS14+3A>T}$ does not affect the activity of early excitatory neurons (3 weeks).* **A –** Representative time-lapse images of the induced activity of 3 weeks iGlut expressing GCaMP6f monitored in calcium imaging buffer with an increased Ca^{2+} (4 mM) and K^+ concentration (8 mM). Scale bar = 100 µm. **B –** Representative calcium traces plotted as the GCaMP6f $\Delta F/F_0$ over time for wildtype, DS1 and corrected iGlut at 3 weeks. **C –** Quantification of the single cell calcium signal amplitude and frequency recorded in iGlut at 3 weeks. N=3 biological replicates, n = 16-39 cells. Error bars represent the SEM, One-way ANOVA Kruskal-Wallis test + Dunn's multiple comparison, ns = $p>0.05$. **D –** Quantification of the synchronous calcium signal frequency recorded in iGlut at 3 weeks. N=3 biological replicates, n = 7 time-lapse recordings. Error bars represent the SEM, One-way ANOVA Kruskal-Wallis test + Dunn's multiple comparison, ns = $p>0.05$.

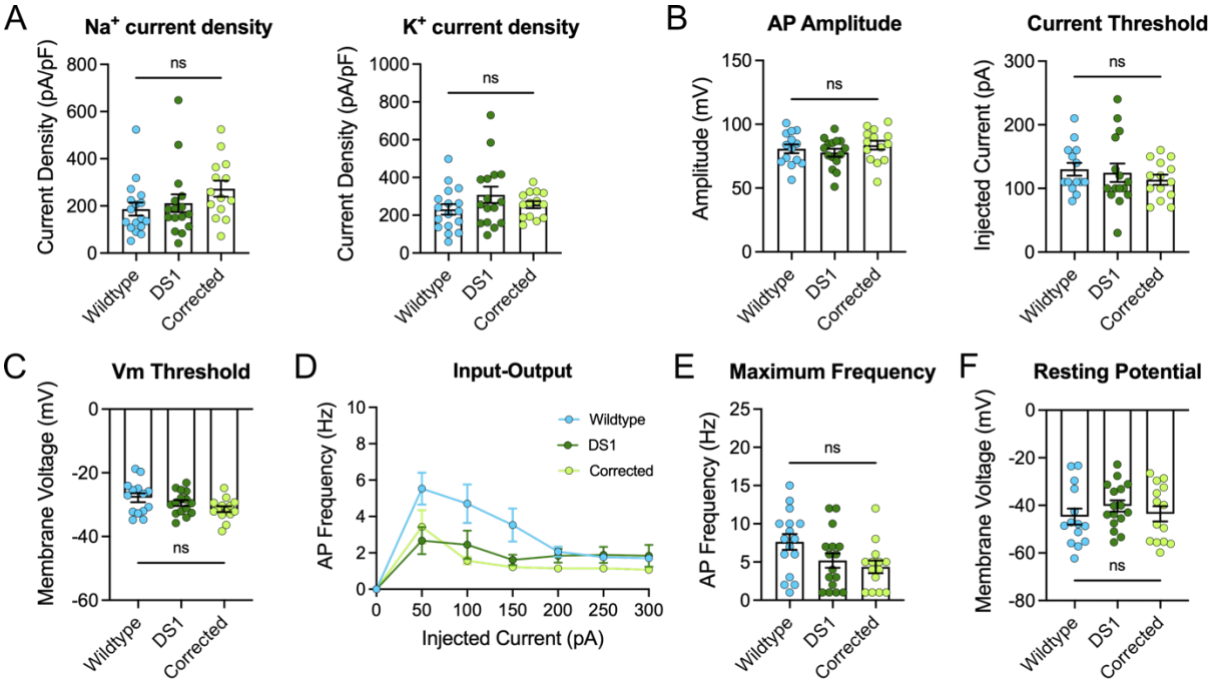

Figure 5.2. *Pathogenic SCN1A$^{IVS14+3A>T}$ does not affect the intrinsic properties of early excitatory neurons (3 weeks).* **A –** Quantification of Na^+ and K^+ currents normalised to the capacitance (current densities) in iGlut at 3 weeks. N=3 biological replicates, n = 14-17 cells. Error bars represent the SEM, One-way ANOVA Kruskal-Wallis test + Dunn's multiple comparison, ns = p>0.05. **B –** Quantification of action potential amplitude and current threshold in iGlut at 3 weeks. N=3 biological replicates, n = 14-15 cells. Error bars represent the SEM, Ordinary One-way ANOVA + Tukey's multiple comparison, ns = p>0.05. **C –** Quantification of action potential voltage (Vm) threshold recorded in iGlut at 3 weeks. N=3 biological replicates, n = 14-15 cells. Error bars represent the SEM, Ordinary One-way ANOVA + Tukey's multiple comparison, ns = p>0.05. **D –** AP frequency in relation to injected current recorded in iGlut at 3 weeks. N=3 biological replicates, n = 14-16 cells. Error bars represent the SEM. **E –** Quantification of the maximum evoked AP frequency recorded in iGlut at 3 weeks. N=3 biological replicates, n = 14-16 cells. Error bars represent the SEM, Ordinary One-way ANOVA + Tukey's multiple comparison, ns = p>0.05. **F –** Quantification of the resting membrane potential recorded in iGlut at 3 weeks. N=3 biological replicates, n = 14-16 cells. Error bars represent the SEM, Ordinary One-way ANOVA + Tukey's multiple comparison, ns = p>0.05.

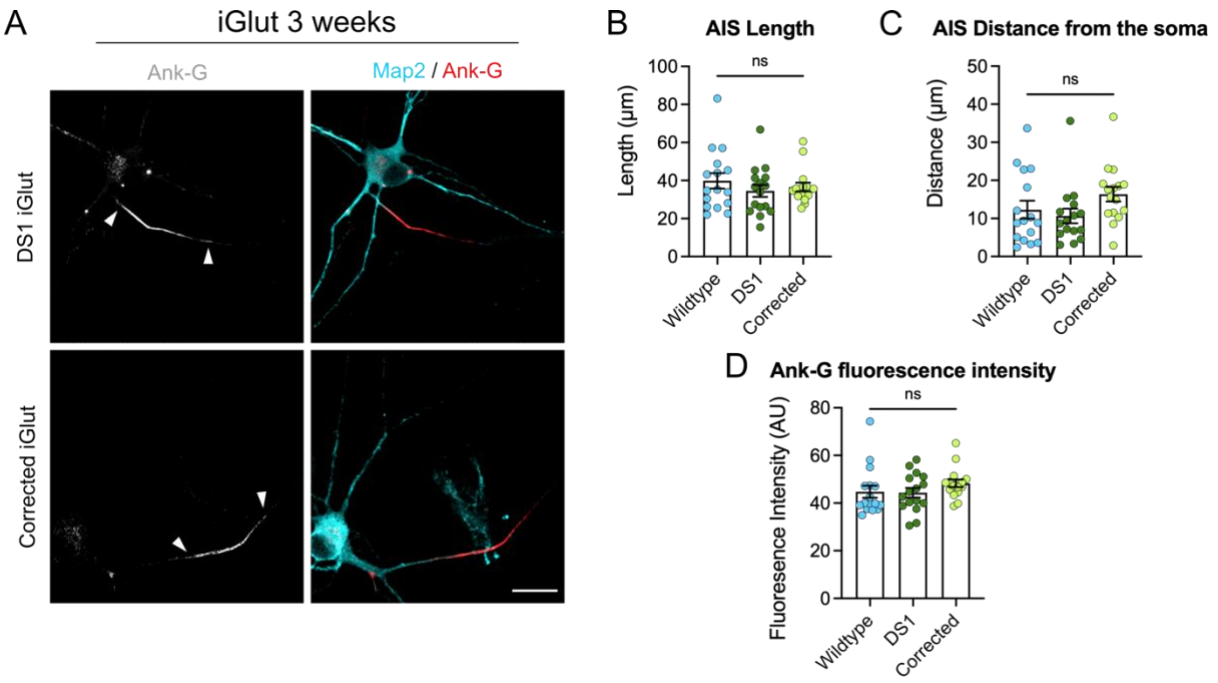

Figure 5.3. *Pathogenic SCN1A$^{IVS14+3A>T}$ does not affect the AIS of early excitatory neurons (3 weeks).* **A –** Representative immunofluorescence images of DS1 and corrected iGlut neurons at 3 weeks stained for Ank-G (grey on the left and red on the right) and Map2 (cyan). Scale bar = 20 µm. **B –** Quantification of AIS length based on Ank-G staining in iGlut at 3 weeks. N=3 biological replicates, n = 16 cells. Error bars represent the SEM, One-way ANOVA Kruskal-Wallis test + Dunn's multiple comparison, ns = p>0.05. **C –** Quantification of AIS distance from the soma based on Ank-G staining (AIS) relative to Map2 staining (soma) in iGlut at 3 weeks. N=3 biological replicates, n = 16 cells. Error bars represent the SEM, One-way ANOVA Kruskal-Wallis test + Dunn's multiple comparison, ns = p>0.05. **D –** Quantification of Ank-G fluorescence intensity in iGlut at 3 weeks. AU = arbitrary unit. N=3 biological replicates, n = 16 cells. Error bars represent the SEM, One-way ANOVA Kruskal-Wallis test + Dunn's multiple comparison, ns = p>0.05.

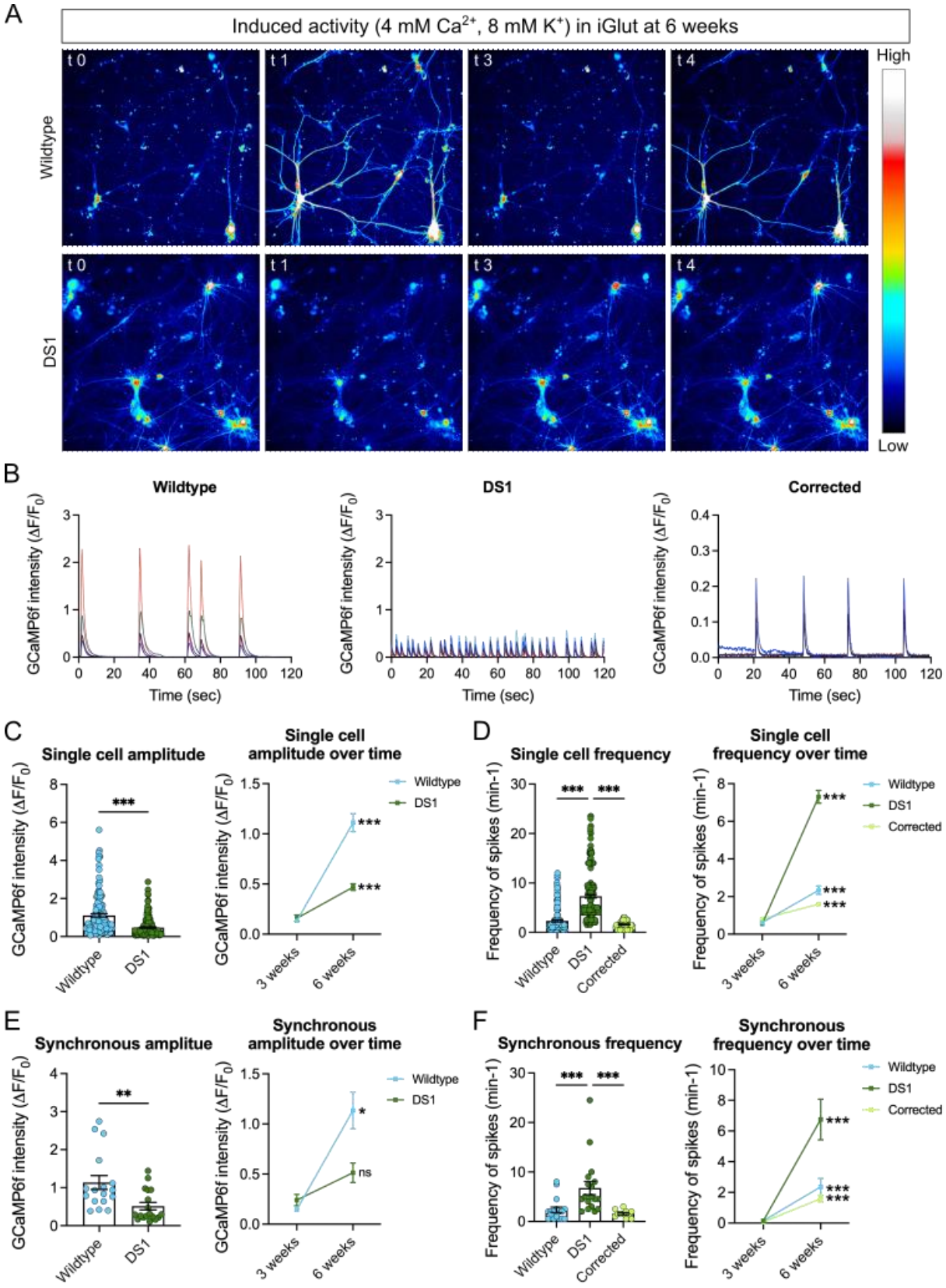

Figure 5.4. *Pathogenic SCN1A$^{IVS14+3A>T}$ causes induced hyperactivity in late excitatory neurons (6 weeks).* **A –** Representative time-lapse images of the induced activity of 6 weeks iGlut expressing GCaMP6f monitored in calcium imaging buffer with an increased Ca^{2+} (4

mM) and K^+ concentration (8 mM). Scale bar = 100 μm. **B –** Representative calcium traces plotted as the GCaMP6f $\Delta F/F_0$ over time for wildtype, DS1 and corrected iGlut at 6 weeks. **C –** Left, quantification of the single cell calcium signal amplitude recorded in iGlut at 6 weeks. N=3 biological replicates, n = 138-216 cells. Error bars represent the SEM, Unpaired nonparametric t test + Mann-Whitney test, *** = $p<0.001$. Right, quantification of single cell calcium signal amplitude over time. N=3 biological replicates, n = 28-216 cells. Error bars represent the SEM, Unpaired nonparametric t test + Mann-Whitney test, *** = $p<0.001$. **D –** Left, quantification of the single cell calcium signal frequency recorded in iGlut at 6 weeks. N=3 biological replicates, n = 48-216 cells. Error bars represent the SEM, One-way ANOVA Kruskal-Wallis test + Dunn's multiple comparison, *** = $p<0.001$. Right, quantification of single cell calcium signal frequency over time. N=3 biological replicates, n = 28-216 cells. Error bars represent the SEM, Unpaired nonparametric t test + Mann-Whitney test, *** = $p<0.001$. **E –** Left, quantification of synchronous calcium signal amplitude recorded in iGlut at 6 weeks. N=3 biological replicates, n = 17-18 time-lapse recordings. Error bars represent the SEM, Unpaired nonparametric t test + Mann-Whitney test, ** = $p<0.01$. Right, quantification of synchronous calcium signal amplitude over time. N=3 biological replicates, n = 2-18 time-lapse recordings. Error bars represent the SEM, Unpaired nonparametric t test + Mann-Whitney test, ns = $p>0.05$, * = $p<0.05$. **F –** Left, quantification of the synchronous calcium signal frequency recorded in iGlut at 6 weeks. N=3 biological replicates, n = 11-18 time-lapse recordings. Error bars represent the SEM, One-way ANOVA Kruskal-Wallis test + Dunn's multiple comparison, *** = $p<0.001$. Right, quantification of synchronous calcium signal frequency over time. N=3 biological replicates, n = 7-18 time-lapse recordings. Error bars represent the SEM, Unpaired nonparametric t test + Mann-Whitney test, *** = $p<0.001$.

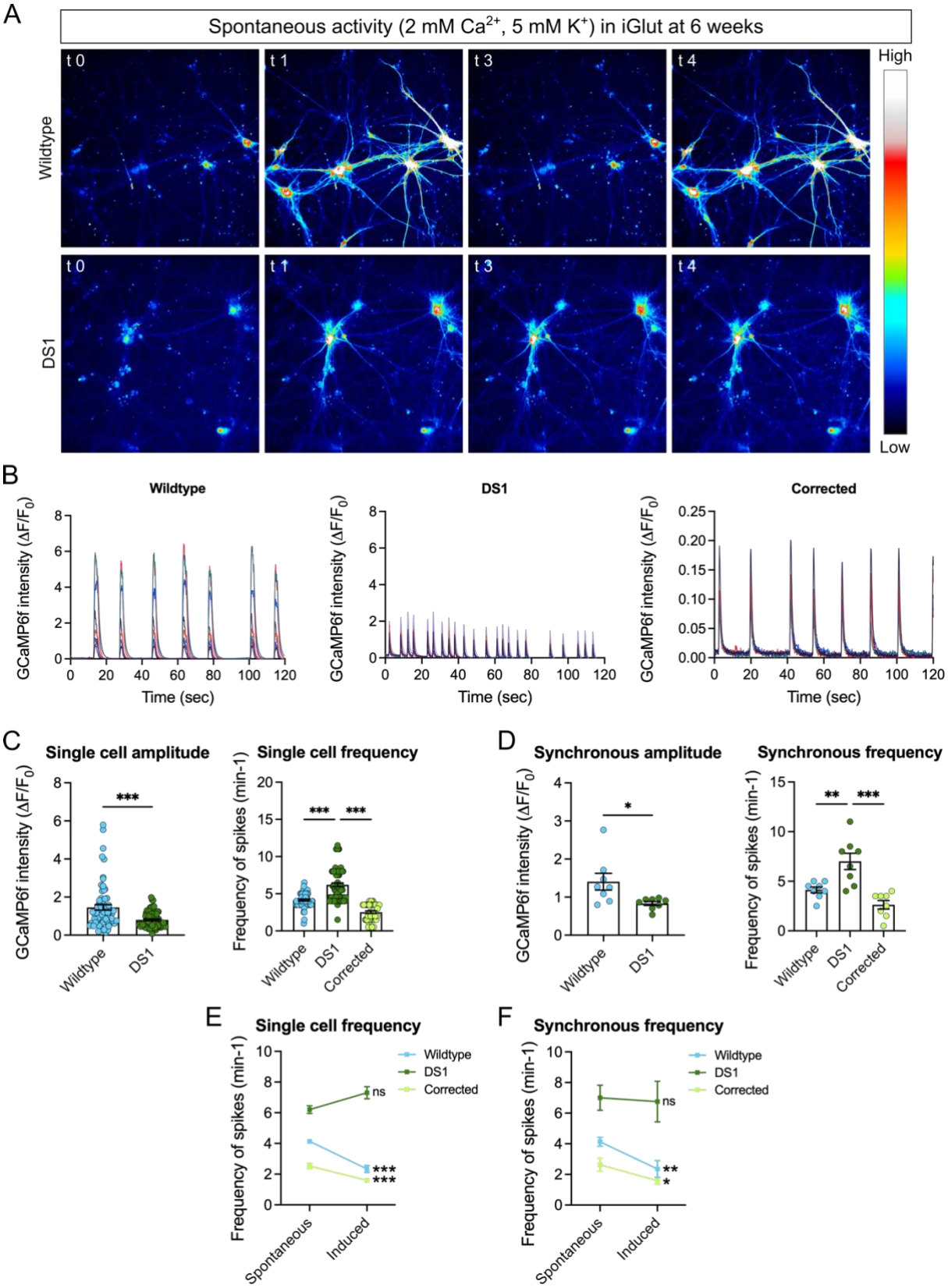

Figure 5.5. *Pathogenic SCN1A$^{IVS14+3A>T}$ causes spontaneous hyperactivity in late excitatory neurons (6 weeks).* **A –** Representative time-lapse images of the spontaneous activity of 6 weeks iGlut expressing GCaMP6f monitored in calcium imaging buffer with physiological Ca^{2+} (2

mM) and K^+ concentration (5 mM). Scale bar = 100 µm. **B –** Representative spontaneous calcium traces plotted as the GCaMP6f $\Delta F/F_0$ over time for wildtype, DS1 and corrected iGlut at 6 weeks. **C –** Left, quantification of the spontaneous single cell calcium signal amplitude recorded in iGlut at 6 weeks. N=3 biological replicates, n = 67-75 cells. Error bars represent the SEM, Unpaired nonparametric t test + Mann-Whitney test, *** = $p<0.001$. Right, quantification of spontaneous single cell calcium signal frequency recorded in iGlut at 6 weeks. N=3 biological replicates, n = 49-75 cells. Error bars represent the SEM, One-way ANOVA Kruskal-Wallis test + Dunn's multiple comparison, *** = $p<0.001$. **D –** Left, quantification of spontaneous synchronous calcium signal amplitude recorded in iGlut at 6 weeks. N=3 biological replicates, n = 8 time-lapse recordings. Error bars represent the SEM, Unpaired parametric t test, * = $p<0.05$. Right, quantification of the spontaneous synchronous calcium signal frequency recorded in iGlut at 6 weeks. N=3 biological replicates, n = 8 time-lapse recordings. Error bars represent the SEM, Ordinary One-way ANOVA + Tukey's multiple comparison, ** = $p<0.01$, *** = $p<0.001$. **E –** Quantification of the single cell calcium signal frequency recorded in iGlut at 6 weeks in spontaneous vs. induced conditions. N=3 biological replicates, n = 48-216 cells. Error bars represent the SEM, Unpaired nonparametric t test + Mann-Whitney test, ns = $p>0.05$, *** = $p<0.001$. **F –** Quantification of the synchronous calcium signal frequency recorded in iGlut at 6 weeks in spontaneous vs. induced conditions. N=3 biological replicates, n = 48-216 cells. Error bars represent the SEM, Unpaired nonparametric t test + Mann-Whitney test, ns = $p>0.05$, * = $p<0.05$, ** = $p<0.01$.

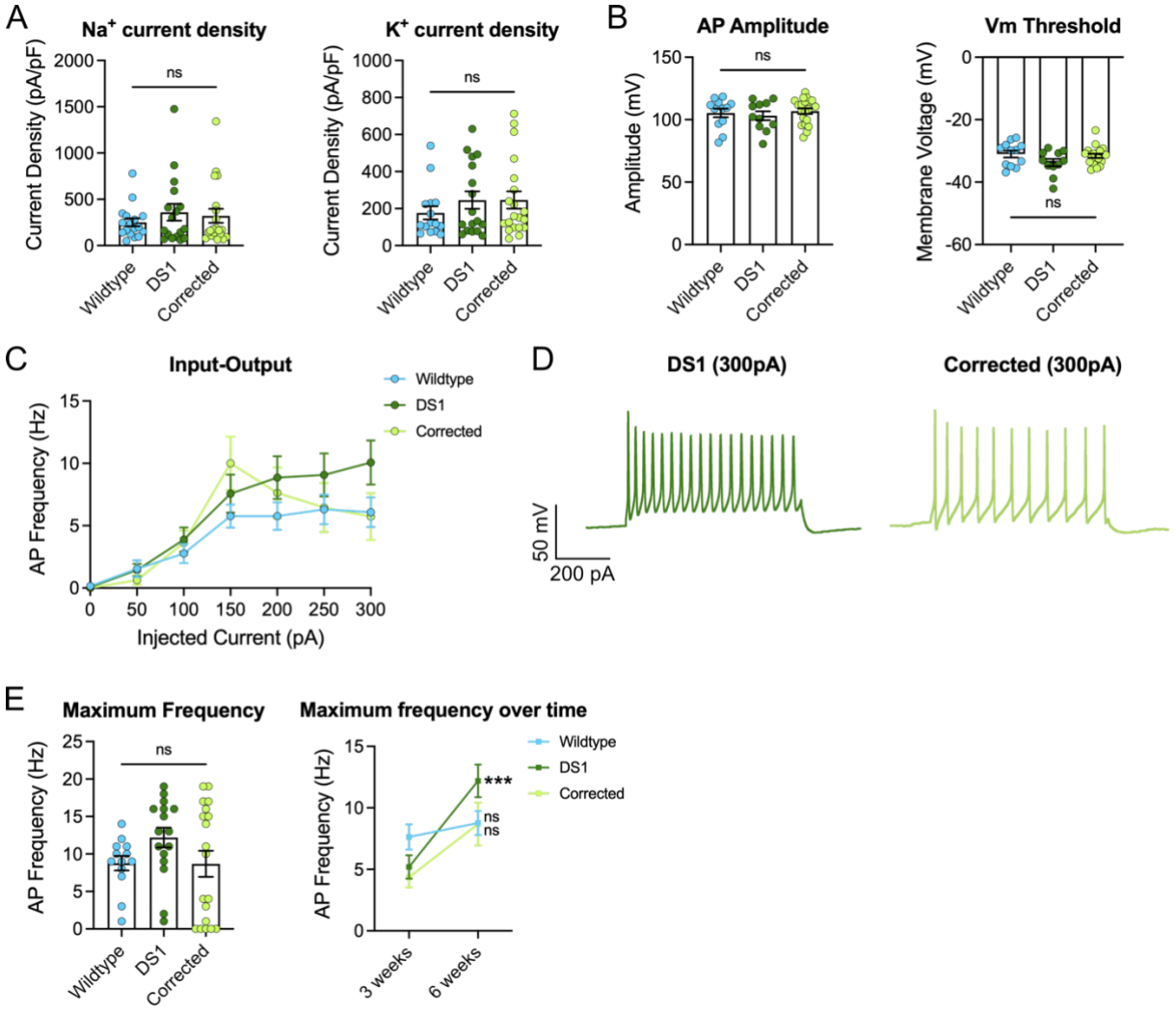

Figure 5.6. *Pathogenic SCN1A$^{IVS14+3A>T}$ might cause intrinsic hyperexcitability in late excitatory neurons (6 weeks).* **A –** Quantification of Na^+ and K^+ currents normalised to the capacitance (current densities) in iGlut at 6 weeks. N=3 biological replicates, n = 17-20 cells. Error bars represent the SEM, One-way ANOVA Kruskal-Wallis test + Dunn's multiple comparison, ns = p>0.05. **B –** Quantification of action potential amplitude and membrane voltage (Vm) threshold in iGlut at 6 weeks. N=3 biological replicates, n = 11-20 cells. Error bars represent the SEM, Ordinary One-way ANOVA + Tukey's multiple comparison, ns = p>0.05. **C –** AP frequency in relation to injected current recorded in iGlut at 6 weeks. N=3 biological replicates, n = 13-19 cells. Error bars represent the SEM. **D –** Representative traces of AP fired in response to 300pA of injected current from DS1 and corrected iGlut at 6 weeks. **E –** Left, quantification of the maximum evoked AP frequency recorded in iGlut at 6 weeks. N=3 biological replicates, n = 13-19 cells. Error bars represent the SEM, One-way ANOVA Kruskal-Wallis test + Dunn's multiple comparison, ns = p>0.05. Right, quantification of maximum AP frequency over time. N=3 biological replicates, n = 13-19 cells. Error bars represent the SEM, Unpaired parametric t test, ns = p>0.05, *** = p<0.001.

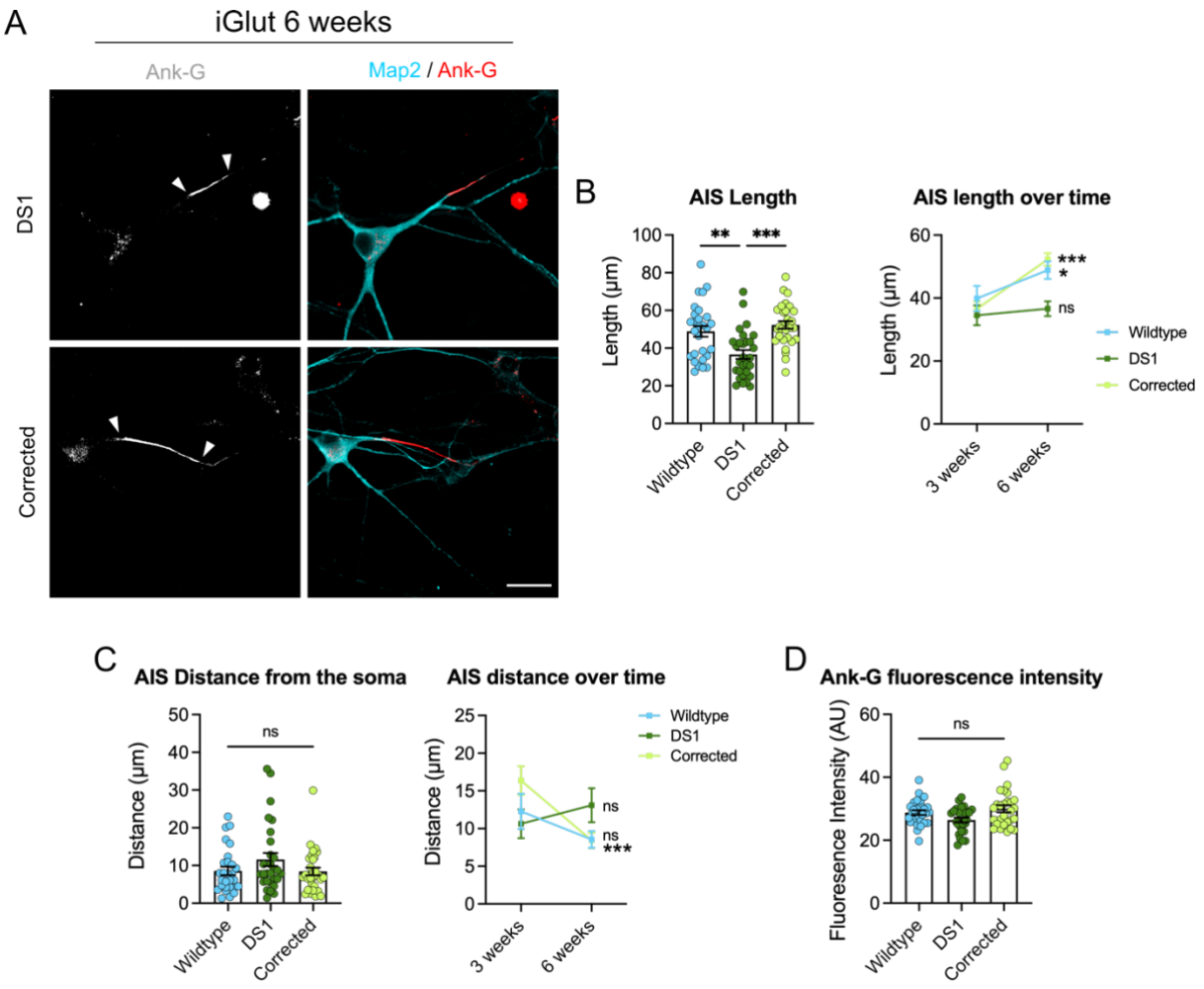

Figure 5.7. *Pathogenic SCN1A$^{IVS14+3A>T}$ causes decreased AIS length and Ankyrin-G content in late excitatory neurons (6 weeks).* **A –** Representative immunofluorescence images of DS1 and corrected iGlut neurons at 6 weeks stained for Ank-G (grey on the left and red on the right) and Map2 (cyan). Scale bar = 20 µm. **B –** Left, quantification of AIS length based on Ank-G staining in iGlut at 6 weeks. N=3 biological replicates, n = 28-30 cells. Error bars represent the SEM, Ordinary One-way ANOVA + Tukey's multiple comparison, ** = p<0.01, *** = p<0.001. Right, quantification of AIS length over time. N=3 biological replicates, n = 16-30 cells. Error bars represent the SEM, Unpaired parametric t test, ns = p>0.05, * = p<0.05, *** = p<0.001. **C –** Left, quantification of AIS distance from the soma based on Ank-G staining (AIS) relative to Map2 staining (soma) in iGlut at 6 weeks. N=3 biological replicates, n = 28-30 cells. Error bars represent the SEM, One-way ANOVA Kruskal-Wallis test + Dunn's multiple comparison, ns = p>0.05. Right, quantification of AIS distance from the soma over time in iGlut. N=3 biological replicates, n = 16-30 cells. Error bars represent the SEM, Unpaired nonparametric t test + Mann-Whitney test, ns = p>0.05, *** = p<0.001. **D –** Quantification of Ank-G fluorescence intensity in iGlut at 6 weeks. AU = arbitrary unit. N=3 biological replicates, n = 28-30 cells. Error bars represent the SEM, One-way ANOVA Kruskal-Wallis test + Dunn's multiple comparison, ns = p>0.05.

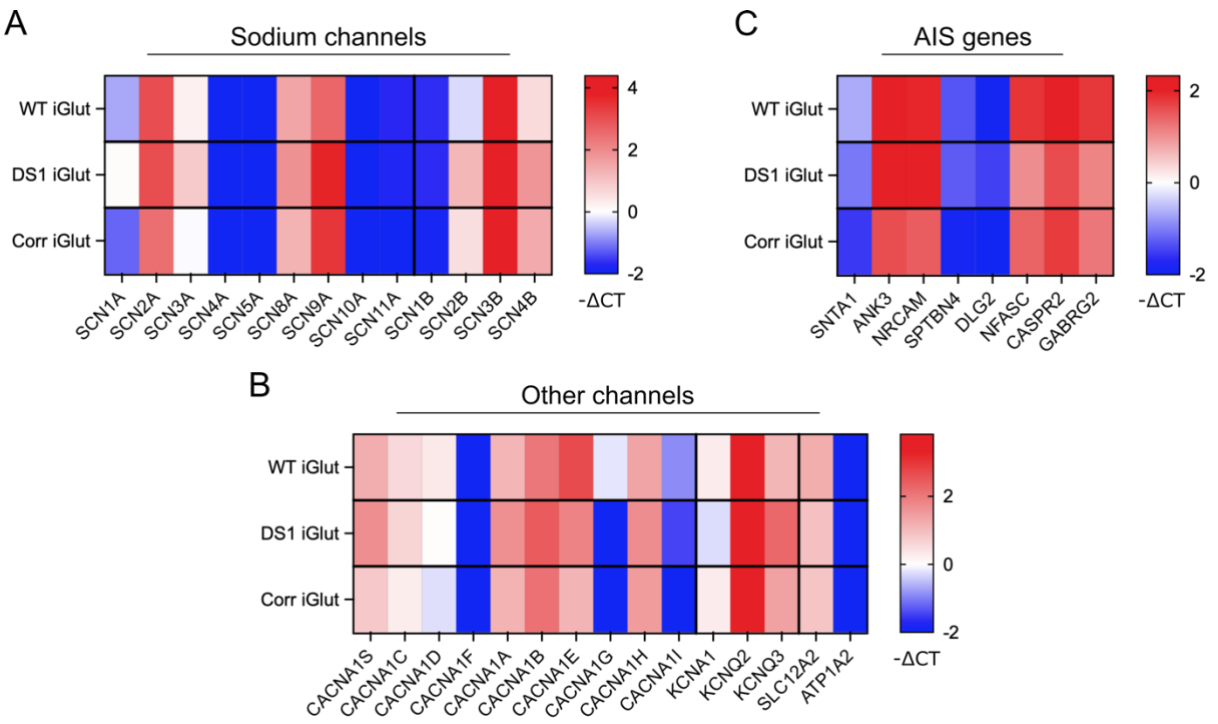

Figure 5.8. *Hyperexcitability in late DS1 excitatory neurons might be caused by transcriptional upregulation of sodium and calcium channels (6 weeks).* **A –** Heatmap representation of RT-qPCR analysis of sodium channels α and β subunits in wildtype, DS1 and corrected iGlut neurons at 6 weeks. Gene expression levels are normalised to the housekeeping gene TBP and expressed as -ΔCT. N=3 biological replicates with n=3 technical replicates per sample. **B –** Heatmap representation of RT-qPCR analysis of different ion channels in wildtype, DS1 and corrected iGlut neurons at 6 weeks. Gene expression levels are normalised to the housekeeping gene TBP and expressed as -ΔCT. N=3 biological replicates with n=3 technical replicates per sample. **C –** Heatmap representation of RT-qPCR analysis of AIS genes in wildtype, DS1 and corrected iGlut neurons at 6 weeks. Gene expression levels are normalised to the housekeeping gene TBP and expressed as -ΔCT. N=3 biological replicates with n=3 technical replicates per sample.

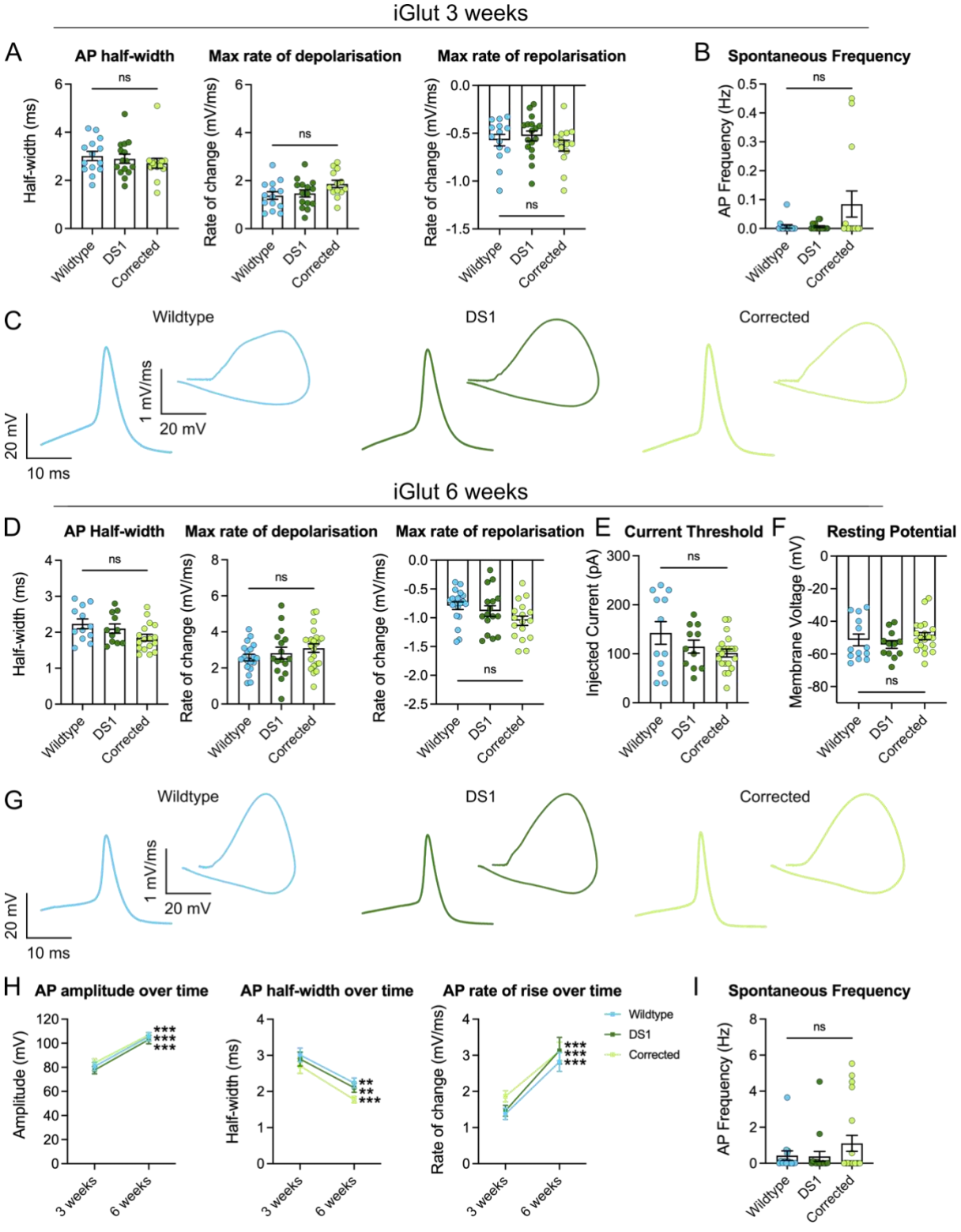
iGlut 3 weeks
A
AP half-width
Max rate of depolarisation
Max rate of repolarisation
B
Spontaneous Frequency
Half-width (ms)
Rate of change (mV/ms)
AP Frequency (Hz)
ns
Wildtype
DS1
Corrected
C
Wildtype
DS1
Corrected
1 mV/ms
20 mV
20 mV
10 ms
iGlut 6 weeks
D
AP Half-width
Max rate of depolarisation
Max rate of repolarisation
E
Current Threshold
F
Resting Potential
Injected Current (pA)
Membrane Voltage (mV)
G
Wildtype
DS1
Corrected
1 mV/ms
20 mV
20 mV
10 ms
H
AP amplitude over time
AP half-width over time
AP rate of rise over time
Amplitude (mV)
Half-width (ms)
Rate of change (mV/ms)
3 weeks
6 weeks
Wildtype
DS1
Corrected
I
Spontaneous Frequency
AP Frequency (Hz)

Supplementary Figure 5.1. **A –** Quantification of action potential half-width, maximum rate of depolarisation and repolarisation recorded in iGlut at 3 weeks. N=3 biological replicates, n = 14-15 cells. Error bars represent the SEM, Ordinary One-way ANOVA + Tukey's multiple comparison, ns = $p>0.05$. **B –** Quantification of spontaneous action potential frequency recorded in iGlut at 3 weeks. N=3 biological replicates, n = 14-16 cells. Error bars represent the SEM, One-way ANOVA Kruskal-Wallis test + Dunn's multiple comparison, ns = $p>0.05$. **C –** Average single AP traces and phase plots from wildtype, DS1 and corrected iGlut at 3 weeks. **D –** Quantification of action potential half-width, maximum rate of depolarisation and repolarisation recorded in iGlut at 6 weeks. N=3 biological replicates, n = 11-20 cells. Error bars represent the SEM, Ordinary One-way ANOVA + Tukey's multiple comparison, ns = $p>0.05$. **E –** Quantification of action potential current threshold recorded in iGlut at 6 weeks. N=3 biological replicates, n = 11-20 cells. Error bars represent the SEM, Ordinary One-way ANOVA + Tukey's multiple comparison, ns = $p>0.05$. **F –** Quantification of the resting membrane potential recorded in iGlut at 6 weeks. N=3 biological replicates, n = 12-20 cells. Error bars represent the SEM, One-way ANOVA Kruskal-Wallis test + Dunn's multiple comparison, ns = $p>0.05$. **G –** Average single AP traces and phase plots from wildtype, DS1 and corrected iGlut at 6 weeks. **H –** Quantification of action potential amplitude, half-width and rate of rise in iGlut over time. N=3 biological replicates, n = 11-20 cells. Error bars represent the SEM, Unpaired parametric t test or Unpaired nonparametric t test + Mann-Whitney test, ** = $p<0.01$, *** = $p<0.001$. **I –** Quantification of spontaneous action potential frequency recorded in iGlut at 6 weeks. N=3 biological replicates, n = 14-20 cells. Error bars represent the SEM, One-way ANOVA Kruskal-Wallis test + Dunn's multiple comparison, ns = $p>0.05$.

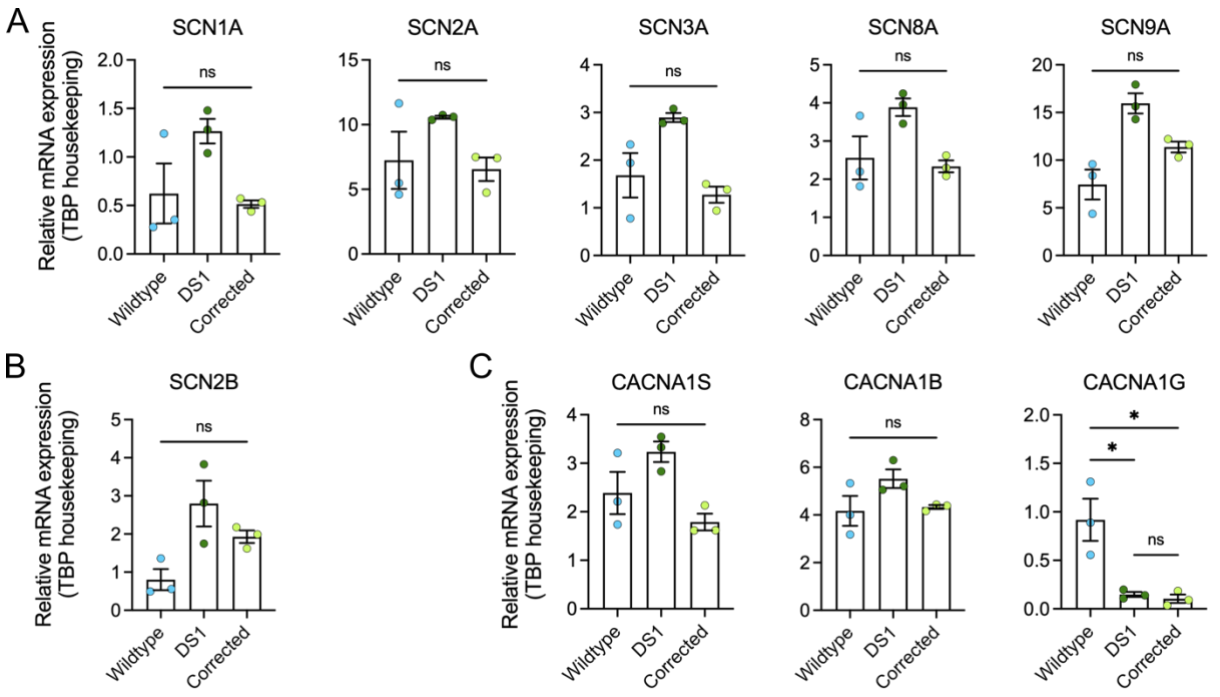

Supplementary Figure 5.2. **A –** RT-qPCR analysis of sodium channel α subunits SCN1A, SCN2A, SCN3A, SCN8A and SCN9A mRNA expression relative to the housekeeping gene TBP, performed in 6-weeks iGlut derived from wildtype, DS1 and corrected lines. N=3 biological replicates with n=3 technical replicates per sample. Error bars represent the SEM, Ordinary One-way ANOVA + Tukey's multiple comparison, ns = $p>0.05$. **B –** RT-qPCR analysis of sodium channel β subunit SCN2B mRNA expression relative to the housekeeping gene TBP, performed in 6-weeks iGlut derived from wildtype, DS1 and corrected lines. N=3 biological replicates with n=3 technical replicates per sample. Error bars represent the SEM, Ordinary One-way ANOVA + Tukey's multiple comparison, ns = $p>0.05$. **C –** RT-qPCR analysis of calcium channels CACNA1S, CACNA1A and CACNA1G mRNA expression relative to the housekeeping gene TBP, performed in 6-weeks iGlut derived from wildtype, DS1 and corrected lines. N=3 biological replicates with n=3 technical replicates per sample. Error bars represent the SEM, Ordinary One-way ANOVA + Tukey's multiple comparison. ns = $p>0.05$, * = $p<0.05$.

Experiment: iGlut Ca^{2+} imaging at 3 weeks.

Dataset analysed	Sample size	Normality	Statistical test	P Value (Significance)
Single cell Amplitude	Wildtype N = 28 DS1 N = 39 Corrected N = 16 N = cells from multiple coverslips	WT = NO DS1 = NO Corr = NO	One-way ANOVA Kruskal-Wallis test + Dunn's multiple comparison	Wildtype vs. DS1 = >0.9999 (ns) Wildtype vs. Corrected = 0.3246 (ns) DS1 vs. Corrected = 0.0954 (ns)
Single cell Frequency	Wildtype N = 28 DS1 N = 39 Corrected N = 16 N = cells from multiple coverslips	WT = NO DS1 = NO Corr = NO	One-way ANOVA Kruskal-Wallis test + Dunn's multiple comparison	Wildtype vs. DS1 = >0.9999 (ns) Wildtype vs. Corrected = 0.5770 (ns) DS1 vs. Corrected = 0.0877 (ns)
Synchronous Frequency	Wildtype N = 7 DS1 N = 7 Corrected N = 7 N = time-lapse recordings	WT = NO DS1 = NO Corr = NO	One-way ANOVA Kruskal-Wallis test + Dunn's multiple comparison	Wildtype vs. DS1 = >0.9999 (ns) Wildtype vs. Corrected = >0.9999 (ns) DS1 vs. Corrected = >0.9999 (ns)

Table 5.1. Statistical details of iGlut Ca^{2+} imaging at 3 weeks.

Experiment: iGlut electrophysiological characterisation at 3 weeks. For all samples, N = cells from multiple coverslips.

Dataset analysed	Sample size	Normality	Statistical test	P Value (Significance)
Na^+ current density	Wildtype N = 17 DS1 N = 16 Corrected N = 14	WT = NO DS1 = NO Corr = YES	One-way ANOVA Kruskal-Wallis test + Dunn's multiple comparison	Wildtype vs. DS1 = >0.9999 (ns) Wildtype vs. Corrected = 0.1102 (ns) DS1 vs. Corrected = 0.2917 (ns)
K^+ current density	Wildtype N = 17 DS1 N = 16 Corrected N = 14	WT = YES DS1 = YES Corr = NO	Ordinary One-way ANOVA + Tukey's multiple comparison	Wildtype vs. DS1 = 0.2071 (ns) Wildtype vs. Corrected = 0.8485 (ns) DS1 vs. Corrected = 0.5174 (ns)
AP Amplitude	Wildtype N = 14 DS1 N = 15 Corrected N = 14	WT = YES DS1 = YES Corr = YES	Ordinary One-way ANOVA + Tukey's multiple comparison	Wildtype vs. DS1 = 0.7921 (ns) Wildtype vs. Corrected = 0.8248 (ns) DS1 vs. Corrected = 0.4284 (ns)
AP Half-width	Wildtype N = 14 DS1 N = 15 Corrected N = 14	WT = YES DS1 = YES Corr = NO	One-way ANOVA Kruskal-Wallis test + Dunn's multiple comparison	Wildtype vs. DS1 = >0.9999 (ns) Wildtype vs. Corrected = 0.9717 (ns) DS1 vs. Corrected = >0.9999 (ns)
AP Rate of rise	Wildtype N = 14 DS1 N = 15 Corrected N = 14	WT = YES DS1 = YES Corr = YES	Ordinary One-way ANOVA + Tukey's multiple comparison	Wildtype vs. DS1 = 0.9152 (ns) Wildtype vs. Corrected = 0.0860 (ns) DS1 vs. Corrected = 0.1734 (ns)

Current threshold	Wildtype N = 14 DS1 N = 15 Corrected N = 14	WT = YES DS1 = NO Corr = YES	One-way ANOVA Kruskal-Wallis test + Dunn's multiple comparison	Wildtype vs. DS1 = >0.9999 (ns) Wildtype vs. Corrected = 0.9211 (ns) DS1 vs. Corrected = >0.9999 (ns)
Vm Threshold	Wildtype N = 14 DS1 N = 15 Corrected N = 14	WT = YES DS1 = YES Corr = YES	Ordinary One-way ANOVA + Tukey's multiple comparison	Wildtype vs. DS1 = 0.5250 (ns) Wildtype vs. Corrected = 0.0644 (ns) DS1 vs. Corrected = 0.4206 (ns)
Maximum Frequency	Wildtype N = 16 DS1 N = 16 Corrected N = 14	WT = YES DS1 = YES Corr = YES	Ordinary One-way ANOVA + Tukey's multiple comparison	Wildtype vs. DS1 = 0.1659 (ns) Wildtype vs. Corrected = 0.0537 (ns) DS1 vs. Corrected = 0.8161 (ns)
Spontaneous Frequency	Wildtype N = 14 DS1 N = 16 Corrected N = 14	WT = NO DS1 = NO Corr = NO	One-way ANOVA Kruskal-Wallis test + Dunn's multiple comparison	Wildtype vs. DS1 = >0.9999 (ns) Wildtype vs. Corrected = 0.8632 (ns) DS1 vs. Corrected = >0.9999 (ns)
Resting potential	Wildtype N = 14 DS1 N = 16 Corrected N = 14	WT = YES DS1 = YES Corr = YES	Ordinary One-way ANOVA + Tukey's multiple comparison	Wildtype vs. DS1 = 0.5301 (ns) Wildtype vs. Corrected = 0.9593 (ns) DS1 vs. Corrected = 0.7059 (ns)
Membrane capacitance (Cm)	WT N = 17 (25.54 ± 2.715 pF) DS1 N = 16 (19.09 ± 2.265 pF) Corr N = 14 (20.69 ± 2.158 pF)	WT = YES DS1 = YES Corr = YES	Ordinary One-way ANOVA + Tukey's multiple comparison	Wildtype vs. DS1 = 0.1446 (ns) Wildtype vs. Corrected = 0.3531 (ns) DS1 vs. Corrected = 0.8926 (ns)
Membrane resistance (Rm)	WT N = 17 (814.5 ± 94.39 MΩ) DS1 N = 16 (560.3 ± 71.75 MΩ) Corr N = 14 (562.2 ± 52.72 MΩ)	WT = YES DS1 = YES Corr = YES	Ordinary One-way ANOVA + Tukey's multiple comparison	Wildtype vs. DS1 = 0.0540 (ns) Wildtype vs. Corrected = 0.0672 (ns) DS1 vs. Corrected = 0.9998 (ns)
Access resistance (Rs)	WT N = 17 (11.08 ± 0.973 MΩ) DS1 N = 16 (10.32 ± 0.701 MΩ) Corr N = 14 (10.45 ± 0.620 MΩ)	WT = NO DS1 = NO Corr = YES	One-way ANOVA Kruskal-Wallis test + Dunn's multiple comparison	Wildtype vs. DS1 = >0.9999 (ns) Wildtype vs. Corrected = >0.9999 (ns) DS1 vs. Corrected = >0.9999 (ns)

Table 5.2. Statistical details of iGlut electrophysiological characterisation at 3 weeks.

Experiment: iGlut AIS characterisation at 3 weeks. For all samples, N = cells from multiple wells.

Dataset analysed	Sample size	Normality	Statistical test	P Value (Significance)
AIS length	Wildtype N = 16 DS1 N = 16 Corrected N = 16	WT = YES DS1 = YES Corr = NO	One-way ANOVA Kruskal-Wallis test + Dunn's multiple comparison	Wildtype vs. DS1 = >0.9999 (ns) Wildtype vs. Corrected = >0.9999 (ns) DS1 vs. Corrected = >0.9999 (ns)
AIS distance	Wildtype N = 16 DS1 N = 16 Corrected N = 16	WT = NO DS1 = NO Corr = YES	One-way ANOVA Kruskal-Wallis test + Dunn's multiple comparison	Wildtype vs. DS1 = >0.9999 (ns) Wildtype vs. Corrected = 0.1797 (ns) DS1 vs. Corrected = 0.0546 (ns)
Ank-G intensity	Wildtype N = 16 DS1 N = 16 Corrected N = 16	WT = NO DS1 = YES Corr = NO	One-way ANOVA Kruskal-Wallis test + Dunn's multiple comparison	Wildtype vs. DS1 = >0.9999 (ns) Wildtype vs. Corrected = 0.1340 (ns) DS1 vs. Corrected = 0.5547 (ns)

Table 5.3. Statistical details of iGlut AIS characterisation at 3 weeks.

Experiment: iGlut Ca^{2+} imaging of induced activity at 6 weeks and over time.

Dataset analysed	Sample size	Normality	Statistical test	P Value (Significance)
Single cell Amplitude	Wildtype N = 138 DS1 N = 216 N = cells from multiple coverslips	WT = NO DS1 = NO	Unpaired nonparametric t test + Mann-Whitney test	Wildtype vs. DS1 = <0.001 (***)
Single cell Amplitude over time – Wildtype	3 weeks N = 26 6 weeks N = 138 N = cells from multiple coverslips	3 weeks = NO 6 weeks = NO	Unpaired nonparametric t test + Mann-Whitney test	3 weeks vs. 6 weeks = <0.001 (***)
Single cell Amplitude over time – DS1	3 weeks N = 39 6 weeks N = 216 N = cells from multiple coverslips	3 weeks = NO 6 weeks = NO	Unpaired nonparametric t test + Mann-Whitney test	3 weeks vs. 6 weeks = <0.001 (***)
Single cell Frequency	Wildtype N = 138 DS1 N = 216 Corrected N = 48 N = cells from multiple coverslips	WT = NO DS1 = NO Corr = NO	One-way ANOVA Kruskal-Wallis test + Dunn's multiple comparison	Wildtype vs. DS1 = <0.001 (***) Wildtype vs. Corrected = >0.9999 (ns) DS1 vs. Corrected = <0.001 (***)
Single cell Frequency over time – Wildtype	3 weeks N = 26 6 weeks N = 138 N = cells from multiple coverslips	3 weeks = NO 6 weeks = NO	Unpaired nonparametric t test + Mann-Whitney test	3 weeks vs. 6 weeks = <0.001 (***)
Single cell Frequency over time – DS1	3 weeks N = 39 6 weeks N = 216 N = cells from multiple coverslips	3 weeks = NO 6 weeks = NO	Unpaired nonparametric t test + Mann-Whitney test	3 weeks vs. 6 weeks = <0.001 (***)

Single cell Frequency over time – Corrected	3 weeks N = 16 6 weeks N = 48 N = cells from multiple coverslips	3 weeks = NO 6 weeks = NO	Unpaired nonparametric t test + Mann-Whitney test	3 weeks vs. 6 weeks = <0.001 (***)
Synchronous Amplitude	Wildtype N = 17 DS1 N = 18 N = time-lapse recordings	WT = NO DS1 = NO	Unpaired nonparametric t test + Mann-Whitney test	Wildtype vs. DS1 = 0.0027 (**)
Synchronous Amplitude over time – Wildtype	3 weeks N = 2 6 weeks N = 17 N = time-lapse recordings	3 weeks = NO 6 weeks = NO	Unpaired nonparametric t test + Mann-Whitney test	3 weeks vs. 6 weeks = 0.0117 (*)
Synchronous Amplitude over time – DS1	3 weeks N = 2 6 weeks N = 18 N = time-lapse recordings	3 weeks = NO 6 weeks = NO	Unpaired nonparametric t test + Mann-Whitney test	3 weeks vs. 6 weeks = 0.5158 (ns)
Synchronous Frequency	Wildtype N = 17 DS1 N = 18 Corrected N = 11 N = time-lapse recordings	WT = NO DS1 = NO Corr = YES	One-way ANOVA Kruskal-Wallis test + Dunn's multiple comparison	Wildtype vs. DS1 = <0.001 (***) Wildtype vs. Corrected = >0.9999 (ns) DS1 vs. Corrected = <0.001 (***)
Synchronous Frequency over time – Wildtype	3 weeks N = 7 6 weeks N = 17 N = time-lapse recordings	3 weeks = NO 6 weeks = NO	Unpaired nonparametric t test + Mann-Whitney test	3 weeks vs. 6 weeks = <0.001 (***)
Synchronous Frequency over time – DS1	3 weeks N = 7 6 weeks N = 18 N = time-lapse recordings	3 weeks = NO 6 weeks = NO	Unpaired nonparametric t test + Mann-Whitney test	3 weeks vs. 6 weeks = <0.001 (***)
Synchronous Frequency over time – Corrected	3 weeks N = 7 6 weeks N = 11 N = time-lapse recordings	3 weeks = NO 6 weeks = YES	Unpaired nonparametric t test + Mann-Whitney test	3 weeks vs. 6 weeks = <0.001 (***)

Table 5.4 Statistical details of iGlut Ca^{2+} imaging of induced activity at 6 weeks and over time.

Experiment: iGlut Ca^{2+} imaging of spontaneous activity at 6 weeks.

Dataset analysed	Sample size	Normality	Statistical test	P Value (Significance)
Single cell Amplitude	Wildtype N = 67 DS1 N = 75 N = cells from multiple coverslips	WT = NO DS1 = NO	Unpaired nonparametric t test + Mann-Whitney test	Wildtype vs. DS1 = <0.001 (***)
Single cell Frequency	Wildtype N = 67 DS1 N = 75 Corrected N = 49 N = cells from multiple coverslips	WT = NO DS1 = NO Corr = NO	One-way ANOVA Kruskal-Wallis test + Dunn's multiple comparison	Wildtype vs. DS1 = <0.001 (***) Wildtype vs. Corrected = <0.001 (***) DS1 vs. Corrected = <0.001 (***)
Synchronous Amplitude	Wildtype N = 8 DS1 N = 8 N = time-lapse recordings	WT = YES DS1 = YES	Unpaired parametric t test	Wildtype vs. DS1 = 0.0241 (*)
Synchronous Frequency	Wildtype N = 8 DS1 N = 8 Corrected N = 8 N = time-lapse recordings	WT = YES DS1 = YES Corr = YES	Ordinary One-way ANOVA + Tukey's multiple comparison	Wildtype vs. DS1 = 0.0045 (**) Wildtype vs. Corrected = 0.1681 (ns) DS1 vs. Corrected = <0.001 (***)
Single cell Frequency – Wildtype	Spontaneous N = 67 Induced N = 138 N = cells from multiple coverslips	Spont = NO Induced = NO	Unpaired nonparametric t test + Mann-Whitney test	3 weeks vs. 6 weeks = <0.001 (***)
Single cell Frequency – DS1	Spontaneous N = 75 Induced N = 216 N = cells from multiple coverslips	Spont = NO Induced = NO	Unpaired nonparametric t test + Mann-Whitney test	3 weeks vs. 6 weeks = 0.9368 (ns)
Single cell Frequency – Corrected	Spontaneous N = 49 Induced N = 48 N = cells from multiple coverslips	Spont = NO Induced = YES	Unpaired nonparametric t test + Mann-Whitney test	3 weeks vs. 6 weeks = <0.001 (***)
Synchronous Frequency – Wildtype	Spontaneous N = 8 Induced N = 17 N = time-lapse recordings	Spont = YES Induced = NO	Unpaired nonparametric t test + Mann-Whitney test	3 weeks vs. 6 weeks = 0.0051 (**)
Synchronous Frequency – DS1	Spontaneous N = 8 Induced N = 18 N = time-lapse recordings	Spont = YES Induced = NO	Unpaired nonparametric t test + Mann-Whitney test	3 weeks vs. 6 weeks = 0.2769 (ns)
Synchronous Frequency – Corrected	Spontaneous N = 8 Induced N = 11 N = time-lapse recordings	Spont = YES Induced = YES	Unpaired parametric t test	3 weeks vs. 6 weeks = 0.0362 (*)

Table 5.5 Statistical details of iGlut Ca^{2+} imaging of spontaneous activity at 6 weeks.

Experiment: iGlut electrophysiological characterisation at 6 weeks. For all samples, N = cells from multiple coverslips.

Dataset analysed	Sample size	Normality	Statistical test	P Value (Significance)
Na^+ current density	Wildtype N = 17 DS1 N = 17 Corrected N = 20	WT = NO DS1 = NO Corr = NO	One-way ANOVA Kruskal-Wallis test + Dunn's multiple comparison	Wildtype vs. DS1 = >0.9999 (ns) Wildtype vs. Corrected = >0.9999 (ns) DS1 vs. Corrected = >0.9999 (ns)
K^+ current density	Wildtype N = 17 DS1 N = 17 Corrected N = 20	WT = NO DS1 = NO Corr = NO	One-way ANOVA Kruskal-Wallis test + Dunn's multiple comparison	Wildtype vs. DS1 = >0.9999 (ns) Wildtype vs. Corrected = 0.9268 (ns) DS1 vs. Corrected = >0.9999 (ns)
AP Amplitude	Wildtype N = 12 DS1 N = 11 Corrected N = 20	WT = YES DS1 = YES Corr = YES	Ordinary One-way ANOVA + Tukey's multiple comparison	Wildtype vs. DS1 = 0.8818 (ns) Wildtype vs. Corrected = 0.9329 (ns) DS1 vs. Corrected = 0.6573 (ns)
AP Half-width	Wildtype N = 12 DS1 N = 11 Corrected N = 20	WT = YES DS1 = YES Corr = YES	Ordinary One-way ANOVA + Tukey's multiple comparison	Wildtype vs. DS1 = 0.4619 (ns) Wildtype vs. Corrected = 0.0630 (ns) DS1 vs. Corrected = 0.2476 (ns)
AP Rate of rise	Wildtype N = 12 DS1 N = 11 Corrected N = 20	WT = YES DS1 = YES Corr = YES	Ordinary One-way ANOVA + Tukey's multiple comparison	Wildtype vs. DS1 = 0.7799 (ns) Wildtype vs. Corrected = 0.7533 (ns) DS1 vs. Corrected = 0.9987 (ns)
Current threshold	Wildtype N = 12 DS1 N = 11 Corrected N = 20	WT = NO DS1 = YES Corr = YES	One-way ANOVA Kruskal-Wallis test + Dunn's multiple comparison	Wildtype vs. DS1 = >0.9999 (ns) Wildtype vs. Corrected = 0.6908 (ns) DS1 vs. Corrected = >0.9999 (ns)
Vm Threshold	Wildtype N = 12 DS1 N = 11 Corrected N = 20	WT = YES DS1 = YES Corr = YES	Ordinary One-way ANOVA + Tukey's multiple comparison	Wildtype vs. DS1 = 0.1535 (ns) Wildtype vs. Corrected = 0.8882 (ns) DS1 vs. Corrected = 0.2427 (ns)
Maximum Frequency	Wildtype N = 13 DS1 N = 16 Corrected N = 19	WT = YES DS1 = YES Corr = NO	One-way ANOVA Kruskal-Wallis test + Dunn's multiple comparison	Wildtype vs. DS1 = 0.2009 (ns) Wildtype vs. Corrected = >0.9999 (ns) DS1 vs. Corrected = 0.3859 (ns)
Spontaneous Frequency	Wildtype N = 14 DS1 N = 17 Corrected N = 20	WT = NO DS1 = NO Corr = NO	One-way ANOVA Kruskal-Wallis test + Dunn's multiple comparison	Wildtype vs. DS1 = 0.9333 (ns) Wildtype vs. Corrected = >0.9999 (ns) DS1 vs. Corrected = >0.9999 (ns)
Resting potential	Wildtype N = 13 DS1 N = 12 Corrected N = 20	WT = NO DS1 = YES Corr = YES	One-way ANOVA Kruskal-Wallis test + Dunn's multiple comparison	Wildtype vs. DS1 = >0.9999 (ns) Wildtype vs. Corrected = 0.8491 (ns) DS1 vs. Corrected = 0.5919 (ns)
Membrane capacitance (Cm)	WT N = 16 (46.52 ± 7.152 pF) DS1 N = 17 (44.28 ± 8.278 pF) Corr N = 20 (46.35 ± 7.088 pF)	WT = YES DS1 = YES Corr = YES	Ordinary One-way ANOVA + Tukey's multiple comparison	Wildtype vs. DS1 = 0.9775 (ns) Wildtype vs. Corrected = 0.9999 (ns) DS1 vs. Corrected = 0.9787 (ns)

Membrane resistance (Rm)	WT N = 16 (638.1 ± 87.26 MΩ) DS1 N = 17 (694.0 ± 149.4 MΩ) Corr N = 20 (725.8 ± 202.6 MΩ)	WT = NO DS1 = YES Corr = NO	One-way ANOVA Kruskal-Wallis test + Dunn's multiple comparison	Wildtype vs. DS1 = >0.9999 (ns) Wildtype vs. Corrected = 0.7576 (ns) DS1 vs. Corrected = >0.9999 (ns)
Access resistance (Rs)	WT N = 16 (9.60 ± 1.131 MΩ) DS1 N = 17 (10.26 ± 0.980 MΩ) Corr N = 20 (9.14 ± 0.795 MΩ)	WT = NO DS1 = NO Corr = NO	One-way ANOVA Kruskal-Wallis test + Dunn's multiple comparison	Wildtype vs. DS1 = >0.9999 (ns) Wildtype vs. Corrected = >0.9999 (ns) DS1 vs. Corrected = 0.9620 (ns)

Table 5.6a. Statistical details of iGlut electrophysiological characterisation at 6 weeks.

Experiment: iGlut electrophysiological parameters over time. For all samples, N = cells from multiple coverslips.

Dataset analysed	**Sample size**	**Normality**	**Statistical test**	**P Value (Significance)**
AP amplitude over time – Wildtype	3 weeks N = 14 6 weeks N = 12	3 weeks = YES 6 weeks = YES	Unpaired parametric t test	3 weeks vs. 6 weeks = <0.001 (***)
AP amplitude over time – DS1	3 weeks N = 15 6 weeks N = 11	3 weeks = YES 6 weeks = YES	Unpaired parametric t test	3 weeks vs. 6 weeks = <0.001 (***)
AP amplitude over time – Corrected	3 weeks N = 14 6 weeks N = 20	3 weeks = YES 6 weeks = YES	Unpaired parametric t test	3 weeks vs. 6 weeks = <0.001 (***)
AP half-width over time – Wildtype	3 weeks N = 14 6 weeks N = 12	3 weeks = YES 6 weeks = YES	Unpaired parametric t test	3 weeks vs. 6 weeks = 0.0039 (**)
AP half-width over time – DS1	3 weeks N = 15 6 weeks N = 11	3 weeks = YES 6 weeks = YES	Unpaired parametric t test	3 weeks vs. 6 weeks = 0.0042 (**)
AP half-width over time – Corrected	3 weeks N = 14 6 weeks N = 20	3 weeks = NO 6 weeks = YES	Unpaired nonparametric t test + Mann-Whitney test	3 weeks vs. 6 weeks = <0.001 (***)
AP rate of rise over time – Wildtype	3 weeks N = 14 6 weeks N = 12	3 weeks = YES 6 weeks = YES	Unpaired parametric t test	3 weeks vs. 6 weeks = <0.001 (***)
AP rate of rise over time – DS1	3 weeks N = 15 6 weeks N = 11	3 weeks = YES 6 weeks = YES	Unpaired parametric t test	3 weeks vs. 6 weeks = <0.001 (***)
AP rate of rise over time – Corrected	3 weeks N = 14 6 weeks N = 20	3 weeks = YES 6 weeks = YES	Unpaired parametric t test	3 weeks vs. 6 weeks = <0.001 (***)
Maximum frequency over time – Wildtype	3 weeks N = 16 6 weeks N = 13	3 weeks = YES 6 weeks = YES	Unpaired parametric t test	3 weeks vs. 6 weeks = 0.4352 (ns)
Maximum frequency over time – DS1	3 weeks N = 16 6 weeks N = 16	3 weeks = YES 6 weeks = YES	Unpaired parametric t test	3 weeks vs. 6 weeks = <0.001 (***)
Maximum frequency over time – Corrected	3 weeks N = 14 6 weeks N = 19	3 weeks = YES 6 weeks = NO	Unpaired nonparametric t test + Mann-Whitney test	3 weeks vs. 6 weeks = 0.3996 (ns)

Table 5.6b. Statistical details of iGlut electrophysiological parameters overtime.

Experiment: iGlut AIS characterisation at 6 weeks and over time. For all samples, N = cells from multiple wells.

Dataset analysed	Sample size	Normality	Statistical test	P Value (Significance)
AIS length	Wildtype N = 28 DS1 N = 29 Corrected N = 30	WT = YES DS1 = YES Corr = YES	Ordinary One-way ANOVA + Tukey's multiple comparison	Wildtype vs. DS1 = 0.0017 (**) Wildtype vs. Corrected = 0.5773 (ns) DS1 vs. Corrected = <0.001 (***)
AIS length over time – Wildtype	3 weeks N = 16 6 weeks N = 28	3 weeks = YES 6 weeks = YES	Unpaired parametric t test	3 weeks vs. 6 weeks = 0.0105 (*)
AIS length over time – DS1	3 weeks N = 16 6 weeks N = 29	3 weeks = YES 6 weeks = YES	Unpaired parametric t test	3 weeks vs. 6 weeks = 0.5953 (ns)
AIS length over time – Corrected	3 weeks N = 16 6 weeks N = 30	3 weeks = NO 6 weeks = YES	Unpaired nonparametric t test + Mann-Whitney test	3 weeks vs. 6 weeks = <0.001 (***)
AIS distance	Wildtype N = 28 DS1 N = 29 Corrected N = 30	WT = NO DS1 = NO Corr = NO	One-way ANOVA Kruskal-Wallis test + Dunn's multiple comparison	Wildtype vs. DS1 = 0.4863 (ns) Wildtype vs. Corrected = >0.9999 (ns) DS1 vs. Corrected = 0.5476 (ns)
AIS Distance over time – Wildtype	3 weeks N = 16 6 weeks N = 28	3 weeks = NO 6 weeks = NO	Unpaired nonparametric t test + Mann-Whitney test	3 weeks vs. 6 weeks = 0.2396 (ns)
AIS Distance over time – DS1	3 weeks N = 16 6 weeks N = 29	3 weeks = NO 6 weeks = NO	Unpaired nonparametric t test + Mann-Whitney test	3 weeks vs. 6 weeks = 0.8974 (ns)
AIS Distance over time – Corrected	3 weeks N = 16 6 weeks N = 30	3 weeks = NO 6 weeks = NO	Unpaired nonparametric t test + Mann-Whitney test	3 weeks vs. 6 weeks = <0.001 (***)
Ank-G intensity	Wildtype N = 28 DS1 N = 29 Corrected N = 30	WT = YES DS1 = YES Corr = NO	One-way ANOVA Kruskal-Wallis test + Dunn's multiple comparison	Wildtype vs. DS1 = 0.1855 (ns) Wildtype vs. Corrected = >0.9999 (ns) DS1 vs. Corrected = 0.0574 (ns)

Table 5.7. Statistical details of iGlut AIS characterisation at 6 weeks and over time.

Experiment: iGlut differential expression analysis at 6 weeks. For all samples, N = 3 biological replicates with 3 technical replicates.

Dataset analysed	Normality	Statistical test	P Value (Significance)
SCN1A	WT = YES DS1 = YES Corr = YES	Ordinary One-way ANOVA + Tukey's multiple comparison	Wildtype vs. DS1 = 0.1124 (ns) Wildtype vs. Corrected = 0.7064 (ns) DS1 vs. Corrected = 0.0985 (ns)
SCN2A	WT = YES DS1 = YES Corr = NO	One-way ANOVA Kruskal-Wallis test + Dunn's multiple comparison	Wildtype vs. DS1 = 0.6991 (ns) Wildtype vs. Corrected = >0.9999 (ns) DS1 vs. Corrected = 0.4081 (ns)
SCN3A	WT = NO DS1 = YES Corr = YES	One-way ANOVA Kruskal-Wallis test + Dunn's multiple comparison	Wildtype vs. DS1 = 0.2209 (ns) Wildtype vs. Corrected = >0.9999 (ns) DS1 vs. Corrected = 0.0760 (ns)
SCN8A	WT = YES DS1 = YES Corr = YES	Ordinary One-way ANOVA + Tukey's multiple comparison	Wildtype vs. DS1 = 0.0915 (ns) Wildtype vs. Corrected = 0.9032 (ns) DS1 vs. Corrected = 0.0531 (ns)
SCN9A	WT = YES DS1 = YES Corr = NO	One-way ANOVA Kruskal-Wallis test + Dunn's multiple comparison	Wildtype vs. DS1 = 0.0519 (ns) Wildtype vs. Corrected = 0.5391 (ns) DS1 vs. Corrected = 0.5391 (ns)
SCN2B	WT = YES DS1 = YES Corr = YES	Ordinary One-way ANOVA + Tukey's multiple comparison	Wildtype vs. DS1 = 0.1303 (ns) Wildtype vs. Corrected = 0.0927 (ns) DS1 vs. Corrected = 0.5477 (ns)
CACNA1S	WT = YES DS1 = YES Corr = NO	One-way ANOVA Kruskal-Wallis test + Dunn's multiple comparison	Wildtype vs. DS1 = 0.6991 (ns) Wildtype vs. Corrected = 0.6991 (ns) DS1 vs. Corrected = 0.0512 (ns)
CACNA1B	WT = YES DS1 = YES Corr = YES	Ordinary One-way ANOVA + Tukey's multiple comparison	Wildtype vs. DS1 = 0.1920 (ns) Wildtype vs. Corrected = 0.8014 (ns) DS1 vs. Corrected = 0.1920 (ns)
CACNA1G	WT = YES DS1 = YES Corr = YES	Ordinary One-way ANOVA + Tukey's multiple comparison	Wildtype vs. DS1 = 0.0129 (*) Wildtype vs. Corrected = 0.0129 (*) DS1 vs. Corrected = 0.8169 (ns)

Table 5.8. Statistical details of iGlut differential expression analysis at 6 weeks.

5.3 Conclusions

- Pathogenic *SCN1A*$^{IVS14+3A>T}$ does **not affect** early excitatory neurons at 3 weeks.
  - Early DS1 iGlut neurons exhibit normal calcium spike frequency when activity is induced by elevated Ca^{2+} and K^{+} concentrations.
  - Early DS1 iGlut neurons display normal electrophysiological properties, comparable to wildtype and corrected iGlut.
  - No differences were observed in the morphology of the AIS in early DS1 iGlut neurons compared to wildtype and corrected lines.
- Pathogenic *SCN1A*$^{IVS14+3A>T}$ causes **hyperexcitability** in late excitatory neurons at 6 weeks.
  - Late DS1 iGlut neurons exhibit increased calcium signal frequency when neuronal activity is induced by elevated Ca^{2+} and K^{+} concentrations.
  - Late DS1 iGlut neurons also exhibit increased calcium signal frequency when spontaneous neuronal activity is analysed at physiological concentrations of Ca^{2+} and K^{+}.
  - Late DS1 iGlut neurons display increased current-induced repetitive firing and higher action potential maximum frequency compared to wildtype and corrected iGlut lines.
  - Late DS1 iGlut neurons have a shorter AIS compared to wildtype and corrected iGlut.

Chapter 6

Excitatory and inhibitory neurons both contribute to the SCN1A$^{IVS14+3A>T}$ pathogenic phenotype

6.1 Introduction

In Chapter 4 and 5 we have described the effect of the Dravet-related *SCN1A*$^{IVS14+3A>T}$ mutation on patient-derived inhibitory and excitatory neurons in monocultures. We found that, at an early time point (3 weeks), inhibitory neurons showed signs of hyperexcitability while the function of excitatory neurons was unaffected. Upon further maturation (6 weeks), inhibitory interneurons exhibited reduced neuronal activity while excitatory neurons developed a hyperexcitable phenotype. As previously discussed, the epileptic phenotype in Dravet syndrome (DS) is thought to be caused by the compromised function of inhibitory interneurons, causing a lack of inhibition which eventually results in hyperexcitation and hypersynchrony of excitatory neurons. However, mounting evidence suggests that excitatory neurons might play more than a passive role in the pathophysiology of this disease. Indeed, similarly to our results, hyperexcitability of pyramidal neurons – independent from lack of inhibition – has been observed in pure glutamatergic cultures derived from Dravet patient hiPSCs (Jiao et al., 2013b; Y. Liu, Lopez-Santiago, et al., 2013; van Hugte et al., 2023). An active contribution of pyramidal neurons to the epileptic phenotype could explain the limited efficacy of pharmacological treatments aimed exclusively at restoring physiological levels of inhibition (i.e., GABA-agonists) (He et al., 2022).

In chapter 3, we have shown that iGlut and iGABA neurons can be assembled into long-term co-culture models of cortical circuits with a stable ratio of 70% excitatory neurons and 30% inhibitory interneurons to resemble the human cortex E/I ratio. In this chapter, we use this co-culture model to investigate the relative contribution of excitatory and inhibitory neurons to the overall disease phenotype mediated by the *SCN1A*$^{IVS14+3A>T}$ mutation. Specifically, two colour-calcium imaging is used to assess the activity of both excitatory and inhibitory neurons in co-culture. Finally, AIS structural changes are assessed in the context of functional neuronal networks.

6.2 Results

6.2.1 Increased activity of early DS1 inhibitory interneurons results in decreased activity of DS1 excitatory neurons in co-culture

DS1 and corrected iGABA (expressing jrGECO1a) and iGlut neurons (expressing GCaMP6f) were derived and assembled, together with mAstro, into ratio-defined co-cultures as previously described (Fig.6.1-A). Co-cultures were maintained for 3 weeks before calcium imaging experiments were conducted according to Sun & Südhof (Z. Sun & Südhof, 2021b). Co-cultures at 3 weeks were first equilibrated in Modified Tyrode Solution (2 mM Ca^{2+}, 5 mM K^{+}), then incubated in Ca^{2+} imaging buffer (4 mM Ca^{2+}, 8 mM K^{+}) for the recordings – full buffer compositions in *Chapter 2, Table 2.12*. Using sequential acquisition, we were able to simultaneously image the Ca^{2+} signal emitted from both probes, GCaMP6f and jrGECO1a. Time-lapse recordings were carried out over 120 sec at a frame rate of 10-20 frames/sec and the fluorescence intensity profile of each probe was analysed for the active cells within the field of view. The GCaMP6f or jrGECO1a signal intensity for each neuron was normalised by calculating the ratio ($\Delta F/F_0$) of the increase in fluorescence (ΔF) to the baseline (F_0) and plotted over time (Fig. 6.1-B).

Similarly to what was observed in iGABA monocultures, DS1 iGABA neurons in co-culture were found to have a higher Ca^{2+} signal frequency compared to corrected iGABA in co-culture. Instead, Ca^{2+} signal amplitude of iGABA neurons was comparable in both DS1 and corrected co-cultures (Fig.6.1-C – Table 6.1). Simultaneously, contrarily to iGlut monocultures, DS1 iGlut neurons in co-culture were found to have a significantly lower Ca^{2+} signal frequency (1.33 ± 0.04 spikes/min) compared to corrected co-cultures (1.81 ± 0.05 spikes/min). Ca^{2+} signal amplitude of iGlut neurons was comparable in both DS1 and corrected co-cultures (Fig.6.1-D – Table 6.1).

Overall, the data obtained from the early co-culture models support our previous observations on hyperexcitability of DS1 iGABA neurons at 3 weeks. In the context of a co-culture with excitatory neurons, the increased activity of DS1 inhibitory interneurons results in a significantly reduced activity of DS1 excitatory neurons.

6.2.2 Increased activity of late DS1 excitatory neurons is maintained in co-culture with DS1 inhibitory interneurons

Co-cultures were maintained for 6 weeks before calcium imaging experiments were conducted as previously described. Briefly, DS1 and wildtype co-cultures (Fig.6.2-A) at 6 weeks were incubated in Ca^{2+} imaging buffer (4 mM Ca^{2+}, 8 mM K^{+}) for the recordings and the GCaMP6f signal intensity for each neuron was normalised by calculating the ratio ($\Delta F/F_0$) of the increase in fluorescence (ΔF) to the baseline (F_0) and plotted over time (Fig. 6.2-B). Once again, due to the protracted unavailability of the microscope used for the acquisition of the early time point, 6 weeks experiments were performed using a different imaging system. This created two problems. Firstly, as previously discussed, Ca^{2+} signal amplitude detected at 3 weeks was not comparable with the one detected for the later time point. Secondly, the imaging system used for the acquisition of the 6 weeks time point was not appropriately equipped for two colour imaging. For this reason, only the GCaMP6f signal, and therefore iGlut activity, could be analysed.

Similarly to what was observed in late iGlut monocultures, we found that in co-culture, DS1 iGlut neurons displayed a higher Ca^{2+} signal frequency (3.20 ± 0.14 spikes/min) compared to wildtype iGlut in co-culture (2.48 ± 0.36 spikes/min). Ca^{2+} signal amplitude was also found to be lower in DS1 iGlut neurons in co-culture (0.04 ± 0.006 $\Delta F/F_0$) compared to wildtype iGlut in co-culture (0.07 ± 0.01 $\Delta F/F_0$) (Fig. 6.2-C – Table 6.2). Interestingly, even though we were not able to assess the activity of iGABA neurons, we found that the DS1 iGlut phenotype was dampened by the presence of DS1 iGABA neurons in co-culture. Indeed, the Ca^{2+} signal frequency observed in DS1 iGlut neurons in co-culture was substantially lower compared to DS1 iGlut neurons in monoculture (Fig.6.1-D – Table 6.2). This is not surprising since, in spite of the reduced activity of late DS1 iGABA neurons, they still contribute some degree of inhibition to the network.

Overall, the data obtained from the late co-culture models support our previous observations on the hyperexcitability of DS1 iGlut neurons at 6 weeks. Unfortunately, the activity of iGABA neurons in co-culture could not be assessed.

6.2.3 *Excitatory and inhibitory neurons both contribute to the late SCN1A$^{IVS14+3A>T}$ pathogenic phenotype*

To test the relative contribution of excitatory and inhibitory neurons to the disease phenotype mediated by the *SCN1A*$^{IVS14+3A>T}$ mutation at the late time point, we generated mixed genotype co-culture models. Specifically, this experiment was designed to assess the relative contribution that impaired inhibition (DS1 iGABA neurons) and increased excitation (DS1 iGlut neurons) have, respectively, on the overall network activity. To this end, we cultured wildtype iGlut neurons with DS1 iGABA neurons (WT-iGlut+DS1-iGABA) and DS1 iGlut neurons with wildtype iGABA neurons (DS1-iGlut+WT-iGABA) and compared their activity with fully wildtype (WT-iGlut+WT-iGABA) and fully Dravet (DS1-iGlut+DS1-iGABA) co-cultures (Fig. 6.3-A). Mixed genotype cultures were maintained for 6 weeks before two-colour calcium imaging experiments were conducted in Ca^{2+} imaging buffer (4 mM Ca^{2+}, 8 mM K^{+}) as previously described. The GCaMP6f or jrGECO1a signal intensity for each neuron was normalised by calculating the ratio ($\Delta F/F_0$) of the increase in fluorescence (ΔF) to the baseline (F_0) and plotted over time (Fig. 6.3-B).

In the following description of results, we discuss the Ca^{2+} signal frequencies derived specifically from the iGlut population within the co-cultures. Interestingly, we found that in WT-iGlut+DS1-iGABA, the Ca^{2+} signal frequency was significantly higher (4.29 ± 0.39 spikes/min) compared to WT-iGlut+WT-iGABA (2.48 ± 0.36 spikes/min). This higher frequency was comparable to the one displayed by DS1-iGlut+DS1-iGABA neurons (3.20 ± 0.13 spikes/min) (Fig. 6.3-C- Table 6.3). This result suggests that, in accordance with the current view on the pathophysiology of DS, compromised inhibition causes an excess of excitation. On the other hand, DS1-iGlut+WT-iGABA cultures displayed a higher Ca^{2+} signal frequency (4.06 ± 0.28 spikes/min) compared to WT-iGlut+WT-iGABA (2.48 ± 0.36 spikes/min). This higher frequency was comparable to the frequency displayed by DS1-iGlut+DS1-iGABA neurons (3.20 ± 0.13 spikes/min) and, interestingly, it was also comparable to the frequency displayed by WT-iGlut+DS1-iGABA (4.29 ± 0.39 spikes/min) (Fig. 6.3-C-Table 6.3). This result suggests that contrary to the current view, DS1 excitatory neurons have a phenotype that, alone, results in an excess of excitation.

In the following description of results, we discuss the Ca^{2+} signal frequencies derived specifically from the iGABA population within the co-cultures. We observed that DS1-

iGlut+WT-iGABA showed a trend towards a higher Ca^{2+} signal frequency (6.89 ± 1.29 spikes/min) compared to WT-iGlut+DS1-iGABA (4.62 ± 0.99 spikes/min) (Fig. 6.3-D- Table 6.3). However, this difference was not statistically significant.

Overall, these results indicate that the presence of the *SCN1A*$^{IVS14+3A>T}$ mutation in either the excitatory or the inhibitory component of the network is sufficient, in both cases, to cause a disease phenotype characterised by increased network activity. This suggests that the intrinsically increased activity of DS1 iGlut neurons and the intrinsically reduced activity of DS1 iGABA neurons both contribute to the overall disease phenotype. Such an observation could have important implications in the context of DS therapeutical intervention. Currently, the first- and second-line drugs adopted in the treatment of DS are GABA-agonists used with the aim of restoring appropriate levels of inhibition, however, they typically fail to achieve seizure-control (He et al., 2022). If excitatory neurons are indeed playing an active role in mediating the epileptic phenotype of DS, this could explain why restoring inhibition, alone, is not sufficient to achieve seizure-freedom. This might suggest that a second drug which targets hyperexcitation in excitatory neurons could be required for effective treatment.

6.2.4 Pathogenic SCN1A$^{IVS14+3A>T}$ causes decreased AIS length in both excitatory and inhibitory neurons in early co-cultures (3 weeks)

AIS length and distance from the soma change in relation to neuronal inputs. Such changes mediate a direct effect on neuronal excitability. Therefore, structural properties of the AIS were investigated in early co-cultures based on Ank-G staining. Neuronal identity could be assessed, within the co-culture, based on the expression of GCaMP6f (iGlut neurons) and jrGECO1a (iGABA neurons) counterstained by anti-GFP and anti-RFP antibodies, respectively (Fig. 6.4-A).

In excitatory neurons, AIS length was found to be reduced in DS1 iGlut (34.19 ± 1.19 μm) compared to wildtype (41.64 ± 1.62 μm) and corrected cultures (46.34 ± 2.06 μm) (Fig. 6.4-B – Table 6.4). Contrarily, the AIS of iGlut neurons was equally distant from the soma in all co-culture conditions. Similarly, average Ank-G fluorescence intensity of iGlut neurons was comparable across cultures (Fig. 6.4-B – Table 6.4), indicating that Ank-G levels in the AIS were unchanged.

In inhibitory interneurons, AIS length was also found to be reduced in DS1 iGABA neurons (31.50 ± 1.52 μm) compared to wildtype (37.39 ± 1.64 μm) and corrected cultures (38.06 ±

1.62 μm) (Fig. 6.4-C – Table 6.4). Contrarily, AIS distance from the soma and average Ank-G fluorescence intensity were comparable in iGABA neurons across all co-culture conditions (Fig. 6.4-C – Table 6.4).

Overall, AIS characterisation in 3-week-old co-cultures revealed shorter AIS in both iGlut and iGABA neurons in DS1 cultures. In contrast, in monocultures at 3 weeks we observed no differences in the AIS length of DS1 iGlut or iGABA neurons (Fig. 5.3, Fig. 4.3 respectively). Different phenotypes from those observed in monocultures were to be expected due to the presence of network interactions between the excitatory and inhibitory components, which are lacking in monocultures. Indeed, calcium imaging experiments in early co-cultures confirmed that the increased inhibitory activity of DS1 iGABA neurons results in a decrease of DS1 iGlut neurons activity in co-culture (Fig. 6.1). In response to increased levels of inhibition, DS1 iGlut neurons might try to reduce their intrinsic excitability by shortening the AIS – a recognised mechanism of AIS homeostatic plasticity (Evans et al., 2015; Galliano et al., 2021; Jamann et al., 2021b; Sohn et al., 2019). Similarly, increased interneuron activity can induce activity-dependant AIS shortening in DS1 iGABA neurons, in order to reduce their excitability and therefore activity.

6.2.5 AIS homeostatic plasticity fails to restore normal excitability in late excitatory and inhibitory neurons carrying the pathogenic SCN1A$^{IVS14+3A>T}$ mutation (6 weeks)

Similarly to early cultures, structural properties of the AIS were also investigated in late co-cultures based on Ank-G, GFP and RFP staining (Fig. 6.5-A).

In late excitatory neurons, AIS length was found to be substantially reduced in DS1 iGlut neurons (36.29 ± 1.66 μm) compared to wildtype (56.60 ± 1.98 μm) and corrected cultures (53.40 ± 2.47 μm) (Fig. 6.5-B – Table 6.5a). Over time, AIS increased in length in wildtype and corrected iGlut neurons, but it maintained the same length in DS1iGlut neurons (Fig. 6.5-C – Table 6.5b). In late co-cultures, the AIS of iGlut neurons was again found to have the same distance from the soma in all populations, suggesting that proximal-distal positioning of the AIS is not involved in activity regulation in these neurons (Fig. 6.5-D – Table 6.5a). Similarly, average Ank-G fluorescence intensity was comparable across all conditions. Over time, a substantial increase in Ank-G fluorescence intensity was observed in all iGlut populations, consistent with neuronal maturation (Supplementary Fig. 6.1-A – Table 6.5b).

In inhibitory interneurons, AIS length was found to be significantly increased in DS1 iGABA neurons (42.87 ± 1.83 μm) compared to wildtype (38.00 ± 2.23 μm) and corrected cultures (37.24 ± 1.25 μm) (Fig. 6.5-E – Table 6.5a). Over time, AIS increased in length only in DS1 iGABA neurons while it maintained the same length in wildtype and corrected cultures (Fig. 6.5-F – Table 6.5c). The AIS distance from the soma was found to be comparable across all iGABA populations (Fig. 6.5-G – Table 6.5a). However, similarly to late iGABA monocultures, DS1 iGABA in co-culture were found to have a lower Ank-G fluorescence intensity (88.15 ± 3.68 AU), compared to wildtype (102.20 ± 6.43 AU) and corrected (106.30 ± 4.82 AU) co-cultures (Fig. 6.5-G – Table 6.5a). A significant increase in Ank-G fluorescence intensity over time was observed in all iGABA populations (Supplementary Fig. 6.1-B – Table 6.5c).

Similarly to monocultures, DS1 iGlut in co-culture exhibited a much shorter AIS compared to wildtype and corrected lines. We previously speculated that this might be a normal homeostatic response to the increased excitatory activity in the culture. Indeed, shortening of the AIS is a well-established plasticity mechanism by which neurons decrease their intrinsic excitability in response to chronic depolarisation (Evans et al., 2015; Galliano et al., 2021; Jamann et al., 2021b; Sohn et al., 2019). However, in DS1 iGlut neurons this response does not seem to be sufficient to counterbalance the primary cause of increased neuronal excitability. Similarly, DS1 iGABA neurons in late co-cultures extend their AIS, possibly in an attempt to increase their excitability and restore E/I balance in the network. However even in this case, this response is not sufficient to overcome the decrease in neuronal excitability caused by *SCN1A*$^{IVS14+3A>T}$ in late DS1 iGABA neurons. Further characterisation of AIS homeostatic plasticity mechanisms in our co-culture system might confirm if these might be affected in DS.

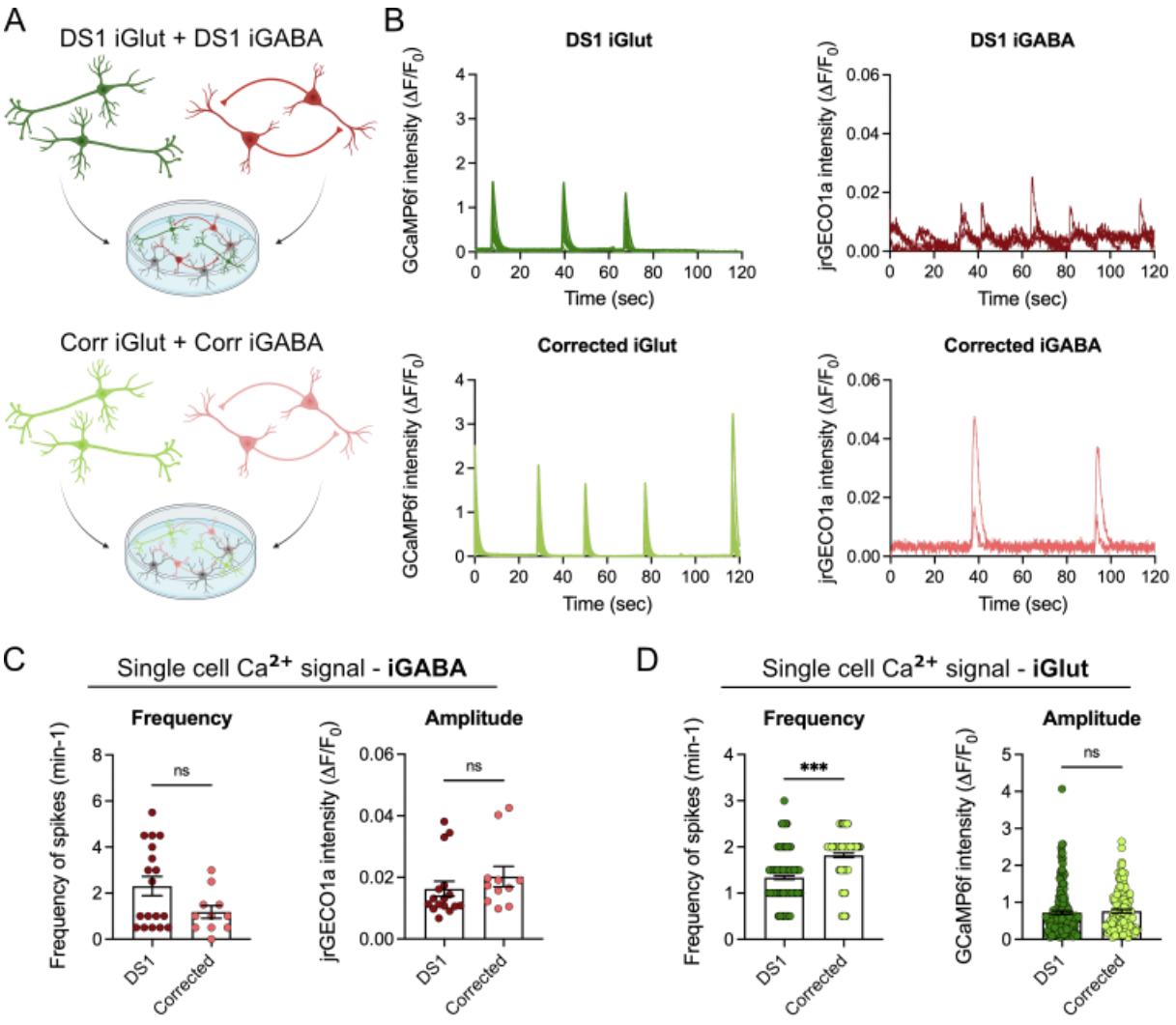

Figure 6.1. *Increased activity of early DS1 interneurons results in decreased activity of early DS1 pyramidal neurons in co-culture (3 weeks).* **A** – Schematic representation of the co-cultures used in this study. Top, a co-culture of DS1 iGlut and DS1 iGABA neurons. Bottom, a co-culture of corrected iGlut and corrected iGABA neurons. **B** – Left, representative calcium traces plotted as the GCaMP6f □F/F0 over time (in green) for DS1 and corrected iGlut in co-cultures at 3 weeks. Right, representative calcium traces plotted as the jrGECO1a □F/F0 over time (in red) for DS1 and corrected iGABA in co-cultures at 3 weeks. **C** – Quantification of the single cell calcium signal amplitude and frequency recorded in iGABA neurons in co-culture at 3 weeks. N=3 biological replicates, n = 11-18 cells. Error bars represent the SEM, Unpaired nonparametric t test + Mann-Whitney test, ns = $p>0.05$. **D** – Quantification of the single cell calcium signal amplitude and frequency recorded in iGlut neurons in co-culture at 3 weeks. N=3 biological replicates, n = 132-186 cells. Error bars represent the SEM, Unpaired nonparametric t test + Mann-Whitney test, ns = $p>0.05$, *** = $p<0.001$.

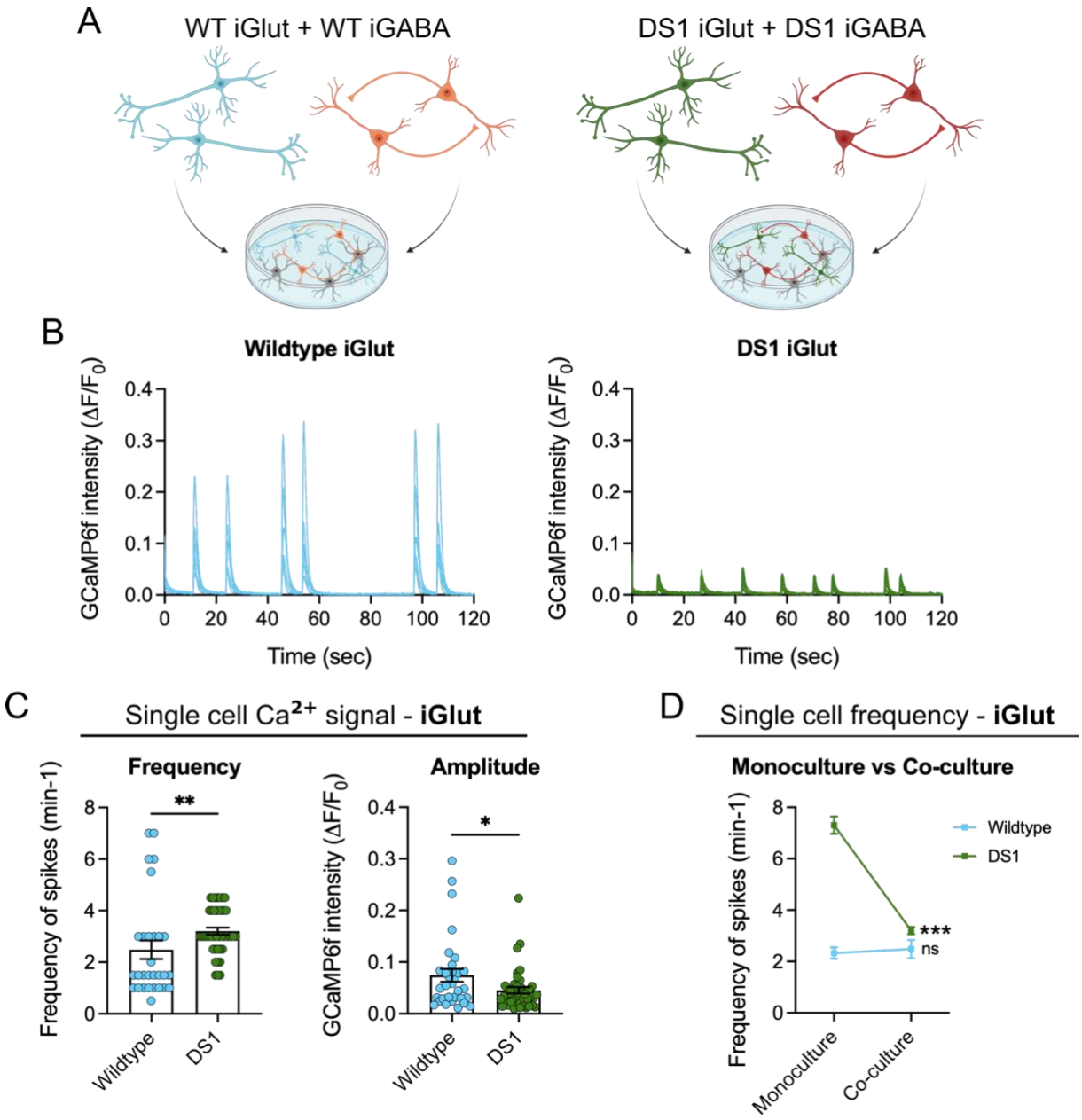

Figure 6.2. *Increased activity of late DS1 excitatory neurons is maintained in co-culture with DS1 inhibitory interneurons (6 weeks).* **A –** Schematic representation of the co-cultures used in this study. Left, a co-culture of WT iGlut and WT iGABA neurons. Right, a co-culture of DS1 iGlut and DS1 iGABA neurons. **B –** Representative calcium traces plotted as the GCaMP6f $\Delta F/F_0$ over time for wildtype and DS1 co-cultures at 6 weeks. **C –** Quantification of the single cell calcium signal amplitude and frequency recorded in iGlut neurons in co-culture at 6 weeks. N=3 biological replicates, n = 32-42 cells. Error bars represent the SEM, Unpaired nonparametric t test + Mann-Whitney test, * = $p<0.05$, ** = $p<0.01$. **D –** Quantification of single cell calcium signal frequency recorded in iGlut neurons in monoculture compared to co-culture at 6 weeks. N=3 biological replicates, n = 29-216 cells. Error bars represent the SEM, Unpaired nonparametric t test + Mann-Whitney test, ns = $p>0.05$, *** = $p<0.001$.

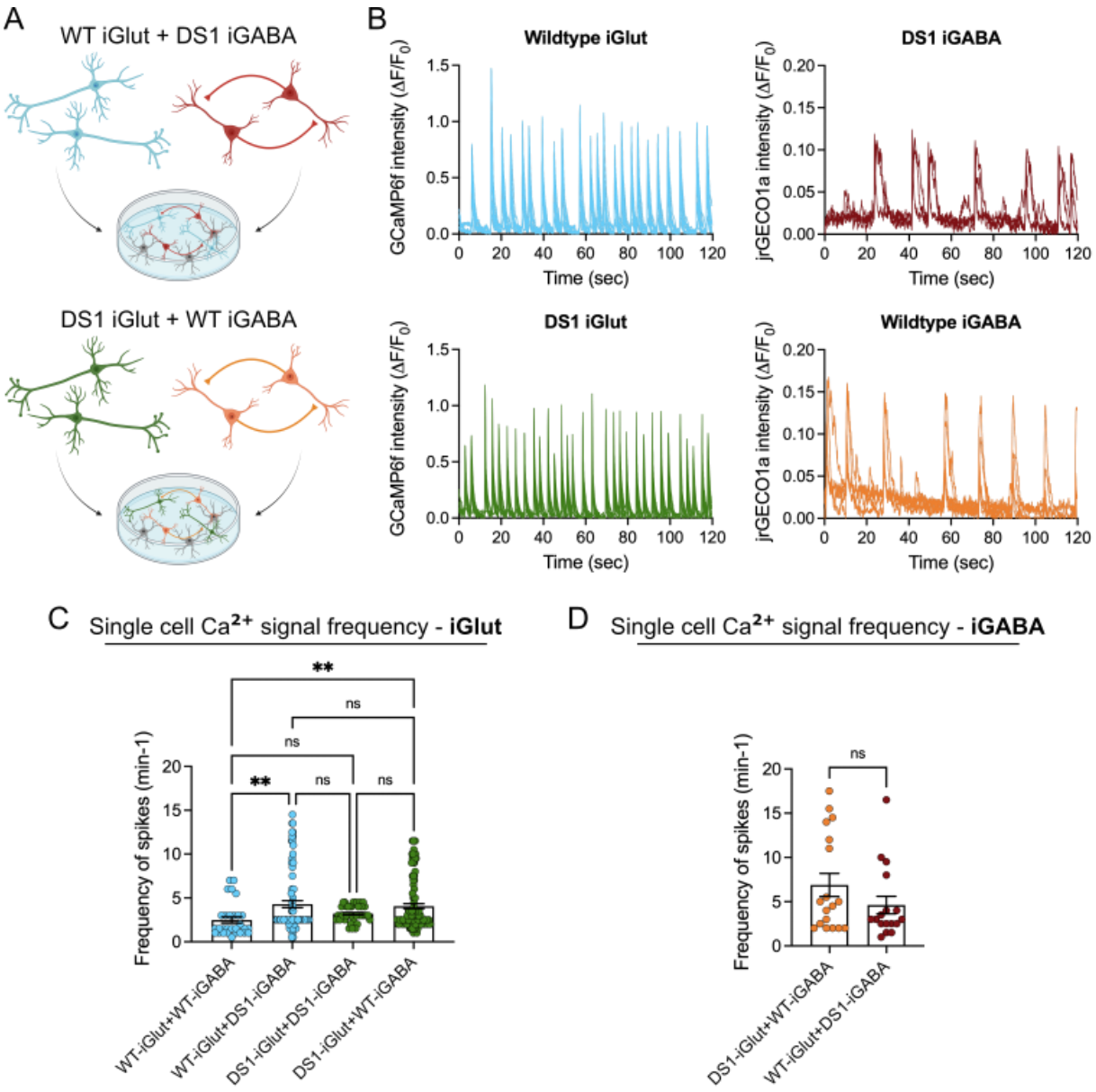

Figure 6.3. *Excitatory and inhibitory neurons contribute equally to the late SCN1A$^{IVS14+3A>T}$ pathogenic phenotype (6 weeks).* **A –** Schematic representation of the mixed genotype co-cultures used in this study. Top, a co-culture of WT iGlut and DS1 iGABA neurons. Bottom, a co-culture of DS1 iGlut and WT iGABA neurons. **B –** Left, representative calcium traces plotted as the GCaMP6f $\Delta F/F_0$ over time (in green) for wildtype and DS1 iGlut in mixed genotype co-cultures at 6 weeks. Right, representative calcium traces plotted as the jrGECO1a $\Delta F/F_0$ over time (in red) for DS1 and wildtype iGABA in mixed genotype co-cultures at 6 weeks. **C –** Quantification of the single cell calcium signal frequency recorded for iGlut neurons in different co-culture combinations at 6 weeks. N=3 biological replicates, n = 29-106 cells. Error bars represent the SEM, Two-way ANOVA with multiple comparison, ns = $p>0.05$, ** = $p<0.01$. **D –** Quantification of the single cell calcium signal frequency recorded for iGABA neurons in different co-culture combinations at 6 weeks. N=3 biological replicates, n = 17-18 cells. Error bars represent the SEM, Unpaired nonparametric t test + Mann-Whitney test, ns = $p>0.05$.

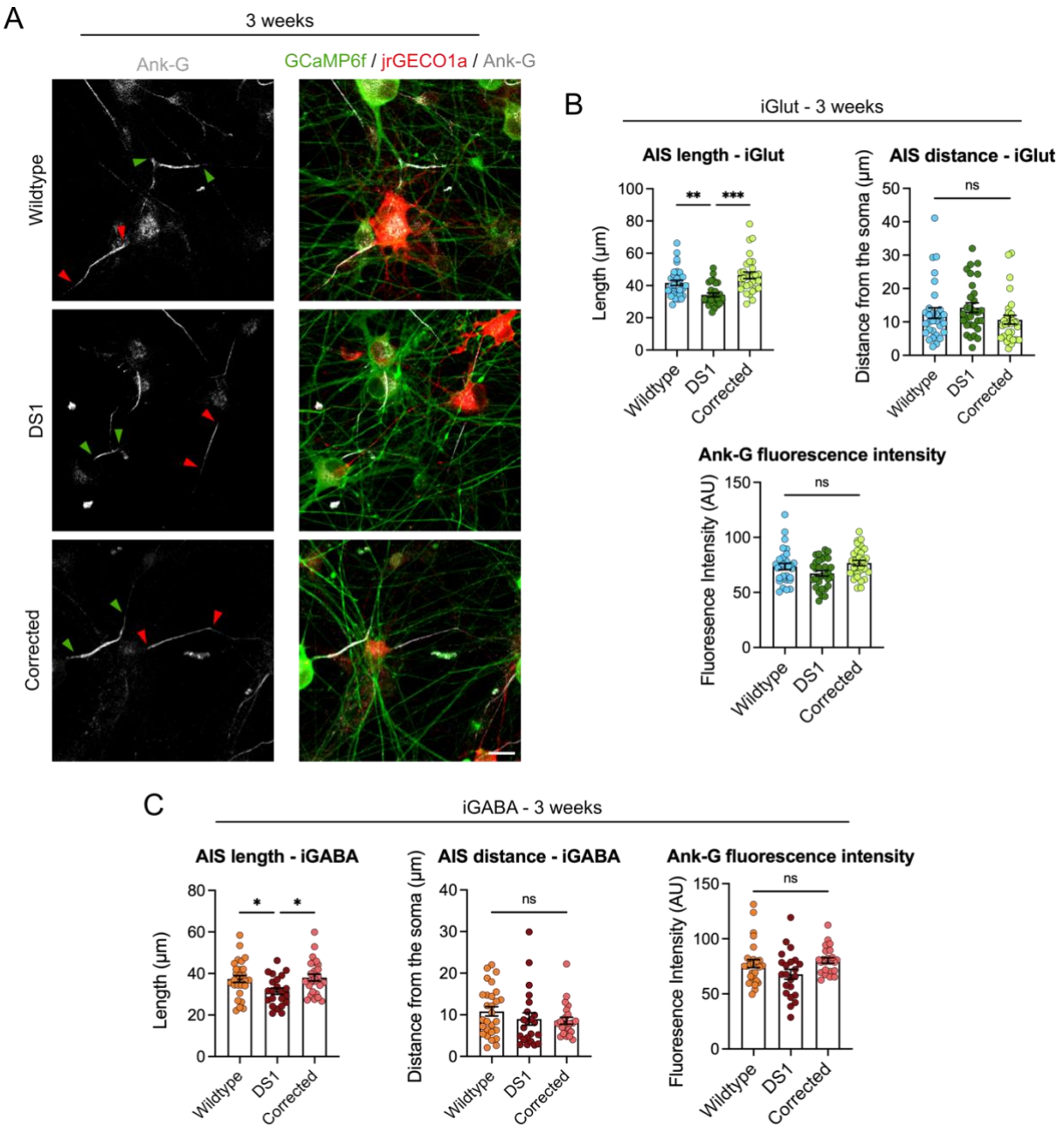

Figure 6.4. *Pathogenic SCN1A$^{IVS14+3A>T}$ causes decreased AIS length in both excitatory and inhibitory neurons in early co-cultures (3 weeks).* **A –** Representative immunofluorescence images of wildtype, DS1 and corrected co-cultures at 3 weeks stained for Ank-G (grey), GFP (GCaMP6f – green) and RFP (jrGECO1a - red). Scale bar = 20 µm. **B –** Quantification of AIS length, distance from the soma and Ank-G fluorescence intensity (based on Ank-G staining relative to GFP staining) in iGlut in co-culture at 3 weeks. N=3 biological replicates, n = 30-31 cells. Error bars represent the SEM, One-way ANOVA Kruskal-Wallis test + Dunn's multiple comparison, ns = $p>0.05$, ** = $p<0.01$, *** = $p<0.001$. **C –** Quantification of AIS length, distance from the soma and Ank-G fluorescence intensity (based on Ank-G staining relative to RFP staining) in iGABA in co-culture at 3 weeks. N=3 biological replicates, n = 22-28 cells. Error bars represent the SEM, Ordinary One-way ANOVA + Tukey's multiple comparison and One-way ANOVA Kruskal-Wallis test + Dunn's multiple comparison, ns = $p>0.05$, * = $p<0.05$.

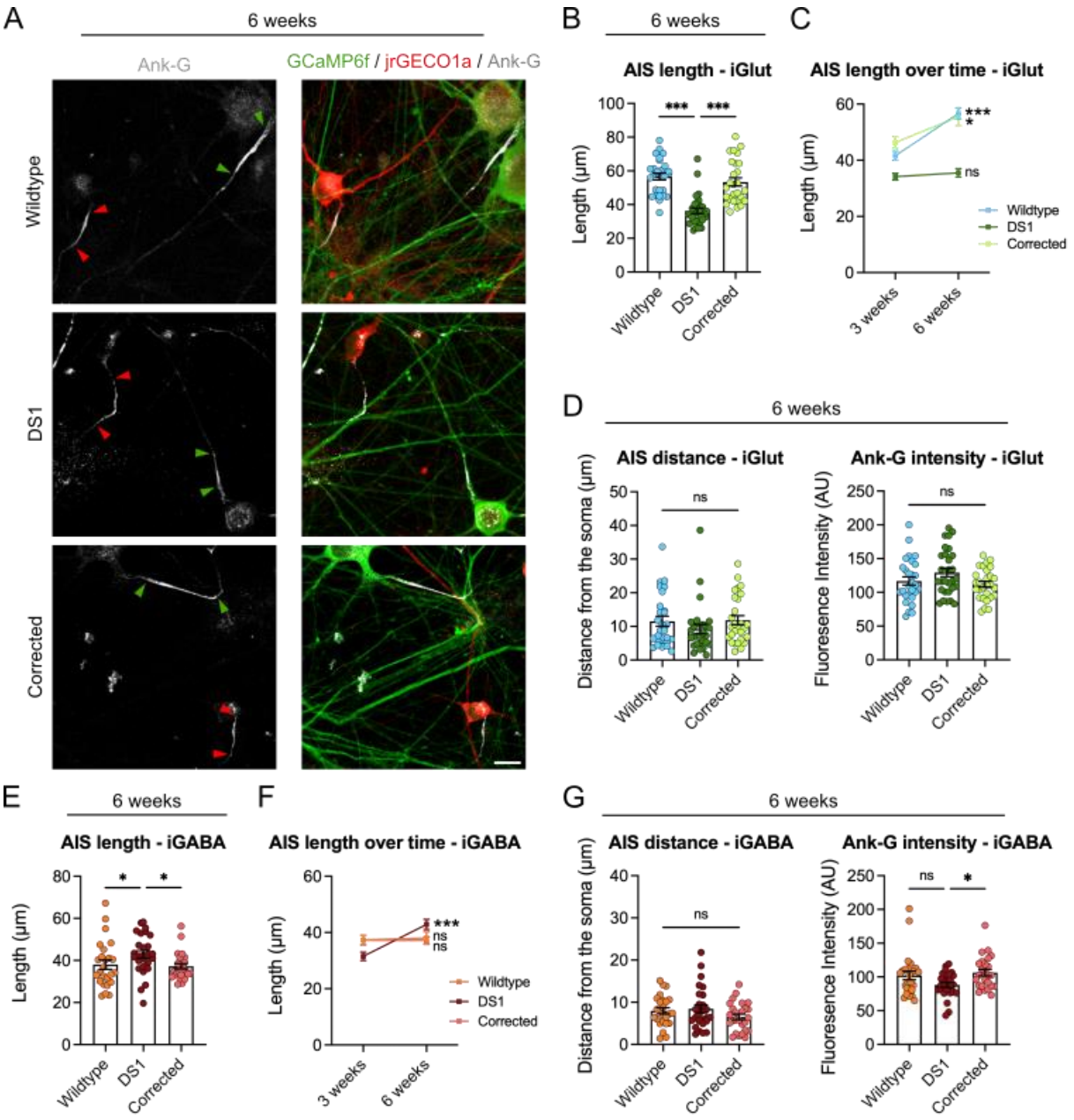

Figure 6.5. *Pathogenic SCN1A$^{IVS14+3A>T}$ impairs AIS homeostatic plasticity in excitatory and inhibitory neurons in late co-cultures (6 weeks).* **A –** Representative immunofluorescence images of wildtype, DS1 and corrected co-cultures at 6 weeks stained for Ank-G (grey), GFP (GCaMP6f – green) and RFP (jrGECO1a - red). Scale bar = 20 µm. **B –** Quantification of AIS length based on Ank-G staining relative to GFP staining in iGlut in co-culture at 6 weeks. N=3 biological replicates, n = 27-30 cells. Error bars represent the SEM, One-way ANOVA Kruskal-Wallis test + Dunn's multiple comparison, *** = p<0.001. **C –** Quantification of AIS length over time in iGlut neurons in co-culture. N=3 biological replicates, n = 27-31 cells. Error bars represent the SEM, Unpaired parametric t test or Unpaired nonparametric t test + Mann-Whitney test, ns = p>0.05, * = p<0.05, *** = p<0.001. **D –** Quantification of AIS distance from the soma and Ank-G fluorescence intensity (based on Ank-G staining relative to GFP staining) in iGlut neurons in co-culture at 6 weeks. N=3 biological replicates, n = 27-30 cells. Error bars represent the SEM, One-way ANOVA Kruskal-Wallis test + Dunn's multiple comparison and Ordinary One-way ANOVA + Tukey's multiple comparison, ns = p>0.05. **E –** Quantification of

AIS length based on Ank-G staining relative to RFP staining in iGABA in co-culture at 6 weeks. N=3 biological replicates, n = 25-27 cells. Error bars represent the SEM, One-way ANOVA Kruskal-Wallis test + Dunn's multiple comparison, * = p<0.05. **F –** Quantification of AIS length over time in iGABA neurons in co-culture. N=3 biological replicates, n = 22-28 cells. Error bars represent the SEM, Unpaired parametric t test or Unpaired nonparametric t test + Mann-Whitney test, ns = p>0.05, *** = p<0.001. **G –** Quantification of AIS distance from the soma and Ank-G fluorescence intensity (based on Ank-G staining relative to RFP staining) in iGABA neurons in co-culture at 6 weeks. N=3 biological replicates, n = 25-27 cells. Error bars represent the SEM, One-way ANOVA Kruskal-Wallis test + Dunn's multiple comparison, ns = p>0.05, * = p<0.05, ** = p<0.01.

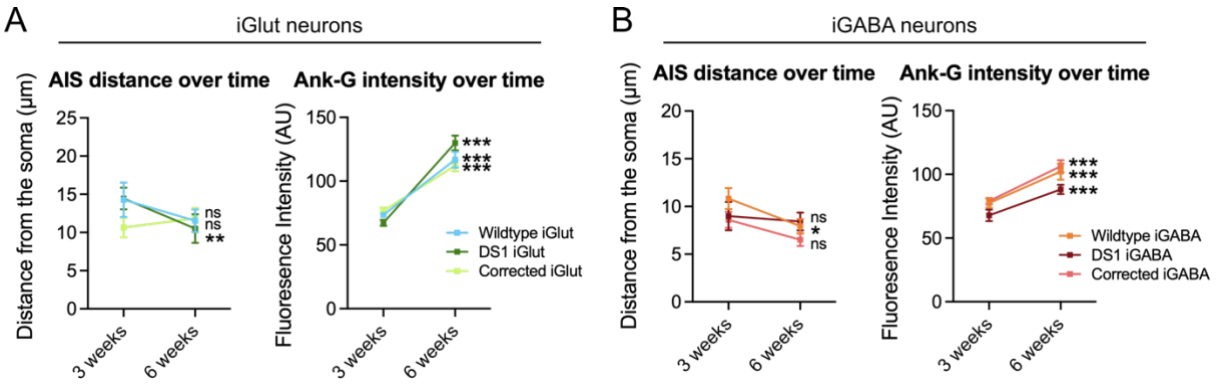

Supplementary Figure 6.1. A – Quantification of AIS distance from the soma and Ank-G fluoresce intensity over time in iGlut neurons in co-culture. N=3 biological replicates, n = 28-31 cells. Error bars represent the SEM, Unpaired parametric t test or Unpaired nonparametric t test + Mann-Whitney test, ns = p>0.05, ** = p<0.01, *** = p<0.001. **B –** Quantification of AIS distance from the soma and Ank-G fluoresce intensity over time in iGABA neurons in co-culture. N=3 biological replicates, n = 22-28 cells. Error bars represent the SEM, Unpaired parametric t test or Unpaired nonparametric t test + Mann-Whitney test, ns = p>0.05, * = p<0.05, *** = p<0.001.

Experiment: Two-colour Ca^{2+} imaging in co-cultures at 3 weeks.

Dataset analysed	Sample size	Normality	Statistical test	P Value (Significance)
iGlut - Single cell Frequency	DS1 N = 186 Corrected N = 132 N = cells from multiple coverslips	DS1 = NO Corr = NO	Unpaired nonparametric t test + Mann-Whitney test	DS1 vs. Corrected = <0.001 (***)
iGlut - Single cell Amplitude	DS1 N = 186 Corrected N = 132 N = cells from multiple coverslips	DS1 = NO Corr = NO	Unpaired nonparametric t test + Mann-Whitney test	DS1 vs. Corrected = 0.2687 (ns)
iGABA - Single cell Frequency	DS1 N = 18 Corrected N = 11 N = cells from multiple coverslips	DS1 = NO Corr = YES	Unpaired nonparametric t test + Mann-Whitney test	DS1 vs. Corrected = 0.2711 (ns)
iGABA - Single cell Amplitude	DS1 N = 18 Corrected N = 11 N = cells from multiple coverslips	DS1 = NO Corr = NO	Unpaired nonparametric t test + Mann-Whitney test	DS1 vs. Corrected = 0.1214 (ns)

Table 6.1. Statistical details of two-colour Ca^{2+} imaging in co-cultures at 3 weeks.

Experiment: Two-colour Ca^{2+} imaging in co-cultures at 6 weeks.

Dataset analysed	Sample size	Normality	Statistical test	P Value (Significance)
iGlut - Single cell Frequency	Wildtype N = 32 DS1 N = 42 N = cells from multiple coverslips	WT = NO DS1 = NO	Unpaired nonparametric t test + Mann-Whitney test	Wildtype vs. DS1 = 0.0011 (**)
iGlut - Single cell Amplitude	Wildtype N = 32 DS1 N = 42 N = cells from multiple coverslips	WT = NO DS1 = NO	Unpaired nonparametric t test + Mann-Whitney test	Wildtype vs. DS1 = 0.0425 (*)
DS1 iGlut single cell Frequency – **Monoculture vs. Co-culture**	Monoculture N = 216 Co-culture N = 42 N = cells from multiple coverslips	WT = NO DS1 = NO	Unpaired nonparametric t test + Mann-Whitney test	Monoculture vs. Co-culture = <0.001 (***)
WT iGlut single cell Frequency – **Monoculture vs. Co-culture**	Monoculture N = 138 Co-culture N = 32 N = cells from multiple coverslips	WT = NO DS1 = NO	Unpaired nonparametric t test + Mann-Whitney test	Monoculture vs. Co-culture = 0.1166 (ns)

Table 6.2. Statistical details of two-colour Ca^{2+} imaging in co-cultures at 6 weeks.

Experiment: Two-colour Ca^{2+} imaging in **mixed genotype** co-cultures at 6 weeks. For all samples, N = cells from multiple coverslips

Dataset analysed	Sample size	Normality	Statistical test	P Value (Significance)
iGlut - Single cell Frequency	WT-iGlut+WT-iGABA N = 32 WT-iGlut+DS1-iGABA N = 83 DS1-iGlut+DS1-iGABA N = 42 DS1-iGlut+WT-iGABA N = 106	NO NO NO NO	Two-way ANOVA with multiple comparison	WT-iGlut+WT-iGABA vs. WT-iGlut+DS1-iGABA = 0.007 (**) WT-iGlut+WT-iGABA vs. DS1-iGlut+DS1-iGABA = 0.26 (ns) WT-iGlut+WT-iGABA vs. DS1-iGlut+WT-iGABA = 0.007 (**) WT-iGlut+DS1-iGABA vs. DS1-iGlut+DS1-iGABA = 0.41 (ns) WT-iGlut+DS1-iGABA vs. DS1-iGlut+WT-iGABA = >0.9999 (ns) DS1-iGlut+DS1-iGABA vs. DS1-iGlut+WT-iGABA = 0.41 (ns)
iGABA - Single cell Frequency	DS1-iGlut+WT-iGABA N = 18 WT-iGlut+DS1-iGABA N = 17	NO NO	Unpaired nonparametric t test + Mann-Whitney test	DS1-iGlut+WT-iGABA vs. WT-iGlut+DS1-iGABA = 0.2329 (ns)

Table 6.3. Statistical details of two-colour Ca^{2+} imaging in **mixed genotype** co-cultures at 6 weeks.

Experiment: AIS characterisation in co-cultures at 3 weeks. For all samples, N = cells from multiple wells

Dataset analysed	Sample size	Normality	Statistical test	P Value (Significance)
AIS length - iGlut	Wildtype N = 31 DS1 N = 30 Corrected N = 30	WT = YES DS1 = NO Corr = NO	One-way ANOVA Kruskal-Wallis test + Dunn's multiple comparison	Wildtype vs. DS1 = 0.0025 (**) Wildtype vs. Corrected = 0.3583 (ns) DS1 vs. Corrected = <0.001 (***)
AIS distance - iGlut	Wildtype N = 31 DS1 N = 30 Corrected N = 30	WT = NO DS1 = NO Corr = NO	One-way ANOVA Kruskal-Wallis test + Dunn's multiple comparison	Wildtype vs. DS1 = 0.6094 (ns) Wildtype vs. Corrected = 0.9014 (ns) DS1 vs. Corrected = 0.0630 (ns)
Ank-G intensity - iGlut	Wildtype N = 31 DS1 N = 30 Corrected N = 30	WT = NO DS1 = YES Corr = YES	One-way ANOVA Kruskal-Wallis test + Dunn's multiple comparison	Wildtype vs. DS1 = 0.6780 (ns) Wildtype vs. Corrected = 0.7487 (ns) DS1 vs. Corrected = 0.0545 (ns)
AIS length - iGABA	Wildtype N = 28 DS1 N = 22 Corrected N = 26	WT = YES DS1 = YES Corr = YES	Ordinary One-way ANOVA + Tukey's multiple comparison	Wildtype vs. DS1 = 0.0348 (*) Wildtype vs. Corrected = 0.9505 (ns) DS1 vs. Corrected = 0.0185 (*)

AIS distance - iGABA	Wildtype N = 28 DS1 N = 22 Corrected N = 26	WT = YES DS1 = NO Corr = NO	One-way ANOVA Kruskal-Wallis test + Dunn's multiple comparison	Wildtype vs. DS1 = 0.3747 (ns) Wildtype vs. Corrected = 0.7820 (ns) DS1 vs. Corrected = >0.9999 (ns)
Ank-G intensity - iGABA	Wildtype N = 28 DS1 N = 22 Corrected N = 26	WT = NO DS1 = YES Corr = NO	One-way ANOVA Kruskal-Wallis test + Dunn's multiple comparison	Wildtype vs. DS1 = 0.4597 (ns) Wildtype vs. Corrected = 0.9199 (ns) DS1 vs. Corrected = 0.0596 (ns)

Table 6.4. Statistical details of AIS characterisation in co-cultures at 3 weeks.

Experiment: AIS characterisation in co-cultures at 6 weeks. For all samples, N = cells from multiple wells

Dataset analysed	**Sample size**	**Normality**	**Statistical test**	**P Value (Significance)**
AIS length - iGlut	Wildtype N = 28 DS1 N = 30 Corrected N = 27	WT = YES DS1 = NO Corr = NO	One-way ANOVA Kruskal-Wallis test + Dunn's multiple comparison	Wildtype vs. DS1 = <0.001 (***) Wildtype vs. Corrected = <0.9999 (ns) DS1 vs. Corrected = <0.001 (***)
AIS distance - iGlut	Wildtype N = 28 DS1 N = 30 Corrected N = 27	WT = NO DS1 = NO Corr = NO	One-way ANOVA Kruskal-Wallis test + Dunn's multiple comparison	Wildtype vs. DS1 = 0.7498 (ns) Wildtype vs. Corrected = >0.9999 (ns) DS1 vs. Corrected = 0.3438 (ns)
Ank-G intensity - iGlut	Wildtype N = 28 DS1 N = 30 Corrected N = 27	WT = YES DS1 = YES Corr = YES	Ordinary One-way ANOVA + Tukey's multiple comparison	Wildtype vs. DS1 = 0.4244 (ns) Wildtype vs. Corrected = >0.9999 (ns) DS1 vs. Corrected = 0.2276 (ns)
AIS length - iGABA	Wildtype N = 25 DS1 N = 27 Corrected N = 26	WT = YES DS1 = YES Corr = NO	One-way ANOVA Kruskal-Wallis test + Dunn's multiple comparison	Wildtype vs. DS1 = 0.0398 (*) Wildtype vs. Corrected = >0.9999 (ns) DS1 vs. Corrected = 0.0318 (*)
AIS distance - iGABA	Wildtype N = 25 DS1 N = 27 Corrected N = 26	WT = YES DS1 = NO Corr = YES	One-way ANOVA Kruskal-Wallis test + Dunn's multiple comparison	Wildtype vs. DS1 = >0.9999 (ns) Wildtype vs. Corrected = 0.5619 (ns) DS1 vs. Corrected = 0.6795 (ns)
Ank-G intensity - iGABA	Wildtype N = 25 DS1 N = 27 Corrected N = 26	WT = NO DS1 = YES Corr = NO	One-way ANOVA Kruskal-Wallis test + Dunn's multiple comparison	Wildtype vs. DS1 = 0.4086 (ns) Wildtype vs. Corrected = 0.9815 (ns) DS1 vs. Corrected = 0.0395 (*)

Table 6.5a. Statistical details of AIS characterisation in co-cultures at 6 weeks.

Experiment: AIS characterisation in **iGlut** neurons in co-cultures over time. For all samples, N = cells from multiple wells.

Dataset analysed	Sample size	Normality	Statistical test	P Value (Significance)
AIS length over time – Wildtype	3 weeks N = 31 6 weeks N = 28	3 weeks = YES 6 weeks = YES	Unpaired parametric t test	3 weeks vs. 6 weeks = <0.001 (***)
AIS length over time – DS1	3 weeks N = 30 6 weeks N = 30	3 weeks = NO 6 weeks = NO	Unpaired nonparametric t test + Mann-Whitney test	3 weeks vs. 6 weeks = 0.3447 (ns)
AIS length over time – Corrected	3 weeks N = 30 6 weeks N = 27	3 weeks = NO 6 weeks = NO	Unpaired nonparametric t test + Mann-Whitney test	3 weeks vs. 6 weeks = 0.0405 (*)
AIS Distance over time – Wildtype	3 weeks N = 31 6 weeks N = 28	3 weeks = NO 6 weeks = NO	Unpaired nonparametric t test + Mann-Whitney test	3 weeks vs. 6 weeks = 0.5087 (ns)
AIS Distance over time – DS1	3 weeks N = 30 6 weeks N = 30	3 weeks = YES 6 weeks = NO	Unpaired nonparametric t test + Mann-Whitney test	3 weeks vs. 6 weeks = 0.0041 (**)
AIS Distance over time – Corrected	3 weeks N = 30 6 weeks N = 27	3 weeks = NO 6 weeks = NO	Unpaired nonparametric t test + Mann-Whitney test	3 weeks vs. 6 weeks = 0.5441 (ns)
Ank-G intensity over time – Wildtype	3 weeks N = 31 6 weeks N = 28	3 weeks = YES 6 weeks = YES	Unpaired parametric t test	3 weeks vs. 6 weeks = <0.001 (***)
Ank-G intensity over time – DS1	3 weeks N = 30 6 weeks N = 30	3 weeks = YES 6 weeks = YES	Unpaired parametric t test	3 weeks vs. 6 weeks = <0.001 (***)
Ank-G intensity over time – Corrected	3 weeks N = 30 6 weeks N = 27	3 weeks = YES 6 weeks = YES	Unpaired parametric t test	3 weeks vs. 6 weeks = <0.001 (***)

Table 6.5b. Statistical details of AIS characterisation in **iGlut** neurons in co-cultures over time.

Experiment: AIS characterisation in **iGABA** neurons in co-cultures over time. For all samples, N = cells from multiple wells.

Dataset analysed	Sample size	Normality	Statistical test	P Value (Significance)
AIS length over time – Wildtype	3 weeks N = 28 6 weeks N = 25	3 weeks = YES 6 weeks = YES	Unpaired parametric t test	3 weeks vs. 6 weeks = 0.8221 (ns)
AIS length over time – DS1	3 weeks N = 22 6 weeks N = 27	3 weeks = YES 6 weeks = YES	Unpaired parametric t test	3 weeks vs. 6 weeks = <0.001 (***)
AIS length over time – Corrected	3 weeks N = 26 6 weeks N = 26	3 weeks = YES 6 weeks = NO	Unpaired nonparametric t test + Mann-Whitney test	3 weeks vs. 6 weeks = 0.6532 (ns)
AIS Distance over time – Wildtype	3 weeks N = 28 6 weeks N = 25	3 weeks = YES 6 weeks = YES	Unpaired parametric t test	3 weeks vs. 6 weeks = 0.0390 (*)
AIS Distance over time – DS1	3 weeks N = 22 6 weeks N = 27	3 weeks = NO 6 weeks = NO	Unpaired nonparametric t test + Mann-Whitney test	3 weeks vs. 6 weeks = 0.8695 (ns)

AIS Distance over time – Corrected	3 weeks N = 26 6 weeks N = 26	3 weeks = NO 6 weeks = YES	Unpaired nonparametric t test + Mann-Whitney test	3 weeks vs. 6 weeks = 0.0975 (ns)
Ank-G intensity over time – Wildtype	3 weeks N = 28 6 weeks N = 25	3 weeks = NO 6 weeks = NO	Unpaired nonparametric t test + Mann-Whitney test	3 weeks vs. 6 weeks = <0.001 (***)
Ank-G intensity over time – DS1	3 weeks N = 22 6 weeks N = 27	3 weeks = YES 6 weeks = YES	Unpaired parametric t test	3 weeks vs. 6 weeks = <0.001 (***)
Ank-G intensity over time – Corrected	3 weeks N = 26 6 weeks N = 26	3 weeks = NO 6 weeks = NO	Unpaired nonparametric t test + Mann-Whitney test	3 weeks vs. 6 weeks = <0.001 (***)

Table 6.5c. Statistical details of AIS characterisation in **iGABA** neurons in co-cultures over time.

6.3 Conclusions

- Hyperexcitability of early inhibitory interneurons causes reduced excitatory activity in co-cultures at **3 weeks**.
    - Early DS1 iGABA neurons display a higher Ca^{2+} signal frequency compared to the corrected line.
    - Increased inhibitory activity in DS1 co-cultures results in a lower Ca^{2+} signal frequency observed for DS1 iGlut neurons compared to the corrected line.
- At **6 weeks**, late DS1 co-cultures display increased excitatory activity compared to wildtype cultures.
- Hypoexcitability of DS1 iGABA neurons and hyperexcitability of DS1 iGlut neurons both contribute to the *SCN1A*$^{IVS14+3A>T}$ -mediated pathogenic phenotype at **6 weeks**.
    - When wildtype iGlut neurons are cultured with DS1 iGABA neurons, their activity increases and becomes comparable to DS1 iGlut neurons.
    - When DS1-iGlut neurons are cultured with WT-iGABA neurons their activity remains increased to the same degree as when they are cultured with DS1 iGABA neurons.
- Activity-dependant AIS homeostatic plasticity in late DS1 co-cultures is not sufficient to overcome the *SCN1A*$^{IVS14+3A>T}$ -mediated pathogenic phenotype.
    - Late DS1 iGlut neurons display homeostatic shortening of the AIS in response to increased network activity, however, this does not restore normal neuronal excitability.
    - Late DS1 iGABA neurons display homeostatic lengthening of the AIS in response to increased network activity, however, this does not restore normal neuronal excitability.

Chapter 7

Discussion, limitations and future perspectives

7.1 Discussion

While the majority of Dravet syndrome (DS) research has historically been carried out using animal models, more recently, an increasing number of studies have used patient-derived hiPSCs to generate neuronal models that recapitulate the exact genetic background of Dravet patients. However, characterisation of DS phenotypes within these models was performed in isolated cultures of either inhibitory or excitatory neurons. While these models offered important new insights into the pathophysiology of DS, the lack of interactions between the excitatory and inhibitory components of neural networks did not allow for a comprehensive study of synergic phenotypes. The aim of this thesis was to establish a novel and comprehensive hiPSC-based disease model of DS suitable for the study of disease mechanisms in the context of neuronal networks with physiological excitation/inhibition balance.

Chapter 3: Engineering hiPSC-derived cortical neurons to model Dravet syndrome

This first result chapter described the development of our human iPSC-derived cortical co-culture system to model Dravet syndrome. To achieve this, different methods for the differentiation of hiPSCs into glutamatergic excitatory neurons, GABAergic inhibitory interneurons and astrocytes were first explored. Classic directed differentiation protocols, based on the temporally controlled application of various small molecules and signalling proteins, were compared with forward programming strategies, based instead on the forced expression of fate-defining transcription factors. Both these methods have been shown to successfully generate mature functional neurons of various subtype identities. The aim was to establish differentiation protocols that would reliably generate homogenous populations of the desired neuronal types, so that they can be assembled in a co-culture system with a strict composition of excitatory and inhibitory neurons in a 70:30 ratio, to resemble the human cortex E/I neuron ratio. For these reasons, one of the main criteria for the selection of an appropriate differentiation strategy was the efficiency of fate specification or, in other words, the efficiency in generating exclusively the desired cell type.

For the generation of excitatory glutamatergic neurons using directed differentiation, two versions of the Shi et al. dorsal differentiation protocol were tested (Y. Shi, Kirwan, & Livesey, 2012). Both versions (D-V1 and D-V2) were successful in generating neural progenitor cells after 35 days. Gene expression analysis revealed that, while these progenitors displayed a prevalently dorsal identity, indicated by high expression of *PAX6*, they also expressed markers of ventral identity, suggesting inefficient fate specification towards the desired dorsal phenotype (Fig. 3.1). For the generation of GABAergic inhibitory interneurons using directed differentiation, the Maroof et al. (Maroof et al., 2013) ventral differentiation protocol (V-V1) was compared with a ventrally adapted version of the Shi et al. protocol (V-V2). While V-V1 differentiation failed, V-V2 was successfully used to generate progenitor cells after 35 days. However, similarly to the dorsal progenitors, gene expression analysis revealed that the obtained ventral progenitors expressed markers of both dorsal (*PAX6*) and ventral identity (*ASCL1*), suggesting poor fate specification efficiency towards the desired ventral phenotype (Fig. 3.2). Although these experiments were only performed once, these results were not unexpected, as poor differentiation efficiency is a common criticism of directed differentiation (S. M. Ho et al., 2015). These approaches typically yield low numbers of differentiating cells and the resulting neuronal populations often contains cells at different developmental stages and even unrelated cell types (B. Y. Hu et al., 2010). In order to use directed differentiation to generate pure populations of excitatory and inhibitory neurons it would be necessary to introduce a purification step to enrich the differentiating cultures for the desired cells. To this end, a Magnetic-Activated Cell Sorting (MACS)-based purification strategy was designed and tested. Specifically, the interneuron specific promoter DLX5/6 was used to drive the expression of the human CD14 cell surface antigen, which could be labelled and used to MACS sort transiently transfected interneuron progenitors from a mixed cell population (Fig. 3.3). The addition of a cell type-specific sorting step represents an important innovation in this differentiation strategy however, it also adds an additional layer of complication and variability to an already time-consuming and labour-intensive process. In fact, another important aspect to consider is the time required by these protocols to generate functional neurons. Neural directed differentiation protocols required 5 weeks to generate neuronal progenitors and a much longer time (up to 3 months) would be needed to achieve functional maturation (Tao & Zhang, 2016). Additionally, even though these protocols were only performed once, they are known to be characterised by high variability and low reproducibility. This is mainly caused by variability in the hiPSC response to signalling molecules, which results in intrinsic differences in

differentiation potential across cell lines (B. Y. Hu et al., 2010; K. Kim et al., 2011; Koyanagi-Aoi et al., 2013; Osafune et al., 2008). These are all important aspects to consider when neuronal populations are derived from different hiPSC lines in order to compare phenotypes across different genetic backgrounds. Forward programming overcomes these limitations by rapidly inducing a neuronal fate through the forced expression of master transcription factors that supersede the effects of intrinsic heterogeneity between hiPSC lines (Y. Zhang et al., 2013). As previously discussed, in forward programming, the transgene expression is typically regulated by a Tet-ON system. Integration of the Tet-ON-regulated transgenes into hiPSC lines is commonly achieved by lentiviral transduction, however, this strategy can result in variability of expression levels, random genomic insertion and transgene silencing and it requires additional selection steps to enrich for the transduced cell population (Darabi et al., 2012; J. R. Smith et al., 2008b). For this project, an alternative and more refined approach was chosen, consisting of targeting genomic safe harbour sites to achieve stable and reproducible transgene integration. Using this strategy, hiPSC lines stably expressing doxycycline inducible transcription factor combinations were generated using TALEN-mediated integration at the AAVS1 safe-harbour locus. Specifically, 3 different hiPSC lines were generated from each genetic background, each expressing the following transcription factors included in a Tet-ON system: (i) NGN2 – for the differentiation of glutamatergic cortical neurons (iGlut) (C. Wang et al., 2017); (ii) ASCL1 and DLX2 – for the generation of GABAergic inhibitory interneurons (iGABA) (Yang et al., 2017); (iii) NF1B and SOX9 – for the generation of astrocytes (iAstro) (Canals et al., 2018) (Fig. 3.4). The forward programming differentiation of each of these lines was easily performed and produced comparable results across all genetic backgrounds. Both neuronal differentiations (iGlut and iGABA) generated morphologically mature neurons in just 10 days. The neurons expressed both pre- and post-synaptic proteins and, by day 35, displayed mature gene expression profiles consistent with their excitatory or inhibitory identity (Fig. 3.5 – 3.6). Neuronal induction and development were reliable and homogenous among the differentiated cell population and, importantly, reproducible across different hiPSC lines. Critically, both neuronal differentiation protocols had very high fate specification efficiency. This was demonstrated by the expression of identity-specific markers as well as lack of expression of markers of the opposite identity (Fig. 3.5 – 3.6). The results obtained with forward programming differentiation were extremely encouraging, especially when compared to directed differentiation. Thanks to its faster developmental time and higher fate specification efficiency, forward programming was chosen, moving forward, as the strategy to use to derive homogenous populations of excitatory and inhibitory neurons.

Using forward programming, it was also possible to generate S100b/GFAP$^+$ astrocytes in less than 14 days (Fig. 3.7). By Day 21, iAstro expressed many astrocyte-specific functional genes, however, when co-cultured with hiPSC-derived neurons, it was found that iAstro impeded neuronal survival (Fig. 3.8). Previous publications have shown that astrocytes constitutively expressing GDNF had a beneficial effect on the survival of motor-neurons (Machado et al., 2019). In order to improve the performance of human iAstro, an iAstro subclone which stably expresses GDNF was generated, however, this line had the same detrimental effect on neuronal survival (Fig. 3.8). Further investigation would be necessary to understand why iAstro exerted this negative effect. It is possible that iAstro were not sufficiently mature yet and further maturation may improve their capacity to support neuron survival. Indeed, well-established directed differentiation approaches to derive astrocytes from hiPSCs require a minimum of 45-60 days to generate mature astrocytes (Taha et al., 2022; Tyzack et al., 2016). Another possibility is that the transcriptomic networks activated by the forced expression of NF1B and SOX9 in human iPSCs are not sufficient to fully recapitulate the functions of mature astrocytes, or they might favour the development of reactive astrocytes. In fact, while GFAP is a widely used marker of astrocytic identity, high expression levels of GFAP are associated with a reactive state of the astrocytes which can contribute to neuronal damage and death (G. L. Yu et al., 2021). An additional problem encountered when using iAstro was their inability to grow on glass surfaces or on any coating reagent other than Matrigel (Supplementary Fig. 3.2). It is unclear whether the astrocytes simply detached from the plate and subsequently died or detached as a consequence of cell death. Either way, this represented a problematic behaviour. The initial phases of iAstro differentiation were always performed on Matrigel-coated tissue culture plastic, before the cells were transferred onto glass or plastic plates coated with a different reagent. For this reason, it is possible that during the initial phase of differentiation, iAstro developed Matrigel-specific adhesion molecules and were incapable of adapting when transferred to new ECM substrates. Novel and improved forward programming approaches for the rapid differentiation of hiPSCs into functionally mature astrocytes have been recently published (Cvetkovic et al., 2022; X. Li et al., 2018b; Neyrinck et al., 2021). These strategies will be tested in the Lieberam lab but lie outside the scope of this PhD thesis.

Given the many problems associated with the use of iAstro, this approach was abandoned. Instead, astrocytes were generated from mouse ESCs using a well-established technology already in use in the Lieberam Lab. mESCs are differentiated and sorted into a pure population of functional astrocytes (mAstro) using a small molecule-based directed differentiation

approach combined with magnetic-activated cell sorting (MACS) of GFAP expressing cells. mAstro were previously engineered to constitutively express GDNF and proven to support long-term neuronal survival (Machado et al., 2019). Using this approach, astrocytes suitable for neuronal co-culture were generated in 19 days (Fig. 3.9) and were shown to support the survival of iGlut and iGABA neurons in long-term co-cultures. mAstro also significantly improved neuronal maturation, as demonstrated by the increased expression levels of many mature neuronal genes (Fig. 3.10). Interestingly, in both wildtype and DS1 iGABA neurons, co-culture with mAstro increased the expression levels of the interneuron subtype-defining genes calbindin, calretinin and somatostatin but not parvalbumin, VIP and NPY. Finally, it was also found that iGlut and iGABA neurons in co-culture with mAstro express increasing levels of *SCN1A* over a 50-day time period (Fig. 3.10). Based on the expression profile, we selected an early (3 weeks) and a late (6 weeks) timepoint to conduct our subsequent experiments. Although *SCN1A* expression was already abundantly detectable at 3 weeks, based on published literature the neuronal cultures have yet to reach maturity so they might not present a significant Dravet-related phenotype (Lam et al., 2017; C. Wang et al., 2017; Yang et al., 2017). As such, a later time point was also selected, at which point the neurons are more mature and more likely to exhibit disease phenotypes.

In order to model DS, patient hiPSCs harbouring a $SCN1A^{IVS14+3A>T}$ loss-of-function mutation (Y. Liu, Lopez-Santiago, et al., 2013) were obtained from the Parent group (University of Michigan) and CRISPR/Cas9-mediated genome editing was used to generate a gene corrected isogenic control line (Fig. 3.11). Plasmid-based delivery of the Cas9 and sgRNA was chosen over synthetic RNP-based delivery. While plasmid transfection has an intrinsically lower efficiency, this method allowed for positive selection of transfected cells through the transient expression of a puromycin resistance gene. To facilitate the identification of edited clones, a silent MspI restriction site was incorporated in the seed region of the sgRNA binding site of the donor template. Mutating the seed region is common practice to prevent the Cas9 enzyme from cleaving template DNA that has already been integrated into the genome. The incorporation of a restriction site allowed a simple PCR and restriction digest screen to be carried out to determine which hiPSC clones had incorporated the donor template DNA. Subsequent Sanger sequencing allowed us to identify a single clone that was successfully edited without "scarring" the region of the genome surrounding the Cas9 cut site or the off-target sites. This clone had normal karyotype and stemness, as well as wildtype-like *SCN1A* transcript production (Fig. 3.11). Incorporating an isogenic control line in this study provides a much higher degree of

confidence that the observed phenotypes are specific to the *SCN1A*$^{IVS14+3A>T}$ mutation and not due to variations between independent hiPSC lines.

The final step in the generation of our *in vitro* model of cortical circuits for the study of DS was the introduction of calcium probes to assess neuronal activity and epileptic phenotypes. Using GECIs, we were able to specifically label excitatory and inhibitory neurons, respectively, with spectrally distinct probes. This allowed us to perform "two-colour" calcium imaging and assign neuronal identity to the recorded calcium signal. Specifically, a GFP-based probe (GCaMP6f) was introduced in excitatory neurons and a mApple-based probe (jrGECO1a) was introduced in inhibitory interneurons (Fig. 3.12). Additionally, having these two distinct fluorescent probes in our system allowed us to confirm that the desired cell-type ratio of 70:30 excitatory to inhibitory neurons could be consistently obtained and reliably maintained in long-term cultures (Fig. 3.12).

The initial aim of this chapter was to generate a fully human model of cortical circuits using hiPSC-derived excitatory neurons, hiPSC-derived inhibitory interneurons and hiPSC-derived astrocytes. Furthermore, the intention was to generate each cell type from wildtype, DS1 and DS1-corrected backgrounds to be able to compare the contribution of the *SCN1A*$^{IVS14+3A>T}$ mutation to Dravet-related phenotypes in a cell type specific manner. The exclusion of forward programming derived astrocytes, and subsequent introduction of mESC-derived astrocytes, meant that this co-culture system could not be used to investigate the astrocytic contribution to the phenotype. While this represented a setback on our initial aims, the primary focus of this study remained neuronal-related phenotypes.

Chapter 4: Pathogenic SCN1A$^{IVS14+3A>T}$ impairs inhibitory interneuron activity

This second result chapter described the characterisation of Dravet-related phenotypes in hiPSC-derived inhibitory interneurons. Specifically, electrophysiological properties were investigated alongside structural properties of the axon initial segment, in early (3 weeks) and late (6 weeks) iGABA neurons derived from wildtype, DS1 and corrected hiPSC lines. We have demonstrated in chapter 3 that, when in co-culture with mAstro, iGABA neurons express relevant amounts of NaV1.1 after 3 weeks of maturation (Chapter 3 Fig. 3.10-G). This led us to believe that a functional impairment of interneuron activity could already be detected in early iGABA. Altered neuronal firing properties in accordance to previous studies on

SCN1A$^{IVS14+3A>T}$ -mediated phenotypes in inhibitory interneurons (Y. Liu, Lopez-Santiago, et al., 2013) were indeed observed at this early time point.

Calcium imaging of induced neuronal activity revealed that early DS1 iGABA neurons have a significantly increased Ca^{2+} signal frequency compared to wildtype and corrected lines (Fig. 4.1), suggesting increased neuronal excitability of DS1 interneurons. Consistent with neuronal hyperexcitability, the AIS of early DS1 iGABA neurons was found to be closer to the cell soma compared to wildtype and corrected lines (Fig. 4.3). Some theoretical models predict that, due to the resistive coupling between the soma and the AIS, a shorter distance between them reduces the axial resistance, which is inversely proportional to the amount of current necessary for axonal depolarisation. Thus, according to these models, a more proximal AIS should be associated with reduced neuronal excitability (Brette, 2013; Telenczuk et al., 2017). In contrast, other theoretical studies have reported reduced excitability when the AIS is more distal (Gulledge & Bravo, 2016). Several experimental studies have shown results in line with these latter models, whereby a distal shift of the AIS is accompanied by reduced neuronal excitability characterised by higher current threshold and lower AP firing frequencies (Grubb & Burrone, 2010; Hatch et al., 2017; Lezmy et al., 2017; Wefelmeyer et al., 2015). We did not observe any changes in current and voltage threshold or AP frequency when intrinsic neuronal excitability was investigated by current clamp experiments in early DS1 iGABA neurons (Fig. 4.2). However, as mentioned previously, it is possible that the high variability observed in the electrophysiological recordings, together with the relatively low number of cells analysed, might be concealing such phenotypes. Furthermore, as previously discussed (*Chapter 3, section 3.2.6*), the derived iGABA cultures contain different interneuron subtypes, each of which is characterised by different electrophysiological properties, including AP amplitude, current and voltage threshold, and AP firing frequency. These intrinsic differences are likely to contribute to the variability observed in the electrophysiological recordings, therefore, in the future, increasing the number of recorded cells could potentially reveal whether a universal interneuron phenotype is present.

Despite the variability within the electrophysiological recordings, early DS1 iGABA neurons were found to have significantly higher Na^+ and K^+ current densities compared to both wildtype and corrected lines (Fig. 4.2) – consistent with neuronal hyperexcitability. This finding is in direct contrast to the phenotype typically observed in animal models of DS, where inhibitory interneurons display reduced Na^+ currents in accordance with the loss-of-function of NaV1.1 (Kalume et al., 2007; F. H. Yu et al., 2006c). Similarly, studies conducted on hiPSC-derived

inhibitory interneurons from DS patients show reduction of Na^+ currents and neuronal excitability (Higurashi et al., 2013b; J. Liu et al., 2016a; Y. Sun et al., 2016). However, inhibitory interneurons derived specifically from the DS1 line, have been previously shown to have a phenotype characterised by increased Na^+ currents and hyperexcitability (Y. Liu, Lopez-Santiago, et al., 2013). Superficially, this might appear to indicate that this phenotype is mutation specific. However, this study recapitulated the same findings in another line derived from a patient with a different Dravet-related mutation (*SCN1A*$^{c.975T>A}$).

In accordance with the authors of this study, we speculated that this hyperexcitability phenotype could be mediated by a compensational mechanism implemented by DS1 interneurons in response to the loss of function of NaV1.1. With this in mind, the expression of different types of sodium, potassium and calcium channels, as well as sodium channel β-subunits and AIS resident proteins was compared in early wildtype, DS1 and corrected iGABA lines (Fig. 4.4). We did not observe any significant difference in the expression level of these genes across populations, suggesting that, if a compensation mechanism is at play, it is either mediated by genes not included in this study or through post-transcriptional mechanisms. A more comprehensive characterisation of differential gene expression, such as through RNA-seq analysis, could possibly reveal if a transcriptionally regulated compensational mechanism exists.

Overall, the characterisation of iGABA neurons at 3 weeks revealed that, at this early time point, iGABA neuronal cultures are still very immature, as evidenced by electrophysiological properties characterised by small AP amplitude and low repetitive firing. As such, the phenotypes observed at this stage might have limited relevance and translatability to the pathophysiological mechanisms of DS. Nonetheless, the study of early phenotypes is essential in order to understand how such phenotypes develop over time.

Interestingly, in contrast to Liu et al., but in line with other studies (Higurashi et al., 2013a; J. Liu et al., 2016b; Y. Sun et al., 2016), when DS1 iGABA neurons were matured for a longer period of time (6 weeks), they started to exhibit a more conventional Dravet phenotype, characterised by reduced excitability. Indeed, calcium imaging of induced neuronal activity revealed that late DS1 iGABA neurons at 6 weeks display a significantly lower Ca^{2+} signal frequency compared to wildtype and corrected iGABA lines (Fig. 4.5), suggesting reduced activity in DS1 interneurons. In further support of this, DS1 iGABA also displayed a lower Ca^{2+}

signal amplitude (Fig. 4.5), indicating lower depolarising amplitudes in these neurons (Akerboom et al., 2012; Shidara et al., 2013).

Hypoexcitability of late DS1 interneurons was also observed in current-clamp recordings. Specifically, the DS1 line showed decreased current-induced repetitive firing and lower maximum AP frequency compared to wildtype and corrected neurons (Fig. 4.6). It is important to note that, while these results are in agreement with a reduction in neuronal excitability, they were not found to be statistically significant. As previously mentioned, the presence in culture of interneuron subtypes with different electrophysiological properties likely contributes to variability within the dataset. Future experiments focussed on increasing the number of recordings might be sufficient to overcome this heterogeneity and possibly reveal a universal interneuron phenotype. This notion is supported by the Ca^{2+} imaging data, which demonstrates statistical significance and is sampled from a higher number of cells.

In both *in vivo* and *in vitro* models of DS, Na^+ currents have been reported to be decreased in inhibitory interneurons (Kalume et al., 2007; J. Liu et al., 2016a; Y. Sun et al., 2016; F. H. Yu et al., 2006c). However, it is important to note that often, in mouse models, reduced Na^+ currents were shown to be dependent on the background strain of the mice owing to strain-specific genetic modifier genes (Miller, Hawkins, Mccollom, et al., 2014; Mistry et al., 2014; F. H. Yu et al., 2006c). This suggests that the heterozygous deletion of NaV1.1, alone, might not be sufficient to cause a reduction in Na^+ currents. While in early DS1 iGABA we found increased Na^+ and K^+ current densities, at the later timepoint, currents were found to be comparable in all populations (Fig. 4.6). In this study, putative Na^+ currents (based on the minimum fast inward current) and putative K^+ currents (based on the average steady-state output) were estimated from voltage clamp recordings. Using this method, measurements of current amplitude, kinetics and voltage dependence could be contaminated by membrane conductance to the non-sodium ions. Additionally, voltage-clamping the soma is not sufficient to control the membrane potential in other neuronal compartments, such as the AIS which is dense in NaV channels. As a result, axonal NaV channels escape voltage clamp and generate uncontrolled currents that cannot be isolated from somatic currents (Bar-Yehuda & Korngreen, 2008; Hartline & Castelfranco, 2003). In the future, accurate assessment of somatic Na^+ currents should be performed in isolation from families of inward and outward currents, using electrophysiological solutions designed to eliminate voltage-dependent potassium and calcium currents (Y. Sun et al., 2016) or a voltage pre-pulse (Milescu et al., 2010). A more accurate characterisation of Na^+ currents might reveal if and how these currents are affected in our model of DS.

Overall, electrophysiological assessment of late DS1 interneurons suggested a phenotype characterised by reduced excitability. Such a phenotype has been previously shown to be associated with shortening and distal relocation of the AIS (Grubb & Burrone, 2010; Hatch et al., 2017; Lezmy et al., 2017; Wefelmeyer et al., 2015). However, the AIS of DS1 iGABA neurons extended in length over time, like wildtype and corrected iGABA, and while it did relocate distally, the distance from the soma at 6 weeks was comparable across all neuronal populations (Fig. 4.7). It is important to consider that a culture containing exclusively inhibitory interneurons represents a unique experimental condition. Neuronal cultures lacking excitatory inputs don't allow for the assessment of activity-dependant phenotypes, such as AIS plasticity. To better understand AIS homeostatic plasticity mechanisms in our cortical interneurons, and how these might be affected in DS, further experiments will need to be performed to assess the AIS response to increased or decreased levels of neuronal activity in cultures (Chand et al., 2015; Grubb & Burrone, 2010). While no differences in AIS length or distance were observed, DS1 iGABA neurons were found to have a lower average of Ank-G fluorescence intensity (Fig. 4.7). A lower availability of Ank-G might reduce the density of NaV channels at the AIS, causing reduced neuronal excitability. To test this hypothesis, future experiments should be performed where the presence of NaV channels at the AIS is quantified by immunolabelling. Together, these observations would support AIS impairment as a potential contributor to the hypoexcitability phenotype in DS1 iGABA neurons.

Interestingly, the stronger phenotypic observations pointing towards hypoexcitabilty of DS1 iGABA neurons were made in experimental conditions where neuronal activity was induced. Specifically, the trend towards decreased current-induced repetitive firing exhibited by late DS1 iGABA was more accentuated by the injection of higher currents. Similarly, the pronounced decreased activity phenotype observed in DS1iGABA by Ca^{2+} imaging was the result of recordings performed in a buffer with increased Ca^{2+} and K^{+} concentration in order to induce neuronal activity. De Stasi et al., (De Stasi et al., 2016) showed that, in brain slices, PV and SST interneurons displayed a decreased efficiency in AP generation in response to depolarising currents, however, these deficits were not observed in recordings of spontaneous cortical dynamics *in vivo*. When interneuron dysfunction was artificially induced (by optogenetic regulation) in wildtype animals, interneuron hypoexcitability elicited significant networks effect. These observations suggest that during spontaneous network dynamics, when the frequencies are below a certain threshold, interneurons might behave normally. Instead, if the network is faced with a strong stimulus, they might lose their ability to fire at higher frequency,

suggesting that additional cellular and network mechanisms may be involved in the pathophysiology of DS (De Stasi et al., 2016).

Chapter 5: Pathogenic SCN1A$^{IVS14+3A>T}$ causes hyperactivity of excitatory neurons

This next chapter described the characterisation of Dravet-related phenotypes in hiPSC-derived excitatory neurons. Like in the previous chapter, electrophysiological properties were investigated, alongside structural properties of the axon initial segment, in early (3 weeks) and late (6 weeks) iGlut derived from wildtype, DS1 and corrected hiPSC lines. We have shown in chapter 4 that DS1 interneurons undergo an initial phase of hyperexcitability, followed by a more conventional state of reduced excitability. Unlike inhibitory interneurons, the excitability of DS1 iGlut neurons seemed initially unaffected (3 weeks) and later characterised by hyperexcitability (6 weeks). Hyperexcitability of pyramidal neurons has been previously observed in multiple animal and hiPSC-based studies (also including *SCN1A*$^{IVS14+3A>T}$ mutation) (Almog et al., 2021; Jiao et al., 2013b; Y. Liu, Lopez-Santiago, et al., 2013; Mistry et al., 2014; van Hugte et al., 2023).

Neuronal function of early DS1 iGlut was initially characterised by calcium imaging. Neuronal activity was studied under stimulating conditions (4 mM Ca^{2+} and 8 mM K^{+}) and the dynamics of Ca^{2+} signal amplitude and frequency were found to be comparable across wildtype, DS1 and corrected neurons (Fig. 5.1). Ionic currents and intrinsic properties of early DS1 iGlut were also characterised, using voltage and current clamp. No differences were observed in Na^{+} and K^{+} current densities in early DS1 iGlut neurons and, similarly, AP properties and intrinsic excitability were found to be comparable across all neuronal populations (Fig. 5.2). Finally, the properties of the AIS were also investigated in early DS1 iGlut neurons. Consistent with the electrophysiological characterisation, all the parameters assessed were found to be comparable across neuronal lines. AIS length, distance from the soma and average Ank-G expression were not altered in DS1 excitatory neurons (Fig. 5.3). Overall, early DS1 iGlut displayed normal neuronal functions.

Interestingly, upon further maturation, DS1 iGlut neurons started to exhibit a phenotype characterised by increased excitability. Specifically, when neuronal function was characterised by calcium imaging under stimulating conditions (4 mM Ca^{2+} and 8 mM K^{+}), late DS1 iGlut neurons displayed considerably increased Ca^{2+} signal frequency comparable to wildtype and corrected neurons. Surprisingly, Ca^{2+} signal amplitude was instead found to be lower in DS1

iGlut neurons (Fig. 5.4). Since Ca^{2+} signals are a direct representation of calcium transients mediated by CaV, we speculated that a lower Ca^{2+} signal amplitude could be caused by altered expression of CaV in DS1 iGlut neurons. Indeed, as part of a subsequent gene expression characterisation, we found that the expression of *CACNA1G*, encoding for the voltage-gated sodium channel CaV3.1, was significantly reduced in both DS1 and corrected iGlut. CaV3.1 is a low-voltage-activated T-type Ca^{2+} channel involved in the generation of low-threshold spikes, which in turn trigger a burst of action potentials mediated by Na^{+} channels (Perez-Reyes, 2003). Interestingly, this gene has been previously identified as a genetic modifier of epilepsy in a mouse model of DS (Calhoun et al., 2017) and epilepsy caused by *SCN2A* mutations (Calhoun et al., 2016; Hawkins & Kearney, 2012). The presence of a *CACNA1G* modifier mutation in the DS1 line could explain why the detected expression of this gene is altered in both DS1 and corrected neurons and might explain why DS1 iGlut neurons display a lower Ca^{2+} signal amplitude. If this was the case, Ca^{2+} signal amplitude in corrected neurons should also be lower, but unfortunately, as previously discussed, amplitude data from the corrected lines couldn't be compared with wildtype and DS1 data. Further work to sequence the CACNA1G gene in the DS1 line will be necessary to confirm this observation.

The same Ca^{2+} signal dynamics were observed when spontaneous neuronal activity was investigated by calcium imaging under physiological conditions (2 mM Ca^{2+} and 5 mM K^{+}). Late DS1 iGlut neurons displayed a reduced Ca^{2+} signal amplitude and a greatly increased Ca^{2+} signal frequency compared to wildtype and corrected neurons (Fig. 5.5). Stimulating imaging conditions were found to decrease Ca^{2+} signal frequencies in wildtype and corrected neurons. Indeed, it is widely known that increasing extracellular Ca^{2+} concentrations decreases neuronal intrinsic excitability (B. L. Jones & Smith, 2016; Lu et al., 2010; Martiszus et al., 2021; Penn et al., 2016; Yue et al., 2008). However, DS1 cultures displayed a similar, or even increased frequency in induced compared to spontaneous conditions (Fig. 5.5). Interestingly, the depolarising shift in voltage-dependence of NaV channels (Martiszus et al., 2021) has been proposed as a possible mechanism to explain decreased excitability in response to high extracellular Ca^{2+} concentrations (Martiszus et al., 2021). Considering the loss of function of NaV1.1 in DS1 neurons, the observation that their excitability is unaffected or even enhanced by higher extracellular Ca^{2+} concentrations could imply a role for NaV1.1 in mediating this mechanism. Independently from this observation, spontaneous and induced calcium imaging data both suggested an increase in neuronal excitability in late DS1 excitatory neurons.

Possible indications of hyperexcitability of late DS1 iGlut neurons were also observed in current-clamp recordings. Specifically, DS1 iGlut showed a trend towards increased current-induced repetitive firing and higher maximum AP frequency compared to wildtype and corrected neurons (Fig. 5.6). It is important to note that, while these results are in agreement with increased neuronal excitability, they were not found to be statistically significant, possibly due to the small size of the dataset. Future experiments with higher numbers of recorded cells could potentially reveal whether the observed trend is representative of a significant difference across populations.

In both *in vivo* and *in vitro* models of DS, Na^+ currents have been occasionally reported to be increased in pyramidal neurons (Jiao et al., 2013b; Y. Liu, Lopez-Santiago, et al., 2013; Mistry et al., 2014). In this study however, contrarily to previously reported DS1 phenotypes (Y. Liu, Lopez-Santiago, et al., 2013), Na^+ and K^+ current densities were comparable across all neuronal populations (Fig. 5.6). As mentioned in for the previous chapter, in this study, putative Na^+ and K^+ currents were estimated from voltage clamp recordings based on the minimum fast inward current and average steady-state output. This method doesn't allow for the accurate assessment of somatic Na^+ currents, as they might be contaminated by membrane conductance to non-sodium ions and cannot be isolated from uncontrolled axonal currents (Bar-Yehuda & Korngreen, 2008; Hartline & Castelfranco, 2003). As suggested for the characterisation of currents in iGABA neurons, future assessment of somatic Na^+ currents should be performed in isolation from families of inward and outward currents, using electrophysiological solutions designed to eliminate voltage-dependent potassium and calcium currents (Y. Sun et al., 2016) or a voltage pre-pulse (Milescu et al., 2010).

Overall, electrophysiological assessment of late DS1 excitatory neurons suggested a phenotype consistent with increased excitability. Neuronal hyperexcitability has been previously shown to be associated with lengthening and proximal relocation of the AIS (Grubb & Burrone, 2010; Hatch et al., 2017; Lezmy et al., 2017; Wefelmeyer et al., 2015). These trends were not observed in DS1 iGlut neurons, where the AIS remained short and did not proximally relocate, contrarily to wildtype and corrected neurons (Fig. 5.7). Shortening of the AIS associated with increased neuronal excitability of pyramidal neurons have been previously reported in animal models of epilepsy (T. T. Liu et al., 2017; Y. Wang et al., 2016). This shortening was attributed to irreversible calpain-mediated proteolysis of Ank-G triggered by seizure-induced hypoxia. Since this is not a condition that could have happened in our *in vitro* system, we speculate that AIS

homeostatic plasticity might be impaired in late DS1 iGlut. Indeed, shortening of the AIS is a well-established plasticity mechanism by which neurons decrease their intrinsic excitability in response to chronic depolarisation (Evans et al., 2015; Galliano et al., 2021; Jamann et al., 2021b; Sohn et al., 2019). It is possible that DS1 iGlut have a normal homeostatic response to the increased excitatory activity in the culture, however, this is not sufficient to counterbalance the primary cause of increased neuronal excitability. Further characterisation of AIS homeostatic plasticity mechanisms in our pyramidal neurons might reveal if and how these might be affected in DS.

Finally, in an attempt to explain the causes of the increased excitability observed in late DS1 iGlut neurons, we investigated whether a transcriptionally-regulated compensational mechanism might be responsible. The expression of different types of sodium, potassium and calcium channels, as well as sodium channel beta subunits and AIS resident proteins was compared in late wildtype, DS1 and corrected iGlut neurons (Fig. 5.8). Interestingly, we found that a variety of different sodium and calcium channels were upregulated in DS1 iGlut neurons. These include NaV1.1 (*SCN1A*), NaV1.2 (*SCN2A*), NaV1.3 (*SCN3A*), NaV1.6 (*SCN8A*), NaV1.7 (*SCN9A*) and sodium channel β subunit 2 (*SCN2B*), as well as CaV1.1 (*CACNA1S*) and CaV2.2 (*CACNA1B*). Although it is important to note that the observed differences did not reach statistical significance, they suggest that an array of different genes may be involved in regulating this phenotype. Indeed, a similar trend towards upregulation has been previously observed for NaV1.2 and NaV1.8 in animal models of DS (Mistry et al., 2014). Considering the important role of these channels in maintaining neuronal excitability, their upregulation might result in elevated activity that goes beyond compensation of NaV1.1 loss-of-function resulting in hyperexcitability.

Chapter 6: Excitatory and inhibitory neurons both contribute to the SCN1A$^{IVS14+3A>T}$ pathogenic phenotype

This final chapter described the characterisation of *SCN1A*$^{IVS14+3A>T}$ -mediated phenotypes in co-culture models of cortical circuits. Specifically, iGlut neurons expressing GCaMP6f and iGABA neurons expressing jrGECO1a were assembled, together with mAstro, into co-cultures with a stable ratio of 70% excitatory neurons and 30% inhibitory interneurons to resemble the human cortex E/I ratio. The presence of two spectrally distinct calcium indicators allowed us

to assess the specific activity and AIS properties of the two different neuronal populations within the co-culture. Crucially, the use of a co-culture model allowed us to assess the relative contribution of individual population phenotypes on the overall network activity.

We have shown that at the early time point of 3 weeks, DS1 iGABA neurons in monoculture displayed increased neuronal activity (Chapter 4) while the activity of early DS1 iGlut neurons in monoculture was not affected by the *SCN1A*$^{IVS14+3A>T}$ mutation (Chapter 5). In co-cultures, early DS1 iGABA neurons still displayed increased levels of activity and this increase in inhibition resulted in a significant decrease in the activity of DS1 iGlut neurons in co-culture (Fig. 6.1). This represented an important experimental indication that iGlut and iGABA neurons were forming functional neuronal networks when assembled into our *in vitro* co-culture system. Furthermore, as a result of these E/I interactions, which were lacking in the monoculture models, early DS1 iGlut and iGABA neurons in co-culture exhibited a shorter AIS (Fig. 6.4). This phenotype, which was not observed in early monocultures (Fig. 4.3 and Fig. 5.3), can be interpreted as an activity-dependant homeostatic response to the increased levels of inhibition. Indeed, as previously discussed, shortening the AIS is an AIS-mediated homeostatic mechanism employed by neurons to decrease their intrinsic excitability and restore physiological levels of activity (Evans et al., 2015; Galliano et al., 2021; Jamann et al., 2021b; Sohn et al., 2019).

The study of *SCN1A*$^{IVS14+3A>T}$ -mediated phenotypes in early neuronal cultures is essential in order to assess how such phenotypes develop over time. However, in isolation, the observations made at this early time point have very limited relevance and translatability to the pathophysiological mechanisms of DS. Indeed, early neuronal cultures are still very immature, as evidenced by the electrophysiological characterisations discussed for chapter 4 and 5. Instead we have shown that, at the later time point of 6 weeks, neurons display more mature electrophysiological properties, including repetitive firing and, for iGlut neurons, synchronous "network-like" activity. Previous studies on DS have demonstrated that hiPSC-derived neurons with a similar level of maturity display relevant disease phenotypes. Specifically, decreased inhibition consistent with Dravet animal models as well as network activity consistent with patient-specific clinical features have both been observed (Higurashi et al., 2013b; J. Liu et al., 2016a; Y. Liu, Lopez-Santiago, et al., 2013; Y. Sun et al., 2016; van Hugte et al., 2023).

In accordance with this literature, in our own late monoculture studies, we found that DS1 iGABA neurons displayed decreased neuronal activity (Chapter 4) while late DS1 iGlut neurons exhibited a pronounced phenotype characterised by hyperexcitability (Chapter 5). In co-culture,

late DS1 iGlut neurons displayed the same phenotypic profile observed in monocultures, namely a higher Ca^{2+} signal frequency compared to wildtype (Fig. 6.2). However, the strength of this phenotype was substantially reduced compared to the one observed in monoculture, owing to the residual inhibitory effect of DS1 iGABA neurons. Even though we were not able to directly assess the activity of iGABA neurons in late co-cultures, we have no reason to believe that the net effect of their activity would differ from the one observed in monocultures. Nonetheless, this should be confirmed in future studies.

Similarly to what we observed in late iGlut monocultures, the increased excitatory activity in late co-cultures is likely to be responsible for the reduced AIS length observed in DS1 iGlut neurons (Fig. 6.5). Indeed, shortening the AIS should result in decreased intrinsic excitability, however, this homeostatic response does not seem to be sufficient to counterbalance the primary cause of increased neuronal excitability in late DS1 iGlut neurons. On the other hand, DS1 iGABA neurons in co-culture extend their AIS (Fig. 6.5). This phenotype was not observed in late iGABA monocultures (Fig. 4.7), where E/I interactions were lacking. For this reason, lengthening of the AIS in DS1 iGABA neurons could also be attributed to the increased excitatory activity in late co-cultures, driving a homeostatic response to potentiate DS1 iGABA neurons inhibitory activity and restore E/I balance in the network. However even in this case, this response is not sufficient to overcome the primary cause of decreased neuronal excitability in late DS1 iGABA neurons. AIS elongation in GABAergic inhibitory interneurons has also been observed in a DS mouse model. Interestingly, this study showed that the impaired activity of interneurons was only limited to the severe stage of the disease, during which inhibitory interneurons extend their AIS but still displayed reduced intrinsic excitability. Following this stage, the AIS remains elongated and the excitability of inhibitory neurons was restored (Favero et al., 2018).

The 'interneuron hypothesis' postulates that seizures in DS arise due to the reduced activity of GABAergic interneurons, producing a network that lacks sufficient inhibitory tone (Chopra & Isom, 2014). Since this hypothesis has been formulated (F. H. Yu et al., 2006b), evidence of pyramidal neuron-specific phenotypes has emerged in animal models as well as hiPSC-derived *in vitro* systems. However, so far excitatory and inhibitory phenotypes have mainly been studied in isolation, or in the context of a homogenous genetic background, such as global *Scn1a*$^{+/-}$ mice models. In some animal studies, one *Scn1a* allele was conditionally inactivated only in parvalbumin interneurons or only in excitatory neurons to assess the contribution of the different mutated populations to the epileptic phenotype (Dutton et al., 2013; Ogiwara et al.,

2013). One study found that conditional *Scn1a* inactivation in parvalbumin interneurons, but not excitatory neurons, was sufficient to increase the susceptibility to fluorothyl (a convulsant agent) and hyperthermia-induced seizures. Furthermore, reduced interneuron-specific *Scn1a* expression resulted in the generation of spontaneous seizures (Dutton et al., 2013). Another study also found that parvalbumin-specific *Scn1a* inactivation was sufficient to cause spontaneous epileptic seizures and when *Scn1a* was inactivated in excitatory neurons, additionally to parvalbumin neurons, this had a beneficial effect on the severe epileptic phenotype (Ogiwara et al., 2013). However, the presence of spontaneous epileptic activity in animals with selective inactivation of *Scn1a* in excitatory neurons only was not investigated in either study.

Using our model of neuronal networks, composed of ratio-defined excitatory and inhibitory neurons, we were able to perform a similar experiment *in vitro*, using Dravet patient-derived neurons. Specifically, we were able to assess the isolated contribution that impaired inhibition (DS1 iGABA neurons) or increased excitation (DS1 iGlut neurons) have, respectively, on the overall network activity. To this end, we generated the following "mixed genotype" co-cultures, WT-iGlut+DS1-iGABA and DS1-iGlut+WT-iGABA, and compared their activity with fully wildtype (WT-iGlut+WT-iGABA) and fully Dravet (DS1-iGlut+DS1-iGABA) co-cultures. Interestingly, we found that the overall excitatory activity in the network was equally increased in WT-iGlut+DS1-iGABA and DS1-iGlut+WT-iGABA compared to fully wildtype cultures, and the observed increase was comparable to the one observed in fully Dravet cultures (Fig. 6.3). These results indicate that the presence of the *SCN1A*$^{IVS14+3A>T}$ mutation in either the excitatory or the inhibitory component of the network is sufficient, in both cases, to cause a disease phenotype characterised by increased excitatory activity.

While these results differed from the ones observed in animal models, if confirmed, the equal contribution to the phenotype from both excitatory and inhibitory neurons could have important implications for the treatment of DS. As previously discussed, first- and second-line Dravet treatments involve the use of GABA-agonists to restore appropriate levels of inhibition. However, these treatments typically fail to achieve seizure-control (He et al., 2022). When used in combination, their combined inhibitory enhancing activity has better results, however, still far from satisfactory seizure-control (Strzelczyk & Schubert-Bast, 2022). If excitatory neurons were indeed playing an active role in mediating the epileptic phenotype of DS, this could explain why restoring inhibition, alone, is not enough to achieve seizure-freedom. Interestingly, two "add-on" treatments recently approved for the management of DS are fenfluramine and

cannabidiol. While the exact mechanism of their anticonvulsant activity is not fully understood yet, both compounds are thought to act through combined effects of increasing GABAergic inhibition as well as decreasing glutamatergic activity (P. Martin et al., 2021; Rosenberg et al., 2017; Y. Sun & Dolmetsch, 2018). Emerging surveillance studies revealed that up to 51% of patients treated with fenfluramine have stopped the concomitant dosage of other anti-seizure medications (Guerrini et al., 2022), suggesting that the effect mediated by this drug is, alone, sufficient to achieve a satisfactory reduction of seizure frequency.

Overall, our co-culture model represents an innovative platform that can be applied to investigate mutation-specific phenotypes in order to identify common and distinct pathological mechanisms and test novel DS treatments. Uncovering common disease mechanisms would substantially contribute to advancing our knowledge on Dravet syndrome pathophysiology and promote the discovery and development of novel therapeutical approaches.

7.2 Limitations

The work described in this thesis provided interesting new insights into the pathophysiology of *SCN1A*$^{IVS14+3A>T}$ -mediated Dravet syndrome however, some of the limitations associated with this work must be discussed. Firstly, we described the generation of a cortical model composed of identity-defined excitatory and inhibitory neurons assembled at physiological ratios to resemble the human cortex. While such model is innovative in the way cortical networks are assembled to have physiological E/I balance, it still constitutes a very basic and reductionist model of cortical circuits. Adherent 2-dimensional (2D) cultures are not a physiological representation of neuronal networks *in vivo*, where neurons assemble into complex 3D anatomical structures. The cerebral cortex has a defined architecture consisting of 6 distinct layers (neocortex) in which neurons are radially organised into cortical columns. Each layer is characterised by a unique neuronal composition and specific connections with other cortical and sub-cortical regions (Lodato & Arlotta, 2015). Such complex anatomical and functional organisation is challenging to reproduce *in vitro*. Even the most advanced organoid technology, at the moment, is not able to recapitulate the physiological architecture of the human cortex (Velasco et al., 2020). For these reasons, *in vitro* cellular models, and in particular 2D models, are less appropriate for the study of complex network behaviours such as epilepsy phenotypes, for which *in vivo* animal models are typically preferred. Nonetheless, cellular models offer the unique opportunity to study disease phenotypes in the context of human neuronal networks and,

even considering the abovementioned limitations, 2D models can still provide valuable insights into more simple cellular phenotypes.

The cellular composition of the model generated in this thesis also presents some limitations. The astrocytic component of our co-culture is of mouse origin and therefore, some important functional differences between mouse and human astrocytes must be considered. Most notably, human cortical astrocytes are bigger and extend 10-fold more processes compared to mouse astrocytes, resulting in the integration of a larger number of synapses (Oberheim et al., 2009). Furthermore, human astrocytes transiently increase cytosolic Ca^{2+} in response to ATP and glutamate and propagate calcium waves much faster than their mouse counterpart, with important implications in the release of gliotransmitters for the modulation of synaptic activity (Oberheim et al., 2009). More in general, the presence of astrocytes in our co-culture model provides only some of the supportive cellular functions offered by glial cells in the CNS. Some of the processes that are key to the formation and development of neuronal networks are exerted by other glial types such as oligodendrocytes and microglia, which are not present in our co-culture model.

Finally, a major limitation of the work described here is represented by the number of disease cell lines included in this study. A single DS patient-derived hiPSC line and its isogenic control were used, together with an unrelated wildtype line, to investigate disease phenotypes. The use of a single disease line restricts any phenotypic observation to the specific mutation harboured by the cell line, in this case *SCN1A*$^{IVS14+3A>T}$. In order to understand general pathomechanisms associated with the loss-of-function of *SCN1A* in human neurons, a study must include multiple disease lines, harbouring different Dravet syndrome-associated mutations.

7.3 Future perspectives

Following up on our current results, future work should firstly focus on expanding and completing some datasets generated herein. As previously discussed, due to the immature electrophysiological phenotype of early neuronal cultures, the observations made at this early time point (3 weeks) have limited relevance to the pathophysiological mechanisms of DS. For this reason, future efforts should focus exclusively on the later time point (6 weeks), when the neurons display relevant pathological phenotypes. Specifically, further electrophysiological characterisation must be performed in order to confirm the altered intrinsic excitability observed in late inhibitory and excitatory neurons. Furthermore, as previously discussed, a more accurate

assessment of isolated somatic sodium currents should be performed, in late neuronal cultures, to assess whether these are affected in *SCN1A*$^{IVS14+3A>T}$ neurons – as previously observed by Liu and colleagues (Y. Liu, Lopez-Santiago, et al., 2013). Finally, calcium imaging datasets in late co-culture models will need to be completed by increasing the number of recordings for inhibitory interneurons.

Continuation of this work will include the application of our model to investigate other Dravet-related *SCN1A* mutations. hiPSC lines suitable for forward programming differentiation into excitatory and inhibitory neurons are easy to generate and, contrarily to small-molecule based approaches, the efficiency of forward programming differentiation is not limited by intrinsic differences in differentiation potential across cell lines (B. Y. Hu et al., 2010; K. Kim et al., 2011; Koyanagi-Aoi et al., 2013; Osafune et al., 2008). For these reasons, our co-culture model can be easily established using neuronal populations generated from Dravet patient-derived hiPSCs carrying different *SCN1A* mutations. Comparing mutation-specific phenotypes would be important to assess whether communal pathophysiological mechanisms are maintained across different disease-causing mutations.

Following up on our observations on transcriptomic upregulation of sodium and calcium channels in *SCN1A*$^{IVS14+3A>T}$ excitatory neurons, further and more comprehensive characterisation can be performed, in the form of RNA-seq, to uncover potential transcriptionally-regulated compensational mechanisms. Furthermore, potential post-transcriptionally-regulated compensational mechanisms could be investigated through active mRNA translation sequencing (Ribo-seq), to reveal if active translation of key proteins is altered, in DS neurons but not healthy neurons, to confer seizure susceptibility.

The presence of distinct fluorescent reporters in our neuronal lines offers the unique opportunity to perform a series of different studies in the context of functional neuronal networks. For example, some studies have suggested that synaptic transmission, inhibitory transmission in particular, might be compromised in DS (Kaneko et al., 2022; Uchino et al., 2021). Our co-culture model would be ideally suited to investigate synaptic transmission phenotypes in DS. Specifically, the strength and frequency of spontaneous and evoked excitatory and inhibitory synaptic currents can be evaluated in our co-culture system through patch-clamp recordings, using the different calcium reporters to distinguish between excitatory and inhibitory neurons. Furthermore, the number and distribution of excitatory and inhibitory synapses can be assessed

– in a neuronal type-specific manner – by immunolabelling of PSD-95 and Gephyrin, markers of excitatory and inhibitory synapses respectively.

Two-colour calcium imaging could also be used to assess temperature-induced epileptic-like activity in our *in vitro* model of DS. Febrile seizures are a common feature of many epileptic disorders, including DS. Many mouse models of DS recapitulate this phenotype, whereby seizure events are induced by exposure to high temperatures (S. Y. Ho et al., 2021; Oakley et al., 2009b; Tran et al., 2020c; Warner et al., 2017). Recently, this phenotype has also been reproduced *in vitro*, in excitatory neuronal networks derived from Dravet patient hiPSCs (van Hugte et al., 2023). To test if such a phenotype can be observed in our *in vitro* model, two-colour calcium imaging can be performed at 40°C to assess the activity of both excitatory and inhibitory neurons in response to fever-like temperatures.

Two-colour calcium imaging allowed for monitoring of neuronal network activity with single cell resolution and distinguishable contributions from each neuronal population. However, the temporal resolution of this technique is limited. Instead, the use of Multi-Electrode Arrays (MEAs) allows for high temporal resolution, multi-point measurement of cultured network activity, including recordings of extracellular potentials, spiking and bursting (Matsuda et al., 2018). In the future, spontaneous and induced epileptic-like activity in late co-culture models can be investigated using MEAs. Furthermore, using MEAs our co-culture model could be adapted to be used as a drug-screening platform for the identification of novel DS treatments. For example, the efficacy of a small compound library in preventing temperature-induced seizures could be assessed using multi-well MEAs.

The co-culture system described in this study could also be implemented to include Dravet patient-hiPSC derived astrocytes. While this was part of our initial design, we failed to generate functional human astrocytes suitable for neuronal co-culture (discussed in Chapter 3). Since then, novel and improved forward programming approaches for the rapid differentiation of hiPSCs into functionally mature astrocytes have been published (Cvetkovic et al., 2022; X. Li et al., 2018b; Neyrinck et al., 2021). The role of astrocytes in DS has only been partially investigated, with recent studies suggesting that their development and function might be altered in DS (Goisis et al., 2022; Martín-Suárez et al., 2020; Uchino et al., 2023). Our co-culture model would be well suited to investigate astrocyte-specific phenotypes and their direct effect on neuronal activity. A number of different parameters could be evaluated, including astrocyte reactive state, electrophysiological activity and glutamate uptake and release.

References

Akerboom, J., Chen, T. W., Wardill, T. J., Tian, L., Marvin, J. S., Mutlu, S., Calderón, N. C., Esposti, F., Borghuis, B. G., Sun, X. R., Gordus, A., Orger, M. B., Portugues, R., Engert, F., Macklin, J. J., Filosa, A., Aggarwal, A., Kerr, R. A., Takagi, R., … Looger, L. L. (2012). Optimization of a GCaMP Calcium Indicator for Neural Activity Imaging. *The Journal of Neuroscience*, *32*(40), 13819. https://doi.org/10.1523/JNEUROSCI.2601-12.2012

Akiyama, H., Tooyama, I., Kawamata, T., Ikeda, K., & McGeer, P. L. (1993). Morphological diversities of CD44 positive astrocytes in the cerebral cortex of normal subjects and patients with Alzheimer's disease. *Brain Research*, *632*(1–2), 249–259. https://doi.org/10.1016/0006-8993(93)91160-T

Almog, Y., Fadila, S., Brusel, M., Mavashov, A., Anderson, K., & Rubinstein, M. (2021). Developmental alterations in firing properties of hippocampal CA1 inhibitory and excitatory neurons in a mouse model of Dravet syndrome. *Neurobiology of Disease*, *148*, 105209. https://doi.org/10.1016/J.NBD.2020.105209

Andersen, J., Revah, O., Miura, Y., Thom, N., Amin, N. D., Kelley, K. W., Singh, M., Chen, X., Thete, M. V., Walczak, E. M., Vogel, H., Fan, H. C., & Paşca, S. P. (2020). Generation of Functional Human 3D Cortico-Motor Assembloids. *Cell*, *183*(7), 1913-1929.e26. https://doi.org/10.1016/j.cell.2020.11.017

Anderson, S. A., Eisenstat, D. D., Shi, L., & Rubenstein, J. L. R. (1997). Interneuron migration from basal forebrain to neocortex: dependence on Dlx genes. *Science (New York, N.Y.)*, *278*(5337), 474–476. https://doi.org/10.1126/SCIENCE.278.5337.474

Aras, L. M., Isla, J., & Mingorance-Le Meur, A. (2015). The European patient with Dravet syndrome: Results from a parent-reported survey on antiepileptic drug use in the European population with Dravet syndrome. *Epilepsy and Behavior*. https://doi.org/10.1016/j.yebeh.2014.12.028

Aydin, B., Kakumanu, A., Rossillo, M., Moreno-Estellés, M., Garipler, G., Ringstad, N., Flames, N., Mahony, S., & Mazzoni, E. O. (2019). Proneural factors Ascl1 and Neurog2 contribute to neuronal subtype identities by establishing distinct chromatin landscapes. *Nature Neuroscience 2019 22:6*, *22*(6), 897–908. https://doi.org/10.1038/s41593-019-0399-y

Baek, J. H., Vignesh, A., Son, H., Lee, D. H., Roh, G. S., Kang, S. S., Cho, G. J., Choi, W. S., & Kim, H. J. (2019). Glutamine Supplementation Ameliorates Chronic Stress-induced Reductions in Glutamate and Glutamine Transporters in the Mouse Prefrontal Cortex. *Experimental Neurobiology*, *28*(2), 270–278. https://doi.org/10.5607/EN.2019.28.2.270

Bagley, J. A., Reumann, D., Bian, S., Lévi-Strauss, J., & Knoblich, J. A. (2017). Fused cerebral organoids model interactions between brain regions. *Nature Methods 2017 14:7*, *14*(7), 743–751. https://doi.org/10.1038/nmeth.4304

Barretto, N., Zhang, H., Powell, S. K., Fernando, M. B., Zhang, S., Flaherty, E. K., Ho, S. M., Slesinger, P. A., Duan, J., & Brennand, K. J. (2020). ASCL1- and DLX2-induced GABAergic neurons from hiPSC-derived NPCs. *Journal of Neuroscience Methods*. https://doi.org/10.1016/j.jneumeth.2019.108548

Bar-Yehuda, D., & Korngreen, A. (2008). Space-clamp problems when voltage clamping neurons expressing voltage-gated conductances. *Journal of Neurophysiology*, *99*(3), 1127–1136. https://doi.org/10.1152/JN.01232.2007

Berecki, G., Bryson, A., Terhag, J., Maljevic, S., Gazina, E. V., Hill, S. L., & Petrou, S. (2019). SCN1A gain of function in early infantile encephalopathy. *Annals of Neurology*, *85*(4), 514–525. https://doi.org/10.1002/ANA.25438

Bertero, A., Pawlowski, M., Ortmann, D., Snijders, K., Yiangou, L., De Brito, M. C., Brown, S., Bernard, W. G., Cooper, J. D., Giacomelli, E., Gambardella, L., Hannan, N. R. F., Iyer, D., Sampaziotis, F., Serrano, F., Zonneveld, M. C. F., Sinha, S., Kotter, M., & Vallier, L. (2016). Optimized inducible shRNA and CRISPR/Cas9 platforms for in vitro studies of human development using hPSCs. *Development (Cambridge)*. https://doi.org/10.1242/dev.138081

Berzanskyte, I., Riccio, F., Machado, C. B., Bradbury, E. J., & Lieberam, I. (2023). Enrichment of human embryonic stem cell-derived V3 interneurons using an Nkx2-2 gene-specific reporter. *Scientific Reports 2023 13:1*, *13*(1), 1–11. https://doi.org/10.1038/s41598-023-29165-z

Birey, F., Andersen, J., Makinson, C. D., Islam, S., Wei, W., Huber, N., Fan, H. C., Metzler, K. R. C., Panagiotakos, G., Thom, N., O'Rourke, N. A., Steinmetz, L. M., Bernstein, J. A., Hallmayer, J., Huguenard, J. R., & Pasca, S. P. (2017). Assembly of functionally integrated human forebrain spheroids. *Nature 2017 545:7652*, *545*(7652), 54–59. https://doi.org/10.1038/nature22330

Bodi, I., Mikala, G., Koch, S. E., Akhter, S. A., & Schwartz, A. (2005). The L-type calcium channel in the heart: the beat goes on. *Journal of Clinical Investigation*, *115*(12), 3306. https://doi.org/10.1172/JCI27167

Bouza, A. A., & Isom, L. L. (2018). Chapter 14: Voltage-gated sodium channel β subunits and their related diseases. *Handbook of Experimental Pharmacology*, *246*, 423. https://doi.org/10.1007/164_2017_48

Bramanti, V., Tomassoni, D., Avitabile, M., Amenta, F., & Avola, R. (2010). Biomarkers of glial cell proliferation and differentiation in culture. *Frontiers in Bioscience - Scholar*, *2 S*(2), 558–570. https://doi.org/10.2741/S85/PDF

Brette, R. (2013). Sharpness of Spike Initiation in Neurons Explained by Compartmentalization. *PLOS Computational Biology*, *9*(12), e1003338. https://doi.org/10.1371/JOURNAL.PCBI.1003338

Brodal, P. (2016). Neuronal Excitability. *The Central Nervous System*, 32–44. https://doi.org/10.1093/MED/9780190228958.003.0003

Brozzi, F., Arcuri, C., Giambanco, I., & Donato, R. (2009). S100B Protein Regulates Astrocyte Shape and Migration via Interaction with Src Kinase: IMPLICATIONS FOR ASTROCYTE DEVELOPMENT, ACTIVATION, AND TUMOR GROWTH*S. *The Journal of Biological Chemistry*, *284*(13), 8797. https://doi.org/10.1074/JBC.M805897200

Brunklaus, A., Brünger, T., Feng, T., Fons, C., Lehikoinen, A., Panagiotakaki, E., Vintan, M. A., Symonds, J., Andrew, J., Arzimanoglou, A., Delima, S., Gallois, J., Hanrahan, D., Lesca, G., MacLeod, S., Marjanovic, D., McTague, A., Nuñez-Enamorado, N., Perez-Palma, E., … Cestèle, S. (2022). The gain of function SCN1A disorder spectrum: novel epilepsy phenotypes and therapeutic implications. *Brain*, *145*(11), 3816. https://doi.org/10.1093/BRAIN/AWAC210

Brunklaus, A., Ellis, R., Reavey, E., Forbes, G. H., & Zuberi, S. M. (2012). Prognostic, clinical and demographic features in SCN1A mutation-positive Dravet syndrome. *Brain*, *135*(8), 2329–2336. https://doi.org/10.1093/BRAIN/AWS151

Bryson, J. B., Machado, C. B., Crossley, M., Stevenson, D., Bros-Facer, V., Burrone, J., Greensmith, L., & Lieberam, I. (2014). Optical control of muscle function by transplantation of stem cell-derived motor neurons in mice. *Science*. https://doi.org/10.1126/science.1248523

Cahoy, J. D., Emery, B., Kaushal, A., Foo, L. C., Zamanian, J. L., Christopherson, K. S., Xing, Y., Lubischer, J. L., Krieg, P. A., Krupenko, S. A., Thompson, W. J., & Barres, B. A. (2008). A transcriptome database for astrocytes, neurons, and oligodendrocytes: a new resource for understanding brain development and function. *The Journal of Neuroscience : The Official Journal of the Society for Neuroscience*, *28*(1), 264–278. https://doi.org/10.1523/JNEUROSCI.4178-07.2008

Calderón-Martínez, D., Garavito, Z., Spinel, C., & Hurtado, H. (2002). Schwann cell-enriched cultures from adult human peripheral nerve: A technique combining short enzymatic dissociation and treatment with cytosine arabinoside (Ara-C). *Journal of Neuroscience Methods*, *114*(1), 1–8. https://doi.org/10.1016/S0165-0270(01)00493-9

Calhoun, J. D., Hawkins, N. A., Zachwieja, N. J., & Kearney, J. A. (2016). Cacna1g is a genetic modifier of epilepsy caused by mutation of voltage-gated sodium channel Scn2a. *Epilepsia*, *57*(6), e103. https://doi.org/10.1111/EPI.13390

Calhoun, J. D., Hawkins, N. A., Zachwieja, N. J., & Kearney, J. A. (2017). Cacna1g is a genetic modifier of epilepsy in a mouse model of Dravet syndrome. *Epilepsia*, *58*(8), e111. https://doi.org/10.1111/EPI.13811

Camp, J. G., Badsha, F., Florio, M., Kanton, S., Gerber, T., Wilsch-Bräuninger, M., Lewitus, E., Sykes, A., Hevers, W., Lancaster, M., Knoblich, J. A., Lachmann, R., Pääbo, S., Huttner, W. B., & Treutlein, B. (2015). Human cerebral organoids recapitulate gene expression programs of fetal neocortex development. *Proceedings of the National Academy of Sciences of the United States of America*, *112*(51), 15672–15677. https://doi.org/10.1073/PNAS.1520760112/SUPPL_FILE/PNAS.1520760112.SD04.XLSX

Canals, I., Ginisty, A., Quist, E., Timmerman, R., Fritze, J., Miskinyte, G., Monni, E., Hansen, M. G., Hidalgo, I., Bryder, D., Bengzon, J., & Ahlenius, H. (2018). Rapid and efficient induction of functional astrocytes from human pluripotent stem cells. *Nature Methods*. https://doi.org/10.1038/s41592-018-0103-2

Casola, S., Cattoretti, G., Uyttersprot, N., Koralov, S. B., Segal, J., Hao, Z., Waisman, A., Egert, A., Ghitza, D., & Rajewsky, K. (2006). Tracking germinal center B cells expressing germ-line immunoglobulin γ1 transcripts by conditional gene targeting. *Proceedings of the National Academy of Sciences of the United States of America*, *103*(19), 7396. https://doi.org/10.1073/PNAS.0602353103

Catterall, W. A. (2000). From ionic currents to molecular mechanisms: The structure and function of voltage-gated sodium channels. In *Neuron*. https://doi.org/10.1016/S0896-6273(00)81133-2

Cerbini, T., Funahashi, R., Luo, Y., Liu, C., Park, K., Rao, M., Malik, N., & Zou, J. (2015). Transcription activator-like effector nuclease (TALEN)-mediated CLYBL targeting enables enhanced transgene expression and one-step generation of dual reporter human induced pluripotent stem cell (iPSC) and neural stem cell (NSC) lines. *PLoS ONE*. https://doi.org/10.1371/journal.pone.0116032

Chamberlain, K., Riyad, J. M., & Weber, T. (2016). Expressing Transgenes That Exceed the Packaging Capacity of Adeno-Associated Virus Capsids. *Human Gene Therapy Methods*, *27*(1), 1–12. https://doi.org/10.1089/HGTB.2015.140

Chambers, S. M., Fasano, C. A., Papapetrou, E. P., Tomishima, M., Sadelain, M., & Studer, L. (2009). Highly efficient neural conversion of human ES and iPS cells by dual inhibition of SMAD signaling. *Nature Biotechnology*. https://doi.org/10.1038/nbt.1529

Chand, A. N., Galliano, E., Chesters, R. A., & Grubb, M. S. (2015). A Distinct Subtype of Dopaminergic Interneuron Displays Inverted Structural Plasticity at the Axon Initial Segment. *The Journal of Neuroscience*, *35*(4), 1573. https://doi.org/10.1523/JNEUROSCI.3515-14.2015

Cheah, C. S., Yu, F. H., Westenbroek, R. E., Kalume, F. K., Oakley, J. C., Potter, G. B., Rubenstein, J. L., & Catterall, W. A. (2012). Specific deletion of NaV1.1 sodium channels in inhibitory interneurons causes seizures and premature death in a mouse model of Dravet syndrome. *Proceedings of the National Academy of Sciences of the United States of America*, *109*(36), 14646–14651. https://doi.org/10.1073/PNAS.1211591109/SUPPL_FILE/PNAS.201211591SI.PDF

Chen, Q., Luo, W., Veach, R. A., Hickman, A. B., Wilson, M. H., & Dyda, F. (2020). Structural basis of seamless excision and specific targeting by piggyBac transposase. *Nature Communications*, *11*(1). https://doi.org/10.1038/S41467-020-17128-1

Chever, O., Zerimech, S., Scalmani, P., Lemaire, L., Pizzamiglio, L., Loucif, A., Ayrault, M., Krupa, M., Desroches, M., Duprat, F., Léna, I., Cestèle, S., & Mantegazza, M. (2021). Initiation of migraine-related cortical spreading depolarization by hyperactivity of GABAergic neurons and NaV1.1 channels. *The Journal of Clinical Investigation*, *131*(21). https://doi.org/10.1172/JCI142203

Chilcott, E., Díaz, J. A., Bertram, C., Berti, M., & Karda, R. (2022). Genetic therapeutic advancements for Dravet Syndrome. *Epilepsy & Behavior*, *132*, 108741. https://doi.org/10.1016/J.YEBEH.2022.108741

Chiron, C., Marchand, M. C., Tran, A., Rey, E., D'Athis, P., Vincent, J., Dulac, O., & Pons, G. (2000). Stiripentol in severe myoclonic epilepsy in infancy: A randomised placebo-controlled syndrome-dedicated trial. *Lancet*. https://doi.org/10.1016/S0140-6736(00)03157-3

Chopra, R., & Isom, L. L. (2014). Untangling the Dravet Syndrome Seizure Network: The Changing Face of a Rare Genetic Epilepsy. *Epilepsy Currents*, *14*(2), 86. https://doi.org/10.5698/1535-7597-14.2.86

Claes, L., Del-Favero, J., Ceulemans, B., Lagae, L., van Broeckhoven, C., & de Jonghe, P. (2002). De Novo Mutations in the Sodium-Channel Gene SCN1A Cause Severe Myoclonic Epilepsy of Infancy. *The American Journal of Human Genetics*. https://doi.org/10.1086/320609

Clatot, J., Parthasarathy, S., Cohen, S., McKee, J., Massey, S., Somarowthu, A., Goldberg, E. M., & Helbig, I. (2022). The SCN1A Philadelphia variant – a gain-of-function mutation causing an early-onset epileptic encephalopathy. *BioRxiv*, 2022.06.29.498154. https://doi.org/10.1101/2022.06.29.498154

Colasante, G., Lignani, G., Brusco, S., Di Berardino, C., Carpenter, J., Giannelli, S., Valassina, N., Bido, S., Ricci, R., Castoldi, V., Marenna, S., Church, T., Massimino, L., Morabito, G., Benfenati, F., Schorge, S., Leocani, L., Kullmann, D. M., & Broccoli, V. (2020). dCas9-Based Scn1a Gene Activation Restores Inhibitory Interneuron Excitability and Attenuates Seizures in Dravet Syndrome Mice. *Molecular Therapy : The Journal of the American Society of Gene Therapy*, *28*(1), 235–253. https://doi.org/10.1016/J.YMTHE.2019.08.018

Cvetkovic, C., Patel, R., Shetty, A., Hogan, M. K., Anderson, M., Basu, N., Aghlara-Fotovat, S., Ramesh, S., Sardar, D., Veiseh, O., Ward, M. E., Deneen, B., Horner, P. J., & Krencik, R. (2022). Assessing Gq-GPCR–induced human astrocyte reactivity using bioengineered neural organoids. *Journal of Cell Biology*, *221*(4). https://doi.org/10.1083/JCB.202107135/VIDEO-4

Dana, H., Mohar, B., Sun, Y., Narayan, S., Gordus, A., Hasseman, J. P., Tsegaye, G., Holt, G. T., Hu, A., Walpita, D., Patel, R., Macklin, J. J., Bargmann, C. I., Ahrens, M. B., Schreiter, E. R., Jayaraman, V., Looger, L. L., Svoboda, K., & Kim, D. S. (2016). Sensitive red protein calcium indicators for imaging neural activity. *ELife*, *5*(MARCH2016). https://doi.org/10.7554/ELIFE.12727

Darabi, R., Arpke, R. W., Irion, S., Dimos, J. T., Grskovic, M., Kyba, M., & Perlingeiro, R. C. R. (2012). Human ES- and iPS-derived myogenic progenitors restore DYSTROPHIN and improve contractility upon transplantation in dystrophic mice. *Cell Stem Cell*. https://doi.org/10.1016/j.stem.2012.02.015

Das, A. T., Tenenbaum, L., & Berkhout, B. (2016). Tet-On Systems For Doxycycline-inducible Gene Expression. *Current Gene Therapy*, *16*(3), 156. https://doi.org/10.2174/1566523216666160524144041

De Stasi, A. M., Farisello, P., Marcon, I., Cavallari, S., Forli, A., Vecchia, D., Losi, G., Mantegazza, M., Panzeri, S., Carmignoto, G., Bacci, A., & Fellin, T. (2016). Unaltered Network Activity and Interneuronal Firing During Spontaneous Cortical Dynamics In Vivo in a Mouse Model of Severe Myoclonic Epilepsy of Infancy. *Cerebral Cortex (New York, NY)*, *26*(4), 1778. https://doi.org/10.1093/CERCOR/BHW002

Dichgans, M., Freilinger, T., Eckstein, G., Babini, E., Lorenz-Depiereux, B., Biskup, S., Ferrari, M. D., Herzog, J., Van Den Maagdenberg, A. M. J. M., Pusch, M., & Strom, T. M. (2005). Mutation in the neuronal voltage-gated sodium channel SCN1A in familial hemiplegic migraine. *Lancet (London, England)*, *366*(9483), 371–377. https://doi.org/10.1016/S0140-6736(05)66786-4

Dravet, C. (2011). Dravet syndrome history. In *Developmental Medicine and Child Neurology*. https://doi.org/10.1111/j.1469-8749.2011.03964.x

Du, T., Xu, Q., Ocbina, P. J., & Anderson, S. A. (2008). NKX2.1 specifies cortical interneuron fate by activating Lhx6. *Development (Cambridge, England)*, *135*(8), 1559–1567. https://doi.org/10.1242/DEV.015123

Duflocq, A., le Bras, B., Bullier, E., Couraud, F., & Davenne, M. (2008). Nav1.1 is predominantly expressed in nodes of Ranvier and axon initial segments. *Molecular and Cellular Neurosciences*, *39*(2), 180–192. https://doi.org/10.1016/J.MCN.2008.06.008

Dutton, S. B., Makinson, C. D., Papale, L. A., Shankar, A., Balakrishnan, B., Nakazawa, K., & Escayg, A. (2013). Preferential inactivation of Scn1a in parvalbumin interneurons increases seizure susceptibility. *Neurobiology of Disease*, *0*(1), 211. https://doi.org/10.1016/J.NBD.2012.08.012

Escayg, A., & Goldin, A. L. (2010). Sodium channel SCN1A and epilepsy: Mutations and mechanisms. In *Epilepsia*. https://doi.org/10.1111/j.1528-1167.2010.02640.x

Evans, M. D., Dumitrescu, A. S., Kruijssen, D. L. H., Taylor, S. E., & Grubb, M. S. (2015). Rapid Modulation of Axon Initial Segment Length Influences Repetitive Spike Firing. *Cell Reports*, *13*(6), 1233–1245. https://doi.org/10.1016/J.CELREP.2015.09.066

Fadila, S., Quinn, S., Turchetti Maia, A., Yakubovich, D., Ovadia, M., Anderson, K. L., Giladi, M., & Rubinstein, M. (2020). Convulsive seizures and some behavioral comorbidities are uncoupled in the Scn1aA1783V Dravet syndrome mouse model. *Epilepsia*, *61*(10), 2289–2300. https://doi.org/10.1111/EPI.16662

Favero, M., Sotuyo, N. P., Lopez, E., Kearney, J. A., & Goldberg, E. M. (2018). A Transient Developmental Window of Fast-Spiking Interneuron Dysfunction in a Mouse Model of Dravet Syndrome. *Journal of Neuroscience*, *38*(36), 7912–7927. https://doi.org/10.1523/JNEUROSCI.0193-18.2018

Fernandopulle, M. S., Prestil, R., Grunseich, C., Wang, C., Gan, L., & Ward, M. E. (2018). Transcription Factor–Mediated Differentiation of Human iPSCs into Neurons. *Current Protocols in Cell Biology*. https://doi.org/10.1002/cpcb.51

Fisher, J. L. (2009). The anti-convulsant stiripentol acts directly on the GABAA receptor as a positive allosteric modulator. *Neuropharmacology*. https://doi.org/10.1016/j.neuropharm.2008.06.004

Fisher, J. L. (2011). Interactions between modulators of the GABAA receptor: Stiripentol and benzodiazepines. *European Journal of Pharmacology*. https://doi.org/10.1016/j.ejphar.2010.12.037

Fisher, R. S., Acevedo, C., Arzimanoglou, A., Bogacz, A., Cross, J. H., Elger, C. E., Engel, J., Forsgren, L., French, J. A., Glynn, M., Hesdorffer, D. C., Lee, B. I., Mathern, G. W., Moshé, S. L., Perucca, E., Scheffer, I. E., Tomson, T., Watanabe, M., & Wiebe, S. (2014). ILAE official report: a practical clinical definition of epilepsy. *Epilepsia*. https://doi.org/10.1111/epi.12550

Fisher, R. S., Van Emde Boas, W., Blume, W., Elger, C., Genton, P., Lee, P., & Engel, J. (2005). Epileptic seizures and epilepsy: Definitions proposed by the International League Against Epilepsy (ILAE) and the International Bureau for Epilepsy (IBE). In *Epilepsia*. https://doi.org/10.1111/j.0013-9580.2005.66104.x

Frega, M., van Gestel, S. H. C., Linda, K., van der Raadt, J., Keller, J., van Rhijn, J. R., Schubert, D., Albers, C. A., & Kasri, N. N. (2017). Rapid neuronal differentiation of induced pluripotent stem cells for measuring network activity on micro-electrode arrays. *Journal of Visualized Experiments*. https://doi.org/10.3791/54900

Fuccillo, M., Rallu, M., McMahon, A. P., & Fishell, G. (2004). Temporal requirement for hedgehog signaling in ventral telencephalic patterning. *Development (Cambridge, England)*, *131*(20), 5031–5040. https://doi.org/10.1242/DEV.01349

Galliano, E., Hahn, C., Browne, L. P., Villamayor, P. R., Tufo, C., Crespo, A., & Grubb, M. S. (2021). Brief Sensory Deprivation Triggers Cell Type-Specific Structural and Functional Plasticity in Olfactory Bulb Neurons. *Journal of Neuroscience*, *41*(10), 2135–2151. https://doi.org/10.1523/JNEUROSCI.1606-20.2020

Gataullina, S., & Dulac, O. (2017). From genotype to phenotype in Dravet disease. In *Seizure*. https://doi.org/10.1016/j.seizure.2016.10.014

Genton, P., Velizarova, R., & Dravet, C. (2011). Dravet syndrome: The long-term outcome. *Epilepsia*. https://doi.org/10.1111/j.1528-1167.2011.03001.x

Gerdes, J., Lemke, H., Baisch, H., Wacker, H. H., Schwab, U., & Stein, H. (1984). Cell cycle analysis of a cell proliferation-associated human nuclear antigen defined by the monoclonal antibody Ki-67. *The Journal of Immunology*, *133*(4), 1710–1715. https://doi.org/10.4049/JIMMUNOL.133.4.1710

Goff, K. M., & Goldberg, E. M. (2019). Vasoactive intestinal peptide-expressing interneurons are impaired in a mouse model of Dravet syndrome. *ELife*, *8*. https://doi.org/10.7554/ELIFE.46846

Goisis, R. C., Chiavegato, A., Gomez-Gonzalo, M., Marcon, I., Requie, L. M., Scholze, P., Carmignoto, G., & Losi, G. (2022). GABA tonic currents and glial cells are altered during epileptogenesis in a mouse model of Dravet syndrome. *Frontiers in Cellular Neuroscience*, *16*, 381. https://doi.org/10.3389/FNCEL.2022.919493/BIBTEX

Gossen, M., Freundlieb, S., Bender, G., Müller, G., Hillen, W., & Bujard, H. (1995). Transcriptional activation by tetracyclines in mammalian cells. *Science*. https://doi.org/10.1126/science.7792603

Götz, M., Stoykova, A., & Gruss, P. (1998). Pax6 controls radial glia differentiation in the cerebral cortex. *Neuron*, *21*(5), 1031–1044. https://doi.org/10.1016/S0896-6273(00)80621-2

Grabundzija, I., Irgang, M., Mátés, L., Belay, E., Matrai, J., Gogol-Döring, A., Kawakami, K., Chen, W., Ruiz, P., Chuah, M. K. L., Vandendriessche, T., Izsvák, Z., & Ivics, Z. (2010). Comparative Analysis of Transposable Element Vector Systems in Human Cells. *Molecular Therapy*, *18*(6), 1200. https://doi.org/10.1038/MT.2010.47

Griffin, A., Hamling, K. R., Hong, S. G., Anvar, M., Lee, L. P., & Baraban, S. C. (2018). Preclinical Animal Models for Dravet Syndrome: Seizure Phenotypes, Comorbidities and

Drug Screening. *Frontiers in Pharmacology*, *9*(JUN), 573. https://doi.org/10.3389/FPHAR.2018.00573

Grubb, M. S., & Burrone, J. (2010). Activity-dependent relocation of the axon initial segment fine-tunes neuronal excitability. *Nature 2010 465:7301*, *465*(7301), 1070–1074. https://doi.org/10.1038/nature09160

Grubb, M. S., Shu, Y., Kuba, H., Rasband, M. N., Wimmer, V. C., & Bender, K. J. (2011). Mini-Symposium: Short- and Long-Term Plasticity at the Axon Initial Segment. *The Journal of Neuroscience*, *31*(45), 16049. https://doi.org/10.1523/JNEUROSCI.4064-11.2011

Gründemann, J., & Häusser, M. (2010). A plastic axonal hotspot. *Nature 2010 465:7301*, *465*(7301), 1022–1023. https://doi.org/10.1038/4651022a

Guerrini, R., Specchio, N., Aledo-Serrano, Á., Pringsheim, M., Darra, F., Mayer, T., Gil-Nagel, A., Polster, T., Zuberi, S. M., Lothe, A., Gammaitoni, A., & Strzelczyk, A. (2022). An examination of the efficacy and safety of fenfluramine in adults, children, and adolescents with Dravet syndrome in a real-world practice setting: A report from the Fenfluramine European Early Access Program. *Epilepsia Open*, *7*(4), 578–587. https://doi.org/10.1002/EPI4.12624

Gulledge, A. T., & Bravo, J. J. (2016). Neuron Morphology Influences Axon Initial Segment Plasticity. *ENeuro*, *3*(1), 255–265. https://doi.org/10.1523/ENEURO.0085-15.2016

Han, S., Tai, C., Westenbroek, R. E., Yu, F. H., Cheah, C. S., Potter, G. B., Rubenstein, J. L., Scheuer, T., de La Iglesia, H. O., & Catterall, W. A. (2012). Autistic behavior in Scn1a+/− mice and rescue by enhanced GABAergic transmission. *Nature*, *489*(7416), 385. https://doi.org/10.1038/NATURE11356

Han, Z., Chen, C., Christiansen, A., Ji, S., Lin, Q., Anumonwo, C., Liu, C., Leiser, S. C., Meena, Aznarez, I., Liau, G., & Isom, L. L. (2020). Antisense oligonucleotides increase Scn1a expression and reduce seizures and SUDEP incidence in a mouse model of Dravet syndrome. *Science Translational Medicine*, *12*(558). https://doi.org/10.1126/SCITRANSLMED.AAZ6100

Hansen, K. B., Ogden, K. K., Yuan, H., & Traynelis, S. F. (2014). Distinct functional and pharmacological properties of triheteromeric GluN1/GluN2A/GluN2B NMDA receptors. *Neuron*, *81*(5), 1084. https://doi.org/10.1016/J.NEURON.2014.01.035

Harkin, L. A., McMahon, J. M., Iona, X., Dibbens, L., Pelekanos, J. T., Zuberi, S. M., Sadleir, L. G., Andermann, E., Gill, D., Farrell, K., Connolly, M., Stanley, T., Harbord, M., Andermann, F., Wang, J., Batish, S. D., Jones, J. G., Seltzer, W. K., Gardner, A., … Wirrell, E. (2007). The spectrum of SCN1A-related infantile epileptic encephalopathies. *Brain*. https://doi.org/10.1093/brain/awm002

Harley, P., Neves, G., Riccio, F., Machado, C. B., Cheesbrough, A., R'Bibo, L., Burrone, J., & Lieberam, I. (2022). Pathogenic TDP-43 Disrupts Axon Initial Segment Structure and Neuronal Excitability in a Human iPSC Model of ALS. *BioRxiv*, 2022.05.16.492186. https://doi.org/10.1101/2022.05.16.492186

Hartline, D. K., & Castelfranco, A. M. (2003). Simulations of voltage clamping poorly space-clamped voltage-dependent conductances in a uniform cylindrical neurite. *Journal of Computational Neuroscience*, *14*(3), 253–269. https://doi.org/10.1023/A:1023208926805

Hatch, R. J., Wei, Y., Xia, D., & Götz, J. (2017). Hyperphosphorylated tau causes reduced hippocampal CA1 excitability by relocating the axon initial segment. *Acta Neuropathologica*, *133*(5), 717–730. https://doi.org/10.1007/S00401-017-1674-1

Hawkins, N. A., & Kearney, J. A. (2012). Confirmation of an Epilepsy Modifier Locus on Mouse Chromosome 11 and Candidate Gene Analysis by RNA-Seq. *Genes, Brain, and Behavior*, *11*(4), 452. https://doi.org/10.1111/J.1601-183X.2012.00790.X

He, Z., Li, Y., Zhao, X., & Li, B. (2022). Dravet syndrome: Advances in etiology, clinical presentation, and treatment. *Epilepsy Research*, *188*, 107041. https://doi.org/10.1016/J.EPLEPSYRES.2022.107041

Hedegaard, A., Monzón-Sandoval, J., Newey, S. E., Whiteley, E. S., Webber, C., & Akerman, C. J. (2020). Pro-maturational Effects of Human iPSC-Derived Cortical Astrocytes upon iPSC-Derived Cortical Neurons. *Stem Cell Reports*, *15*(1), 38. https://doi.org/10.1016/J.STEMCR.2020.05.003

Heighway, J., Sedo, A., Garg, A., Eldershaw, L., Perreau, V., Berecki, G., Reid, C. A., Petrou, S., & Maljevic, S. (2022). Sodium channel expression and transcript variation in the developing brain of human, Rhesus monkey, and mouse. *Neurobiology of Disease*, *164*, 105622. https://doi.org/10.1016/J.NBD.2022.105622

Helbig, I., & Goldberg, E. (2021). The dose makes the poison—Novel insights into Dravet syndrome and SCN1A regulation through nonproductive splicing. *PLOS Genetics*, *17*(1), e1009214. https://doi.org/10.1371/JOURNAL.PGEN.1009214

Hernandez, C. C., Tian, X. J., Hu, N., Shen, W., Catron, M. A., Yang, Y., Chen, J., Jiang, Y., Zhang, Y., & MacDonald, R. L. (2021). Dravet syndrome-associated mutations in GABRA1, GABRB2 and GABRG2 define the genetic landscape of defects of GABAA receptors. *Brain Communications*, *3*(2). https://doi.org/10.1093/BRAINCOMMS/FCAB033

Hevner, R. F., Hodge, R. D., Daza, R. A. M., & Englund, C. (2006). Transcription factors in glutamatergic neurogenesis: conserved programs in neocortex, cerebellum, and adult hippocampus. *Neuroscience Research*, *55*(3), 223–233. https://doi.org/10.1016/J.NEURES.2006.03.004

Higurashi, N., Broccoli, V., & Hirose, S. (2022). Genetics and gene therapy in Dravet syndrome. *Epilepsy & Behavior*, *131*, 108043. https://doi.org/10.1016/J.YEBEH.2021.108043

Higurashi, N., Uchida, T., Lossin, C., Misumi, Y., Okada, Y., Akamatsu, W., Imaizumi, Y., Zhang, B., Nabeshima, K., Mori, M. X., Katsurabayashi, S., Shirasaka, Y., Okano, H., & Hirose, S. (2013a). A human Dravet syndrome model from patient induced pluripotent stem cells. *Molecular Brain*. https://doi.org/10.1186/1756-6606-6-19

Higurashi, N., Uchida, T., Lossin, C., Misumi, Y., Okada, Y., Akamatsu, W., Imaizumi, Y., Zhang, B., Nabeshima, K., Mori, M. X., Katsurabayashi, S., Shirasaka, Y., Okano, H., & Hirose, S. (2013b). A human Dravet syndrome model from patient induced pluripotent stem cells. *Molecular Brain*, *6*(1), 19. https://doi.org/10.1186/1756-6606-6-19

Ho, S. M., Topol, A., & Brennand, K. J. (2015). From "Directed Differentiation" to "Neuronal Induction": Modeling Neuropsychiatric Disease. *Biomarker Insights*, *10*(Suppl 1), 31. https://doi.org/10.4137/BMI.S20066

Ho, S. Y., Lin, L., Chen, I. C., Tsai, C. W., Chang, F. C., & Liou, H. H. (2021). Perampanel Reduces Hyperthermia-Induced Seizures in Dravet Syndrome Mouse Model. *Frontiers in Pharmacology*, *12*, 1659. https://doi.org/10.3389/FPHAR.2021.682767/BIBTEX

Hsiao, J., Yuan, T. Y., Tsai, M. S., Lu, C. Y., Lin, Y. C., Lee, M. L., Lin, S. W., Chang, F. C., Liu Pimentel, H., Olive, C., Coito, C., Shen, G., Young, M., Thorne, T., Lawrence, M., Magistri, M., Faghihi, M. A., Khorkova, O., & Wahlestedt, C. (2016). Upregulation of Haploinsufficient Gene Expression in the Brain by Targeting a Long Non-coding RNA Improves Seizure Phenotype in a Model of Dravet Syndrome. *EBioMedicine*, *9*, 257. https://doi.org/10.1016/J.EBIOM.2016.05.011

Hu, B. Y., Weick, J. P., Yu, J., Ma, L. X., Zhang, X. Q., Thomson, J. A., & Zhang, S. C. (2010). Neural differentiation of human induced pluripotent stem cells follows developmental principles but with variable potency. *Proceedings of the National*

Academy of Sciences of the United States of America. https://doi.org/10.1073/pnas.0910012107

Hu, W., Tian, C., Li, T., Yang, M., Hou, H., & Shu, Y. (2009). Distinct contributions of Na(v)1.6 and Na(v)1.2 in action potential initiation and backpropagation. *Nature Neuroscience*, *12*(8), 996–1002. https://doi.org/10.1038/NN.2359

Hu, X. L., Liu, X. P., Deng, Y. C., Lin, S. X., Wu, L., Zhang, J., Wang, L. F., Wang, X. bin, Li, X., Shen, L., Zhang, Y. Q., & Yao, L. B. (2006). Expression analysis of the NDRG2 gene in mouse embryonic and adult tissues. *Cell and Tissue Research*, *325*(1), 67–76. https://doi.org/10.1007/S00441-005-0137-5/TABLES/2

Huang, C. Y. M., & Rasband, M. N. (2018). Axon initial segments: structure, function, and disease. *Annals of the New York Academy of Sciences*, *1420*(1), 46. https://doi.org/10.1111/NYAS.13718

Hulme, A. J., Maksour, S., St, M., Glover, -Clair, Miellet, S., & Dottori, M. (2022). Stem Cell Reports Review Making neurons, made easy: The use of Neurogenin-2 in neuronal differentiation. *Stem Cell Reports*, *17*, 14–34. https://doi.org/10.1016/j.stemcr.2021.11.015

Hurst, D. L. (1990). Epidemiology of Severe Myoclonic Epilepsy of Infancy. *Epilepsia*. https://doi.org/10.1111/j.1528-1157.1990.tb05494.x

Iida, S., Shimba, K., Sakai, K., Kotani, K., & Jimbo, Y. (2018). Synchronous firing patterns of induced pluripotent stem cell-derived cortical neurons depend on the network structure consisting of excitatory and inhibitory neurons. *Biochemical and Biophysical Research Communications*. https://doi.org/10.1016/j.bbrc.2018.04.197

Isom, L. L. (2017). Opposing Phenotypes in Dravet Syndrome Patient-Derived Induced Pluripotent Stem Cell Neurons: Can Everyone be Right? *Https://Doi.Org/10.5698/1535-7597.17.4.244*, *17*(4), 244–247. https://doi.org/10.5698/1535-7597.17.4.244

Jaber, D., Gitiaux, C., Blesson, S., Marguet, F., Buard, D., Varela Salgado, M., Kaminska, A., Saada, J., Fallet-Bianco, C., Martinovic, J., Laquerriere, A., & Melki, J. (2021). De novo mutations of SCN1A are responsible for arthrogryposis broadening the SCN1A-related phenotypes. *Journal of Medical Genetics*, *58*(11), 737–742. https://doi.org/10.1136/JMEDGENET-2020-107166

Jablonski, J., Hoffmann, L., Blümcke, I., Fejtová, A., Uebe, S., Ekici, A. B., Gnatkovsky, V., & Kobow, K. (2021). Experimental epileptogenesis in a cell culture model of primary neurons from rat brain: A temporal multi-scale study. *Cells*, *10*(11). https://doi.org/10.3390/CELLS10113004/S1

Jamann, N., Dannehl, D., Lehmann, N., Wagener, R., Thielemann, C., Schultz, C., Staiger, J., Kole, M. H. P., & Engelhardt, M. (2021a). Sensory input drives rapid homeostatic scaling of the axon initial segment in mouse barrel cortex. *Nature Communications*, *12*(1). https://doi.org/10.1038/S41467-020-20232-X

Jamann, N., Dannehl, D., Lehmann, N., Wagener, R., Thielemann, C., Schultz, C., Staiger, J., Kole, M. H. P., & Engelhardt, M. (2021b). Sensory input drives rapid homeostatic scaling of the axon initial segment in mouse barrel cortex. *Nature Communications*, *12*(1). https://doi.org/10.1038/S41467-020-20232-X

Jia, Y. F., Wininger, K., Ho, A. M. C., Peyton, L., Baker, M., & Choi, D. S. (2020). Astrocytic Glutamate Transporter 1 (GLT1) Deficiency Reduces Anxiety- and Depression-Like Behaviors in Mice. *Frontiers in Behavioral Neuroscience*, *14*, 57. https://doi.org/10.3389/FNBEH.2020.00057/BIBTEX

Jiao, J., Yang, Y., Shi, Y., Chen, J., Gao, R., Fan, Y., Yao, H., Liao, W., Sun, X. F., & Gao, S. (2013a). Modeling Dravet syndrome using induced pluripotent stem cells (iPSCs) and directly converted neurons. *Human Molecular Genetics*. https://doi.org/10.1093/hmg/ddt275

Jiao, J., Yang, Y., Shi, Y., Chen, J., Gao, R., Fan, Y., Yao, H., Liao, W., Sun, X. F., & Gao, S. (2013b). Modeling Dravet syndrome using induced pluripotent stem cells (iPSCs) and directly converted neurons. *Human Molecular Genetics*, *22*(21), 4241–4252. https://doi.org/10.1093/HMG/DDT275

Johannesen, K., Marini, C., Pfeffer, S., Møller, R. S., Dorn, T., Niturad, C., Gardella, E., Weber, Y., Søndergård, M., Hjalgrim, H., Nikanorova, M., Becker, F., Larsen, L. H. G., Dahl, H. A., Maier, O., Mei, D., Biskup, S., Klein, K. M., Reif, P. S., … Maljevic, S. (2016). Phenotypic spectrum of GABRA1: From generalized epilepsies to severe epileptic encephalopathies. *Neurology*, *87*(11), 1140–1151. https://doi.org/10.1212/WNL.0000000000003087

Jones, B. L., & Smith, S. M. (2016). Calcium-sensing receptor: A key target for extracellular calcium signaling in neurons. *Frontiers in Physiology*, *7*(MAR), 116. https://doi.org/10.3389/FPHYS.2016.00116/BIBTEX

Jones, E. G., Huntley, G. W., & Benson, D. L. (1994). Alpha calcium/calmodulin-dependent protein kinase II selectively expressed in a subpopulation of excitatory neurons in monkey sensory-motor cortex: comparison with GAD-67 expression. *The Journal of Neuroscience : The Official Journal of the Society for Neuroscience*, *14*(2), 611–629. https://doi.org/10.1523/JNEUROSCI.14-02-00611.1994

Jones, S. P., O'Neill, N., Muggeo, S., Colasante, G., Kullmann, D. M., & Lignani, G. (2022). Developmental instability of CA1 pyramidal cells in Dravet Syndrome. *BioRxiv*, 2022.09.12.507264. https://doi.org/10.1101/2022.09.12.507264

Jurga, A. M., Paleczna, M., Kadluczka, J., & Kuter, K. Z. (2021). Beyond the GFAP-Astrocyte Protein Markers in the Brain. *Biomolecules*, *11*(9). https://doi.org/10.3390/BIOM11091361

Jurga, A. M., Paleczna, M., & Kuter, K. Z. (2020). Overview of General and Discriminating Markers of Differential Microglia Phenotypes. *Frontiers in Cellular Neuroscience*, *14*, 198. https://doi.org/10.3389/FNCEL.2020.00198/BIBTEX

Kadoshima, T., Sakaguchi, H., Nakano, T., Soen, M., Ando, S., Eiraku, M., & Sasai, Y. (2013). Self-organization of axial polarity, inside-out layer pattern, and species-specific progenitor dynamics in human ES cell-derived neocortex. *Proceedings of the National Academy of Sciences of the United States of America*, *110*(50), 20284–20289. https://doi.org/10.1073/PNAS.1315710110/SUPPL_FILE/SM03.MOV

Kalume, F., Westenbroek, R. E., Cheah, C. S., Yu, F. H., Oakley, J. C., Scheuer, T., & Catterall, W. A. (2013). Sudden unexpected death in a mouse model of Dravet syndrome. *The Journal of Clinical Investigation*, *123*(4), 1798. https://doi.org/10.1172/JCI66220

Kalume, F., Yu, F. H., Westenbroek, R. E., Scheuer, T., & Catterall, W. A. (2007). Reduced Sodium Current in Purkinje Neurons from NaV1.1 Mutant Mice: Implications for Ataxia in Severe Myoclonic Epilepsy in Infancy. *The Journal of Neuroscience*, *27*(41), 11065. https://doi.org/10.1523/JNEUROSCI.2162-07.2007

Kaneko, K., Currin, C. B., Goff, K. M., Wengert, E. R., Somarowthu, A., Vogels, T. P., & Goldberg, E. M. (2022). Developmentally regulated impairment of parvalbumin interneuron synaptic transmission in an experimental model of Dravet syndrome. *Cell Reports*, *38*(13), 110580. https://doi.org/10.1016/J.CELREP.2022.110580

Kang, J. Q., & MacDonald, R. L. (2016). GABRG2 Mutations Associated with a spectrum of epilepsy syndromes from Generalized Absence Epilepsy to Dravet syndrome. *JAMA Neurology*, *73*(8), 1009. https://doi.org/10.1001/JAMANEUROL.2016.0449

Kawasaki, H., Mizuseki, K., Nishikawa, S., Kaneko, S., Kuwana, Y., Nakanishi, S., Nishikawa, S. I., & Sasai, Y. (2000). Induction of midbrain dopaminergic neurons from ES cells by stromal cell-derived inducing activity. *Neuron*. https://doi.org/10.1016/S0896-6273(00)00083-0

Khan, L., van Lanen, R., Hoogland, G., Schijns, O., Rijkers, K., Kapsokalyvas, D., van Zandvoort, M., & Haeren, R. (2021). Two-Photon Imaging to Unravel the Pathomechanisms Associated with Epileptic Seizures: A Review. *Applied Sciences 2021, Vol. 11, Page 2404*, *11*(5), 2404. https://doi.org/10.3390/APP11052404

Kidambi, S., Lee, I., & Chan, C. (2008). Primary Neuron/Astrocyte Co-Culture on Polyelectrolyte Multilayer Films: A Template for Studying Astrocyte-Mediated Oxidative Stress in Neurons. *Advanced Functional Materials*, *18*(2), 294. https://doi.org/10.1002/ADFM.200601237

Kiese, K., Jablonski, J., Hackenbracht, J., Wrosch, J. K., Groemer, T. W., Kornhuber, J., Blümcke, I., & Kobow, K. (2017). Epigenetic control of epilepsy target genes contributes to a cellular memory of epileptogenesis in cultured rat hippocampal neurons. *Acta Neuropathologica Communications*, *5*(1), 79. https://doi.org/10.1186/S40478-017-0485-X/FIGURES/7

Kim, E., & Sheng, M. (2004). PDZ domain proteins of synapses. *Nature Reviews. Neuroscience*, *5*(10), 771–781. https://doi.org/10.1038/NRN1517

Kim, H. W., Quan, Z., Kim, Y. B., Cheong, E., Kim, H. D., Cho, M., Jang, J., Yoo, Y. R., Lee, J. S., Kim, J. H., Kim, Y. I., Kim, D. S., & Kang, H. C. (2018). Differential effects on sodium current impairments by distinct SCN1A mutations in GABAergic neurons derived from Dravet syndrome patients. *Brain and Development*, *40*(4), 287–298. https://doi.org/10.1016/J.BRAINDEV.2017.12.002

Kim, J.-E., O'Sullivan, M. L., Sanchez, C. A., Hwang, M., Israel, M. A., Brennand, K., Deerinck, T. J., Goldstein, L. S. B., Gage, F. H., Ellisman, M. H., & Ghosh, A. (2011). Investigating synapse formation and function using human pluripotent stem cell-derived neurons. *Proceedings of the National Academy of Sciences*. https://doi.org/10.1073/pnas.1007753108

Kim, K., Zhao, R., Doi, A., Ng, K., Unternaehrer, J., Cahan, P., Hongguang, H., Loh, Y. H., Aryee, M. J., Lensch, M. W., Li, H., Collins, J. J., Feinberg, A. P., & Daley, G. Q. (2011). Donor cell type can influence the epigenome and differentiation potential of human induced pluripotent stem cells. *Nature Biotechnology*. https://doi.org/10.1038/nbt.2052

Kirwan, P., Turner-Bridger, B., Peter, M., Momoh, A., Arambepola, D., Robinson, H. P. C., & Livesey, F. J. (2015). Development and function of human cerebral cortex neural networks from pluripotent stem cells in vitro. *Development*. https://doi.org/10.1242/dev.123851

Kole, M. H. P., Ilschner, S. U., Kampa, B. M., Williams, S. R., Ruben, P. C., & Stuart, G. J. (2008). Action potential generation requires a high sodium channel density in the axon initial segment. *Nature Neuroscience 2008 11:2*, *11*(2), 178–186. https://doi.org/10.1038/nn2040

Koyanagi-Aoi, M., Ohnuki, M., Takahashi, K., Okita, K., Noma, H., Sawamura, Y., Teramoto, I., Narita, M., Sato, Y., Ichisaka, T., Amanoa, N., Watanabe, A., Morizane, A., Yamada, Y., Sato, T., Takahashi, J., & Yamanaka, S. (2013). Differentiation-defective phenotypes revealed by large-scale analyses of human pluripotent stem cells. *Proceedings of the National Academy of Sciences of the United States of America*. https://doi.org/10.1073/pnas.1319061110

Kuba, H., Oichi, Y., & Ohmori, H. (2010). Presynaptic activity regulates Na+ channel distribution at the axon initial segment. *Nature 2010 465:7301*, *465*(7301), 1075–1078. https://doi.org/10.1038/nature09087

Kuo, F. S., Cleary, C. M., Loturco, J. J., Chen, X., & Mulkey, D. K. (2019). Disordered breathing in a mouse model of Dravet syndrome. *ELife*, *8*. https://doi.org/10.7554/ELIFE.43387

Lagae, L., Brambilla, I., Mingorance, A., Gibson, E., & Battersby, A. (2018). Quality of life and comorbidities associated with Dravet syndrome severity: a multinational cohort survey. *Developmental Medicine and Child Neurology*, *60*(1), 63–72. https://doi.org/10.1111/DMCN.13591/ABSTRACT

Lam, R. S., Töpfer, F. M., Wood, P. G., Busskamp, V., & Bamberg, E. (2017). Functional Maturation of Human Stem Cell-Derived Neurons in Long-Term Cultures. *PLoS ONE*, *12*(1). https://doi.org/10.1371/JOURNAL.PONE.0169506

Lancaster, M. A., Renner, M., Martin, C. A., Wenzel, D., Bicknell, L. S., Hurles, M. E., Homfray, T., Penninger, J. M., Jackson, A. P., & Knoblich, J. A. (2013). Cerebral organoids model human brain development and microcephaly. *Nature 2013 501:7467*, *501*(7467), 373–379. https://doi.org/10.1038/nature12517

Lee, H., Shamy, G. al, Elkabetz, Y., Schofield, C. M., Harrsion, N. L., Panagiotakos, G., Socci, N. D., Tabar, V., & Studer, L. (2007). Directed Differentiation and Transplantation of Human Embryonic Stem Cell-Derived Motoneurons. *Stem Cells*. https://doi.org/10.1634/stemcells.2007-0097

Lee, K. S., Zhou, W., Scott-McKean, J. J., Emmerling, K. L., Cai, G. yun, Krah, D. L., Costa, A. C., Freed, C. R., & Levin, M. J. (2012). Human Sensory Neurons Derived from Induced Pluripotent Stem Cells Support Varicella-Zoster Virus Infection. *PLoS ONE*. https://doi.org/10.1371/journal.pone.0053010

Leung, R. F., George, A. M., Roussel, E. M., Faux, M. C., Wigle, J. T., & Eisenstat, D. D. (2022). Genetic Regulation of Vertebrate Forebrain Development by Homeobox Genes. *Frontiers in Neuroscience*, *16*. https://doi.org/10.3389/FNINS.2022.843794

Lezmy, J., Lipinsky, M., Khrapunsky, Y., Patrich, E., Shalom, L., Peretz, A., Fleidervish, I. A., & Attali, B. (2017). M-current inhibition rapidly induces a unique CK2-dependent plasticity of the axon initial segment. *Proceedings of the National Academy of Sciences of the United States of America*, *114*(47), E10234–E10243. https://doi.org/10.1073/PNAS.1708700114/SUPPL_FILE/PNAS.1708700114.SM02.AVI

Li, T., Tian, C., Scalmani, P., Frassoni, C., Mantegazza, M., Wang, Y., Yang, M., Wu, S., & Shu, Y. (2014). Action Potential Initiation in Neocortical Inhibitory Interneurons. *PLOS Biology*, *12*(9), e1001944. https://doi.org/10.1371/JOURNAL.PBIO.1001944

Li, W., Schneider, A. L., & Scheffer, I. E. (2021). Defining Dravet syndrome: An essential pre-requisite for precision medicine trials. *Epilepsia*, *62*(9), 2205. https://doi.org/10.1111/EPI.17015

Li, X., Tao, Y., Bradley, R., Du, Z., Tao, Y., Kong, L., Dong, Y., Jones, J., Yan, Y., Harder, C. R. K., Friedman, L. M., Bilal, M., Hoffmann, B., & Zhang, S. C. (2018a). Fast Generation of Functional Subtype Astrocytes from Human Pluripotent Stem Cells. *Stem Cell Reports*. https://doi.org/10.1016/j.stemcr.2018.08.019

Li, X., Tao, Y., Bradley, R., Du, Z., Tao, Y., Kong, L., Dong, Y., Jones, J., Yan, Y., Harder, C. R. K., Friedman, L. M., Bilal, M., Hoffmann, B., & Zhang, S. C. (2018b). Fast Generation of Functional Subtype Astrocytes from Human Pluripotent Stem Cells. *Stem Cell Reports*, *11*(4), 998. https://doi.org/10.1016/J.STEMCR.2018.08.019

Liao, Y., Deprez, L., Maljevic, S., Pitsch, J., Claes, L., Hristova, D., Jordanova, A., Ala-Mello, S., Bellan-Koch, A., Blazevic, D., Schubert, S., Thomas, E. A., Petrou, S., Becker, A. J., De Jonghe, P., & Lerche, H. (2010). Molecular correlates of age-dependent seizures in an inherited neonatal-infantile epilepsy. *Brain*, *133*(5), 1403–1414. https://doi.org/10.1093/BRAIN/AWQ057

Liebmann, M., Stahr, A., Guenther, M., Witte, O. W., & Frahm, C. (2013). Astrocytic Cx43 and Cx30 differentially modulate adult neurogenesis in mice. *Neuroscience Letters*, *545*, 40–45. https://doi.org/10.1016/J.NEULET.2013.04.013

Lim, K. H., Han, Z., Jeon, H. Y., Kach, J., Jing, E., Weyn-Vanhentenryck, S., Downs, M., Corrionero, A., Oh, R., Scharner, J., Venkatesh, A., Ji, S., Liau, G., Ticho, B., Nash, H., & Aznarez, I. (2020). Antisense oligonucleotide modulation of non-productive alternative splicing upregulates gene expression. *Nature Communications 2020 11:1*, *11*(1), 1–13. https://doi.org/10.1038/s41467-020-17093-9

Liu, J., Gao, C., Chen, W., Ma, W., Li, X., Shi, Y., Zhang, H., Zhang, L., Long, Y., Xu, H., Guo, X., Deng, S., Yan, X., Yu, D., Pan, G., Chen, Y., Lai, L., Liao, W., & Li, Z. (2016a). CRISPR/Cas9 facilitates investigation of neural circuit disease using human iPSCs: mechanism of epilepsy caused by an SCN1A loss-of-function mutation. *Translational Psychiatry*, *6*(1), e703. https://doi.org/10.1038/TP.2015.203

Liu, J., Gao, C., Chen, W., Ma, W., Li, X., Shi, Y., Zhang, H., Zhang, L., Long, Y., Xu, H., Guo, X., Deng, S., Yan, X., Yu, D., Pan, G., Chen, Y., Lai, L., Liao, W., & Li, Z. (2016b). CRISPR/Cas9 facilitates investigation of neural circuit disease using human iPSCs: Mechanism of epilepsy caused by an SCN1A loss-of-function mutation. *Translational Psychiatry*. https://doi.org/10.1038/tp.2015.203

Liu, T. T., Feng, L., Liu, H. F., Shu, Y., & Xiao, B. (2017). Altered axon initial segment in hippocampal newborn neurons, associated with recurrence of temporal lobe epilepsy in rats. *Molecular Medicine Reports*, *16*(3), 3169–3178. https://doi.org/10.3892/MMR.2017.7017/HTML

Liu, Y., Liu, H., Sauvey, C., Yao, L., Zarnowska, E. D., & Zhang, S. C. (2013). Directed differentiation of forebrain GABA interneurons from human pluripotent stem cells. *Nature Protocols*. https://doi.org/10.1038/nprot.2013.106

Liu, Y., Lopez-Santiago, L. F., Yuan, Y., Jones, J. M., Zhang, H., O'Malley, H. A., Patino, G. A., O'Brien, J. E., Rusconi, R., Gupta, A., Thompson, R. C., Natowicz, M. R., Meisler, M. H., Isom, L. L., & Parent, J. M. (2013). Dravet syndrome patient-derived neurons suggest a novel epilepsy mechanism. *Annals of Neurology*. https://doi.org/10.1002/ana.23897

Livak, K. J., & Schmittgen, T. D. (2001). Analysis of Relative Gene Expression Data Using Real-Time Quantitative PCR and the 2−ΔΔCT Method. *Methods*, *25*(4), 402–408. https://doi.org/10.1006/METH.2001.1262

Lodato, S., & Arlotta, P. (2015). Generating Neuronal Diversity in the Mammalian Cerebral Cortex. *Annual Review of Cell and Developmental Biology*, *31*, 699. https://doi.org/10.1146/ANNUREV-CELLBIO-100814-125353

Lorincz, A., & Nusser, Z. (2008). Coverarticle: Twij: Cell-Type-Dependent Molecular Composition of the Axon Initial Segment. *The Journal of Neuroscience*, *28*(53), 14329. https://doi.org/10.1523/JNEUROSCI.4833-08.2008

Lu, B., Zhang, Q., Wang, H., Wang, Y., Nakayama, M., & Ren, D. (2010). Extracellular Calcium Controls Background Current and Neuronal Excitability via an UNC79-UNC80-NALCN Cation Channel Complex. *Neuron*, *68*(3), 488. https://doi.org/10.1016/J.NEURON.2010.09.014

Machado, C. B., Pluchon, P., Harley, P., Rigby, M., Sabater, V. G., Stevenson, D. C., Hynes, S., Lowe, A., Burrone, J., Viasnoff, V., & Lieberam, I. (2019). In Vitro Modelling of Nerve-Muscle Connectivity in a Compartmentalised Tissue Culture Device. *Advanced Biosystems*, *3*(7). https://doi.org/10.1002/ADBI.201800307

Maillard, P. Y., Baer, S., Schaefer, É., Desnous, B., Villeneuve, N., Lépine, A., Fabre, A., Lacoste, C., El Chehadeh, S., Piton, A., Porter, L. F., Perriard, C., Wardé, M. T. A., Spitz, M. A., Laugel, V., Lesca, G., Putoux, A., Ville, D., Mignot, C., … Milh, M. (2022). Molecular and clinical descriptions of patients with GABAA receptor gene variants (GABRA1, GABRB2, GABRB3, GABRG2): A cohort study, review of literature, and

genotype–phenotype correlation. *Epilepsia*, *63*(10), 2519–2533. https://doi.org/10.1111/epi.17336

Maňáková, Š., Puttonen, K. A., Raasmaja, A., & Männistö, P. T. (2003). Ara-C induces apoptosis in monkey fibroblast cells. *Toxicology in Vitro*, *17*(3), 367–373. https://doi.org/10.1016/S0887-2333(03)00024-9

Mantegazza, M. (2011). Dravet syndrome: Insights from in vitro experimental models. *Epilepsia*. https://doi.org/10.1111/j.1528-1167.2011.03005.x

Mantegazza, M., & Cestèle, S. (2018). Pathophysiological mechanisms of migraine and epilepsy: Similarities and differences. *Neuroscience Letters*, *667*, 92–102. https://doi.org/10.1016/J.NEULET.2017.11.025

Mariani, J., Simonini, M. V., Palejev, D., Tomasini, L., Coppola, G., Szekely, A. M., Horvath, T. L., & Vaccarino, F. M. (2012). Modeling human cortical development in vitro using induced pluripotent stem cells. *Proceedings of the National Academy of Sciences*. https://doi.org/10.1073/pnas.1202944109

Marín, O., Anderson, S. A., & Rubenstein, J. L. R. (2000). Origin and molecular specification of striatal interneurons. *The Journal of Neuroscience : The Official Journal of the Society for Neuroscience*, *20*(16), 6063–6076. https://doi.org/10.1523/JNEUROSCI.20-16-06063.2000

Marini, C., Scheffer, I. E., Nabbout, R., Mei, D., Cox, K., Dibbens, L. M., McMahon, J. M., Iona, X., Carpintero, R. S., Elia, M., Cilio, M. R., Specchio, N., Giordano, L., Striano, P., Gennaro, E., Cross, J. H., Kivity, S., Neufeld, M. Y., Afawi, Z., … Mulley, J. C. (2009). SCN1A duplications and deletions detected in Dravet syndrome: Implications for molecular diagnosis. *Epilepsia*. https://doi.org/10.1111/j.1528-1167.2009.02013.x

Marini, C., Scheffer, I. E., Nabbout, R., Suls, A., de Jonghe, P., Zara, F., & Guerrini, R. (2011). The genetics of Dravet syndrome. *Epilepsia*. https://doi.org/10.1111/j.1528-1167.2011.02997.x

Maroof, A. M., Keros, S., Tyson, J. A., Ying, S. W., Ganat, Y. M., Merkle, F. T., Liu, B., Goulburn, A., Stanley, E. G., Elefanty, A. G., Widmer, H. R., Eggan, K., Goldstein, P. A., Anderson, S. A., & Studer, L. (2013). Directed differentiation and functional maturation of cortical interneurons from human embryonic stem cells. *Cell Stem Cell*. https://doi.org/10.1016/j.stem.2013.04.008

Martin, M. S., Dutt, K., Papale, L. A., Dubé, C. M., Dutton, S. B., De Haan, G., Shankar, A., Tufik, S., Meisler, M. H., Baram, T. Z., Goldin, A. L., & Escayg, A. (2010). Altered Function of the SCN1A Voltage-gated Sodium Channel Leads to γ-Aminobutyric Acid-ergic (GABAergic) Interneuron Abnormalities. *The Journal of Biological Chemistry*, *285*(13), 9823. https://doi.org/10.1074/JBC.M109.078568

Martin, P., Reeder, T., Sourbron, J., de Witte, P. A. M., Gammaitoni, A. R., & Galer, B. S. (2021). An emerging role for sigma-1 receptors in the treatment of developmental and epileptic encephalopathies. *International Journal of Molecular Sciences*, *22*(16). https://doi.org/10.3390/IJMS22168416/S1

Martín-Suárez, S., Abiega, O., Ricobaraza, A., Hernandez-Alcoceba, R., & Encinas, J. M. (2020). Alterations of the Hippocampal Neurogenic Niche in a Mouse Model of Dravet Syndrome. *Frontiers in Cell and Developmental Biology*, *8*, 654. https://doi.org/10.3389/FCELL.2020.00654/FULL

Martiszus, B. J., Tsintsadze, T., Chang, W., & Smith, S. M. (2021). Enhanced excitability of cortical neurons in low-divalent solutions is primarily mediated by altered voltage-dependence of voltage-gated sodium channels. *ELife*, *10*. https://doi.org/10.7554/ELIFE.67914

Matsuda, N., Odawara, A., Katoh, H., Okuyama, N., Yokoi, R., & Suzuki, I. (2018). Detection of synchronized burst firing in cultured human induced pluripotent stem cell-derived

neurons using a 4-step method. *Biochemical and Biophysical Research Communications*. https://doi.org/10.1016/j.bbrc.2018.02.117

McIntire, S. L., Reimer, R. J., Schuske, K., Edwards, R. H., & Jorgensen, E. M. (1997). Identification and characterization of the vesicular GABA transporter. *Nature*, *389*(6653), 870–876. https://doi.org/10.1038/39908

Meisler, M. H., & Kearney, J. A. (2005). Sodium channel mutations in epilepsy and other neurological disorders. In *Journal of Clinical Investigation*. https://doi.org/10.1172/JCI25466

Meng, H., Xu, H. Q., Yu, L., Lin, G. W., He, N., Su, T., Shi, Y. W., Li, B., Wang, J., Liu, X. R., Tang, B., Long, Y. S., Yi, Y. H., & Liao, W. P. (2015). The SCN1A Mutation Database: Updating Information and Analysis of the Relationships among Genotype, Functional Alteration, and Phenotype. *Human Mutation*, *36*(6), 573–580. https://doi.org/10.1002/HUMU.22782

Messner, D. J., & Catterall, W. A. (1985). The sodium channel from rat brain. Separation and characterization of subunits. *Journal of Biological Chemistry*.

Milescu, L. S., Bean, B. P., & Smith, J. C. (2010). Isolation of Somatic Na+ Currents by Selective Inactivation of Axonal Channels with a Voltage Prepulse. *The Journal of Neuroscience*, *30*(22), 7740. https://doi.org/10.1523/JNEUROSCI.6136-09.2010

Miller, A. R., Hawkins, N. A., McCollom, C. E., & Kearney, J. A. (2014). Mapping genetic modifiers of survival in a mouse model of Dravet syndrome. *Genes, Brain, and Behavior*, *13*(2), 163–172. https://doi.org/10.1111/gbb.12099

Miller, A. R., Hawkins, N. A., Mccollom, C. E., & Kearney, J. A. (2014). Mapping genetic modifiers of survival in a mouse model of Dravet syndrome. *Genes, Brain, and Behavior*, *13*(2), 163. https://doi.org/10.1111/GBB.12099

Mistry, A. M., Thompson, C. H., Miller, A. R., Vanoye, C. G., George, A. L., & Kearney, J. A. (2014). Strain- and Age-dependent Hippocampal Neuron Sodium Currents Correlate with Epilepsy Severity in Dravet Syndrome Mice. *Neurobiology of Disease*, *65*, 1. https://doi.org/10.1016/J.NBD.2014.01.006

Modi, J., Prentice, H., & Wu, J.-Y. (2015). Regulation of GABA Neurotransmission by Glutamic Acid Decarboxylase (GAD). *Current Pharmaceutical Design*, *21*(34), 4939–4942. https://doi.org/10.2174/1381612821666150917094343

Mora-Jimenez, L., Valencia, M., Sanchez-Carpintero, R., Tønnesen, J., Fadila, S., Rubinstein, M., Gonzalez-Aparicio, M., Bunuales, M., Fernandez-Pierola, E., Nicolas, M. J., Puerta, E., Miguelez, C., Minguez, P. G., Lumbreras, S., Gonzalez-Aseguinolaza, G., Ricobaraza, A., & Hernandez-Alcoceba, R. (2021). Transfer of SCN1A to the brain of adolescent mouse model of Dravet syndrome improves epileptic, motor, and behavioral manifestations. *Molecular Therapy - Nucleic Acids*, *25*, 585–602. https://doi.org/10.1016/j.omtn.2021.08.003

Moreau, T., Evans, A. L., Vasquez, L., Tijssen, M. R., Yan, Y., Trotter, M. W., Howard, D., Colzani, M., Arumugam, M., Wu, W. H., Dalby, A., Lampela, R., Bouet, G., Hobbs, C. M., Pask, D. C., Payne, H., Ponomaryov, T., Brill, A., Soranzo, N., … Ghevaert, C. (2016). Large-scale production of megakaryocytes from human pluripotent stem cells by chemically defined forward programming. *Nature Communications*. https://doi.org/10.1038/ncomms11208

Nadadhur, A. G., Melero, J. E., Meijer, M., Schut, D., Jacobs, G., Wan Li, K., Hjorth, J. J. J., Meredith, R. M., Toonen, R. F., Van Kesteren, R. E., Smit, A. B., Verhage, M., & Heine, V. M. (2017). Multi-level characterization of balanced inhibitory-excitatory cortical neuron network derived from human pluripotent stem cells. *PLoS ONE*. https://doi.org/10.1371/journal.pone.0178533

Nakajima, S., & Kunugi, H. (2020). Lauric acid promotes neuronal maturation mediated by astrocytes in primary cortical cultures. *Heliyon*, *6*(5), e03892. https://doi.org/10.1016/J.HELIYON.2020.E03892

Narsinh, K. H., Plews, J., & Wu, J. C. (2011). Comparison of Human Induced Pluripotent and Embryonic Stem Cells: Fraternal or Identical Twins? *Molecular Therapy*, *19*(4), 635–638. https://doi.org/10.1038/MT.2011.41

Negraes, P. D., Trujillo, C. A., Yu, N. K., Wu, W., Yao, H., Liang, N., Lautz, J. D., Kwok, E., McClatchy, D., Diedrich, J., de Bartolome, S. M., Truong, J., Szeto, R., Tran, T., Herai, R. H., Smith, S. E. P., Haddad, G. G., Yates, J. R., & Muotri, A. R. (2021). Altered network and rescue of human neurons derived from individuals with early-onset genetic epilepsy. *Molecular Psychiatry 2021 26:11*, *26*(11), 7047–7068. https://doi.org/10.1038/s41380-021-01104-2

Nehme, R., Zuccaro, E., Ghosh, S. D., Li, C., Sherwood, J. L., Pietilainen, O., Barrett, L. E., Limone, F., Worringer, K. A., Kommineni, S., Zang, Y., Cacchiarelli, D., Meissner, A., Adolfsson, R., Haggarty, S., Madison, J., Muller, M., Arlotta, P., Fu, Z., … Eggan, K. (2018). Combining NGN2 Programming with Developmental Patterning Generates Human Excitatory Neurons with NMDAR-Mediated Synaptic Transmission. *Cell Reports*. https://doi.org/10.1016/j.celrep.2018.04.066

Neyrinck, K., van den Daele, J., Vervliet, T., de Smedt, J., Wierda, K., Nijs, M., Vanbokhoven, T., D'hondt, A., Planque, M., Fendt, S. M., Shih, P. Y., Seibt, F., Almenar, J. P., Kreir, M., Kumar, D., Broccoli, V., Bultynck, G., Ebneth, A., Cabrera-Socorro, A., & Verfaillie, C. (2021). SOX9-induced Generation of Functional Astrocytes Supporting Neuronal Maturation in an All-human System. *Stem Cell Reviews and Reports*, *17*(5), 1855–1873. https://doi.org/10.1007/S12015-021-10179-X/FIGURES/5

Ng, A. H. M., Khoshakhlagh, P., Rojo Arias, J. E., Pasquini, G., Wang, K., Swiersy, A., Shipman, S. L., Appleton, E., Kiaee, K., Kohman, R. E., Vernet, A., Dysart, M., Leeper, K., Saylor, W., Huang, J. Y., Graveline, A., Taipale, J., Hill, D. E., Vidal, M., … Church, G. M. (2020). A comprehensive library of human transcription factors for cell fate engineering. *Nature Biotechnology 2020 39:4*, *39*(4), 510–519. https://doi.org/10.1038/s41587-020-0742-6

Oakley, J. C., Kalume, F., Yu, F. H., Scheuer, T., & Catterall, W. A. (2009a). Temperature- and age-dependent seizures in a mouse model of severe myoclonic epilepsy in infancy. *Proceedings of the National Academy of Sciences of the United States of America*, *106*(10), 3994. https://doi.org/10.1073/PNAS.0813330106

Oakley, J. C., Kalume, F., Yu, F. H., Scheuer, T., & Catterall, W. A. (2009b). Temperature- and age-dependent seizures in a mouse model of severe myoclonic epilepsy in infancy. *Proceedings of the National Academy of Sciences of the United States of America*, *106*(10), 3994–3999. https://doi.org/10.1073/PNAS.0813330106/SUPPL_FILE/0813330106SI.PDF

Oberheim, N. A., Takano, T., Han, X., He, W., Lin, J. H. C., Wang, F., Xu, Q., Wyatt, J. D., Pilcher, W., Ojemann, J. G., Ransom, B. R., Goldman, S. A., & Nedergaard, M. (2009). Uniquely Hominid Features of Adult Human Astrocytes. *Journal of Neuroscience*, *29*(10), 3276–3287. https://doi.org/10.1523/JNEUROSCI.4707-08.2009

Oceguera-Yanez, F., Kim, S. Il, Matsumoto, T., Tan, G. W., Xiang, L., Hatani, T., Kondo, T., Ikeya, M., Yoshida, Y., Inoue, H., & Woltjen, K. (2016). Engineering the AAVS1 locus for consistent and scalable transgene expression in human iPSCs and their differentiated derivatives. *Methods*. https://doi.org/10.1016/j.ymeth.2015.12.012

Ogiwara, I., Ito, K., Sawaishi, Y., Osaka, H., Mazaki, E., Inoue, I., Montal, M., Hashikawa, T., Shike, T., Fujiwara, T., Inoue, Y., Kaneda, M., & Yamakawa, K. (2009). De novo

mutations of voltage-gated sodium channel αiI gene SCN2A in intractable epilepsies. *Neurology*. https://doi.org/10.1212/WNL.0b013e3181b9cebc

Ogiwara, I., Iwasato, T., Miyamoto, H., Iwata, R., Yamagata, T., Mazaki, E., Yanagawa, Y., Tamamaki, N., Hensch, T. K., Itohara, S., & Yamakawa, K. (2013). Nav1.1 haploinsufficiency in excitatory neurons ameliorates seizure-associated sudden death in a mouse model of Dravet syndrome. *Human Molecular Genetics*, *22*(23), 4784–4804. https://doi.org/10.1093/HMG/DDT331

Ogiwara, I., Miyamoto, H., Morita, N., Atapour, N., Mazaki, E., Inoue, I., Takeuchi, T., Itohara, S., Yanagawa, Y., Obata, K., Furuichi, T., Hensch, T. K., & Yamakawa, K. (2007a). Nav1.1 Localizes to Axons of Parvalbumin-Positive Inhibitory Interneurons: A Circuit Basis for Epileptic Seizures in Mice Carrying an Scn1a Gene Mutation. *Journal of Neuroscience*. https://doi.org/10.1523/jneurosci.5270-06.2007

Ogiwara, I., Miyamoto, H., Morita, N., Atapour, N., Mazaki, E., Inoue, I., Takeuchi, T., Itohara, S., Yanagawa, Y., Obata, K., Furuichi, T., Hensch, T. K., & Yamakawa, K. (2007b). Nav1.1 Localizes to Axons of Parvalbumin-Positive Inhibitory Interneurons: A Circuit Basis for Epileptic Seizures in Mice Carrying an Scn1a Gene Mutation. *Journal of Neuroscience*, *27*(22), 5903–5914. https://doi.org/10.1523/JNEUROSCI.5270-06.2007

Oh, J., Lee, C., & Kaang, B. K. (2019). Imaging and analysis of genetically encoded calcium indicators linking neural circuits and behaviors. *The Korean Journal of Physiology & Pharmacology : Official Journal of the Korean Physiological Society and the Korean Society of Pharmacology*, *23*(4), 237. https://doi.org/10.4196/KJPP.2019.23.4.237

O'Leary, L. A., Davoli, M. A., Belliveau, C., Tanti, A., Ma, J. C., Farmer, W. T., Turecki, G., Murai, K. K., & Mechawar, N. (2020). Characterization of Vimentin-Immunoreactive Astrocytes in the Human Brain. *Frontiers in Neuroanatomy*, *14*. https://doi.org/10.3389/FNANA.2020.00031

Olsen, R. W., & DeLorey, T. M. (1999). *GABA Receptor Physiology and Pharmacology*. https://www.ncbi.nlm.nih.gov/books/NBK28090/

Osafune, K., Caron, L., Borowiak, M., Martinez, R. J., Fitz-Gerald, C. S., Sato, Y., Cowan, C. A., Chien, K. R., & Melton, D. A. (2008). Marked differences in differentiation propensity among human embryonic stem cell lines. *Nature Biotechnology*. https://doi.org/10.1038/nbt1383

Pacico, N., & Meur, A. M. Le. (2014). New In Vitro Phenotypic Assay for Epilepsy: Fluorescent Measurement of Synchronized Neuronal Calcium Oscillations. *PLOS ONE*, *9*(1), e84755. https://doi.org/10.1371/JOURNAL.PONE.0084755

Pang, Z. P., Yang, N., Vierbuchen, T., Ostermeier, A., Fuentes, D. R., Yang, T. Q., Citri, A., Sebastiano, V., Marro, S., Südhof, T. C., & Wernig, M. (2011). Induction of human neuronal cells by defined transcription factors. In *Nature*. https://doi.org/10.1038/nature10202

Paredes, R. M., Etzler, J. C., Watts, L. T., Zheng, W., & Lechleiter, J. D. (2008). Chemical Calcium Indicators. *Methods (San Diego, Calif.)*, *46*(3), 143. https://doi.org/10.1016/J.YMETH.2008.09.025

Paredes-Redondo, A., Harley, P., Maniati, E., Ryan, D., Louzada, S., Meng, J., Kowala, A., Fu, B., Yang, F., Liu, P., Marino, S., Pourquié, O., Muntoni, F., Wang, J., Lieberam, I., & Lin, Y. Y. (2021). Optogenetic modeling of human neuromuscular circuits in Duchenne muscular dystrophy with CRISPR and pharmacological corrections. *Science Advances*, *7*(37), 8787–8797. https://doi.org/10.1126/SCIADV.ABI8787

Pasca, A. M., Sloan, S. A., Clarke, L. E., Tian, Y., Makinson, C. D., Huber, N., Kim, C. H., Park, J. Y., O'Rourke, N. A., Nguyen, K. D., Smith, S. J., Huguenard, J. R., Geschwind, D. H., Barres, B. A., & Pasca, S. P. (2015). Functional cortical neurons and astrocytes

from human pluripotent stem cells in 3D culture. *Nature Methods 2015 12:7*, *12*(7), 671–678. https://doi.org/10.1038/nmeth.3415

Patino, G. A., Claes, L. R. F., Lopez-Santiago, L. F., Slat, E. A., Dondeti, R. S. R., Chen, C., O'Malley, H. A., Gray, C. B. B., Miyazaki, H., Nukina, N., Oyama, F., De Jonghe, P., & Isom, L. L. (2009). A Functional Null Mutation of SCN1B in a Patient with Dravet Syndrome. *Journal of Neuroscience*. https://doi.org/10.1523/jneurosci.2475-09.2009

Pavani, G., & Amendola, M. (2021). Targeted Gene Delivery: Where to Land. *Frontiers in Genome Editing*, *2*, 36. https://doi.org/10.3389/FGEED.2020.609650

Penn, Y., Segal, M., & Moses, E. (2016). Network synchronization in hippocampal neurons. *Proceedings of the National Academy of Sciences of the United States of America*, *113*(12), 3341–3346. https://doi.org/10.1073/PNAS.1515105113/-/DCSUPPLEMENTAL

Perez, J., Chiron, C., Musial, C., Rey, E., Blehaut, H., D'Athis, P., Vincent, J., & Dulac, O. (1999). Stiripentol: Efficacy and tolerability in children with epilepsy. *Epilepsia*. https://doi.org/10.1111/j.1528-1157.1999.tb02048.x

Perez-Reyes, E. (2003). Molecular physiology of low-voltage-activated t-type calcium channels. *Physiological Reviews*, *83*(1), 117–161. https://doi.org/10.1152/PHYSREV.00018.2002

Petryniak, M. A., Potter, G. B., Rowitch, D. H., & Rubenstein, J. L. R. (2007). Dlx1 and Dlx2 Control Neuronal versus Oligodendroglial Cell Fate Acquisition in the Developing Forebrain. *Neuron*, *55*(3), 417–433. https://doi.org/10.1016/j.neuron.2007.06.036

Puri, M. C., & Nagy, A. (2012). Concise Review: Embryonic Stem Cells Versus Induced Pluripotent Stem Cells: The Game Is On. *STEM CELLS*, *30*(1), 10–14. https://doi.org/10.1002/STEM.788

Purves, D., Augustine, G. J., Fitzpatrick, D., Katz, L. C., LaMantia, A.-S., McNamara, J. O., & Williams, S. M. (2001). *The Molecular Basis of Neural Induction*. https://www.ncbi.nlm.nih.gov/books/NBK10823/

Qian, X., Nguyen, H. N., Song, M. M., Hadiono, C., Ogden, S. C., Hammack, C., Yao, B., Hamersky, G. R., Jacob, F., Zhong, C., Yoon, K. J., Jeang, W., Lin, L., Li, Y., Thakor, J., Berg, D. A., Zhang, C., Kang, E., Chickering, M., … Ming, G. L. (2016). Brain-Region-Specific Organoids Using Mini-bioreactors for Modeling ZIKV Exposure. *Cell*, *165*(5), 1238–1254. https://doi.org/10.1016/j.cell.2016.04.032

Quadrato, G., Nguyen, T., Macosko, E. Z., Sherwood, J. L., Yang, S. M., Berger, D. R., Maria, N., Scholvin, J., Goldman, M., Kinney, J. P., Boyden, E. S., Lichtman, J. W., Williams, Z. M., McCarroll, S. A., & Arlotta, P. (2017). Cell diversity and network dynamics in photosensitive human brain organoids. *Nature 2017 545:7652*, *545*(7652), 48–53. https://doi.org/10.1038/nature22047

Quilichini, P. P., Chiron, C., Ben-Ari, Y., & Gozlan, H. (2006). Stiripentol, a putative antiepileptic drug, enhances the duration of opening of GABAA-receptor channels. *Epilepsia*. https://doi.org/10.1111/j.1528-1167.2006.00497.x

Rhee, H. J., Shaib, A. H., Rehbach, K., Lee, C. K., Seif, P., Thomas, C., Gideons, E., Guenther, A., Krutenko, T., Hebisch, M., Peitz, M., Brose, N., Brüstle, O., & Rhee, J. S. (2019). An Autaptic Culture System for Standardized Analyses of iPSC-Derived Human Neurons. *Cell Reports*. https://doi.org/10.1016/j.celrep.2019.04.059

Ricobaraza, A., Gonzalez-Aparicio, M., Mora-Jimenez, L., Lumbreras, S., & Hernandez-Alcoceba, R. (2020). High-Capacity Adenoviral Vectors: Expanding the Scope of Gene Therapy. *International Journal of Molecular Sciences*, *21*(10). https://doi.org/10.3390/IJMS21103643

Ricobaraza, A., Mora-Jimenez, L., Puerta, E., Sanchez-Carpintero, R., Mingorance, A., Artieda, J., Nicolas, M. J., Besne, G., Bunuales, M., Gonzalez-Aparicio, M., Sola-Sevilla, N., Valencia, M., & Hernandez-Alcoceba, R. (2019). Epilepsy and

neuropsychiatric comorbidities in mice carrying a recurrent Dravet syndrome SCN1A missense mutation. *Scientific Reports*, *9*(1). https://doi.org/10.1038/S41598-019-50627-W

Rosahl, T. W., Spillane, D., Missler, M., Herz, J., Selig, D. K., Wolff, J. R., Hammer, R. E., Malenka, R. C., & Südhof, T. C. (1995). Essential functions of synapsins I and II in synaptic vesicle regulation. *Nature*, *375*(6531), 488–493. https://doi.org/10.1038/375488A0

Rosch, R. E., Hunter, P. R., Baldeweg, T., Friston, K. J., & Meyer, M. P. (2018). Calcium imaging and dynamic causal modelling reveal brain-wide changes in effective connectivity and synaptic dynamics during epileptic seizures. *PLoS Computational Biology*, *14*(8). https://doi.org/10.1371/JOURNAL.PCBI.1006375

Rosenberg, E. C., Patra, P. H., & Whalley, B. J. (2017). Therapeutic effects of cannabinoids in animal models of seizures, epilepsy, epileptogenesis, and epilepsy-related neuroprotection. *Epilepsy & Behavior : E&B*, *70*(Pt B), 319. https://doi.org/10.1016/J.YEBEH.2016.11.006

Rowitch, D. H., & Kriegstein, A. R. (2010). Developmental genetics of vertebrate glial–cell specification. *Nature 2010 468:7321*, *468*(7321), 214–222. https://doi.org/10.1038/nature09611

Rubinstein, M., Han, S., Tai, C., Westenbroek, R. E., Hunker, A., Scheuer, T., & Catterall, W. A. (2015). Dissecting the phenotypes of Dravet syndrome by gene deletion. *Brain*, *138*(8), 2219–2233. https://doi.org/10.1093/BRAIN/AWV142

Rubinstein, M., Westenbroek, R. E., Yu, F. H., Jones, C. J., Scheuer, T., & Catterall, W. A. (2015). Genetic Background Modulates Impaired Excitability of Inhibitory Neurons in a Mouse Model of Dravet Syndrome. *Neurobiology of Disease*, *73*, 106. https://doi.org/10.1016/J.NBD.2014.09.017

Sadelain, M., Papapetrou, E. P., & Bushman, F. D. (2012). Safe harbours for the integration of new DNA in the human genome. In *Nature Reviews Cancer*. https://doi.org/10.1038/nrc3179

Sadleir, L. G., Mountier, E. I., Gill, D., Davis, S., Joshi, C., Devile, C., Kurian, M. A., Mandelstam, S., Wirrell, E., Nickels, K. C., Murali, H. R., Carvill, G., Myers, C. T., Mefford, H. C., & Scheffer, I. E. (2017). Not all SCN1A epileptic encephalopathies are Dravet syndrome: Early profound Thr226Met phenotype. *Neurology*, *89*(10), 1035–1042. https://doi.org/10.1212/WNL.0000000000004331

Scalmani, P., Rusconi, R., Armatura, E., Zara, F., Avanzini, G., Franceschetti, S., & Mantegazza, M. (2006). Effects in neocortical neurons of mutations of the Na(v)1.2 Na+ channel causing benign familial neonatal-infantile seizures. *The Journal of Neuroscience : The Official Journal of the Society for Neuroscience*, *26*(40), 10100–10109. https://doi.org/10.1523/JNEUROSCI.2476-06.2006

Schafer, D. P., Jha, S., Liu, F., Akella, T., McCullough, L. D., & Rasband, M. N. (2009). Disruption of the Axon Initial Segment Cytoskeleton Is a New Mechanism for Neuronal Injury. *The Journal of Neuroscience*, *29*(42), 13242. https://doi.org/10.1523/JNEUROSCI.3376-09.2009

Schubert-Bast, S., Wolff, M., Wiemer-Kruel, A., von Spiczak, S., Trollmann, R., Reif, P. S., Pritchard, C., Polster, T., Neubauer, B. A., Mayer, T., Macdonald, D., Kurlemann, G., Kluger, G., Klein, K. M., Kieslich, M., Kay, L., Kalski, M., Irwin, J., Herting, A., … Strzelczyk, A. (2019). Seizure management and prescription patterns of anticonvulsants in Dravet syndrome: A multicenter cohort study from Germany and review of literature. *Epilepsy & Behavior*, *98*, 88–95. https://doi.org/10.1016/j.yebeh.2019.06.021

Scimemi, A. (2014). Structure,function,and plasticity of GABA transporters. *Frontiers in Cellular Neuroscience*, *8*(JUN), 161. https://doi.org/10.3389/FNCEL.2014.00161/BIBTEX

Seymour, T., Twigger, A. J., & Kakulas, F. (2015). Pluripotency Genes and Their Functions in the Normal and Aberrant Breast and Brain. *International Journal of Molecular Sciences*, *16*(11), 27288. https://doi.org/10.3390/IJMS161126024

Shan, L., Zhang, T., Fan, K., Cai, W., & Liu, H. (2021). Astrocyte-Neuron Signaling in Synaptogenesis. *Frontiers in Cell and Developmental Biology*, *9*, 1786. https://doi.org/10.3389/FCELL.2021.680301/BIBTEX

Shi, X., Yasumoto, S., Nakagawa, E., Fukasawa, T., Uchiya, S., & Hirose, S. (2009). Missense mutation of the sodium channel gene SCN2A causes Dravet syndrome. *Brain and Development*. https://doi.org/10.1016/j.braindev.2009.08.009

Shi, Y., Kirwan, P., & Livesey, F. J. (2012). Directed differentiation of human pluripotent stem cells to cerebral cortex neurons and neural networks. *Nature Protocols*. https://doi.org/10.1038/nprot.2012.116

Shi, Y., Kirwan, P., Smith, J., Robinson, H. P. C., & Livesey, F. J. (2012). Human cerebral cortex development from pluripotent stem cells to functional excitatory synapses. *Nature Neuroscience*. https://doi.org/10.1038/nn.3041

Shidara, H., Kobayashi, J., Tanamoto, R., Hotta, K., & Oka, K. (2013). Odorant-induced membrane potential depolarization of AIY interneuron in Caenorhabditis elegans. *Neuroscience Letters*, *541*, 199–203. https://doi.org/10.1016/J.NEULET.2013.02.016

Shmuely, S., Sisodiya, S. M., Gunning, W. B., Sander, J. W., & Thijs, R. D. (2016). Mortality in Dravet syndrome: A review. In *Epilepsy and Behavior*. https://doi.org/10.1016/j.yebeh.2016.09.007

Siddiqi, F., Trakimas, A. L., Joseph, D. J., Lippincott, M. L., Marsh, E. D., & Wolfe, J. H. (2021). Islet1 Precursors Contribute to Mature Interneuron Subtypes in Mouse Neocortex. *Cerebral Cortex (New York, NY)*, *31*(11), 5206. https://doi.org/10.1093/CERCOR/BHAB152

Singh, N. A., Pappas, C., Dahle, E. J., Claes, L. R. F., Pruess, T. H., De Jonghe, P., Thompson, J., Dixon, M., Gurnett, C., Peiffer, A., White, H. S., Filloux, F., & Leppert, M. F. (2009). A role of SCN9A in human epilepsies, as a cause of febrile seizures and as a potential modifier of Dravet syndrome. *PLoS Genetics*. https://doi.org/10.1371/journal.pgen.1000649

Singh, P., Doshi, S., Spaethling, J. M., Hockenberry, A. J., Patel, T. P., Geddes-Klein, D. M., Lynch, D. R., & Meaney, D. F. (2011). N-Methyl-D-aspartate Receptor Mechanosensitivity Is Governed by C Terminus of NR2B Subunit * and the Departments of ¶. *Journal of Biological Chemistry*, *287*, 4348–4359. https://doi.org/10.1074/jbc.M111.253740

Skylar-Scott, M. A., Huang, J. Y., Lu, A., Ng, A. H. M., Duenki, T., Liu, S., Nam, L. L., Damaraju, S., Church, G. M., & Lewis, J. A. (2022). Orthogonally induced differentiation of stem cells for the programmatic patterning of vascularized organoids and bioprinted tissues. *Nature Biomedical Engineering 2022 6:4*, *6*(4), 449–462. https://doi.org/10.1038/s41551-022-00856-8

Sloan, S. A., Andersen, J., Paşca, A. M., Birey, F., & Paşca, S. P. (2018). Generation and assembly of human brain region–specific three-dimensional cultures. *Nature Protocols 2018 13:9*, *13*(9), 2062–2085. https://doi.org/10.1038/s41596-018-0032-7

Sloan, S. A., Darmanis, S., Huber, N., Khan, T. A., Birey, F., Caneda, C., Reimer, R., Quake, S. R., Barres, B. A., & Paşca, S. P. (2017a). Human Astrocyte Maturation Captured in 3D Cerebral Cortical Spheroids Derived from Pluripotent Stem Cells. *Neuron*, *95*(4), 779-790.e6. https://doi.org/10.1016/J.NEURON.2017.07.035

Sloan, S. A., Darmanis, S., Huber, N., Khan, T. A., Birey, F., Caneda, C., Reimer, R., Quake, S. R., Barres, B. A., & Paşca, S. P. (2017b). Human Astrocyte Maturation Captured in 3D Cerebral Cortical Spheroids Derived from Pluripotent Stem Cells. *Neuron*, *95*(4), 779-790.e6. https://doi.org/10.1016/j.neuron.2017.07.035

Smith, D. M., McGinnis, E. J., Walleigh, D. J., & Abend, N. S. (2016). Management of Status Epilepticus in Children. *Journal of Clinical Medicine*, *5*(4). https://doi.org/10.3390/JCM5040047

Smith, J. R., Maguire, S., Davis, L. A., Alexander, M., Yang, F., Chandran, S., ffrench-Constant, C., & Pedersen, R. A. (2008a). Robust, Persistent Transgene Expression in Human Embryonic Stem Cells Is Achieved with AAVS1-Targeted Integration. *Stem Cells*. https://doi.org/10.1634/stemcells.2007-0039

Smith, J. R., Maguire, S., Davis, L. A., Alexander, M., Yang, F., Chandran, S., ffrench-Constant, C., & Pedersen, R. A. (2008b). Robust, Persistent Transgene Expression in Human Embryonic Stem Cells Is Achieved with AAVS1-Targeted Integration. *Stem Cells*, *26*(2), 496–504. https://doi.org/10.1634/STEMCELLS.2007-0039

Sohn, P. D., Huang, C. T. L., Yan, R., Fan, L., Tracy, T. E., Camargo, C. M., Montgomery, K. M., Arhar, T., Mok, S. A., Freilich, R., Baik, J., He, M., Gong, S., Roberson, E. D., Karch, C. M., Gestwicki, J. E., Xu, K., Kosik, K. S., & Gan, L. (2019). Pathogenic Tau Impairs Axon Initial Segment Plasticity and Excitability Homeostasis. *Neuron*, *104*(3), 458. https://doi.org/10.1016/J.NEURON.2019.08.008

Somarowthu, A., Goff, K. M., & Goldberg, E. M. (2021). Two-photon calcium imaging of seizures in awake, head-fixed mice. *Cell Calcium*, *96*, 102380. https://doi.org/10.1016/J.CECA.2021.102380

Somogyi, P., Tamás, G., Lujan, R., & Buhl, E. H. (1998). Salient features of synaptic organisation in the cerebral cortex. *Brain Research Reviews*. https://doi.org/10.1016/S0165-0173(97)00061-1

Spagnoli, C., Frattini, D., Rizzi, S., Salerno, G. G., & Fusco, C. (2019). Early infantile SCN1A epileptic encephalopathy: Expanding the genotype-phenotype correlations. *Seizure*, *65*, 62–64. https://doi.org/10.1016/J.SEIZURE.2019.01.002

Steel, D., Symonds, J. D., Zuberi, S. M., & Brunklaus, A. (2017). Dravet syndrome and its mimics: Beyond SCN1A. *Epilepsia*, *58*(11), 1807–1816. https://doi.org/10.1111/EPI.13889

Strzelczyk, A., Kalski, M., Bast, T., Wiemer-Kruel, A., Bettendorf, U., Kay, L., Kieslich, M., Kluger, G., Kurlemann, G., Mayer, T., Neubauer, B. A., Polster, T., Herting, A., von Spiczak, S., Trollmann, R., Wolff, M., Irwin, J., Carroll, J., Macdonald, D., … Schubert-Bast, S. (2019). Burden-of-illness and cost-driving factors in Dravet syndrome patients and carers: A prospective, multicenter study from Germany. *European Journal of Paediatric Neurology : EJPN : Official Journal of the European Paediatric Neurology Society*, *23*(3), 392–403. https://doi.org/10.1016/J.EJPN.2019.02.014

Strzelczyk, A., & Schubert-Bast, S. (2022). A Practical Guide to the Treatment of Dravet Syndrome with Anti-Seizure Medication. *CNS Drugs*, *36*(3), 217–237. https://doi.org/10.1007/S40263-022-00898-1/TABLES/2

Styr, B., Gonen, N., Zarhin, D., Ruggiero, A., Atsmon, R., Gazit, N., Braun, G., Frere, S., Vertkin, I., Shapira, I., Harel, M., Heim, L. R., Katsenelson, M., Rechnitz, O., Fadila, S., Derdikman, D., Rubinstein, M., Geiger, T., Ruppin, E., & Slutsky, I. (2019). Mitochondrial Regulation of the Hippocampal Firing Rate Set Point and Seizure Susceptibility. *Neuron*, *102*(5), 1009. https://doi.org/10.1016/J.NEURON.2019.03.045

Sun, D. A., Sombati, S., & DeLorenzo, R. J. (2001). Glutamate Injury–Induced Epileptogenesis in Hippocampal Neurons. *Stroke*, *32*(10), 2344–2350. https://doi.org/10.1161/HS1001.097242

Sun, H., Zhang, Y., Liu, X., Ma, X., Yang, Z., Qin, J., Jiang, Y., Qi, Y., & Wu, X. (2010). Analysis of SCN1A mutation and parental origin in patients with Dravet syndrome. *Journal of Human Genetics*. https://doi.org/10.1038/jhg.2010.39

Sun, Y., & Dolmetsch, R. E. (2018). Investigating the Therapeutic Mechanism of Cannabidiol in a Human Induced Pluripotent Stem Cell (iPSC)-Based Model of Dravet Syndrome. *Cold Spring Harbor Symposia on Quantitative Biology*, *83*, 185–191. https://doi.org/10.1101/SQB.2018.83.038174

Sun, Y., Paşca, S. P., Portmann, T., Goold, C., Worringer, K. A., Guan, W., Chan, K. C., Gai, H., Vogt, D., Chen, Y. J. J., Mao, R., Chan, K., Rubenstein, J. L. R., Madison, D. v., Hallmayer, J., Froehlich-Santino, W. M., Bernstein, J. A., & Dolmetsch, R. E. (2016). A deleterious Nav1.1 mutation selectively impairs telencephalic inhibitory neurons derived from Dravet Syndrome patients. *ELife*. https://doi.org/10.7554/eLife.13073

Sun, Z., & Südhof, T. C. (2021a). A simple Ca2+-imaging approach to neural network analyses in cultured neurons. *Journal of Neuroscience Methods*, *349*. https://doi.org/10.1016/J.JNEUMETH.2020.109041

Sun, Z., & Südhof, T. C. (2021b). A simple Ca2+-imaging approach to neural network analyses in cultured neurons. *Journal of Neuroscience Methods*, *349*, 109041. https://doi.org/10.1016/J.JNEUMETH.2020.109041

Tai, C., Abe, Y., Westenbroek, R. E., Scheuer, T., & Catterall, W. A. (2014). Impaired excitability of somatostatin- and parvalbumin-expressing cortical interneurons in a mouse model of Dravet syndrome. *Proceedings of the National Academy of Sciences of the United States of America*, *111*(30), E3139–E3148. https://doi.org/10.1073/PNAS.1411131111/SUPPL_FILE/PNAS.201411131SI.PDF

Tamim, I., Chung, D. Y., de Morais, A. L., Loonen, I. C. M., Qin, T., Misra, A., Schlunk, F., Endres, M., Schiff, S. J., & Ayata, C. (2021). Spreading depression as an innate antiseizure mechanism. *Nature Communications*, *12*(1). https://doi.org/10.1038/S41467-021-22464-X

Tanenhaus, A., Stowe, T., Young, A., McLaughlin, J., Aeran, R., Lin, I. W., Li, J., Hosur, R., Chen, M., Leedy, J., Chou, T., Pillay, S., Vila, M. C., Kearney, J. A., Moorhead, M., Belle, A., & Tagliatela, S. (2022). Cell-Selective Adeno-Associated Virus-Mediated SCN1A Gene Regulation Therapy Rescues Mortality and Seizure Phenotypes in a Dravet Syndrome Mouse Model and Is Well Tolerated in Nonhuman Primates. *Human Gene Therapy*, *33*(11–12), 579. https://doi.org/10.1089/HUM.2022.037

Tang, Z., Sun, X., Huo, G., Xie, Y., Shi, Q., Chen, S., Wang, X., & Liao, Z. (2013). Protective effects of erythropoietin on astrocytic swelling after oxygen-glucose deprivation and reoxygenation: mediation through AQP4 expression and MAPK pathway. *Neuropharmacology*, *67*, 8–15. https://doi.org/10.1016/J.NEUROPHARM.2012.10.017

Tao, Y., & Zhang, S. C. (2016). Neural Subtype Specification from Human Pluripotent Stem Cells. In *Cell Stem Cell*. https://doi.org/10.1016/j.stem.2016.10.015

Tatsukawa, T., Ogiwara, I., Mazaki, E., Shimohata, A., & Yamakawa, K. (2018). Impairments in social novelty recognition and spatial memory in mice with conditional deletion of Scn1a in parvalbumin-expressing cells. *Neurobiology of Disease*, *112*, 24–34. https://doi.org/10.1016/J.NBD.2018.01.009

Telenczuk, M., Fontaine, B., & Brette, R. (2017). The basis of sharp spike onset in standard biophysical models. *PLOS ONE*, *12*(4), e0175362. https://doi.org/10.1371/JOURNAL.PONE.0175362

Tian, C., Wang, K., Ke, W., Guo, H., & Shu, Y. (2014). Molecular identity of axonal sodium channels in human cortical pyramidal cells. *Frontiers in Cellular Neuroscience*, *8*. https://doi.org/10.3389/FNCEL.2014.00297/ABSTRACT

Tornero, D., Wattananit, S., Madsen, M. G., Koch, P., Wood, J., Tatarishvili, J., Mine, Y., Ge, R., Monni, E., Devaraju, K., Hevner, R. F., Brüstle, O., Lindvall, O., & Kokaia, Z. (2013). Human induced pluripotent stem cell-derived cortical neurons integrate in stroke-injured cortex and improve functional recovery. *Brain*. https://doi.org/10.1093/brain/awt278

Tran, C. H., Vaiana, M., Nakuci, J., Somarowthu, A., Goff, K. M., Goldstein, N., Murthy, P., Muldoon, S. F., & Goldberg, E. M. (2020a). Interneuron Desynchronization Precedes Seizures in a Mouse Model of Dravet Syndrome. *Journal of Neuroscience*, *40*(13), 2764–2775. https://doi.org/10.1523/JNEUROSCI.2370-19.2020

Tran, C. H., Vaiana, M., Nakuci, J., Somarowthu, A., Goff, K. M., Goldstein, N., Murthy, P., Muldoon, S. F., & Goldberg, E. M. (2020b). Interneuron Desynchronization Precedes Seizures in a Mouse Model of Dravet Syndrome. *Journal of Neuroscience*, *40*(13), 2764–2775. https://doi.org/10.1523/JNEUROSCI.2370-19.2020

Tran, C. H., Vaiana, M., Nakuci, J., Somarowthu, A., Goff, K. M., Goldstein, N., Murthy, P., Muldoon, S. F., & Goldberg, E. M. (2020c). Interneuron Desynchronization Precedes Seizures in a Mouse Model of Dravet Syndrome. *Journal of Neuroscience*, *40*(13), 2764–2775. https://doi.org/10.1523/JNEUROSCI.2370-19.2020

Traynelis, S. F., Wollmuth, L. P., McBain, C. J., Menniti, F. S., Vance, K. M., Ogden, K. K., Hansen, K. B., Yuan, H., Myers, S. J., & Dingledine, R. (2010). Glutamate Receptor Ion Channels: Structure, Regulation, and Function. *Pharmacological Reviews*, *62*(3), 405. https://doi.org/10.1124/PR.109.002451

Trump, N., McTague, A., Brittain, H., Papandreou, A., Meyer, E., Ngoh, A., Palmer, R., Morrogh, D., Boustred, C., Hurst, J. A., Jenkins, L., Kurian, M. A., & Scott, R. H. (2016). Improving diagnosis and broadening the phenotypes in early-onset seizure and severe developmental delay disorders through gene panel analysis. *Journal of Medical Genetics*, *53*(5), 310–317. https://doi.org/10.1136/JMEDGENET-2015-103263

Tsai, M. S., Lee, M. L., Chang, C. Y., Fan, H. H., Yu, I. S., Chen, Y. T., You, J. Y., Chen, C. Y., Chang, F. C., Hsiao, J. H., Khorkova, O., Liou, H. H., Yanagawa, Y., Lee, L. J., & Lin, S. W. (2015). Functional and structural deficits of the dentate gyrus network coincide with emerging spontaneous seizures in an Scn1a mutant Dravet Syndrome model during development. *Neurobiology of Disease*, *77*, 35–48. https://doi.org/10.1016/J.NBD.2015.02.010

Uchino, K., Kawano, H., Tanaka, Y., Adaniya, Y., Asahara, A., Deshimaru, M., Kubota, K., Watanabe, T., Katsurabayashi, S., Iwasaki, K., & Hirose, S. (2021). Inhibitory synaptic transmission is impaired at higher extracellular Ca2+ concentrations in Scn1a+/− mouse model of Dravet syndrome. *Scientific Reports*, *11*(1), 10634. https://doi.org/10.1038/S41598-021-90224-4

Uchino, K., Tanaka, Y., Ikezawa, W., Deshimaru, M., Kubota, K., Watanabe, T., Katsurabayashi, S., Iwasaki, K., & Hirose, S. (2023). Astrocyte Ca2+ signaling is facilitated in Scn1a+/− mouse model of Dravet syndrome. *Biochemical and Biophysical Research Communications*, *643*, 169–174. https://doi.org/10.1016/J.BBRC.2022.12.084

Urbach, R., & Technau, G. M. (2013). *Dorsoventral Patterning of the Brain: A Comparative Approach*. https://www.ncbi.nlm.nih.gov/books/NBK6006/

Vahedi, K., Depienne, C., Le Fort, D., Riant, F., Chaine, P., Trouillard, O., Gaudric, A., Morris, M. A., LeGuern, E., Tournier-Lasserve, E., & Bousser, M. G. (2009). Elicited repetitive daily blindness: a new phenotype associated with hemiplegic migraine and SCN1A mutations. *Neurology*, *72*(13), 1178–1183. https://doi.org/10.1212/01.WNL.0000345393.53132.8C

van Hugte, E. J. H., Lewerissa, E. I., Wu, K. M., Parodi, G., van Voorst, T., Kogo, N., Keller, J. M., Schubert, D., Schelhaas, H. J., Verhoeven, J., Majoie, M., van Bokhoven, H.,

Kasri, N. N., & Conceived, N. N. K. E. J. H. V. H. (2023). SCN1A-deficient hiPSC-derived excitatory neuronal networks display mutation-specific phenotypes. *BioRxiv*, 2023.01.11.523598. https://doi.org/10.1101/2023.01.11.523598

Velasco, S., Kedaigle, A. J., Simmons, S. K., Nash, A., Rocha, M., Quadrato, G., Paulsen, B., Nguyen, L., Adiconis, X., Regev, A., Levin, J. Z., & Arlotta, P. (2019). Individual brain organoids reproducibly form cell diversity of the human cerebral cortex. *Nature 2019 570:7762*, *570*(7762), 523–527. https://doi.org/10.1038/s41586-019-1289-x

Velasco, S., Paulsen, B., & Arlotta, P. (2020). 3D Brain Organoids: Studying Brain Development and Disease Outside the Embryo. *Https://Doi.Org/10.1146/Annurev-Neuro-070918-050154*, *43*, 375–389. https://doi.org/10.1146/ANNUREV-NEURO-070918-050154

Verbeek, N. E., Wassenaar, M., van Campen, J. S., Sonsma, A., Gunning, B., Knoers, N., Lindhout, D., Jansen, F. E., Leijten, F., Brilstra, E. H., & Kasteleijn-Nolst Trenité, D. (2015). Seizure precipitants in Dravet syndrome: What events and activities are specifically provocative compared with other epilepsies? *Epilepsy & Behavior : E&B*, *47*, 39–44. https://doi.org/10.1016/J.YEBEH.2015.05.008

Vigneault, É., Poirel, O., Riad, M., Prud'homme, J., Dumas, S., Turecki, G., Fasano, C., Mechawar, N., & el Mestikawy, S. (2015). Distribution of vesicular glutamate transporters in the human brain. *Frontiers in Neuroanatomy*, *9*(MAR), 23. https://doi.org/10.3389/FNANA.2015.00023/BIBTEX

Vogt, N. (2021). Assembloids. *Nature Methods 2021 18:1*, *18*(1), 27–27. https://doi.org/10.1038/s41592-020-01026-x

Vong, K. I., Leung, C. K. Y., Behringer, R. R., & Kwan, K. M. (2015). Sox9 is critical for suppression of neurogenesis but not initiation of gliogenesis in the cerebellum. *Molecular Brain*, *8*(1), 1–18. https://doi.org/10.1186/S13041-015-0115-0/FIGURES/8

Voskobiynyk, Y., Battu, G., Felker, S. A., Cochran, J. N., Newton, M. P., Lambert, L. J., Kesterson, R. A., Myers, R. M., Cooper, G. M., Roberson, E. D., & Barsh, G. S. (2021). Aberrant regulation of a poison exon caused by a non-coding variant in a mouse model of Scn1a-associated epileptic encephalopathy. *PLOS Genetics*, *17*(1), e1009195. https://doi.org/10.1371/JOURNAL.PGEN.1009195

Wang, C., Ward, M. E., Chen, R., Liu, K., Tracy, T. E., Chen, X., Xie, M., Sohn, P. D., Ludwig, C., Meyer-Franke, A., Karch, C. M., Ding, S., & Gan, L. (2017). Scalable Production of iPSC-Derived Human Neurons to Identify Tau-Lowering Compounds by High-Content Screening. *Stem Cell Reports*. https://doi.org/10.1016/j.stemcr.2017.08.019

Wang, R. N., Green, J., Wang, Z., Deng, Y., Qiao, M., Peabody, M., Zhang, Q., Ye, J., Yan, Z., Denduluri, S., Idowu, O., Li, M., Shen, C., Hu, A., Haydon, R. C., Kang, R., Mok, J., Lee, M. J., Luu, H. L., & Shi, L. L. (2014). Bone Morphogenetic Protein (BMP) signaling in development and human diseases. *Genes & Diseases*, *1*(1), 87–105. https://doi.org/10.1016/J.GENDIS.2014.07.005

Wang, W., Takashima, S., Segawa, Y., Itoh, M., Shi, X., Hwang, S. K., Nabeshima, K., Takeshita, M., & Hirose, S. (2011). The developmental changes of Nav1.1 and Nav1.2 expression in the human hippocampus and temporal lobe. *Brain Research*, *1389*, 61–70. https://doi.org/10.1016/J.BRAINRES.2011.02.083

Wang, Y., & Mandelkow, E. (2015). Tau in physiology and pathology. *Nature Reviews Neuroscience 2015 17:1*, *17*(1), 22–35. https://doi.org/10.1038/nrn.2015.1

Wang, Y., Sun, D., Yue, Z., Tang, W., Xiao, B., & Feng, L. (2016). Rats with Malformations of Cortical Development Exhibit Decreased Length of AIS and Hypersensitivity to Pilocarpine-Induced Status Epilepticus. *Neurochemical Research*, *41*(9), 2215–2222. https://doi.org/10.1007/S11064-016-1936-7/FIGURES/4

Warner, T. A., Liu, Z., Macdonald, R. L., & Kang, J. Q. (2017). Heat induced temperature dysregulation and seizures in Dravet Syndrome/GEFS+ Gabrg2+/Q390X mice. *Epilepsy Research*, *134*, 1–8. https://doi.org/10.1016/J.EPLEPSYRES.2017.04.020

Watanabe, K., Kamiya, D., Nishiyama, A., Katayama, T., Nozaki, S., Kawasaki, H., Watanabe, Y., Mizuseki, K., & Sasai, Y. (2005). Directed differentiation of telencephalic precursors from embryonic stem cells. *Nature Neuroscience*. https://doi.org/10.1038/nn1402

Wefelmeyer, W., Cattaert, D., & Burrone, J. (2015). Activity-dependent mismatch between axo-axonic synapses and the axon initial segment controls neuronal output. *Proceedings of the National Academy of Sciences of the United States of America*, *112*(31), 9757–9762. https://doi.org/10.1073/PNAS.1502902112/SUPPL_FILE/PNAS.201502902SI.PDF

Wegner, M. (2001). Expression of transcription factors during oligodendroglial development. *Microscopy Research and Technique*, *52*(6), 746–752. https://doi.org/10.1002/JEMT.1059

Wengert, E. R., Wagley, P. K., Strohm, S. M., Reza, N., Wenker, I. C., Gaykema, R. P., Christiansen, A., Liau, G., & Patel, M. K. (2022). Targeted Augmentation of Nuclear Gene Output (TANGO) of Scn1a rescues parvalbumin interneuron excitability and reduces seizures in a mouse model of Dravet Syndrome. *Brain Research*, *1775*. https://doi.org/10.1016/J.BRAINRES.2021.147743

Wenzel, M., Hamm, J. P., Peterka, D. S., & Yuste, R. (2019). Acute Focal Seizures Start As Local Synchronizations of Neuronal Ensembles. *Journal of Neuroscience*, *39*(43), 8562–8575. https://doi.org/10.1523/JNEUROSCI.3176-18.2019

Wiese, S., Karus, M., & Faissner, A. (2012). Astrocytes as a source for extracellular matrix molecules and cytokines. *Frontiers in Pharmacology*, *3 JUN*, 120. https://doi.org/10.3389/FPHAR.2012.00120/BIBTEX

Wimmer, V. C., Reid, C. A., So, E. Y. W., Berkovic, S. F., & Petrou, S. (2010). Axon initial segment dysfunction in epilepsy. *The Journal of Physiology*, *588*(Pt 11), 1829. https://doi.org/10.1113/JPHYSIOL.2010.188417

Wonders, C. P., & Anderson, S. A. (2006). The origin and specification of cortical interneurons. In *Nature Reviews Neuroscience*. https://doi.org/10.1038/nrn1954

Xiang, Y., Tanaka, Y., Patterson, B., Kang, Y. J., Govindaiah, G., Roselaar, N., Cakir, B., Kim, K. Y., Lombroso, A. P., Hwang, S. M., Zhong, M., Stanley, E. G., Elefanty, A. G., Naegele, J. R., Lee, S. H., Weissman, S. M., & Park, I. H. (2017). Fusion of Regionally Specified hPSC-Derived Organoids Models Human Brain Development and Interneuron Migration. *Cell Stem Cell*, *21*(3), 383-398.e7. https://doi.org/10.1016/j.stem.2017.07.007

Xu, J. C., Fan, J., Wang, X., Eacker, S. M., Kam, T. I., Chen, L., Yin, X., Zhu, J., Chi, Z., Jiang, H., Chen, R., Dawson, T. M., & Dawson, V. L. (2016). Cultured networks of excitatory projection neurons and inhibitory interneurons for studying human cortical neurotoxicity. *Science Translational Medicine*. https://doi.org/10.1126/scitranslmed.aad0623

Xu, L., Ding, X., Wang, T., Mou, S., Sun, H., & Hou, T. (2019). Voltage-gated sodium channels: structures, functions, and molecular modeling. In *Drug Discovery Today*. https://doi.org/10.1016/j.drudis.2019.05.014

Xu, Q., Cobos, I., de La Cruz, E. D., Rubenstein, J. L., & Anderson, S. A. (2004). Origins of Cortical Interneuron Subtypes. *The Journal of Neuroscience*, *24*(11), 2612. https://doi.org/10.1523/JNEUROSCI.5667-03.2004

Yamada, R., & Kuba, H. (2016). Structural and Functional Plasticity at the Axon Initial Segment. *Frontiers in Cellular Neuroscience*, *10*(OCT2016). https://doi.org/10.3389/FNCEL.2016.00250

Yang, N., Chanda, S., Marro, S., Ng, Y. H., Janas, J. A., Haag, D., Ang, C. E., Tang, Y., Flores, Q., Mall, M., Wapinski, O., Li, M., Ahlenius, H., Rubenstein, J. L., Chang, H. Y., Buylla, A. A., Südhof, T. C., & Wernig, M. (2017). Generation of pure GABAergic neurons by transcription factor programming. *Nature Methods*. https://doi.org/10.1038/nmeth.4291

Yu, F. H., Mantegazza, M., Westenbroek, R. E., Robbins, C. A., Kalume, F., Burton, K. A., Spain, W. J., McKnight, G. S., Scheuer, T., & Catterall, W. A. (2006a). Reduced sodium current in GABAergic interneurons in a mouse model of severe myoclonic epilepsy in infancy. *Nature Neuroscience*. https://doi.org/10.1038/nn1754

Yu, F. H., Mantegazza, M., Westenbroek, R. E., Robbins, C. A., Kalume, F., Burton, K. A., Spain, W. J., McKnight, G. S., Scheuer, T., & Catterall, W. A. (2006b). Reduced sodium current in GABAergic interneurons in a mouse model of severe myoclonic epilepsy in infancy. *Nature Neuroscience 2006 9:9*, *9*(9), 1142–1149. https://doi.org/10.1038/nn1754

Yu, F. H., Mantegazza, M., Westenbroek, R. E., Robbins, C. A., Kalume, F., Burton, K. A., Spain, W. J., McKnight, G. S., Scheuer, T., & Catterall, W. A. (2006c). Reduced sodium current in GABAergic interneurons in a mouse model of severe myoclonic epilepsy in infancy. *Nature Neuroscience 2006 9:9*, *9*(9), 1142–1149. https://doi.org/10.1038/nn1754

Yu, G. L., Zhang, Y., & Ning, B. (2021). Reactive Astrocytes in Central Nervous System Injury: Subgroup and Potential Therapy. *Frontiers in Cellular Neuroscience*, *15*, 538. https://doi.org/10.3389/FNCEL.2021.792764/BIBTEX

Yue, W. D., Zhang, Y. H., Gu, F., Wang, J., Zhang, J. Y., & Gu, R. M. (2008). Mechanisms underlying low [Ca2+]o-induced increased excitability of hippocampal neurons. *Neuroscience Bulletin*, *24*(6), 367–373. https://doi.org/10.1007/S12264-008-0429-3

Zhang, X., Qiao, Z., Liu, N., Gao, L., Wei, L., Liu, A., Ma, Z., Wang, F., Hou, S., Li, J., & Shen, H. (2019). Stereotypical patterns of epileptiform calcium signal in hippocampal CA1, CA3, dentate gyrus and entorhinal cortex in freely moving mice. *Scientific Reports 2019 9:1*, *9*(1), 1–9. https://doi.org/10.1038/s41598-019-41241-x

Zhang, Y., Pak, C. H., Han, Y., Ahlenius, H., Zhang, Z., Chanda, S., Marro, S., Patzke, C., Acuna, C., Covy, J., Xu, W., Yang, N., Danko, T., Chen, L., Wernig, M., & Südhof, T. C. (2013). Rapid single-step induction of functional neurons from human pluripotent stem cells. *Neuron*. https://doi.org/10.1016/j.neuron.2013.05.029